Dissertation
submitted to the
Combined Faculties for the Natural Sciences and for Mathematics
of the Ruperto-Carola University of Heidelberg, Germany
for the degree of
Doctor of Natural Sciences

Put forward by
Dipl.-Phys. Christoph Aberle
Born in Villingen-Schwenningen
Oral examination: December 1st, 2011

Optimization, simulation and analysis of the scintillation signals in the Double Chooz experiment

Referees: Prof. Dr. Manfred Lindner
Prof. Dr. Klaus Blaum

Optimierung, Simulation und Analyse der Szintillationssignale im Double Chooz experiment

Das Reaktorneutrinoexperiment Double Chooz sucht nach dem letzten unbekannten Neutrinomischungswinkel θ_{13}, der mit fundamentalen offenen Fragen der Teilchenphysik verbunden ist. Ein Konzept mit zwei Detektoren wird eingesetzt, um ein mögliches Defizit an Elektron-Antineutrinos im Abstand von einem Kilometer zur Quelle zu messen. Ein Gadolinium-beladener organischer Flüssigszintillator dient als Neutrino-Target. Der Gadolinium-freie Gamma Catcher Szintillator umgibt das Neutrino-Target, um die Detektoreffizienz und deren Fehler zu verbessern.
Die Lichtausbeuten von Target und Gamma Catcher wurden optimiert und angeglichen mithilfe von Labormessungen, einem Energietransfermodell und Monte Carlo Simulationen. Eine Analyse von Detektordaten zeigt, dass das Angleichen der Lichtausbeute erfolgreich war mit einer Genauigkeit von einem Prozent. Die optische Stabilität für die ersten 3.5 Monate konnte mit Daten des fernen Detektors gezeigt werden. Die Energieauflösung wurde verbessert, indem Labormessungen und eine Anpassung der Monte Carlo Simulation des Ionisationsquenchingeffekts für Elektronen und Alphateilchen durchgeführt wurden. Zusätzlich führten Simulationen der positionsabhängigen Effizienz der Lichtsammlung im Detektor zu einer Methode, um Inhomogenitäten zu korrigieren. Das Zeitverhalten der Detektorantwort wurde für Elektronen und Alphateilchen untersucht und die Zeitverteilung der Szintillatoremission wurde aktiv verändert, um Pulsformanalysemöglichkeiten zu verbessern.

Optimization, simulation and analysis of the scintillation signals in the Double Chooz experiment

The reactor neutrino experiment Double Chooz searches for the last unknown neutrino mixing angle θ_{13} which is connected to fundamental open questions in particle physics. A two-detector concept is employed to analyze disappearance of electron antineutrinos at a baseline of one kilometer. A gadolinium-loaded organic liquid scintillator is used as a neutrino target. The gadolinium-free Gamma Catcher scintillator surrounds the neutrino target to improve the detector efficiency and its error.
The light yields of Target and Gamma Catcher have been optimized and matched with laboratory measurements, an energy transfer model and Monte Carlo simulations. An analysis of detector data demonstrates that the light yield matching was successful at the one percent level. Optical stability for the first 3.5 months of far detector data taking is shown. The energy reconstruction was improved by laboratory measurements and Monte Carlo tuning of the ionization quenching effect for electrons and alpha particles. In addition, simulations of the position dependent detector light collection efficiency led to an inhomogeneity correction method. The detector response timing was studied for alphas and electrons and the scintillator photon emission times were actively tuned to enhance pulse shape discrimination capabilities.

Contents

1 Introduction **1**
- 1.1 Neutrino oscillations . . . 2
  - 1.1.1 Neutrino oscillation formalism . . . 2
  - 1.1.2 The neutrino mixing angle θ_{13} . . . 4
- 1.2 The Double Chooz reactor neutrino experiment . . . 8
  - 1.2.1 Concept of Double Chooz and θ_{13} sensitivity . . . 8
  - 1.2.2 Detector design . . . 12
  - 1.2.3 Background . . . 13
  - 1.2.4 Detector calibration . . . 16
  - 1.2.5 The Double Chooz Monte Carlo software DOGS . . . 17
  - 1.2.6 The Double Chooz liquid scintillators . . . 20

2 Light yield optimization and analysis of the Double Chooz scintillators **26**
- 2.1 Introduction and Motivation . . . 26
- 2.2 Experimental setup . . . 26
- 2.3 Light yield model . . . 31
- 2.4 Laboratory measurement results . . . 33
- 2.5 Target composition . . . 35
- 2.6 Light yield, photoelectron yield and density matching . . . 36
- 2.7 Absolute light yield and long term stability . . . 42
- 2.8 Photoelectron yield matching analysis with detector data . . . 43
- 2.9 Light yield stability analysis of detector data . . . 54
- 2.10 Summary . . . 55

3 Nonlinearity in the scintillation light production of low energy electrons **58**
- 3.1 Introduction and Motivation . . . 58
- 3.2 The ionization quenching process . . . 59
- 3.3 Laboratory measurement setup . . . 60
- 3.4 Laboratory measurement results . . . 67
- 3.5 Monte Carlo tuning . . . 71
- 3.6 Summary . . . 82

4 Alpha quenching laboratory measurements and Monte Carlo simulation tuning **85**
- 4.1 Introduction and Motivation . . . 85
- 4.2 Energy loss of alpha particles passing through matter . . . 86

4.3 Alpha sources for the laboratory measurements . . . 88
4.3.1 The ^{210}Po source . . . 89
4.3.2 The ^{222}Rn, ^{218}Po and ^{214}Po source . . . 89
4.4 Experimental setup . . . 90
4.5 Quenching factor results from laboratory measurements . . . 95
4.6 Determination of the Birks parameter and Monte Carlo tuning . . . 101
4.7 Summary . . . 107

5 Scintillator emission time studies 109
5.1 Introduction and Motivation . . . 109
5.2 Experimental setup . . . 110
5.3 Extraction of the time profiles . . . 117
5.4 Evaluation of the experimental emission time probability density functions 119
5.5 Results and discussion . . . 121
5.6 Summary . . . 129

6 Detector homogeneity studies with simulation 131
6.1 Introduction and Motivation . . . 131
6.2 Attenuation length effects with 1 MeV electrons . . . 131
6.2.1 Implementation of a hypothetical attenuation length degradation in the Monte Carlo simulation . . . 131
6.2.2 Results for 1 MeV electrons . . . 133
6.3 Attenuation length effect on neutrino candidate selection . . . 137
6.4 Detector efficiency inhomogeneity correction . . . 143
6.4.1 Detector efficiency map concept . . . 143
6.4.2 Production of the Monte Carlo detector efficiency map . . . 143
6.4.3 PE_{reco} correction with the detector efficiency map . . . 144
6.5 Summary . . . 147

7 Summary 149

A The energy reconstruction tool ERecoHD 151

B List of analysed runs 156

List of Figures 160

List of Tables 164

Bibliography 165

1 Introduction

The Standard Model of particle physics contains six different fundamental leptons. Although it is extremely successful in describing the interactions of these particles to high precision there are observations which show that it is not complete. The first clear evidence for physics beyond the Standard Model was obtained in the neutrino sector. It was discovered that neutrinos have non-zero masses by observing neutrino oscillations. Neutrino oscillations are not possible if neutrinos are massless which is the case in the Standard Model.

First proposed by Pontecorvo [1] in analogy to the transformations of neutral kaons, the neutrino oscillation mechanism was further developed to describe the mixture of neutrino flavor states (section 1.1.1). Although huge progress has been made in the field of neutrino oscillation physics, the understanding of flavor in particle physics is still incomplete. The questions why there are three different flavors and where the masses of the elementary fermions come from, are open. The goal is to find a theory beyond the Standard Model which explains the patterns of lepton masses and flavor mixing.

The complete determination of the parameters which govern neutrino oscillations will help unveil the patterns of neutrino mixing and thus contribute to the advancement of theoretical particle physics on a fundamental level. Currently, an effort is made to measure the last unknown mixing angle θ_{13} (section 1.1.2). Combining all available data on neutrino oscillations, a hint for a non-zero θ_{13} is obtained. This indicates that there is a good chance for the current generation of reactor neutrino experiments to measure the value of θ_{13}. It is closely related to the possibility of discovering CP violation in the lepton sector with neutrino oscillations. Depending on the value of θ_{13} the next generation of experiments (e.g. neutrino factories and superbeams), which will test the fundamental CP symmetry, can be designed. CP violation in the lepton sector could provide an explanation for the matter-antimatter asymmetry of the universe via leptogenesis [2, 3].

Reactor neutrino experiments with a baseline of a few kilometers give a clean measurement of the size of θ_{13}. The systematic error of the measurement can be kept small by using two or more detectors in order to measure the neutrino flux at different distances from the neutrino source. Recent results for the prediction of neutrino fluxes from nuclear reactors obtain different results than the previous standard calculation. The new result predicts higher neutrino fluxes. Measuring the flux closer to the reactor with a second detector helps to cancel the uncertainties coming from the flux prediction.

The reactor neutrino experiment Double Chooz employs a two phase concept (section 1.2). The sensitivity on θ_{13} can be improved rapidly with only one detector. In the second phase, another detector is installed closer to the reactor in order to measure the unoscillated neutrino flux and thus lower the overall systematic error of the experiment.

Neutrinos are detected via the inverse beta decay with a newly developed gadolinium-loaded liquid scintillator. The presence of gadolinium improves the signal to background ratio for neutrino-induced events significantly. Apart from the Neutrino Target (also: Target) a second, gadolinium-free layer of scintillator (Gamma Catcher) is used in the inner part of the detector. It surrounds the Target in order to produce light from gammas which escape the Target volume after neutrino interactions.

This work investigates the central optical properties of the liquid scintillators as light yield, attenuation lengths, ionization quenching and photon emission time. The results were used to optimize the final composition of the Double Chooz Target and Gamma Catcher scintillators. The scintillator properties have been investigated with laboratory measurements. The obtained scintillator characteristics are used to tune the Monte Carlo simulation of Double Chooz which is needed to model the detector response accurately. On the level of precision which is aimed for in the measurement of θ_{13}, a well-tuned Monte Carlo simulation is mandatory. The Monte Carlo simulation could then in turn be used to study the detector response. The Double Chooz data taking started recently and first analyses of the light yield and detector stability with actual Double Chooz far detector data are presented.

1.1 Neutrino oscillations

1.1.1 Neutrino oscillation formalism

Neutrinos do only interact via the gravitational and the weak force. It is therefore difficult to detect them. Nevertheless, three different neutrinos (or their antiparticles) could be first experimentally discovered by weak interactions with the corresponding charged lepton: In 1956, Reines and Cowan detected the electron antineutrino $\bar{\nu}_e$ [4, 5] and were awarded the Nobel Prize in 1995. The second neutrino type (ν_μ and $\bar{\nu}_\mu$) was detected in 1962 [6] and in the year 2001 the direct detection of the tau neutrino ν_τ succeeded [7].

The present standard description of neutrino oscillations comprises the transformation of three flavor states ν_e, ν_μ and ν_τ (and their antiparticles) into each other. Neutrino oscillations in vacuum were first developed for two neutrino types and then later extended to three flavors [8, 9]. They are based on the difference between flavor eigenstates and mass eigenstates. A flavor eigenstate can be written as a linear superposition of the three mass eigenstates [10]:

$$|\nu_\alpha\rangle = \sum_{i=1}^{3} U_{\alpha i}|\nu_i\rangle \qquad \alpha = e, \mu, \tau \quad i = 1, 2, 3. \tag{1.1}$$

In the three flavor scenario, $U_{\alpha i}$ are the elements of an unitarian mixing matrix U, which contains the probabilities for the various oscillations. The Pontecorvo-Maki-Nakagawa-

Sakata (PMNS) matrix parametrization [8] is usually chosen:

$$U = \begin{pmatrix} 1 & 0 & 0 \\ 0 & \cos(\theta_{23}) & \sin(\theta_{23}) \\ 0 & -\sin(\theta_{23}) & \cos(\theta_{23}) \end{pmatrix} \times \begin{pmatrix} \cos(\theta_{13}) & 0 & \sin(\theta_{13})e^{-i\delta_{CP}} \\ 0 & 1 & 0 \\ -\sin(\theta_{13})e^{i\delta_{CP}} & 0 & \cos(\theta_{13}) \end{pmatrix} \times \begin{pmatrix} \cos(\theta_{12}) & \sin(\theta_{12}) & 0 \\ -\sin(\theta_{12}) & \cos(\theta_{12}) & 0 \\ 0 & 0 & 1 \end{pmatrix} \times \begin{pmatrix} e^{i\phi_1} & 0 & 0 \\ 0 & e^{i\phi_2} & 0 \\ 0 & 0 & 1 \end{pmatrix}. \tag{1.2}$$

This parametrization contains three mixing angles θ_{ij}, the CP-violating Dirac phase δ_{CP} and the two CP-violating Majorana phases ϕ_1 and ϕ_2.

By inserting the time evolution of the mass eigenstates in equation (1.1) and projecting the flavor eigenstate onto the evolved state after the time t, the oscillation probability from flavor state α to flavor state β can be derived:

$$P_{\alpha\to\beta}(t) = |\langle\nu_\beta|\nu_\alpha(t)\rangle|^2 = |\sum_{i=1}^{3} U_{\alpha i}U^*_{\beta i}e^{-iE_i t}|^2. \tag{1.3}$$

For neutrino energies accessible in experiments, the assumption can be made that the neutrinos are ultra-relativistic. The oscillation probability can then be expressed in terms of a distance L from the point where the neutrino has been generated as a flavor eigenstate. Using the PMNS matrix parametrization, we arrive at the general oscillation probabilities for three neutrino generations:

$$P_{\alpha\to\beta}(L) = \sum_{i=1,j=1}^{3} U_{\alpha i}U^*_{\beta i}U^*_{\alpha j}U_{\beta j}e^{-i\frac{m_i^2-m_j^2}{2E}L}. \tag{1.4}$$

In principle, two types of experiments can be done: So-called 'appearance experiments' search for a neutrino flavor which is not produced in the neutrino source. 'Disappearance experiments' measure the same flavor which is generated by the source. Due to neutrino oscillations, the number of measured events can be lowered compared to the expectation without oscillations.

Multiple experiments with solar, atmospheric and reactor neutrinos as well as neutrinos generated at accelerators (see [11] and references therein) have established the neutrino oscillation scenario with three active neutrinos. Up to now, two of the three mixing angles have been measured. The squared mass differences which fix the oscillation lengths are known, too. Due to matter effects in neutrino oscillations [12, 13] one of the signs of the two squared mass differences could be obtained. Table 1.1 shows the current status for the values of the relevant parameters for three generation neutrino oscillations.

The two Majorana phases cancel in neutrino oscillations and have to be addressed by other means. The CP-violating Dirac phase, the second sign for the squared mass differences (corresponding to normal or inverted hierarchy respectively) and the third mixing angle θ_{13} are still unknown. An extensive experimental effort is ongoing to obtain

parameter	best fit value with 1σ errors
$\Delta m^2_{21}[10^{-5}\text{eV}^2]$	$7.59^{+0.20}_{-0.18}$
$\Delta m^2_{31}[10^{-3}\text{eV}^2]$	$2.50^{+0.09}_{-0.16}$ (n.H.), $-2.40^{+0.08}_{-0.09}$ (i.H.)
$\sin^2(\theta_{12})$	$0.312^{+0.017}_{-0.015}$
$\sin^2(\theta_{23})$	0.52 ± 0.06

Table 1.1: Neutrino oscillation parameter best fit values from a global analysis [14, 15]. The squared mass differences are defined as $\Delta m^2_{21} = m^2_2 - m^2_1$. The values in case of normal hierarchy ($\Delta m^2_{31} > 0$) are indicated by (n.H.), the values for the inverted hierarchy ($\Delta m^2_{31} < 0$) are followed by (i.H.).

the remaining parameters of neutrino oscillations in order to unveil the underlying theory of neutrino masses and mixings. In the next section, the status on θ_{13} and its connection with δ_{CP} and the mass hierarchy (sign of Δm^2_{31}) is discussed.

1.1.2 The neutrino mixing angle θ_{13}

In this section two complementary approaches for measuring θ_{13} are discussed. First, reactor neutrino measurements are described briefly and second, long-baseline accelerator neutrinos experiments are outlined. Then, the status of a global analysis of the neutrino oscillation parameters is summarized.

Reactor neutrino experiments The basic idea for reactor neutrino experiments is the measurement of the disappearance of electron antineutrinos $\bar{\nu}_e$. Reactors are a well localized and strong source of $\bar{\nu}_e$ without contributions of other neutrino types and a reasonable knowledge of the flux on the few percent level can be obtained. The energy of the neutrinos produced in a nuclear reactor is in the range of ≤ 10 MeV. It is thus energetically impossible to produce the charged leptons μ and τ via CC interactions. A measurement of the fraction of unoscillated $\bar{\nu}_e$ gives the survival probability

$$\begin{aligned} P_{\bar{\nu}_e \to \bar{\nu}_e}(L) = 1 &- 4c^2_{12}c^2_{13}s^2_{12}c^2_{13} \cdot \sin^2\left(\frac{\Delta m^2_{21}}{4E}L\right) \\ &- 4c^2_{12}c^2_{13}s^2_{13} \cdot \sin^2\left(\frac{\Delta m^2_{21}}{4E}L\right) \\ &- 4s^2_{12}c^2_{13}s^2_{13} \cdot \sin^2\left(\frac{\Delta m^2_{32}}{4E}L\right). \end{aligned} \tag{1.5}$$

This expression was obtained from equation (1.4). The abbreviations c_{ij} and s_{ij} denote $\cos(\theta_{ij})$ and $\sin(\theta_{ij})$, respectively. In Figure 1.1 the survival probability is shown graphically. The leading oscillation with the first minimum at a baseline of about 50 km was investigated with the KamLAND experiment [16]. The measurement contributed to the measurement of θ_{12} and most notably to Δm^2_{21} presented in table 1.1. For shorter

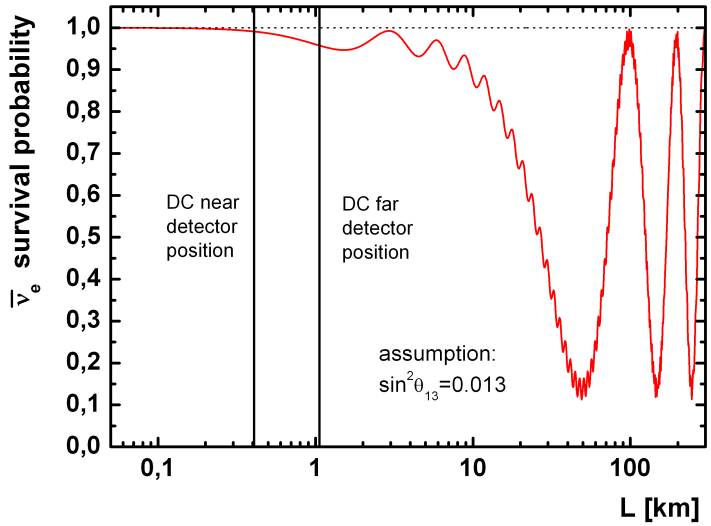

Figure 1.1: Survival probability $P_{\bar{\nu}_e \to \bar{\nu}_e}(L)$ (see equation (1.5)) for electron antineutrinos at a distance L from the source. A typical neutrino energy for reactor antineutrinos of 3 MeV and the best fit values for the normal hierarchy shown in table 1.1 are used. For the unknown subleading oscillation amplitude an assumption of $\sin^2(\theta_{13}) = 0.013$ is made (coming from the hint presented below). Two oscillation patterns occur at different length scales. The oscillation with the higher amplitude at a length scale above tens of kilometers has been probed by the KamLAND experiment [16]. The positions of the two Double Chooz far and near detectors are shown (see section 1.2).

baselines of the order of 1 km, the subleading oscillation mode can be cleanly measured. At these baselines the effect of the Δm^2_{21}-driven oscillation is small and thus the first term in equation (1.5) can be approximately neglected. If additionally $\Delta m^2_{31} \approx \Delta m^2_{32}$ is inserted the survival probability at distances in the km range becomes

$$P_{\bar{\nu}_e \to \bar{\nu}_e}(L) = 1 - \sin^2(2\theta_{13}) \cdot \sin^2(\frac{\Delta m^2_{23}}{4E} L). \tag{1.6}$$

This result shows that for reactor neutrino experiments at distances $\mathcal{O}(1\text{ km})$ the amplitude of the oscillation probability provides a clean measurement of the mixing angle θ_{13}. The experiments Double Chooz [17], RENO [18] and Daya Bay [19] belong to the newest generation of reactor neutrino experiments which employ the concept of two or more detectors at different distances to the reactors to provide a relative measurement of the neutrino fluxes and thus decrease the systematic error related to the prediction of the neutrino flux.

Accelerator neutrino oscillation experiments Experiments with muon (anti-)neutrino beams generated at accelerators provide additional measurements which are sensitive to θ_{13}. The appearance of electron neutrinos in a muon neutrino beam and the appearance of electron antineutrinos in a muon antineutrino beam can be studied. From equation (1.4) the corresponding probabilities $P_{\nu_\mu \to \nu_e}(L)$ and $P_{\bar{\nu}_\mu \to \bar{\nu}_e}(L)$ can be derived [20]. Opposed to the $\bar{\nu}_e$ disappearance reactor experiments described with equation (1.6), the measurement of θ_{13} with these neutrino beams is correlated with δ_{CP} and the mass hierarchy. This means that there is a complementarity between reactor experiments and accelerator experiments in the determination of the remaining unknown neutrino mixing parameters: For a single accelerator experiment the parameters are degenerated and can not be disentangled. The unambiguous information on θ_{13} from reactor neutrino experiments thus helps to disentangle the degeneracies. Depending on the outcome of the new generation of reactor neutrino experiments (either measurement of θ_{13} or better upper limits) a new generation of accelerator based neutrino oscillation experiments can be designed: superbeams and neutrino factories [21, 22, 23].

The appearance of electron neutrinos ν_e in a ν_μ beam has been investigated recently by the first generation superbeam experiment T2K [24] and the conventional beam experiments MINOS [25] and K2K [26]. In conventional beams protons are accelerated and directed onto a Target where mainly pions and kaons are produced. In the subsequent decay of the hadrons muons and muon neutrinos are generated. Superbeams provide higher neutrino fluxes with less beam contamination (here a contamination would be the presence of ν_e or $\bar{\nu}_e$). T2K is one of the first generation superbeam experiments using an off-axis muon neutrino beam to suppress beam contamination and get a cleaner energy distribution. The beam is produced at the J-PARC accelerator and then directed to the Super Kamiokande detector. The observed number of electron neutrino candidates is 6 with expected 1.5 ± 0.3 (syst.) events if θ_{13} is zero. This corresponds to a significance for a non-zero θ_{13} at the 2.5 σ level. MINOS finds 62 candidate events at an expected background of 49.6 $\pm$ 7.0 (stat.) $\pm$ 2.7 (syst.). This result can be combined with the T2K result. In the next paragraph, the overall status on θ_{13} is discussed.

Status of θ_{13} A global analysis of the experimental data on neutrino oscillations gives a hint for a non-zero θ_{13}. The main contribution to this hint comes from the T2K experiment. However, a combination of solar, atmospheric, reactor and accelerator experiments can be jointly analyzed [14]. The resulting significance of a nonzero θ_{13} of about 3 σ "depends somewhat on assumptions concerning the analysis of reactor neutrino data" [14]. The ambiguity comes from a re-analysis of reactor neutrino fluxes [27, 28] which predicts a 3 % higher flux compared to the previous prediction in [29]. Depending on the way this new result is treated in the global neutrino oscillation analysis, the significance of θ_{13} varies. The hint persists if the new reactor fluxes are treated differently [14] or if the old flux estimate is taken into account. In Figure 1.2 the results of the global analysis for $\sin^2(\theta_{13})$ are shown for one of the options of including the new reactor fluxes. The best fit value obtained is $\sin^2(\theta_{13}) = 0.013^{+0.007}_{-0.005}$ for the normal hierarchy and $0.016^{+0.008}_{-0.006}$ for the inverted hierarchy. The current best upper limit coming from a single

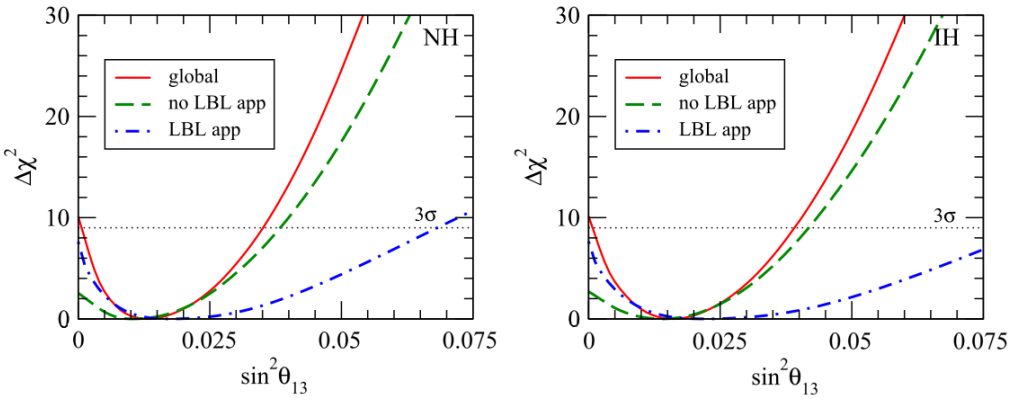

Figure 1.2: Plot taken from [14]: The label 'LBL app' corresponds to T2K and MINOS ν_e appearance data (long baseline experiments), 'no LBL app' denotes the other available neutrino oscillation data. The red lines correspond to the combined global analysis. The left (right) plot shows the normal (inverted) hierarchy. For these plots the new reactor neutrino flux has been applied together with the data from short baseline ($\lesssim$ 100m) reactor experiments.

experiment is $\sin^2(\theta_{13}) \leq 0.039$ (90 % CL) [11] measured by the CHOOZ collaboration [30, 31].

In summary, there seems to be a good chance that a measurement of the value of θ_{13} is imminent. The reactor neutrino experiment Double Chooz has already started to take data in spring 2011 and results are expected at the end of 2011.

1.2 The Double Chooz reactor neutrino experiment

1.2.1 Concept of Double Chooz and θ_{13} sensitivity

The concept of the Double Chooz (DC) [17] experiment is based on a two-detector disappearance measurement of the $\bar{\nu}_e$ flux at distances of 1.05 km and 400 m from the two reactor cores of a nuclear power plant. An overview of the Double Chooz site is shown in Figure 1.3. In Figure 1.1 the survival probability of electron antineutrinos is shown. For this plot, $\sin^2(\theta_{13})$ which is to be determined, is assumed to be 0.013 (coming from the hint presented in [14]). The far and near detector positions are indicated in Figure 1.1. It can be seen that the near detector is at a position where the neutrinos are largely unoscillated. Thus, the near detector provides a measurement of the reactor flux. The far detector is close to the first minimum in the survival probability. If a deficit in the neutrino flux is found, it can be concluded that part of the electron antineutrinos from the reactor changed their flavor and from this, θ_{13} can be obtained via equation (1.6).

Figure 1.3: The Double Chooz experiment site with two reactor cores and two detectors.

The predecessor-experiment CHOOZ obtained the current best upper limit of $\sin^2(\theta_{13}) \leq 0.039$ (90 % CL) [11, 30, 31] with only one detector. Similar sensitivity was achieved by the Palo Verde experiment [32]. The Double Chooz experiment has an improved

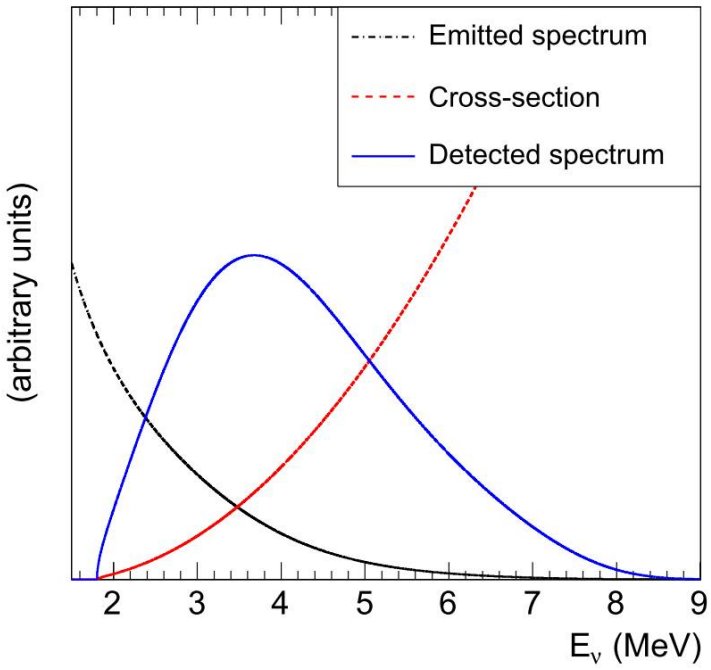

Figure 1.4: Plot taken from [27]. Multiplication of the inverse beta decay cross section (red line) and the electron antineutrino spectrum (black line) gives the spectral shape for the neutrinos which are observable in a reactor neutrino experiment (blue line). Here, fissions from ^{235}U are used as an example.

sensitivity due to an improved detector design and the use of the second detector. It will acquire more statistics (statistical error of 0.4 % instead of 2.8 % for CHOOZ [33]) through a larger sensitive volume and longer measurement time and it will have lower systematic errors (aimed for 0.6 % instead of 2.7 % in CHOOZ [33]). The improvement in the systematic errors comes largely from the second detector which cancels the uncertainties on the reactor neutrino flux. A newly developed gadolinium-loaded liquid scintillator [34, 35, 36] (section 1.2.6) is used in Double Chooz as Neutrino Target to guarantee a high optical stability and thus allow for longer measurement times. The projected sensitivity of the Double Chooz experiment after 5 years is $\sin^2(2\theta_{13}) \leq 0.03$ at 90 % CL.

The neutrino source of Double Chooz is a nuclear reactor with two cores operated by Electricité de France (EdF). It is located in the Ardenne region near the Belgium border. The combined thermal power of the two reactor cores of approximately 8.5 $GW_{th.}$ relates to a neutrino flux of about $1.6 \cdot 10^{21}$ neutrinos per second. The neutron-rich fission products of the fuel components ^{235}U, ^{238}U, ^{239}Pu and ^{241}Pu undergo beta decays which lead to approximately 6 $\bar{\nu}_e$ per fission [37]. The neutrino energy spectra, which are falling off for higher energies, are provided in [27].

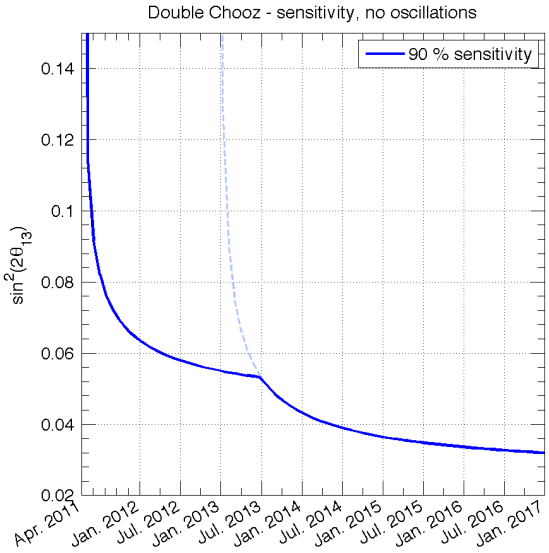

Figure 1.5: Sensitivity on $\sin^2(2\theta_{13})$ at 90 % CL for the time scale of the Double Chooz experiment. After the sensitivity improves quickly in the initial phase with only the near detector it is limited by systematic errors later. Then, the sensitivity improves again with the second (near) detector which will start data taking approximately 1.5 years after the far detector.

The neutrino detection reaction is the inverse beta decay

$$\bar{\nu}_e + p \rightarrow n + e^+. \tag{1.7}$$

Electron antineutrinos are captured on protons in H-atoms in the detection material, releasing a neutron and a positron. The neutrino energy can be directly reconstructed from the kinetic energy of the positron if the kinetic energy of the neutron ($\mathcal{O}(10$ keV)) is neglected:

$$E_{\bar{\nu}_e} \approx E_{e^+} + m_N - m_P. \tag{1.8}$$

From this, the threshold for the detection of inverse beta decay events follows: $m_N - m_P + m_{e^+} = 1.8$ MeV. While the reactor neutrino energy spectrum decreases at higher energies the cross section for the inverse beta decay increases. If the cross section is multiplied with the neutrino energy spectrum, the observable neutrino energy spectrum is obtained (see Figure 1.4). A rate of about 50 neutrinos (350 neutrinos) per day is expected in the far (near) detector. The exact numbers depend on the thermal power of the reactors and the efficiency of the detectors (and of course on θ_{13}).

Double Chooz sensitivity The method for the calculation of the sensitivity of Double Chooz is described in [38]. The results have been updated. In Figure 1.5 [39] the sensitivity of $\sin^2(2\theta_{13})$ at 90 % confidence limit (CL) is shown. The far detector started data taking in April 2011 and the near detector will follow within two years. The near

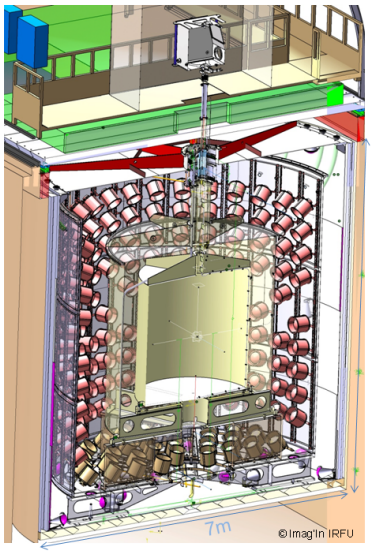

Figure 1.6: Cross section through the Double Chooz detector.

detector does not immediately improve the sensitivity since it has to acquire sufficient statistics first. After about 6 months of near detector data taking the sensitivity will improve faster again. For phase one with the far detector only the uncertainty on the neutrino flux from the reactor is an important systematical errors. With the near detector this uncertainty cancels. In the beginning a neutrino rate analysis will be done. With sufficiently high statistics, the shape of the neutrino energy spectrum can be analyzed as well. Different neutrino energies are differently affected by oscillations at the fixed baseline from the reactor to the far detector (see equation (1.6)). This affects the shape of the measured spectrum.

With the far detector alone the sensitivity is quickly improving in the first months of data taking and first results from Double Chooz can be expected soon. The limit obtained by the T2K analysis presented in section 1.1.2 and the CHOOZ limit of $\sin^2(2\theta_{13}) \leq 0.15$ (90 % CL) [11] will be reached within about 3 months. Relating to the hint on θ_{13}, Double Chooz has a high discovery potential. After five years of data taking the sensitivity limit on $\sin^2(2\theta_{13})$ which was set by the CHOOZ experiment will be improved to $\sin^2(2\theta_{13}) \leq 0.03$ (90 % CL).

Reactor anomaly A new result on the prediction of neutrino fluxes from nuclear reactors has been presented recently [27]. The flux prediction is about 3 % higher than in a previous analysis [29]. However, there is a tension between the new prediction and reactor neutrino experiments at baselines below 100 m which agree better with the old flux prediction. If the new prediction was correct, a possible explanation for the difference would be the existence of a fourth neutrino which reduces the $\bar{\nu}_e$ flux due to oscillations to the fourth state at distances < 10 m [28]. The Double Chooz near detector can

provide a new accurate measurement at a baseline which is still unaffected by the θ_{13} driven oscillation. For the analysis of the first phase of Double Chooz, the measurement from one of the short-baseline experiments can be used for normalization as it was done in CHOOZ.

1.2.2 Detector design

The two detectors are supposed to be as identical as possible in order to reduce systematic effects when the two measured electron antineutrino fluxes are compared. In Figure 1.6 the layout of the detector is shown. The diameter and height of the detector is about 7 m each. It consists of four cylindrical, separated layers which are discussed below along with other main components of the detector.

Neutrino Target The inner volume is the Neutrino Target where the inverse beta decay events (see equation (1.7)) are detected. It is filled with 10.3 m^3 of a newly developed gadolinium-loaded liquid scintillator [34, 35, 36]. The positron from inverse beta decay produces a prompt scintillation signal. It excites the scintillator molecules and then annihilates producing two 511 keV gamma rays. The Compton electrons which are scattered by the gamma rays also contribute to the light production.

After thermalization, neutron capture on hydrogen or gadolinium and subsequent deexcitation of the nucleus and associated gamma production provides the delayed signal. The addition of 1 g/l gadolinium to the scintillator produces a more specific coincidence signal since the energy released at deexcitation is about 8 MeV compared to 2.22 MeV for hydrogen capture events. Additionally, with gadolinium the capture time constant is shorter (≈ 30 μs for 0.1 % Gd) compared to around 180 μs for hydrogen. Gadolinium has a high cross-section for neutron capture: At the concentration of approximately 0.1 % Gd which is used in DC, the probability for capture on Gd is 85 %. A coincidence in time between the prompt and the delayed events is done. With gadolinium the signal to background ratio is increased largely since 8 MeV is above the natural radioactivity energies and an effective cut can be made on the delayed energy deposition. In addition, the coincidence window size can be reduced (e.g. < 100 μs after the prompt event) which leads to lower probabilities for accidental coincidences.

Gamma Catcher The second layer which surrounds the Target is the Gamma Catcher (GC) volume. It is filled with 22.3 m^3 of a gadolinium-free scintillator. Gammas from neutrino induced events which escape the Target volume can be detected in the GC. Thus, the efficiency for neutrino detection is higher and can be determined more accurately than without GC. Two transparent acrylic vessels of 8 mm and 12 mm thickness are used to contain the Target and the GC scintillators, respectively.

Buffer and photomultiplier tubes The Buffer volume is introduced in order to reduce backgrounds coming from external radioactivity and from muon-induced neutrons which can travel from outside the detector to the inner volumes. The volume is filled with

approximately 100 m^3 of a non-scintillating organic liquid. It is contained in a steel tank (3 mm thickness) which is also used to mount 390 photomultipier tubes (PMTs). The 10 inch PMTs (the red cylinders in Figure 1.6 show the magnetic shields of the PMTs) collect the light produced in the inner part of the detector and convert it to electronic signals which are further processed. All PMTs have been tested and calibrated individually before installation in the detector [40, 41].

Inner Muon Veto The Inner Veto (IV) surrounds the Buffer volume. It is optically separated from the inner three volumes by the steel tank of the Buffer. Another scintillator mixture (90 m^3) is used in the IV and the reflecting walls are equipped with 78 PMTs (8 inch). The IV is an active volume which is mainly used to detect atmospheric muons entering the detector. In such a case a veto can be applied in the offline data analysis and events which are close in time can be discarded from the neutrino analysis. The preliminary rate of muons in the IV extracted from Double Chooz detector data is 39 s^{-1} while the rate in the inner three volumes is about 11 s^{-1} [39]. The IV has also the ability to detect part of the fast neutrons via proton recoil. These neutrons are muon induced and can contribute to the correlated background if the muon itself misses the veto systems (see section 1.2.3).

Outer Muon Veto Additionally to the IV, multiple layers of plastic scintillator strips are placed above the detector as an additional vetoing system for muons. The Outer Veto (OV) can be used to check the efficiency of the IV and it covers small insensitive regions in the IV system like for example part of the chimney region. Combining IV and OV a muon tracking can be done with higher precision. In order to reduce the muon flux, the two detectors are built underground with a shielding of 300 mw.e (meters water equivalent) for the far detector and about 115 mw.e. for the near detector. Nevertheless, important backgrounds for the neutrino analysis (see below) are muon-induced.

Simplified signal processing scheme In the PMTs, photons are converted to photoelectrons at the cathode and then further amplified by a cascade of dynodes. The obtained signals are amplified, grouped together and then directed to the trigger system. If the detector readout threshold is exceeded the single, unmodified PMT waveforms are read out one-by-one with flash-analog-to-digital converters (flash-ADCs). The waveforms are stored and can later be processed in an offline analysis.

1.2.3 Background

The neutrino signals are selected based on the energy of the prompt and delayed events and the time difference between prompt and delayed event. In order to be sensitive to disappearance in reactor $\bar{\nu}_e$ oscillations, a good understanding of the experiments' background is crucial. Two different classes of background are distinguished: Accidental coincidences and correlated backgrounds. Accidental coincidences occur if two independent signals (singles) pass the energy cuts within the coincidence time window.

Correlated backgrounds originate from only one physical process which mimics both the prompt and delayed signal.

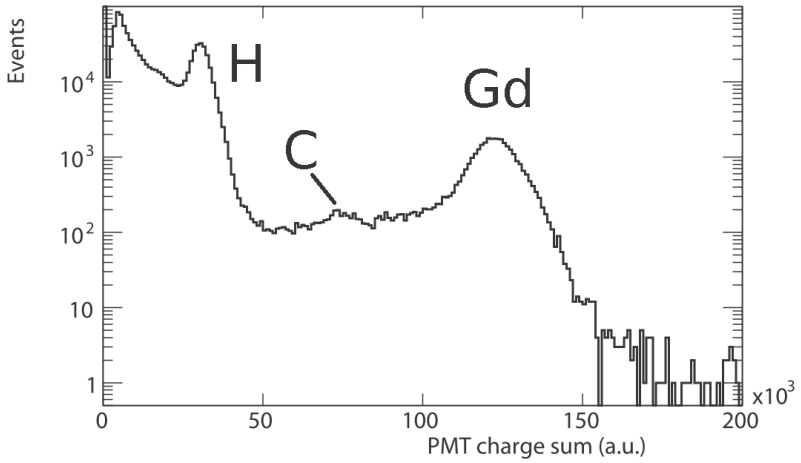

Figure 1.7: Preliminary energy spectrum of energy depositions in coincidence with a muon (30 μs to 300 μs after a muon). Mainly neutron captures are included plus a background from singles which fall into the coincidence window accidentally. It can be seen that to the right of the gadolinium peak (8 MeV) the background is very small. Left of the peak, events with gammas escaping the Target and GC volumes produce a tail. The small carbon capture peak (4.95 MeV) can be seen as well. The hydrogen capture peak (2.223 MeV) is more prominent than the gadolinium peak here because events in the larger GC volume are included where no gadolinium is present.

Accidental background The most important contribution for the prompt signals in accidental background comes from radioactivity-induced events. Also alpha emitters and beta emitters inside the scintillator contribute. However, the effect of ionization quenching discussed in chapter 4 for alpha particles leads to lower light output (factor $\gtrsim 10$) than for electrons if the same amount of energy is deposited. The results of dedicated measurements presented in chapter 4 show that most of the alpha particles in natural radioactivity thus are below the cut for neutrino candidate prompt events. Additionally, alpha particle events can be potentially identified using pulse shape discrimination techniques. In chapter 5 measurements of the scintillator photon emission times are presented for electrons and alpha particles.

Since the delayed energy deposition threshold can be chosen above the radioactivity background, the delayed event in accidental background is provided mainly by neutrons which are captured on gadolinium. Neutrons can be produced by muons. If the muons are not detected by the IV and OV systems no veto is applied.

The accidental rate (along with the prompt energy spectrum) can be measured in the experiment for example by looking for delayed signals in an off-time window. For accidentals the rate is the same regardless of the choice of the time delay between prompt and delayed events. If this delay is chosen high enough to avoid the neutrino-induced signals, a direct measurement can be obtained. The materials of the detector have been carefully chosen and purified if needed. Measurements have been done to ensure that the radiopurity requirements are met and thus the rate from singles is low. Surrounding the IV a 15 cm thick stainless steel layer is installed to shield the detector from gammas coming from the surrounding rock.

The preliminary measured singles rate in the far detector in the prompt event energy region (here: 0.7 MeV to 12 MeV) is about 10 s^{-1} [39] which is close to the design goal in the proposal [17]. The singles rate in the delayed energy region is smaller than 0.1 s^{-1} which is two times better than the specification value from the proposal. The low accidental backgrounds can also be seen in a preliminary energy spectrum (Figure 1.7) coming from an analysis of muon-induced neutrons [39]. In chapter 2 a sophisticated study of the hydrogen capture peak with real detector data is presented.

Correlated background Correlated background is more difficult to analyze. It is hard to quantify and separate from the neutrino signal. Here, the main contributions to the correlated background in Double Chooz are summarized. An important background which is hard to reject comes from cosmogenic isotopes [42] produced inside the active volumes Target and GC. They are produced by interactions of muons with the carbon nuclei in the scintillator. The isotopes ^{8}He, ^{9}Li and (less important) ^{11}Li can be produced. They have half-lifes of 122, 178 and 8.5 milliseconds, respectively [43]. The half-lifes are too high to apply a veto after each muon since the muon rate is about 11 s^{-1} and thus the detector would be essentially always vetoed. These isotopes can decay via β-n cascades. The prompt signal is provided by the electrons and the delayed signal is provided by the neutron. The beta spectra are similar to the prompt energy spectra from inverse beta decay. Since the production rate of the isotopes is not well known (1.5 events per day in Target plus GC are estimated [17], see [44] for KamLAND estimates at a higher overburden) an analysis with Double Chooz can provide important information on this background for inverse beta decay detection which is useful for other experiments as well. Studies about the cosmogenic background can be found in [45].

The second source of correlated background comes from so-called fast neutrons. If a neutron with sufficiently high energy is generated by a muon in the surrounding rock, it can sometimes enter the inner detector without triggering the IV or OV muon systems. The neutron loses energy by colliding with protons in the scintillator. These recoil protons produce light in the scintillator and can mimic prompt signals while the neutron can eventually be captured by gadolinium and provide the delayed signal. The possibilities to treat this background are analyzed in [45].

Instrumental light noise Another source of background events comes from instrumental light emission (also called light noise) at the bases of the photomultiplier tubes

(PMTs) [46]. Since these events do not originate in the scintillator, the light emission follows different patterns both in the shape of the pulses and the distribution of the charge in the PMTs. These differences can be used to distinguish scintillation events and instrumental light noise events. It is thus important to know the emission time of the scintillators. In chapter 5 measurements of the scintillator photon emission times are presented. Specialized cuts have been developed by the DC group in order to reject the light noise events. In section 2.8 these cuts are discussed and applied in a detector data analysis.

Direct background measurement A direct measurement of the background can be done if the nuclear reactors are not running. If enough statistics can be acquired during such a condition a statistical background subtraction can be done. Also with reduced reactor power an estimate of the background can be obtained by extrapolating to zero reactor power. Therefore periods with significantly lowered reactor power are important.

1.2.4 Detector calibration

A calibration program with multiple systems is conducted in order to understand the detector response with precision. Calibration sources at known positions and with known particle energies are essential in testing and optimizing the reconstruction performance of the data analysis and the associated systematics. Here the systems are briefly presented:

- **Light injection system:** LED light can be emitted into the detector from various positions at the walls. Different wavelengths are available. The light can be either emitted diffusely or focused.
- **Guide tube:** The guide tube is suited to bring sources to various positions in the GC volume with the help of wires which are fed through the tube.
- **z-axis system:** Calibration sources can be deployed through the chimney along the z-axis of the Target.
- **Buffer tube:** A vertical tube in the Buffer volume in which sources can be deployed.
- **Articulated arm:** A system which can position sources in three dimensions in the Target volume. This system will become particularly important in the second phase of Double Chooz to reduce the systematic errors for example from detector inhomogeneities.

The LED light injection system is used frequently since no materials have to be introduced into the detector. It is used to check the stability of the detector response and calibrate the individual PMT gains and their relative timing.

Operations with the other systems are more complicated and time-consuming since sources have to be introduced into the detector. Risks for the detector have to be

carefully avoided. Therefore these calibrations are done less frequently. The different sources which are deployed comprise gamma sources, neutron sources and artificial light sources as for example a laser. With this extensive calibration program the energy scale of the detector can be calibrated and the cut efficiencies for the neutrino events can be estimated (a total systematic error of about 2 % is aimed for in the first phase with one detector).

For example the so-called 'spill-in' and 'spill-out' effects can be quantified with neutron sources. Spill-out is a class of neutrino-induced events where the neutron from inverse beta decay travels from the Target through the acrylic vessel to the GC. Since the GC is gadolinium-free the neutron is captured on hydrogen or carbon and the delayed energy cut is not fulfilled. Spill-in is the opposite case where a neutron from a inverse beta decay reaction in the GC travels to the Target volume. There it can be captured on gadolinium and thus identified as neutrino candidate. The neutrino rate has to be corrected for the difference of both effects. Combining both effects, an increase in the neutrino detection rate between 2 % and 3 % is obtained from simulation depending on the cuts (in particular the coincidence time cut) [45]. Apart from calibration, different methods can be used to quantify spill-in and spill-out: One method is to use pulse shape discrimination for the prompt events since the pulse shapes of events in Target and GC have been designed to be different from each other (see chapter 5).

Optical properties of the scintillators can be tested with the calibration systems as well. The experimental studies on the optical properties with small scintillator samples presented in this work provide the tuning of the Monte Carlo simulation at the current stage. The results can later be cross-checked for the large scale scintillators with detector calibration data and a better understanding of the energy scale will be obtained combining the information from the lab measurements with calibration or with detector data coming from natural sources.

1.2.5 The Double Chooz Monte Carlo software DOGS

In this section several selected packages of the Double Chooz Monte Carlo (MC) software `DOGS`[1] (Double Chooz offline group software) and their relationship are described. A complete simulation chain from the reactor cores to the output of the detector electronics is available. Here, relevant software tools for this work are described.

DCNuGen2 The simulation chain starts with the package `DCNuGen2` which simulates the neutrino interactions in the Double Chooz detectors. As input `DCNuGen2` requires information about the location of the individual reactor cores and the detectors. Additionally, the reactor core power can be specified along with the reactor fuel composition. The detector geometry is directly read from the same database which is used for the detector simulation. The protons number (from hydrogen atoms) in the detector is needed and a value for θ_{13} can be specified together with the other relevant neutrino oscillation

[1] DOGS is written in C++ as well as the simulation code `Geant4` which is used for the particle tracking in `DCGLG4sim`.

parameters.
The output of DCNuGen2 consists of the vertices of neutrino interactions in the detector with the corresponding positron and neutron energy from inverse beta decay. An event list is generated with this information which can be read by the detector simulation DCGLG4sim.

DCGLG4sim The tracking of particles in the Double Chooz detector geometry is managed by DCGLG4sim. It can be described as an interface between the tracking algorithm and general physics processes implementation in Geant4 [47] on the one hand and the Double Chooz specific simulation configuration on the other hand. This is for example the geometry, material properties but also choice of the physics processes and the details of the optical model (described below in more detail). During this work, the optical model of the MC simulation was tuned with the newest available data coming from measurements of the scintillator properties. In order to achieve a precise energy calibration of the experiment which is needed for low systematical errors, the details of the scintillator photon emission characteristics is crucial. With laboratory measurements presented in this work, the simulation was tuned to be as realistic as possible even at an early stage when no detector data was available.

As input for DCGLG4sim all kinds of particles can be directly inserted into the detector or alternatively an event list for example from DCNuGen2 can be used. The particles are propagated through the detector in a step approach where they produce photons. The photons are tracked by Geant4 and scintillator absorption (with or without reemission) and reflections on detector components are simulated. If the photon hits the photocathode of a photomultiplier tube (PMT) it can produce a photoelectron (PE) with a certain probability. The DCGLG4sim simulation stops at that point and gives the time for the PE and the corresponding PMT channel number.

DCRoSS After the simulation of the PE distributions for each PMT the electronics of the experiment can be simulated in DCRoSS including for example PMT effects, the flash-ADC (flash-analog-to-digital converter) readout of the data and a trigger simulation. The output of this package has the same format as the detector data (after the data is processed with the so-called 'Dogsifier'). After the RoSS simulation the same reconstruction tools can be applied both for data and MC.

DCRecoPulse The first reconstruction stage consists of a PMT-wise determination of the charge and (with gain calibration) the number of PE. This reconstruction is done by the DCRecoPulse algorithms. The input for this package are the raw waveforms from the flash-ADCs (either from MC or from detector data). It provides the time and the charge of each pulse in the waveforms.

DCReco After pulse reconstruction the next level of reconstruction is the vertex reconstruction. Several different algorithms are available for this task. In this work the highly developed vertex reconstruction RecoBAMA has been used. In RecoBAMA information on

the individual PMT charges and the times at which the charges occur is used to estimate the centroid of the light emission in a given event. Both the vertex reconstruction and the pulse reconstruction are part of the Common Trunk (CT) which provides first reconstruction steps. The CT output is data format which is common to all collaborators for further analysis.

The optical model in DCGLG4sim In the following the scintillation treatment in the optical model of the MC simulation is described shortly. For a realistic simulation of absorption and reemission in the scintillator the MC optical model uses the attenuation lengths of the single components of the scintillators (see section 1.2.6 for a general overview of the scintillator) instead of the attenuation length of the complete liquid: After absorption by PPO or bis-MSB, the photon can be reemitted with a certain probability. The PPO (bis-MSB) molecule has a quantum efficiency of 100 % (94 %) [48]. If a photon is absorbed by one of the solvents or the gadolinium complex, the photon is absorbed and is not reemitted in the simulation. This reflects the fact that for the wavelengths of the primary emission spectrum the attenuation lengths of these three components are dominated by non-fluorescent components or impurities. Thus, the attenuation length (or more precisely the molar extinction coefficients) of the single components have to be measured individually.

The reemission spectrum after absorption by PPO follows the primary scintillation spectrum which is cut at the wavelength of the absorbed photon (since the wavelength of the reemitted photon can not be smaller than the wavelength of the absorbed photon). If bis-MSB absorbs and reemits a photon the wavelength of the photon is drawn from the pure bis-MSB fluorescence spectrum. The effect of the absorption and reemission processes is a shift to higher wavelengths (see section 1.2.6).

The primary scintillation spectrum has been measured with a fluorimeter. It can be described as a combination of the PPO and bis-MSB fluorescence spectra. It is measured using a triangular cell where typically several millimeters of scintillator have already been passed by the photons. The spectrum is thus already partly shifted. Figure 1.8 shows this wavelength shifting process of the primary scintillation spectrum as it is simulated in `DCGLG4sim`.

The reason for using the partly shifted spectrum as the primary spectrum in the simulation is that the light yield and photon emission time measurements have been performed with a similar cell where a similar amount of wavelength shifting occurs before the photomultipliers are hit. Thus, after the MC tuning with measurements in this work, the simulation of the number of photons, the emission time (chapter 5) and the spectral shape are consistent for the generated scintillation light in simulation. The number of photons is primarily determined by the light yield which is studied in detail in chapter 2. Important corrections in the number of photons come from the ionization quenching process (see chapters 3 and 4) and additional light is produced in the Cherenkov process. One part of this work was the tuning of the optical model in order to improve the simulation. For a precision experiment like Double Chooz a well-tuned MC software is essential.

1.2.6 The Double Chooz liquid scintillators

The large scale production (> 40 tons total) of the Target (near and far detector) and GC (far detector) liquids was done in 2010 at MPIK [49]. After production the far detector liquids were shipped to France and the filling was started. During production and filling the scintillators were kept under nitrogen atmosphere. Due to the rather fragile acrylic vessels the filling operation was very delicate since e.g. a height difference of more than three centimeter between two different detector volumes would have already been critical for the mechanical stability.

Before the Double Chooz scintillators are discussed the main processes in scintillation light production are outlined. Then, the main properties of the scintillators and their requirements are given.

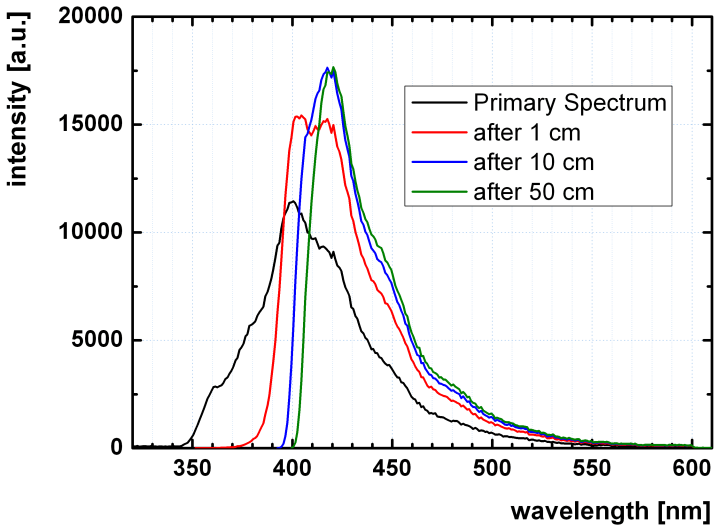

Figure 1.8: Simulated wavelength shifting of the primary scintillation spectrum at different distances from the primary excitation. In the (experimentally determined) primary spectrum the PPO fluorescence spectrum contributes significantly. The part to the right represents the bis-MSB emission contribution. After 1 cm, 10 cm and 50 cm the spectrum is shifted more and more to the emission spectrum of bis-MSB and thus to higher wavelengths.

Production of scintillation light and wavelength shifting Charged particles excite the molecules of the scintillator. Most frequently, the non-localized electrons in the π-bonds of the phenyl groups in the aromatic scintillator components are excited. Following excitation, the possible vibrational and rotational excitation of the molecule is quickly ($\mathcal{O}(10^{-12}$ s) [50]) transformed to heat by collisions with other molecules. The

π-electrons deexcite from higher energy electronic levels to the first excited state by internal radiationless conversion processes ($\mathcal{O}(10^{-11}$ s) [50]). The first excited state of isolated molecules deexcites under photon emission on a time scale of nanoseconds for an excited singlet state (fluorescence) and on longer time scales for triplet states which are populated less often (phosphorescence). In liquid scintillators however, the molecules are not isolated and radiationless energy transfers are important. A quantum mechanical treatment of radiationless energy transfer by Förster [51, 52] quantifies how the radiationless transfer probability increases with increasing overlap between the emission spectrum of the donor molecule with the absorption spectrum of the acceptor molecule.

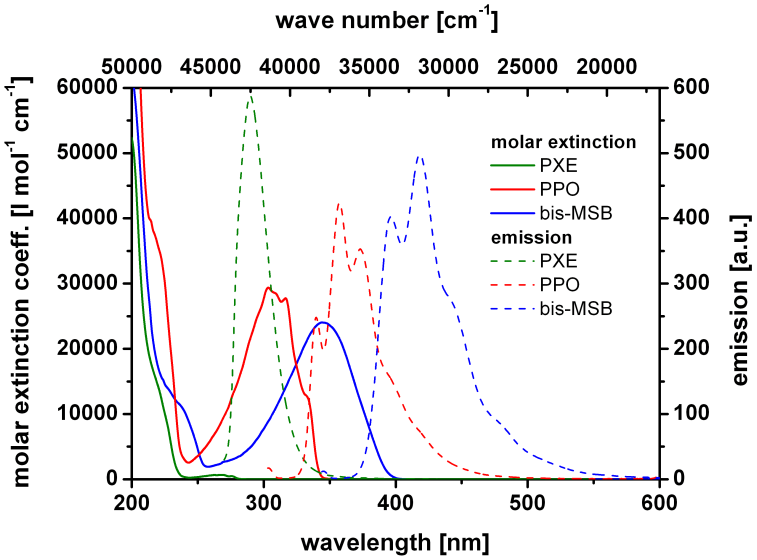

Figure 1.9: Molar extinction coefficients (solid) and emission (dashed) spectra of the aromatic components in the Target and GC scintillators. Due to the Stokes-shift the emission spectra are at higher wavelength than the absorption spectra of the same molecule. Efficient wavelength-shifting is achieved with the two fluors PPO and bis-MSB in PXE (see table 1.2 for information on the chemicals). The emission has been measured with a commercial Cary Eclipse fluorimeter and the molar extinction was measured with a Cary400 UV/Vis spectrometer.

The absorption spectra of aromatic molecules overlap with their own emission spectrum. Thus, if only a pure aromatic component was used in the scintillator, less light would be emitted by the solution due to higher probability for losses after multiple absorptions and reemissions. Therefore, aromatic solutes are added to shift the wavelength of the photons to higher values where the mixture is more transparent. They are chosen such that they have a first excited state at lower energy than the aromatic solvent. This re-

sults in a high overlap between the emission spectrum of the solvent and the absorption spectrum of the solute. The wavelength-shifting aromatic solutes are also called 'fluors' because their most important property (concerning scintillators) is fluorescence.

In Double Chooz two types of fluors are added to shift the wavelength efficiently to a region where the scintillator is transparent. In Figure 1.9 the spectra are shown for the aromatic components of the Target and GC scintillators. It can be seen that the emission spectrum of PXE and the absorption spectrum of PPO as well as the emission spectrum of PPO and the absorption spectrum of bis-MSB have high overlap. This leads to an efficient energy transfer. Most of the scintillation light is eventually emitted by bis-MSB and since its concentration is chosen to be small (20 mg/l) the overall transparency of the scintillator at the scintillator's emission spectrum is high. Thus, more light can reach the PMTs. Additionally, the fluors have been chosen such that the wavelengths of the shifted emission spectrum of the scintillators match the region of the highest quantum efficiency in the PMTs.

The different energy transfer paths between the scintillator components are used to model the light yield of the Double Chooz scintillators (section 2.3). The results presented there lead to an optimization of the scintillator compositions.

Double Chooz scintillator compositions and requirements The scintillator compositions are listed in table 1.2 and general properties are given in table 1.3. In this work, the focus is on the Target and GC scintillators as it was the responsibility of the MPIK to produce these two scintillators. The non-scintillating Buffer and the Veto were designed and produced in Munich and are listed here for completeness.

The basic requirements for the scintillators are discussed along with the resulting compositions of Target and GC:

- **Safety considerations:** The flashpoint of the solvents is required to be high enough. PXE has been chosen since it has a rather high flashpoint. Additionally, the toxicity of PXE is lower than for other solvent candidates.

- **Chemical stability and solubility of gadolinium in the Target scintillator:** In the past, other experiments like CHOOZ [30] and Palo Verde [53] observed a significant degradation of attenuation lengths in their gadolinium-loaded scintillators on a timescale of hundreds of days. In order to avoid this for the gadolinium-loaded Double Chooz Target scintillator, a suitable complex was found at MPIK Heidelberg [34, 35, 36]. Metal-β-diketones were used in neutrino physics for the first time by Hartmann and Naumann [54]. A Gd-β-diketone molecule was synthesized (in collaboration with Sensient Imaging Technologies) to achieve solubility and long-term stability of the rare earth gadolinium in the scintillator. The main difficulty is to dissolve the metal gadolinium in the organic liquid. Because of the organic nature of β-diketones this goal is achieved by incorporating the Gd-atom in a highly stable complex with three β-diketone ligands.

- **Material compatibility (mainly with the acrylic vessels):** For material compatibility reasons (pure PXE can damage the acrylic) n-dodecane (also: dodecane

Scintillator	Component	Chemical Name	CAS	Conc.
ν Target	PXE	ortho-Phenylxylylethane	6196-95-8	20 $\%_{\text{vol.}}$
	Dodecane	n-Dodecane	112-40-3	80 $\%_{\text{vol.}}$
	PPO	2,5-Diphenyloxazole	92-71-7	7 g/l
	bis-MSB	4-bis-(2-Methylstyryl)benzene	13280-61-0	20 mg/l
	$Gd(thd)_3$	Gd(III)-tris-(2,2,6,6-tetra-methyl-heptane-3,5-dionate)	14768-15-1	1 g/l Gd
	THF	Tetrahydrofuran	109-99-9	0.5 $\%_{\text{wt.}}$
GC	PXE	ortho-Phenylxylylethane	6196-95-8	4 $\%_{\text{vol.}}$
	Dodecane	n-Dodecane	112-40-3	30 $\%_{\text{vol.}}$
	Shell Ondina909	Mineral oil	8042-47-5	66 $\%_{\text{vol.}}$
	PPO	2,5-Diphenyloxazole	92-71-7	2 g/l
	bis-MSB	4-bis-(2-Methylstyryl)benzene	13280-61-0	20 mg/l
Buffer	Cobersol C70	n-alkanes	64771-72-8	46.5 $\%_{\text{vol.}}$
	Shell Ondina917	Mineral oil	8042-47-5	53.5 $\%_{\text{vol.}}$
Veto	LAB	linear alkyl benzene	67774-74-7	50.0 $\%_{\text{vol.}}$
	Cobersol C70	n-alkanes	64771-72-8	50.0 $\%_{\text{vol.}}$
	PPO	2,5-Diphenyloxazole	92-71-7	2 g/l
	bis-MSB	4-bis-(2-Methylstyryl)benzene	13280-61-0	20 mg/l

Table 1.2: Components and concentrations of the Double Chooz far detector liquid scintillators.

in this work) is added to the Target.

- **Radiochemical purity:** The contribution to radioactive background from the scintillators is expected to come mainly from the solutes. The components have been carefully selected. Gamma spectroscopy measurements, atomic absoption spectroscopy and neutron activation analyses (DC group in Munich) have been performed to measure the contribution from different isotopes [49]. In addition to the diagnostics, the gadolinium complex has been sublimed and recrystallized to actively get rid of impurities. The singles rate in a preliminary Double Chooz data analysis (including all sources of singles) is found to meet the specifications.

- **Proton number (ν Target):** A detailed analysis of the proton number in the Target scintillator is essential to calculate the disappearance probability from the reactor neutrino flux since the neutrinos are detected by capture on protons in H-atoms (see (1.7)). With two detectors the error on the hydrogen number cancels since the Target scintillator for both detectors has been produced simultaneously and mixed during production. However, for the first DC phase the error on the proton number enters the total systematic error. In the Target it is thus important

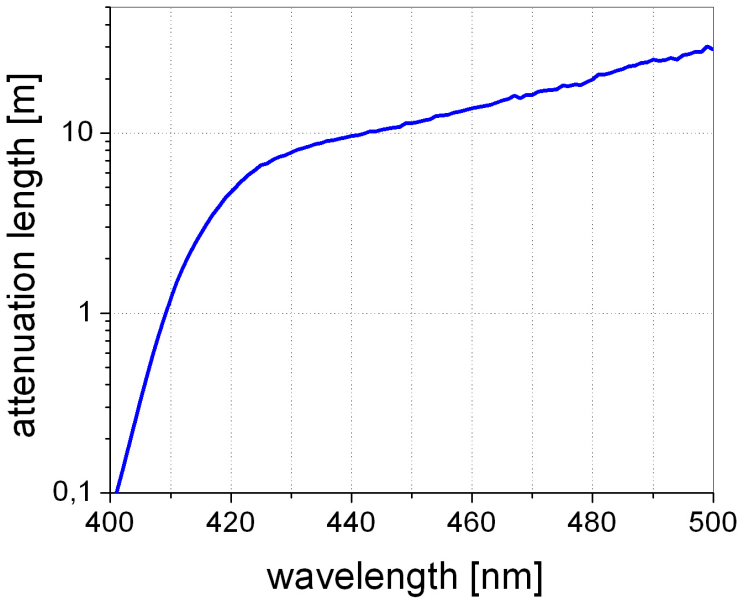

Figure 1.10: Attenuation length of the large scale Target scintillator after shipping to Chooz before the filling of the detector [49]. The attenuation length is above 10 m for wavelength above 440 nm. At the reference wavelength of 430 nm the attenuation length is 7.8 m.

to use chemicals with well-defined atomic composition and high purity. Special care had been taken in weighting the components during the large scale production and when the detector was filled.

- **Adequate optical properties:** The choice of the aromatic fluors PPO and bis-MSB together with the solvent PXE was motivated above by looking at the emission and absorption spectra and the resulting efficient wavelength-shifting for these three components. More efficient wavelength shifting leads to a higher light output. The design goal for the attenuation lengths of the scintillators was 5 m at 430 nm to get a high number of photoelectrons per MeV and a high photon collection homogeneity. The goal was exceeded by selecting high purity chemicals and by removing remaining impurities: Eight tons of PXE have been column-purified before the large scale production by members of the MPIK Double Chooz group [49]. The attenuation lengths of the final large scale liquids before filling to the Double Chooz far detector are Λ_{Target} =7.8 m and Λ_{GC} =13.5 m at 430 nm.

Optimization and characterization of optical properties The scintillator light yield and photon emission time were tuned in this work by defining the concentrations of the scintillator components. A particular requirement in Double Chooz is the matching

	Target	Gamma Catcher
Density [kg/l] at 15°	0.8035 ± 0.0010	0.8041 ± 0.0010
Kinematic viscosity [mm^2/s] at 21°	2.32 ± 0.10	3.70 ± 0.10
Light yield [% BC-505]	48.1 ± 0.5	46.6 ± 1.0
Attenuation length at 430 nm	7.8 m	13.5 m
Refractive index at 405 nm (18°)	1.47	1.46
Hydrogen fraction [wt.%]	13.60 ± 0.04 (calculated)	14.6 ± 0.2 (measured)

Table 1.3: Selected properties of the Target and GC scintillators used in Double Chooz [49]. As a standard for the light yield measurement, the liquid scintillator BC-505 was used: Bicron, St. Gobain Crystals (80% light yield anthracene).

between the Target and GC light yield to have a homogeneous detector response. In the GC the highly transparent medicinal white oil Ondina909 (non-aromatic) is added to get simultaneously the same LY (on the order of few percent) and density ($\ll 1$ %) as in the Target. LY matching is mandatory for an accurate energy reconstruction of the events and in particular for high photon collection efficiency homogeneity. Density matching is crucial for mechanical stability of the acrylic vessels. Successful optimization and adjustment of the LY for Target and GC was done and verified with an analysis of detector data (chapter 2).

Corrections to the amount of produced light come from the ionization quenching effect. The light production efficiency is slightly nonlinear at low energies. For a precise energy reconstruction and thus low systematic errors associated to the neutrino cuts these corrections are important. Ionization quenching is studied and the optical model of the MC simulation is tuned in chapters 3 and 4 for electrons and alpha particles.

Additional to the light yield tuning the scintillator light emission time after excitation was studied and could even be successfully tuned (mainly with the choice of the PPO concentration). The tuning led to an improvement in the possibility to discriminate events in the Target from events in the GC (chapter 5). Detailed knowledge of the scintillator photon emission time is needed to discriminate against backgrounds and to study the neutrino detection efficiency [45]. For example, the photon emission time behavior after excitation with alpha particles differs from electron excitation. These differences can potentially be used in pulse shape discrimination techniques for particle identification.

In chapter 6, hypothetical changes in the attenuation length of the Target have been studied with the Double Chooz Monte Carlo simulation. The effects on detector light collection homogeneity and the neutrino candidate selection have been analyzed and the software tool `ERecoHD` was developed which uses the results of this study to correct for inhomogeneities in the detector.

2 Light yield optimization and analysis of the Double Chooz scintillators

2.1 Introduction and Motivation

The light yield (LY = number of photons per energy) of the liquid scintillators is a central property of the Double Chooz detector since it directly affects the energy resolution. Better energy resolution leads to lower systematic errors in the analysis of the detector data. It is therefore important to optimize the LY. A special requirement for Double Chooz is the LY and density matching between the Target and GC scintillators to guarantee a homogeneous and accurate energy response and mechanical stability of the acrylic vessels. With the help of the results reported in this work it was possible to determine the final compositions of the Double Chooz scintillators. It could be shown that the light yield matching, which was done with small samples in the lab, appears to be successful for the multi-ton scale in the detector and that first data on the stability of the light yield of both scintillators looks promising.

In section 2.2 the experimental setup for light yield measurements is presented. A model was developed to describe the energy transfer paths contribution to the total light yield (section 2.3). The parameters of the model are directly related to the rates of the energy transfers. This model has been used to better understand the scintillator system and to predict the light yield of scintillator compositions. With the help of the model and with dedicated measurements (section 2.4) the Target scintillator composition was fixed (section 2.5). The light yield, or more precisely, photoelectron (PE) yield matching and density matching for the Gamma Catcher is discussed in section 2.6. This section contains laboratory measurements and the Monte Carlo simulations which were done in order to connect the scintillator light yield and the detecor PE yield. The absolute light yield as well as the long-term LY stability of our scintillators from laboratory measurements is discussed in section 2.7. The last two sections 2.8 and 2.9 describe an analysis of the Target/GC PE yield matching and light yield stability with Double Chooz detector data using signals from hydrogen capture events.

2.2 Experimental setup

The 'Compton Backscatter Peak' setup for the LY measurements is shown in Figure 2.1. Irradiated by a ^{137}Cs source, the scintillator inside a quartz cell (1 cm $\times$ 1 cm $\times$ 3.5 cm)

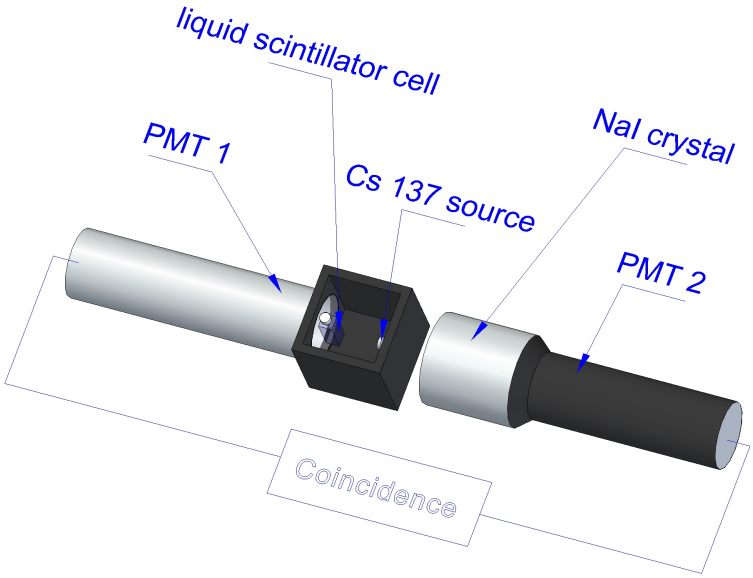

Figure 2.1: Compton Backscatter Peak setup for the LY measurements.

emits light which is collected by a fast (ns time scale) Photonis XP2262 photomultiplier tube (PMT). The cell is carried by a reflecting teflon block (not shown in the figure for clarity) to increase the light collection. The PMT is coupled firmly to a window in the black box next to the scintillator cell with optical silicon coupling grease. The scintillator cell is coupled to the other side of the same window with coupling oil. Tests have been done to check the reproducibility of the coupling quality since after each measurement the scintillator has to be replaced and the coupling has to be renewed. After optimization of the coupling procedure the measured light yield of the same scintillator before and after recoupling was stable at the level of the statistical error of the measurement. The quantum efficiency spectrum of this PMT has a similar shape as the PMTs used in Double Chooz. It is highest around the typical emission spectrum of the examined scintillators (see Figure 1.8). This is important since two scintillators with the same number of photons but different spectra could yield different relative signals in the lab and Double Chooz respectively. Although we do not expect different spectra for Target and Gamma Catcher (both have the same solutes, see table 1.2) it is safer to have the same quantum efficiencies since we want to match the Target and Gamma Catcher light yields at the percent level.

The 662 keV photons from the ^{137}Cs source interact mainly by Compton scattering. Backscattered photons (with an angle of approximately 180 degrees) are detected with a NaI crystal (7.6 cm diameter, 7.6 cm length) equipped with a second PMT. By requiring a time coincidence between the two PMT signals (within 0.4 μs) scattered electron events

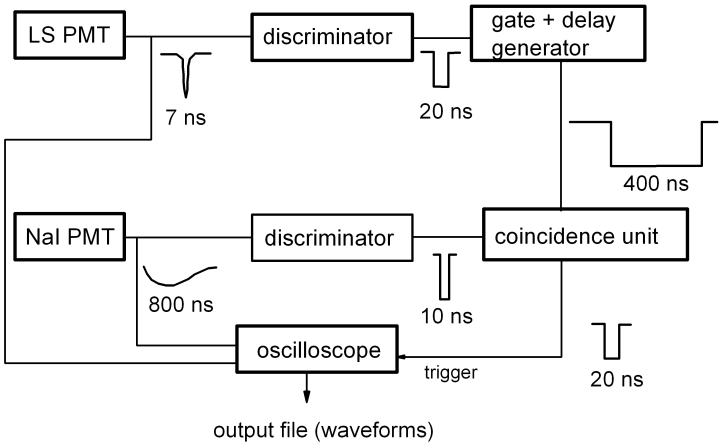

Figure 2.2: Logic of the electronics for the Compton Backscatter Peak setup (LS: liquid scintillator). The quoted numbers are typical time values for the signals.

inside the scintillator with about 476 keV energy are selected. Alternatively, the measurement of the scattered photon can be omitted and the complete Compton spectrum is obtained. Then the Compton edge can be selected ('Compton Edge Method'). Both methods have been used in the measurements. The Compton Backscatter Peak Method is more precise but also the simple Compton Edge Method has advantages. It is faster to acquire sufficient statistics, which is useful for the scans with many different samples. The light yield of a given scintillator is determined relative to a simple scintillator standard: PXE + 6 g/l PPO. All light yield numbers are given compared to this scintillator standard if not stated explicitly otherwise. Figure 2.2 shows how the coincidence is set up. The PMT pulses are recorded and stored with a sampling time interval of 0.2 ns by a digital oscilloscope (Tektronix TDS 7054). The pulses are analyzed off-line (see paragraph 'Data Evaluation' in this section) to determine the collected charge in the PMTs which for PMT 1 in Figure 2.2 is proportional to the light yield of the scintillator sample.

The distances between the source, liquid scintillator cell and NaI crystal have been optimized [55]. If the distances are too big the coincidence rate is too small. On the other hand the range of angles for Compton scattering events which lead to coincidences gets bigger if the distances are too small. This would lead to a broader 'Compton Backscatter Peak' (see Figure 2.4) and thus less accurate results. For Compton effect the scattered electrons have the energy

$$E_{e-}(\varphi) = h\nu \left(1 - \frac{1}{1 + \frac{h\nu}{m_0 c^2}\left(1 - \cos(\varphi)\right)}\right). \tag{2.1}$$

The rate is fixed which is needed to do one measurement in less than two hours including sample preparation (10000 coincidence events at a rate of 2 s^{-1}). This allows us to do

a series of up to five measurements in one day. For this rate the two distances between the source and the liquid scintillator cell and between the source and the NaI crystal are optimized. The allowed angles are required to be as close to 180° as possible. The distances after optimization are in the range of the cell and crystal dimensions: 4.9 cm distance between the source and LS cell and 6.4 cm between the source and the NaI crystal compared to 1 cm. However, due to the small variation of E_{e-} around 180° the energy resolution is not much worsened. A dedicated analysis of the E_{e-} distribution in the chosen configuration is presented in section 4.4.

The background of the measurement has two main contributions: Random coincidences from two independent gammas emitted by the source and photons which hit the NaI crystal first and are backscattered into the liquid scintillator cell. External backgrounds are less important since two rather strong ^{137}Cs sources were used with 270 kBq and 400 kBq, respectively. Both backgrounds can be controlled by choosing a small coincidence time and setting an energy cut on the NaI signal.

Liquid handling for the laboratory measurements Most of the liquid scintillators which have been used in the laboratory measurements done in this work, have been mixed by myself. A quartz cell of the dimensions 1 cm × 1 cm × 3.5 cm was used to contain the scintillator samples. Special care was taken to guarantee the cleanliness of the cell as well as the removal of oxygen and tightness after the cell was filled. The cell was cleaned thoroughly with cyclohexane each time the scintillator sample was changed. In section 4.3 the intentional addition of alpha emitting isotopes into the scintillator is described. In this case additional cleaning steps were performed in order to remove isotopes from the radium series (see Figure 4.2) which can be attached to the cell walls: The cell was exposed to nitric acid at a concentration of 70 %. After that it is rinsed with deionised water to remove the acid, then with isopropanol to remove the water and at last with cyclohexane.

During the filling of the cell the scintillators are exposed to oxygen. After filling it is removed again by purging the scintillator with nitrogen. Oxygen leads to a decrease in the scintillation efficiency (oxygen quenching, [50]) since it can disrupt the energy transfer from the solvent to the solute or the light emission of the solute. Nitrogen has a different absorption spectrum which does not interfere with the energy transfers and the solute emission. It has been checked that purging the scintillators for 10 minutes is sufficient to remove the dissolved oxygen from the quartz cell. Longer purging times did not result in increased scintillation efficiency. Then the cap of the cell is closed and sealed with a teflon strip. Additionally, a special vacuum sealing putty was used for samples with long measurement time.

Data evaluation The oscilloscope stores one pulse per PMT for each coincidence event. Typical pulses are shown in Figure 2.3. The NaI detector consists of the crystal, a PMT and an integrating preamplifier. Thus, the PMT charge information which corresponds to the particle energy is contained in the pulse height of the signal. For the liquid scintillator signals an integration of the pulses is done.

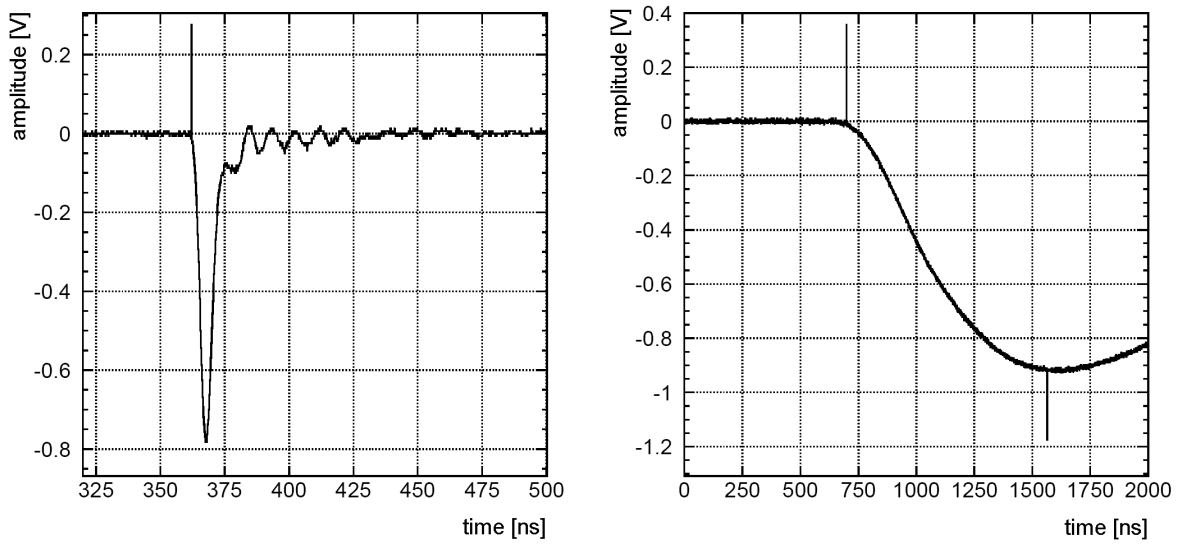

(a) Liquid scintillator pulse (PMT 1).

(b) NaI pulse (PMT 2, preamplified).

Figure 2.3: Typical pulses for PMT 1 and PMT 2. The lines show the pulse onsets and the position of the maximum in (b) from the offline analysis.

The pulse by pulse offline analysis gave us the flexibility to study and optimize different cuts and methods and compare the results with the same set of data. First, the baselines of both pulses are determined at the beginning of the waveform. Then the onset of the pulse is searched by looking for several subsequent channels which are below an adjustable threshold. The onset channel is the first of these channels. After the determination of the onset a new baseline estimation is done by averaging over a fixed number of channels prior to the onset channel. This increases the accuracy if there are slight baseline shifts. With this new baseline estimation the LS pulses are integrated over an optimized fixed range of 120 ns starting from the onset. For the NaI pulses the pulse maximum is searched.

Compton backscattered gammas deposit an energy in the NaI crystal of approximately 184 keV. A cut is set around this value in order to suppress backgrounds coming from random coincidences or photons which travel the opposite way. Additionally, a few quality cuts are applied like rejection of clipped pulses, too high baseline RMS or strong baseline drifts. The charge spectrum of the LS pulses which pass the cuts is shown in Figure 2.4. The tail of this distribution can be explained by remaining accidental coincidences and incomplete energy deposition by some of the electrons in the scintillator cell due to surface effects. In order to compare the light yields of different scintillator samples the peak of the charge distribution is fit with a gaussian function. Possible small deviations from the true peak position due to the tail can be tolerated since only relative light yield measurements are done and the fit procedure was kept the same for all samples.

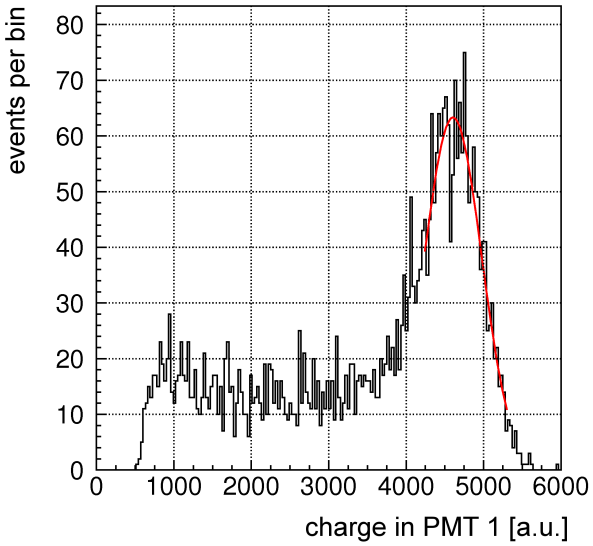

Figure 2.4: The Compton backscatter peak charge spectrum with fit.

2.3 Light yield model

We developed a model which describes the energy transfer paths contributing to the scintillator light yield [55, 56]. The equations are developed in a generic way such that the model can be further extended, generalized and applied to other scintillator systems as well. Here we consider a generalization from one solvent [57, 58] to two solvents, one fluor and one 'quencher' (here: component which does not emit light nor pass on the energy to other molecules) as used in the Target scintillator. Using the model together with experimental data (presented in section 2.4) the model parameters for the Double Chooz scintillators are determined. Since the parameters are directly related to the transfer rates we understand which energy transfer paths contribute most to the scintillation light output and they help us to understand the time scale of the scintillator pulses. Once the model parameters were determined we could predict the LY for all scintillator compositions of our system. In Double Chooz it is required to have two different scintillators with similar LY: the Target (with gadolinium) and Gamma Catcher (without gadolinium). With the help of the model, suitable scintillator compositions can be selected (see sections 2.5 and 2.6)). The considered energy transfer paths are shown schematically in Figure 2.5. Physically, several processes can contribute to one energy transfer path. In our model all of them are combined to a single effective rate regardless of the underlying physical effect. The rates for excitation of the solvent molecules are $\lambda_{D_1^*}$ and $\lambda_{D_2^*}$. The parameters λ_i and λ_i' correspond to internal losses plus other losses, for example due to collisions or excimer formation with subsequent transformation of excitation energy to vibration, rotation or translation energy. Energy transfer to a quenching molecule and 'self-quenching' of the acceptor molecules [50] (e.g. through

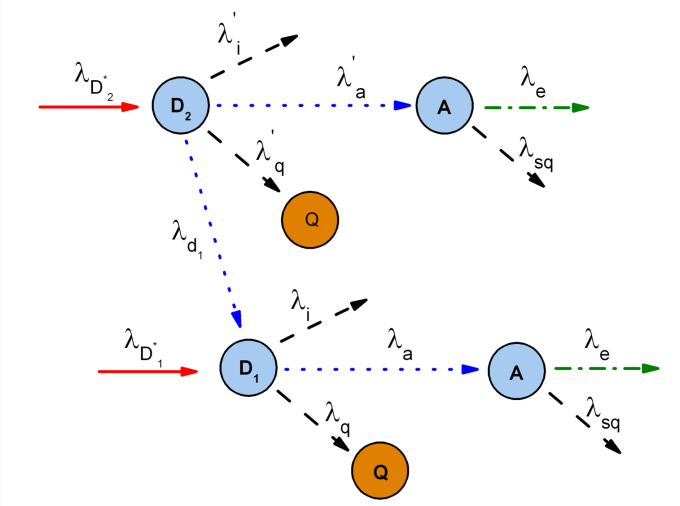

Figure 2.5: Energy transfer paths in a liquid scintillator with two solvents, one fluor and a quenching component. The solid, red lines show the excitation of the solvent molecules. Dashed, black lines represent transfers which do not result in light production. The dotted, blue lines are for (mainly) non-radiative energy transfers and the dash-dotted, green lines show emission of photons. In the case of the Double Chooz Target scintillator, D_1 is PXE, D_2 is dodecane, A is PPO and Q is gadolinium (see text).

excimer formation with a second acceptor molecule followed by transformation to vibration or translation [59]) is described by λ_q and λ_{sq} respectively. The parameters λ'_a and λ_a denote the (mostly non-radiative) energy transfer from the solvent molecules to the acceptor molecules. The rate for possible transfer from the solvent with higher excitation energy (D_2) to the second solvent (D_1) is λ_{d_1} and λ_e is the rate for light emission. We assume that the Compton-scattered electrons excite only the solvent molecules because the concentration of solutes is typically below 1 %. Then the excitation energy can be transferred from the solvent molecules (D, donor) to the fluor molecules (A, acceptor) or quencher molecules (Q). A primary mechanism for these transfers is non-radiative transfer through dipole-dipole interactions described by Förster [51, 52]. The overlap of the donor emission spectrum and the acceptor absorption spectrum directly relate to the strength of the dipole-dipole coupling. A generalization which includes forbidden transitions, dipole-quadrupole interactions and electron exchange by collisions was developed by Dexter [60]. For our model, we further assume that the rates of the different energy transfer paths depend only on the concentrations of the participating molecules. This assumption leads to equations of Stern-Volmer type [58, 61]. The volume in which excitation takes place contains a large number of molecules, therefore the concentration of unexcited molecules can be assumed to be constant in good approximation. We observe experimentally with a commercial Cary Eclipse fluorimeter that the gadolinium complex is non-fluorescent. Therefore in the model, energy which is transferred to the

quencher molecule (in DC: gadolinium) does not contribute to the light yield. For other scintillator systems this assumption could be omitted and the energy transfer model could be generalized. The rate equations are derived and after some calculation [56] we arrive at the number of photons

$$\begin{aligned} N_P &= \int_{-\infty}^{\infty} \lambda_e A^*(t) dt \\ &= D^0_{1,pure} \cdot \frac{\eta \cdot x_1}{\eta \cdot x_1 + (1 - x_1)} \cdot \frac{\lambda_e}{\lambda_e + \lambda_{sq} A} \cdot \frac{\lambda_a A}{\lambda_a A + \lambda_i + \lambda_q Q} \\ &+ D^0_{2,pure} \cdot \frac{1 - x_1}{\eta \cdot x_1 + (1 - x_1)} \cdot \frac{\lambda_e}{\lambda_e + \lambda_{sq} A} \cdot \frac{\lambda_a A}{\lambda_a A + \lambda_i + \lambda_q Q} \cdot \frac{\lambda_{d_1} D_1}{\lambda'_a A + \lambda'_i + \lambda'_q Q + \lambda_{d_1} D_1} \\ &+ D^0_{2,pure} \cdot \frac{1 - x_1}{\eta \cdot x_1 + (1 - x_1)} \cdot \frac{\lambda_e}{\lambda_e + \lambda_{sq} A} \cdot \frac{\lambda'_a A}{\lambda'_a A + \lambda'_i + \lambda'_q Q + \lambda_{d_1} D_1}. \end{aligned} \tag{2.2}$$

The capitals Q, A and D are used for the molar concentrations in mol/l, the star indicates excitation. Rate constants λ have the units of s^{-1}, $l\,mol^{-1}\,s^{-1}$ or $mol\,l^{-1}\,s^{-1}$. In equation (2.2) an empirical factor η was included which describes competition between the two solvents for the available excitation energy which can lead to disproportionately high excitation probability for one of the solvents. $D^0_{1,pure}$ is the number of excited solvent molecules of type one when only this type is present, x_1 is the mole fraction of solvent one: $x_1 = \frac{D_1}{D_1 + D_2}$.

The three terms of equation (2.2) can directly be related to the three energy transfer paths which lead to light output (see Figure 2.5). The first term describes excitation of the first solvent and transfer to the fluor with subsequent light emission. The second term in equation (2.2) relates to excitation of solvent number two, transfer to the first solvent followed by transfer to the fluor and light emission. The third term describes excitation of the second solvent, transfer to the fluor and light emission.

2.4 Laboratory measurement results

The parameters of the model discussed in section 2.3 are ratios of rates for two different energy transfer paths (equation (2.2)). It was found found that these ratios which are directly related to the physics of the scintillator can be determined by light yield measurements alone. Proceeding from the simplest possible scintillator mixture (PXE + PPO) to more complicated ones the branching of the energy transfer was analyzed step by step.

First, varying PPO concentration was considered in the two-component mixtures PXE+PPO and dodecane+PPO (see Figure 2.6 (a)). In these cases equation (2.2) simplifies and we are sensitive on the parameter which describes the competition between energy transfer from the solvent to the fluor and internal losses and on the parameter which describes the self-quenching process. Next, the $Gd(thd)_3$ concentration is varied in PXE+PPO and dodecane+PPO with 6 g/l PPO (Figure 2.6 (b)). The parameters

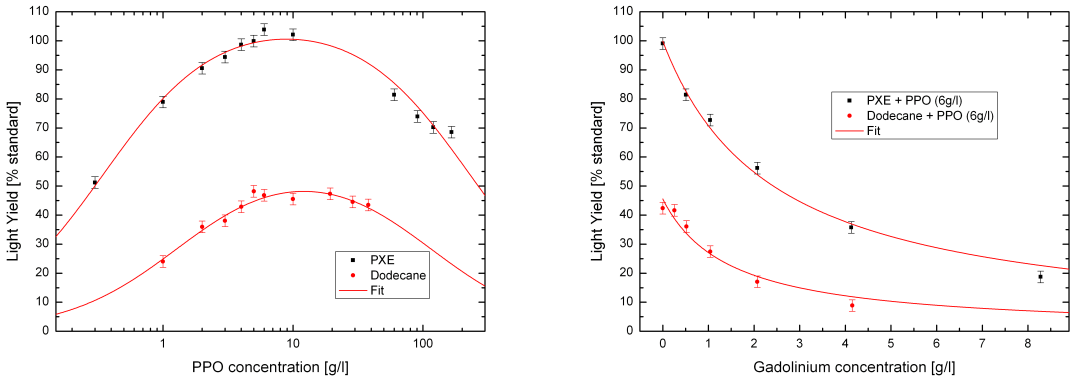

(a) (b)

Figure 2.6: (a): Variation of PPO in PXE and dodecane. (b): Variation of $Gd(thd)_3$ in PXE and dodecane (at 6 g/l PPO). Equation (2.2) is used as fit function. It simplifies if not all the scintillator components are present simultaneously.

obtained at the previous step are fixed. The parameter which describes the competition between transfer from the solvents to PPO and transfer to the gadolinium complex is determined. As a last step the mixture of PXE and dodecane is studied with varying mixing ratio (Figure 2.7 (a)). This gives us information on the empirical factor η and the parameter which quantifies the ratio of rates for transfer from dodecane to PPO and transfer from dodecane to PXE. Table 2.1 shows the results for the parameters of the light yield model.

We also measured and included the parameters λ_i''/λ_a'' and $D^0_{3,pure}$ for Ondina909 which is a component of the GC. They are needed for a model of the Gamma Catcher light yield which contains two more terms with the same structure as in equation (2.2). Other Ondina909 model parameters were assumed to be the same as for dodecane due to the chemical similarity.

We note that the parameter λ_i/λ_a for PXE and the corresponding parameters for dodecane and Ondina909 can be interpreted as a critical concentrations for energy transfer to PPO. This definition of the critical concentration can be related to the critical concentration and the critical molecule distance as defined by Förster [58, 52]. In PXE the transfer is thus significantly more effective than in dodecane and Ondina909. This finding was used to tune the pulse shape of the scintillator emission by adjusting the composition (see section 2.5). However, the light yield of dodecane plus 6 g/l PPO is as high as (46.0 ± 0.8) % of the standard despite the fact that there are negligible aromatic components in dodecane. The normalization is chosen such that the fit at PXE plus 6 g/l PPO (standard) has the value 100 (chosen arbitrarily) and for dodecane plus 6 g/l PPO is 46 (measured ten times relative to the standard).
It is observed that the self-quenching process, which explains the decrease in LY for very

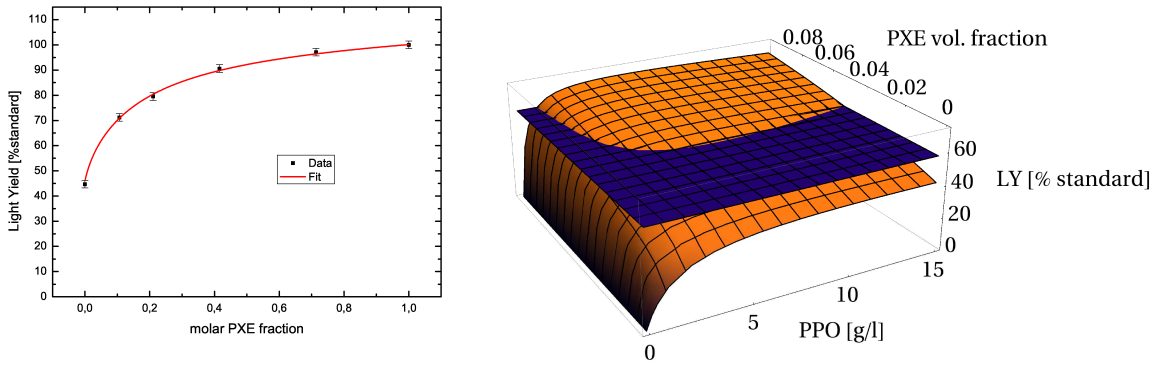

(a) (b)

Figure 2.7: (a): Variation of the PXE/dodecane ratio at 6 g/l PPO (b): Model prediction for the Gamma Catcher light yield (curved, orange surface). The flat (blue) area is the fixed LY for the Target scintillator (57.6 % standard).

high PPO concentrations, is more pronounced in dodecane than in PXE. This difference can be explained with the different viscosities. In dodecane the viscosity is lower and the molecules move faster. That leads to an increase in probability for a self-quenching interaction. For a solvent mixture, the self-quenching parameter is calculated as the sum weighted by the mole fraction of the solvents.

The energy transfer to $Gd(thd)_3$ turned out to be quite effective. Consequently, there is less light yield in the Target scintillator due to the presence of gadolinium.

The fit of the data shown in Figure 2.7 (a) shows that the empirical factor η is well suited to describe the disproportionately higher excitation probability for PXE over dodecane. More details on the light yield model can be found in [56].

2.5 Target composition

The Double Chooz Target composition was fixed with the help of the results presented in the previous section. Since pure PXE would degrade the mechanical stability of the acrylic used for the Target vessel, it is diluted with dodecane. The choice of 20/80 for the PXE/dodecane ratio still gives a high light yield due to the efficient PXE excitation (see Figure 2.7 (a)). The choice of Gd concentration is a trade-off between a high probability of capturing a neutron on Gd on the one hand and a high light yield on the other hand. Thus, 1 g/l Gd is chosen. The probability for a neutron to be captured on Gd is then about 85 %.

The PPO concentration is selected to be 7 g/l. This places it above the critical concentration in the PXE/dodecane/Gd mixture and thus close to maximum light yield. This follows from the model prediction and from additional measurements of the full mixture with varying PPO concentration [55]. The optimal amount of PPO is limited

Rate parameter	Value
$(\lambda_i/\lambda_a) \cdot M_{PPO}$	(0.35 ± 0.03) g/l
$(\lambda'_i/\lambda'_a) \cdot M_{PPO}$	(1.38 ± 0.28) g/l
$(\lambda''_i/\lambda''_a) \cdot M_{PPO}$	(1.54 ± 0.29) g/l
$(\lambda_{sq}/\lambda_e) \cdot 1/M_{PPO}$	(0.0044 ± 0.0003) l/g
$(\lambda'_{sq}/\lambda'_e) \cdot 1/M_{PPO}$	(0.0094 ± 0.0031) l/g
$D^0_{1,pure}$	108.6 ± 1.5
$D^0_{2,pure}$	59.8 ± 4.0
$D^0_{3,pure}$	48.9 ± 4.2
$(\lambda_q/\lambda_a) \cdot (M_a/M_q)$	2.57 ± 0.15
$(\lambda'_q/\lambda'_a) \cdot (M_a/M_q)$	4.88 ± 0.26
$(\lambda_{d_1}/\lambda'_a) \cdot (M_{PPO}/M_{PXE})$	0.3 ± 1.8
η	$5.9^{+0.7}_{-1.2}$

Table 2.1: The rate parameter values obtained by LY measurements. The values are given using grams and liters for the units.

at high concentrations by self-quenching and radiopurity constraints.

In the Double Chooz Target scintillator 20 mg/l bis-MSB are added as a second wavelength shifter. At this low concentration the main energy transfer process from PPO to bis-MSB is via emission and absorption of photons [58]. The bis-MSB molecules emit light at longer wavelengths (with a quantum efficiency of 94 % [48]) where the scintillator is more transparent. In fact, measurements show that the relative LY of two scintillator samples is the same with and without bis-MSB (at 20 mg/l). The addition of bis-MSB is not relevant to the model, as expected.

In summary, the composition of the Double Chooz Target is: 20 % PXE, 80 % dodecane, 7 g/l PPO, 1 g/l Gd, 0.5 $\%_{wt.}$ THF and 20 mg/l bis-MSB (see table 1.2).

2.6 Light yield, photoelectron yield and density matching

Gamma Catcher composition requirements Two important requirements for the Gamma Catcher have to be taken into account when choosing the composition: First, the density has to match the density of the Target scintillator (0.804 kg/l ± 0.001 kg/l at 15 °C) at the sub-percent level. If this was not the case we would have too much differential stress on the acrylic vessel between Target and GC which could then be damaged. Second, the GC light yield has to match the LY of the Target to achieve a good energy reconstruction for the events, irrespective of the location of the energy deposition. More precisely, we want to match the photoelectron (PE) yield of the Gamma Catcher and Target in the Double Chooz detector which depends among other things on the light yields, the detector geometry and the attenuation lengths of the liquids.

Monte Carlo (MC) simulations were done to connect the PE yield in the detector with the light yield measurements (see next paragraph).

The GC contains no gadolinium. This means that we have to find an alternative way to decrease the Gamma Catcher light yield. One can choose between lowering the PXE fraction, lowering the PPO concentration or a combination of both. An adjustment with the PPO concentration alone would lead to a small PPO concentration (below the critical concentration according to the model). The light yield would then be very sensitive to the exact value of the PPO concentration and LY matching would be difficult. Hence, we lower the PXE concentration. Ondina909 (0.811 kg/l at 23 °C for the final batch) is added as a third solvent in order to balance the densities of PXE (0.984 kg/l at 23 °C) and dodecane (0.747 kg/l at 23 °C) and keep the density of the GC the same as for the Target.

In Figure 2.7 (b) on page 35 the LY for the fixed Target composition is shown together with the model prediction for the Gamma Catcher LY. Density matching and the resulting change in solvent fractions has already been considered. Several candidate compositions which lie on the intersection line have been identified and we concentrated mainly on two options: a GC with 2 g/l PPO and a GC with 5 g/l PPO. For 2 g/l PPO we are close to the critical concentration in dodecane and Ondina909 which together account for the main part of the solvent mixture. At 5 g/l the PPO concentration is well above the critical concentration. Additional to the light yield the photon emission time behavior was taken into account. From the model and from dedicated measurements (see chapter 5 and [55]) we know that the scintillation is slower with lower PPO concentrations. This can be used to distinguish Target and GC signals by pulse shape discrimination (PSD) since the Target pulses are shorter in time (section 5.5). With this information the Double Chooz collaboration decided to choose the 2 g/l PPO option.

Detector efficiency Monte Carlo simulations The goal of the PE yield matching is to have an even detector response in Double Chooz. The mean number of photoelectrons (PE) should ideally be independent of the vertex of the particle. Prior to this work, an effort has been made by the collaboration to homogenize the light collection efficiency by optimizing the locations and viewing angles of the photomultiplier tubes (PMTs). Nevertheless, small deviations from homogeneity at the percent level are still possible, for example due to the dependence on the attenuation lengths of the liquids. In chapter 6 these inhomogeneities are studied in more detail.

Since the light yield numbers can be measured and predicted with a precision at this level the simulated detector light collection efficiency inhomogeneity was taken into account for the light yield matching. Here, we are interested in the difference in light collection efficiency averaged over the Target and GC volumes. In sections 6.2 and 6.4 the inhomogeneity on a smaller length scale is studied. When referring to light collection efficiency of the Target (GC) the mean number of photoelectrons per number of scintillation photons is considered, averaged over all the possible Target (GC) vertices. From the simulation the number of scintillation photons after transmission through several millimeters of scintillator is obtained. This quantity is then directly comparable

to the light yield measurements where the photons also have to cross several millimeters of scintillator to exit the cell.

First, the simulation of 10^5 homogeneously distributed electrons (1 MeV energy) was done for the Target. The number of emitted photons and the mean of the PE peak is extracted from the simulation. The (small) tails coming from events in the chimney and from events which deposit part of the energy in the acrylic are not included. If these events which lie outside the peaks would be included, one would get the wrong numbers for the full energy deposit peaks itself for which we want to perform the LY matching. Then the same was done for the GC volume. The mean number of PE was divided by the number of primary photons and one gets $(30.43)^{-1}$ PEs/photon for the Target and $(29.47)^{-1}$ PEs/photon for the GC. These numbers are mainly determined by coverage and quantum efficiency. The relevant parameter for this study is the ratio: The GC photon collection efficiency is 3.3 % higher than for the Target. As a check of this result, the Cherenkov contribution was switched off in the simulation. This can in principle affect the result since the Cherenkov photons have a different initial spectrum and the travel length is different for Target and GC. However, the analysis without Cherenkov light gives almost the same number of 3.4 % higher collection efficiency for the GC. This would be expected as the Cherenkov light contribution is only in the percent range and the wavelengths are efficiently shifted to the typical scintillation wavelengths within short distances. The systematical error on this number is hard to estimate since it depends on the accuracy of multiple parameters like the attenuation lengths for the Target, GC and Buffer liquids, the simulation geometry, reflections on the buffer walls and acrylic and the PMT quantum efficiency (which depends on the incidence angle). However, at this stage the MC was tuned to the best of our knowledge and we decided to tune the LY accordingly. We note that 3.3 % is a small correction and the relative LY between Target and GC itself has an error of about 1.5 %. Nevertheless, this effect was included in the light yield matching.

Final tuning of the GC composition At 2 g/l PPO approximately 4 $\%_{vol.}$ PXE are needed to match the light yield of the Target. In addition the model prediction is calculated how much the LY changes when lowering the PXE fraction from 4 % to 3 %. While the model prediction was 8.1 % a measurement gave a 6.1 % $\pm$ 1.5 % lower LY (see also Figure 2.8). This is another example of how we used the light yield model to identify promising candidate compositions which then could be checked with measurements. Several measurement series were done with varying PPO concentration and varying PXE concentration in order to make sure that the light yield is understood and stable. An example of such a measurement is shown in Figure 2.8.

The fractions for the three solvents changed because of variations (of the order of 2 %) in the density of different Ondina909 batches. Because the density of Ondina909 (0.811 kg/l for the final batch and 0.825 kg/l for older batches at 23 °C) and the density which is needed for the mixture (0.798 kg/l $\pm$ 0.001 kg/l at 23 °C) are similar, the needed fractions of Ondina909 vary significantly: With Ondina909 the lower density of dodecane (0.747 kg/l $\pm$ 0.001 kg/l at 23 °C) has to be balanced in order to match the GC

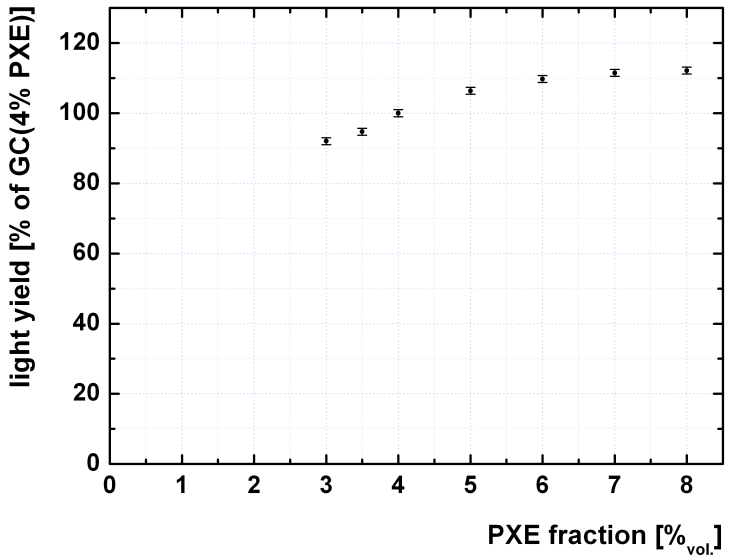

Figure 2.8: GC light yield measurements with varying PXE fractions at a concentration of 2 g/l PPO and without bis-MSB.

and Target density. If the density of Ondina909 is closer to the density which is needed for the complete scintillator, the Ondina909 fraction has to be increased. Temperature dependent measurements of the density have been done to match the density at 14 °C, which is the temperature at the Double Chooz far detector site. For example, in Figure 2.8 a composition of 52 % Ondina909, 44 % dodecane, 2 g/l PPO was used for the 4 % PXE case. In the next paragraph the final solvent composition is discussed. The need for simultaneous density and light yield matching and the fact that the Ondina909 density changed from batch to batch complicated the search for a suitable GC candidate and led to several iterations with many LY measurements.

LY and PE yield matching before the large scale production The lab measurements done with the final components for the large scale production showed that a GC with 4 % PXE, 66 % Ondina909, 30 % dodecane, 2 g/l PPO and 20 mg/l bis-MSB matches the density of the Target and has (97.5 ± 1.5) % of the Target light yield. This value has been obtained by three independent measurements. Due to the higher light collection efficiency for events in the GC (calculated with MC in the previous paragraph) we expect the same number of PE for GC events and Target events (electrons with 1 MeV energy) averaged over the two volumes. The expected ratio PE(GC)/PE(Target) is 1.008 ± 0.015.
This number is obtained using the LY measurements done with the Compton Backscatter

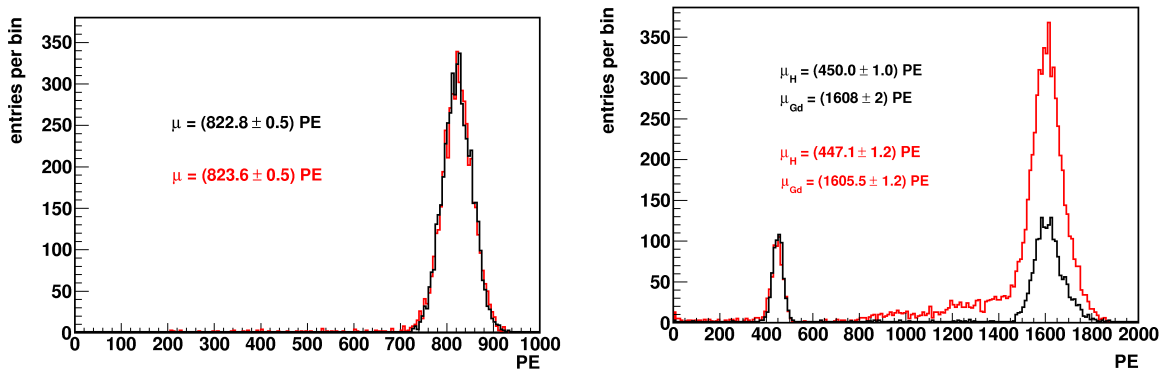

(a) 3 MeV positrons.

(b) 10 keV neutrons.

Figure 2.9: Photoelectron distributions for events which deposit part of the energy in the GC (red) and events which do not deposit energy in the GC (black) from MC. The values μ come from fits of the peaks with a gaussian function. The ranges for the fit were 755 PE to 890 PE for (a) and 400 PE to 500 PE and 1500 PE to 1700 PE for (b). The fit functions are omitted in the plots for clarity.

method which was described above. In this method the scintillator is excited by electrons with about 476 keV energy. The light yield parameters for Target and GC in the MC simulation were adjusted such that the ratio of the number of generated photons matches the laboratory measurement ratio for 476 keV electrons, including ionization quenching (discussed in chapter 3) and Cherenkov light. It has to be noted that it is not possible in principle to adjust the relative light yield simultaneously for all particles and all particle energies. The reason is the difference in the strength of the ionization quenching effect for Target and GC (see section 3.4). Above it was shown that the matching of the PE yield works very well for electrons with 476 keV energy.

Additionally, it was checked with the MC simulation how well the matching is expected to be for other particles and energies which are most relevant for Double Chooz. The LY matching is checked for the inverse beta decay products (positrons and neutrons) with typical energies relevant for Double Chooz. First, positrons are simulated with an energy of 3 MeV homogeneously distributed in the Target. This is a typical energy for the prompt signal of neutrino events. The vertices are only distributed in the Target volume where the majority of prompt events of neutrino candidates is located. That means the spill-in effect is disregarded here since it is itself a correction at the percent level. The spill-in effect is a class of events where a neutrino interaction takes place in the GC and the neutron travels through the acrylic and is captured on gadolinium and therefore can pass the cut on the delayed event energy [45].

With the MC simulation two cases can be compared: part of the energy of the event is deposited in the GC volume or nothing is deposited in the GC. Figure 2.9 (a) shows the PE distributions for both cases. About half of the events deposit some of the energy

in the GC. For these events mostly gammas from the positron annihilation escape the Target. The small tail in the PE distribution comes mainly from events which deposit some energy in the non-scintillating buffer if an annihilation gamma escapes the GC vessel. The observable we are interested in is the mean position of the peak without the tails. The values of the peak positions are the same within their errors, both for events which deposit energy in the GC and events which do not. This means that we expect from MC a good energy reconstruction for both classes of events which is the goal for light yield matching.

Next, the same simulation was done for 10 keV neutrons homogeneously distributed in the Target volume (Figure 2.9 (b)). This energy is typical for the neutrons from inverse beta decay. After thermalization the neutrons are captured on gadolinium or hydrogen. For gadolinium an energy of about 8 MeV is released after deexcitation, shared by typically three to four gammas. If the neutron is captured by hydrogen a single gamma with an energy of 2.223 MeV is emitted. The fraction of events which deposit part of their energy in the GC is about 50 % for the hydrogen capture events (see Figure 2.9 (b)). It is higher for the gadolinium captures because of the higher number of gammas and therefore higher probability of escape of one of them from the Target volume. The hydrogen capture peak number of PEs for events with and without energy deposition in the GC differ by only (0.6 ± 0.4) %. For the gadolinium peak we get the same number of PEs for both cases within the statistical error of the simulation. However, this result is obtained by fitting the two peaks in the range of 1500 to 1700 PE with a simple gaussian function. The gadolinium peaks are more complicated due to the contribution of different isotopes and due to the tail coming from gammas escaping into the Buffer region. Nevertheless, the simple gaussian fit and the distributions in Figure 2.9 (b) demonstrate that we do not expect problems with the PE yield matching for the gadolinium captures.

In summary, it was shown that before mixing, the composition of the GC liquid scintillator was tuned such that the higher collection efficiency in the GC is compensated. From MC we expect that the full energy deposition peak for 3 MeV positrons and neutron capture events is not distorted due to different PE yields for events which deposit part of their energy in the GC. This is the goal of the light yield matching effort. In the next paragraphs the stability of the relative light yield measured in the lab is shown and then we look at the light yield matching in the filled Double Chooz far detector.

LY matching after large scale production and after shipping to Chooz After mixing the Target (10.3 m^3 per detector) and GC (23 m^3 per detector) liquids for the Double Chooz far detector [49] the light yields were measured in the lab again. The GC showed a light yield of (96.9 ± 1.0) % of the Target scintillator (mean of 5 measurements). This is in very good agreement with the number obtained before the large scale production.

After Shipping the liquids to Chooz, new samples of both the Target and GC have been taken just before the liquids were filled to the detector. The number for the relative light yield after all the liquid handling operations was (94.9 ± 1.7) %. This number is

slightly lower than the numbers obtained before shipping the liquids to Chooz. Still it is compatible within the errors. Combined with the 3.3 % higher photon collection efficiency in the GC from MC we expect a PE yield in the GC which is (98.1 ± 1.7) % of the Target PE yield.

2.7 Absolute light yield and long term stability

Absolute light yield The absolute light yield of the Target scintillator was determined by comparing it with the commercial scintillator standard BC505 [62]. The light yield of BC505 is given as 80 % of anthracene, a common organic crystal scintillator standard. The literature values for the absolute light yield of anthracene vary by up to 25 %: 16530 photons/MeV are reported in [63] (43.5 % of NaI(Tl) which has 38000 photons/MeV, consistent with [64]). From other authors, values of 15625 photons/MeV [65] and 20000 photons/MeV [66] are reported. The reason for the 25 % uncertainty is that doing a laboratory measurement of the absolute light yield is difficult [64, 67, 68]. In order to infer the number of emitted photons, a detailed knowledge of the photon collection efficiency (including reflections at the PMT or photodiode surface), the PMT or photodiode quantum efficiency and the photoelectron or electron-hole pair collection efficiency is required. The former two points have to be treated wavelength-dependently.

Since it is advantageous for the detector resolution in Double Chooz if a high number of photons/MeV is produced by the scintillator we took a conservative approach in estimating this number first. Thus, for our light yield estimates we chose the number at the lower end of the reported values for anthracene. With our setup the relative light yield of the Target scintillator with respect to BC505 was measured to be (48.1 ± 0.5) %. This number is the mean value of eight independent measurements. We get the conservative estimate of $0.481 \cdot 0.80 \cdot 15625$ photons/MeV ≈ 6000 photons/MeV. From the higher literature value of 20000 photons/MeV we would expect approximately 7700 photons/MeV.

Long term stability It is very important that the light yield of the scintillator is stable over several years since this is the timescale of the Double Chooz experiment. A dedicated long term Target sample was prepared and stored in an oxygen free and UV-light protected environment. The longterm sample was mixed on October 29 in 2007, then measured relative to BC505 on November 2, 2007 and measured again on March 23, 2010. It has a slightly lower PPO concentration of 6 g/l instead of the final 7 g/l we used for the large scale production. In 2007, the relative light yield was 49.3 % of BC505. Approximately 2.5 years later we got a light yield of 49.4 % relative to BC505 and thus could observe that the light yield was perfectly stable over this time range.

2.8 Photoelectron yield matching analysis with detector data

Since Double Chooz far detector calibration data was not available for the first months of data taking, hydrogen capture signals were used in this work to study the PE yield matching between Target and GC. The advantage of hydrogen capture events is that the event rate after muons is relatively high and the neutrons are homogeneously distributed approximately. Neutrons are produced by interactions of muons with nuclei inside and close to the detector. Several processes like spallation, elastic scattering, photonuclear reactions after electromagnetic showers and muon capture can lead to neutron production [69]. Additionally, it is advantageous that for hydrogen captures the energy is released as a monoenergetic 2.223 MeV gamma.

For this study we used a set of 1920 runs which have been recorded between April 13 and July 26, 2011. The list of analyzed runs is attached in Appendix B. The run time is calculated by subtracting the trigger time of the first event from the trigger time of the last event in each run. The total sum for all 1920 runs is $6.266772 \cdot 10^6$ seconds or 1740.77 hours or 72.532 days.

The output which is common to all analyzers in Double Chooz is the Common Trunk (CT). The CT files contain the basic PMT-wise information as for example flash-analog-to-digital converter (flash-ADC) waveforms (256 ns long) and the reconstructed charge and signal time per channel. Vertex and track reconstruction, which combine information from the individual PMTs to determine the location of events, are also provided. After the CT collaborators can set up their own analyses. For the study presented here we do not need access to the single PMT waveforms which account for the main part of the file size of the CT data. This makes it possible to use light ROOT trees produced by the *Cheetah* [70] code which was developed for faster analysis when not all of the CT information is needed. Many people in the collaboration contributed to the CT and *Cheetah* as a common starting point for Double Chooz analyses.

Starting from these reduced light trees the further analysis of hydrogen capture events was developed during this PhD thesis together with Dr. Bernd Reinhold from MPIK. This analysis is described in more detail below.

Preselection The goal of the preselection stage is to apply basic cuts, select events which are time-correlated to a muon and reject events which are due to instrumental light from PMTs (described in more detail below). First, a condition for muons has to be defined. In this analysis an event is called muon if the total charge in the inner veto (IV) PMTs is above 10^4 DUQ (digital units of charge). This corresponds roughly to an energy deposition of 4 MeV in the IV. The idea of this definition is to select events with energies above the natural radioactivity in the IV. In the ID the conversion factor between DUQ and $\mathrm{MeV_H}$ (preliminary energy scale from H capture) of 13350 $\mathrm{DUQ/MeV_H}$ has been obtained by a previous hydrogen capture peak analysis. An inner detector (ID) trigger is selected at this stage for further analysis if four basic cuts are passed:

- Event energy in the ID above threshold, $\mathrm{E}_{ID} \geq 0.5\ \mathrm{MeV_H} := (0.5 \cdot 13350)$ DUQ.

- The number of PMTs with a signal (PMT multiplicity) is high enough, $N_{hit} \geq 10$.
- The event is not a muon, $Q_{IV} \leq 10^4$ DUQ.
- The time since the last muon event is big enough, $\Delta T_\mu \geq 30 \mu s$.

The first cut can be used safely since we are not interested in very low energy ID events. Cutting on the number of hit PMTs does not remove many additional events. Since physics events above 0.5 MeV_H yield typically over 100 PEs which are distributed fairly homogeneous over the 390 PMTs for physics events, it is safe to apply this cut and useful to study it when looking at the instrumental light emission. The third cut removes the muon events from the preselection sample. But for each trigger which fulfills the preselection cuts the time of the last muon is stored in order to check for temporal coincidences with muons later on. Finally, the fourth basic cut removes events which are too close in time to the previous muon event. Up to about 30 μs after a muon, afterpulse events (originating in the PMT) occur which we do not want to select [71]. We lose some of the hydrogen capture events with this cut but the focus of this study is to get a clean sample of hydrogen captures and get the mean charge for both Target and GC with precision rather than maximizing the cut efficiency.

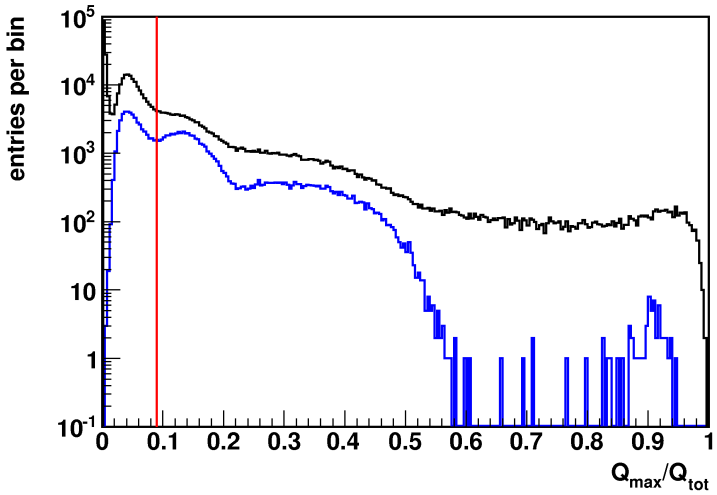

Figure 2.10: The Q_{max}/Q_{tot} distribution for run 21569. Version one, where all channels are included, was used here. The upper (black) histogram shows the distribution without any cuts, in the lower (blue) histogram the four basic cuts have been applied. The red line represents the cut value which was used for this analysis.

The origin of the PMT light emission (referred to as light noise) is the PMT base [46]. Lab tests and dedicated detector runs support this hypothesis. The rate for these events is of the order of 10 s^{-1} between 0.7 MeV_H and 12 MeV_H [72]. Due to the geometry of the PMT magnetic shielding, light emitted by a PMT can reach the photocathode of the

same PMT. This leads to the first light noise cut which is applied during the preselection stage on the ratio between the maximum charge coming from one PMT channel and the total charge summed over all channels Q_{max}/Q_{tot}. Other more sophisticated light noise cuts are based on the pulse shape of the events. Two additional cuts of this kind have been used at the preselection stage in order to efficiently reduce the light noise contribution. The instrumental light is assumed to be accidental and thus will be reduced by requiring a coincidence with a muon later on. Four cuts, which were developed by several members of the collaboration, have been used to separate physics events from light noise events, explanations of the variables are give below:

- The ratio Q_{max}/Q_{tot} is low, $Q_{max}/Q_{tot} \leq 0.09$.
- The rise time of the sum pulse is short, $T_{rise} \leq 20$ ns.
- A combination of the first two variables is used to define an additional cut, $T_{rise} \leq 26\text{ ns} - 125\text{ ns} \cdot Q_{max}/Q_{tot}$.
- The RMS of the pulse start times is restricted, $10\text{ ns} \geq RMS_{Tstart} \leq 40$ ns.

The first light noise cut is robust and simple because it does not depend on waveform information and it has been tested with Monte Carlo simulations that only a negligible part of physics events above threshold is cut away [73]. The physics events which are above $Q_{max}/Q_{tot} = 0.09$ have low energies close to the threshold. This cut has been applied in two different versions simultaneously. In version one there are no restrictions on the PMT channels for both Q_{max} and Q_{tot}. The second version only uses channels which have been flagged as good channels by the `DCRecoPulse` package [74]. This leads to slightly different behavior of the two versions which is not critical for this study. Since we are interested in a pure sample both versions were used simultaneously. The distribution for version one of Q_{max}/Q_{tot} is shown in Figure 2.10 for the latest of the 1920 runs used in this analysis.

It is helpful for our understanding to discuss how the individual basic cuts remove events at different parts of the Q_{max}/Q_{tot} histogram: The cut on the number of hit PMTs removes events with high Q_{max}/Q_{tot}. In the region $Q_{max}/Q_{tot} \leq 0.09$, where the charge is distributed more evenly on all the PMTs, almost no events are rejected. In contrast to this, the muon cut removes only events for low Q_{max}/Q_{tot} values. This is expected since the muons create many photoelectrons which are distributed evenly across the PMTs. The energy threshold cut removes almost all events with $Q_{max}/Q_{tot} \geq 0.6$. But there are also events with $Q_{max}/Q_{tot} \leq 0.09$ which are below the 0.5 MeV_H threshold and thus removed. The time cut after a muon affects all parts of the spectrum. For $Q_{max}/Q_{tot} \geq 0.6$ the energy threshold cut removed almost all events. In this region also the time cut after a muon removes many events which indicates that events below 0.5 MeV_H occur close to a muon trigger. This can be explained by triggers not related to scintillator physics which are induced after large energy depositions in a muon event like for example afterpulses. As explained earlier, also part of the physics events after a muon are rejected by a 30 μs time cut. These events are removed at $Q_{max}/Q_{tot} \leq 0.09$.

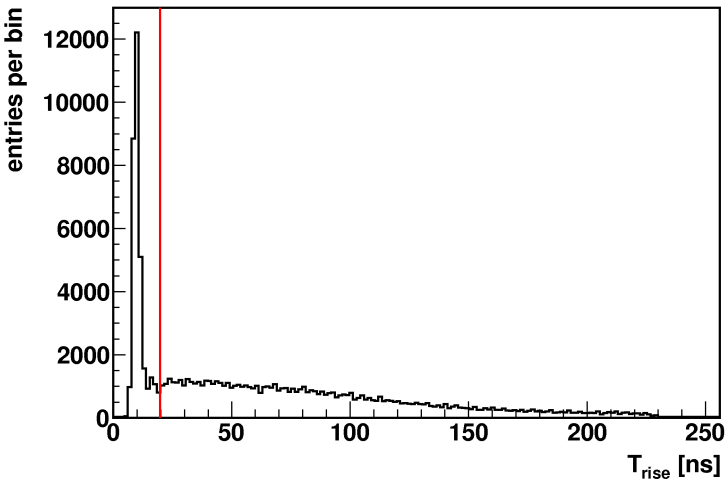

Figure 2.11: The T_{rise} distribution for run 21569 with the four basic cuts applied. The red line represents the cut value.

After applying the four basic cuts, the blue histogram in Figure 2.10 is expected to show mainly light noise above $Q_{max}/Q_{tot} = 0.09$ which is cut away by the first light noise cut. Still we can have light noise contamination below the cut value.

The second light noise cut relies on information about the pulse shapes. It turns out that light noise events can have irregular pulse shapes which can be distinguished from scintillation signals. The waveforms of the PMT pulses are summed to get a total pulse. After the maximum of the sum-pulse has been determined the times when the pulse reaches 10 % and 90 % of the maximum height are used to construct the rise time $T_{rise} = T_{90\ \%} - T_{10\ \%}$ [75]. In Figure 2.11 the distribution is shown after the four basic cuts are applied. The peak in the Figure comes from scintillator physics events. A cut value of 20 ns has been chosen to reject the tail coming from light noise triggers.

The third light noise cut uses a combination of the two variables which were considered in the light noise cut one and two. If we look at the combined information from both variables (see Figure 2.12) we can identify the population of scintillator physics events in the lower left corner. Some additional events can be safely removed in the region where both T_{rise} and Q_{max}/Q_{tot} have rather big values. In this representation there seems to be a tail from the scintillator physics population which has $Q_{max}/Q_{tot} > 0.09$. The events which are cut are most likely low energy events below the energy of the neutrino selection cut in DC. We decided to use this rather hard cut to get a pure sample for this analysis instead of maximizing the efficiency.

The fourth light noise cut uses the information which is contained in the arrival times of the photoelectrons. Light noise events stretch over a wider time range as the scintillator pulses in many cases. A new variable is constructed which can distinguish light noise from scintillator physics events by calculating the root mean square (RMS) of the start times of the signals in each channel [72]. Studies showed that the correction for the

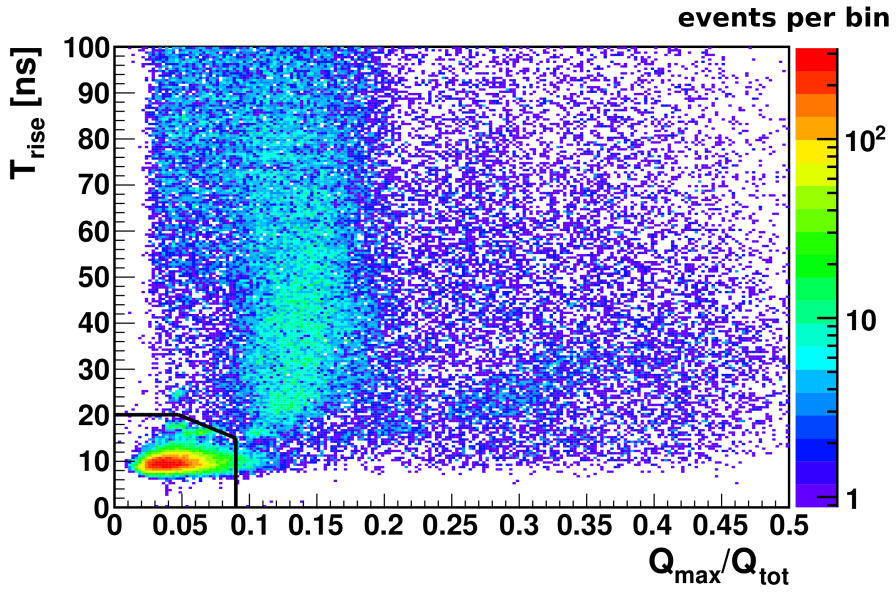

Figure 2.12: The T_{rise} vs. Q_{max}/Q_{tot} distribution for run 21569 with the four basic cuts applied. The black line represents the combined cut after applying the light noise cuts one to three. The color scale is logarithmic.

time-of-flight after vertex reconstruction only has a minor effect on the discrimination power [76]. We used here the default RMS_{Tstart} variable which is available as part of the common *Cheetah* files. Figure 2.13 shows the new variable RMS_{Tstart} in combination with the Q_{max}/Q_{tot} variable and the combined light noise cuts one and four.

As a last cut in the preselection phase a loose time coincidence with muons is defined. The time since the last muon event is required to be smaller than 10 ms ($\Delta T_\mu \leq 10$ ms). The events which pass the preselection steps are stored in new files which can be used for different studies (e.g. ^{12}B studies [77]). The advantage of this two-step approach is that after the preselection the rest of the analysis chain is very quick and can be iterated conveniently. The total file size for the 1920 reduced light tree (*Cheetah*) files which is the starting point for our analysis is about 130 GB. After the preselection stage only the variables which are needed for further studies are stored and the cuts which were described in this section are applied. This results in a total file size of 2.53 GB for the 1920 runs.

Time coincidence and neutron multiplicity cut For the study of neutron capture on hydrogen a more stringent cut is defined on the time since the last muon. A value of 3 ms is chosen in order to have enough data to do a good off-time window background subtraction. An additional cut in energy is done since we are only interested in the hydrogen capture peak:

- $\Delta T_\mu \leq 3$ ms (from the preselection stage we already have $\Delta T_\mu \geq 30$ μs).

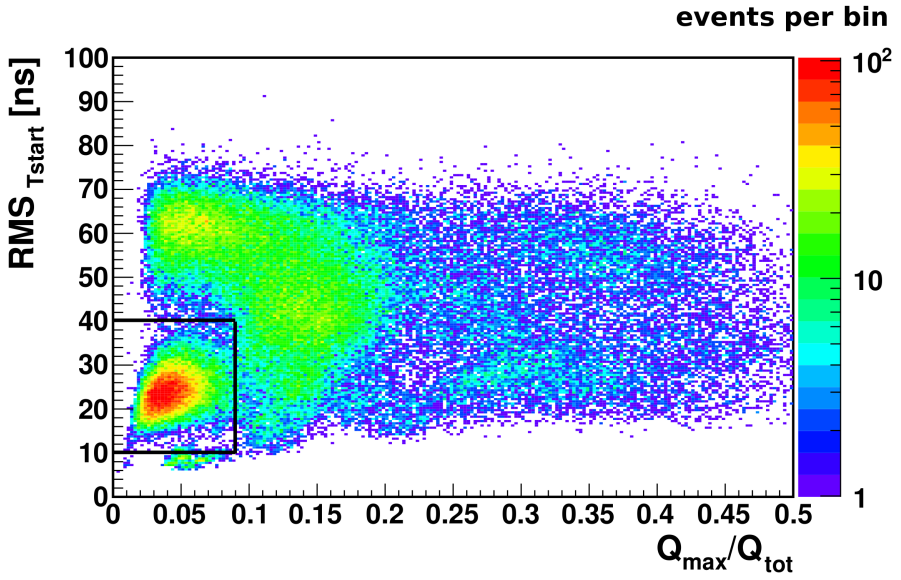

Figure 2.13: The RMS_{Tstart} vs. Q_{max}/Q_{tot} distribution for run 21569 with the four basic cuts applied. The black line represents the combination of the light noise cuts one and four. The color scale is logarithmic.

- $E \leq 4$ $\mathrm{MeV_H} = 4 \cdot 13350$ DUQ.

A signal region is defined as 150 μs $\geq \Delta T_\mu \leq$ 450 μs. The reason for this additional cut in time at 150 μs are baseline variations after the large energy depositions of a muon event which can last up to 150 μs [78]. If we selected events closer in time to a muon we would see biases of the mean charge and sigmas of the distributions. In the Target, where gadolinium is present, a shorter combined neutron capture time is obtained (less than 30 μs). Thus, we see almost no hydrogen capture events which have been captured in the Target within our time window. Nevertheless, there are events in the Target if 2.223 MeV gammas coming from hydrogen capture in the GC cross the Target vessel and deposit their energy. It has to be noted that for this reason the signals from these 'spill-in' gammas in the Target are not homogeneously distributed. Still, we can do a first check of the light yield and PE yield matching with hydrogen capture data.

Eight additional off-time windows from 450 μs to 2850 μs are defined each with 300 μs width. This is useful to study the time dependence of the background behavior. In these windows only few neutron captures on hydrogen occur which are correlated to the previous muon. Then the background subtraction is done by averaging the six background windows from 1050 μs to 2850 μs. This averaged background can be statistically subtracted from the charge histogram in the signal time window. Figure 2.14 shows the effect of the background subtraction. We see that the hydrogen capture peak is very clean after this procedure. The tail on the left side of the peak comes from escaping gammas which only deposit part of their energy in the scintillator. Since also GC events are included here we have events in which the hydrogen capture takes place close to the

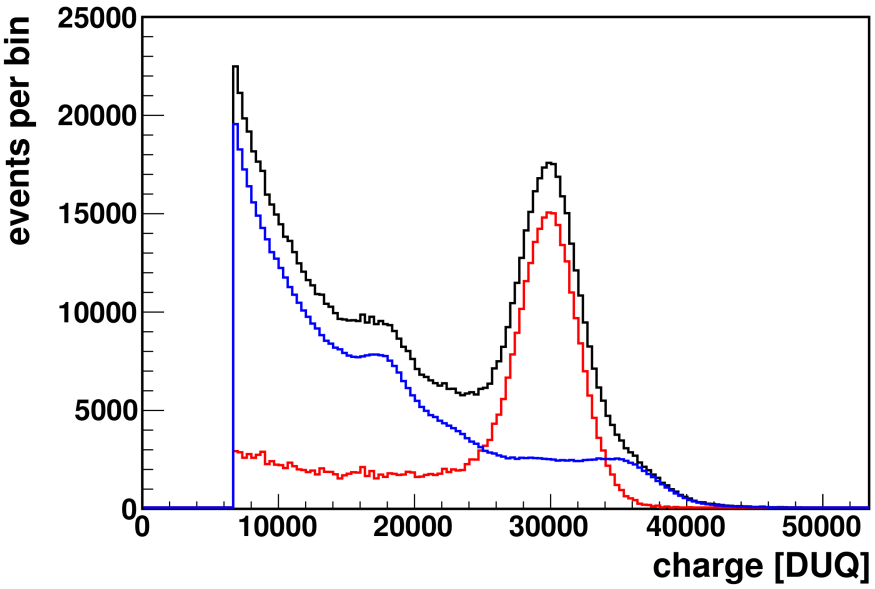

Figure 2.14: The upper (black) histogram represents the charge spectrum in the signal region. The declining (blue) spectrum is the averaged background spectrum. The lower histogram with the peak (red) shows the spectrum after the statistical off-time window background subtraction procedure. The errors of each bin have been propagated correctly, they are bigger than the square root of the number of entries due to the statistical subtraction.

GC wall and the gamma can easily escape into the non-scintillating buffer volume. This hypothesis can be checked by only considering events close to the detector center, which is done in Figure 2.18 (a).

Another cut which can optionally be applied is a neutron multiplicity cut [79]. We only accept the events for which at least one more event corresponds to the same muon. In other words, single events within a time window of 30 μs to 3 ms after a muon are rejected. The idea behind this cut is to reject events where a random coincidence takes place for example with a muon crossing only the inner veto and a radioactivity event in the inner detector. The effect of this cut is shown in Figure 2.15 (a) for the signal region. It is remarkable how well the background is subtracted with this cut. However, a sizable fraction of events in the hydrogen capture peak coming from single neutrons after a muon is rejected, too. The statistical background subtraction has the advantage that the peak can be cleaned up while very little hydrogen capture events are lost. On the other hand we can not decide on an event by event basis which event is a background event. A very clean (but smaller) sample of hydrogen capture events can be selected with the neutron multiplicity cut. The two methods can also be combined. In Figure 2.15 (b) first the neutron multiplicity cut is applied and then a statistical background subtraction is performed. Here is still some background left in the tail of

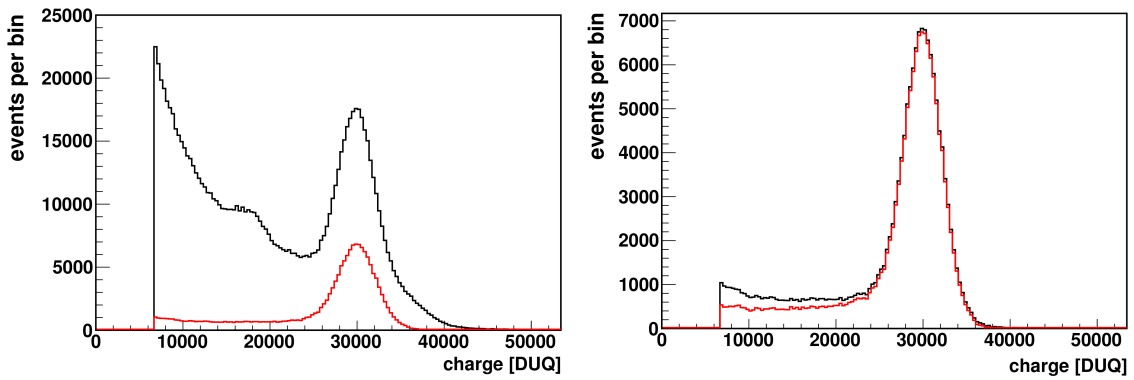

(a) (b)

Figure 2.15: (a) The charge spectrum without (upper, black histogram) and with (lower, red histogram) the neutron multiplicity cut. (b) A combination of statistical off-time window background subtraction and neutron multiplicity cut (lower, red distribution). The upper (black) histogram shows the distribution with only the neutron multiplicity cut.

the distribution after the neutron multiplicity cut. Consistent results are obtained for the background subtraction procedure and the procedure with background subtraction plus neutron multiplicity cut. Since the two methods are conceptually independent, the consistency of the two indicates that neither of them introduces a bias.

For the vertex distributions the neutron multiplicity cut is used. Only the signal time window (150 μs $\geq \Delta T_\mu \leq$ 450 μs) is used and additionally we require the charge to be in the peak region (1.8 $\leq$ MeV$_\mathrm{H}$??? $\geq$ 2.7). The resulting distributions for the reconstructed vertices are shown in Figure 2.16. They show that more events in the GC region are seen as is expected since only spill-in gammas in the Target are selected due to the signal time window lower cut of 150 μs. Another representation of the vertex distribution is shown in Figure 2.17.

Results from detector data Now the hydrogen capture peak charge distributions are examined in more detail. We want to compare the positions (and widths) of the peaks in different detector volumes in order to check the PE yield matching. A comparison of the Target volume and the GC volume can be done separated at their physical boundary. In this comparison we get some events from the GC which are reconstructed wrongly in the Target and vice versa. The RMS in three dimensions of the vertex reconstruction package `RecoBAMA` which was used here is expected to be about 10 cm to 20 cm from MC studies [81]. `RecoBAMA` will be tested with calibration sources at known positions [82] and optimized by tuning the reconstruction software in order to get a precise estimate on the final RMS. In order to get rid of events which are assigned the wrong volume by the vertex reconstruction we can define a 'restricted Target' and 'restricted GC' by not considering events with less than 30 cm distance to the Target vessel. Additionally,

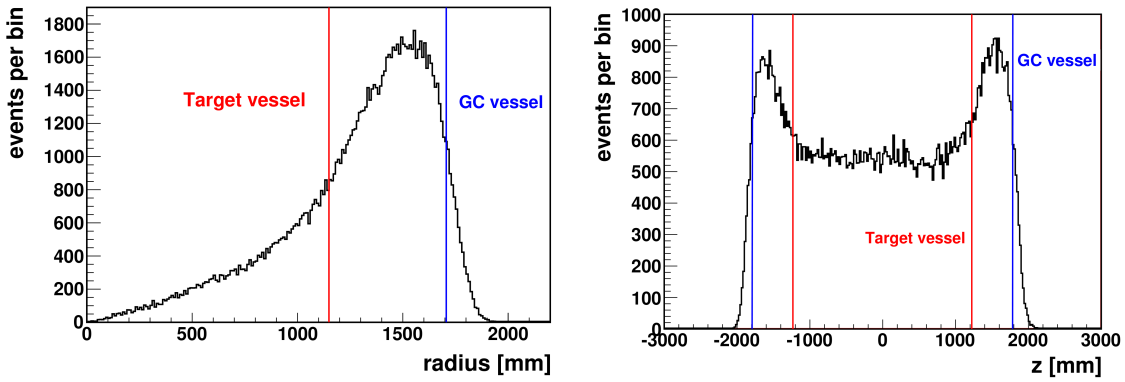

(a) (b)

Figure 2.16: The radius ($\sqrt{x^2+y^2}$) of the reconstructed vertices is shown in (a). (b) displays the z coordinate distribution of the reconstructed vertices. The lines give the positions of the Target and GC vessels. It has to be noted that there are also GC events with low radius and low z.

for the restricted GC volume we only take into account events which are reconstructed in the buffer if the distance to the GC wall is less than 30 cm. The restricted volumes have the disadvantage that we can get a bias in the Target/GC comparison because the photon collection efficiency for the excluded layers can be different from the average. Both methods are applied and compared.

Absolute charge yield and PE yield A new MeV scale calibration constant can be extracted from the hydrogen peak data. For this the combined hydrogen peak is fit for Target plus GC without the neutron multiplicity cut but with background subtraction (red line in Figure 2.14). We arrive at:

$$\frac{29797\ \text{DUQ}}{2.223\ \text{MeV}} = 13400\ \frac{\text{DUQ}}{\text{MeV}}, \qquad 1\ \text{MeV}_{\text{H,new}} = 13400\ \text{DUQ}. \tag{2.3}$$

The new number for MeV_H deviates only by 0.4 % from the older number (1 MeV_H = 13350 DUQ) from a previous analysis with less runs. The conversion factor between DUQ and the number of photoelectrons has been determined to be approximately 50 DUQ/PE [83]. With this factor we get from the hydrogen capture peak 268 PE for 1 MeV. From the MC simulation less PE were expected. Part of the difference can be explained by an underestimation of the absolute scintillator light yield since the literature values of scintillator standards have a rather big error (see section 2.7) but also many other factors can play a role which can lead to a higher than expected absolute PE yield. It has to be noted that the width of the hydrogen capture peak in this preliminary analysis seems to be larger than expected from purely statistical photoelectron statistics. With the calibration data this topic can be investigated in more detail. Here we focus on the relative comparison between Target and GC.

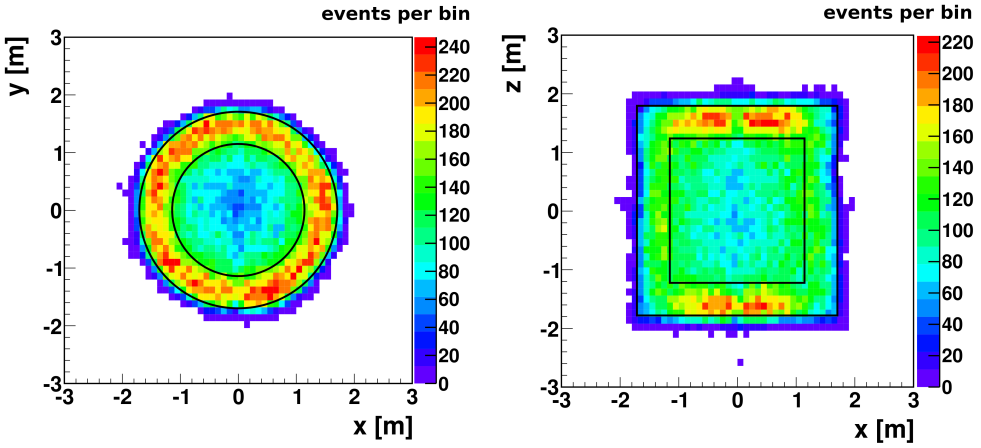

(a) Top view. (b) Side view.

Figure 2.17: Two-dimensional vertex distributions for hydrogen capture events. The vertex reconstruction package `RecoBAMA` [80] has been used in this study. The inner (outer) black lines represent the Target (GC) vessel.

Relative PE yield comparison We start with the comparison between Target and GC using a separation at the physical boundary (Target vessel). In Figure 2.18 the two spectra and the fits of the hydrogen peaks are shown. The neutron multiplicity cut has not been applied in this case. Since the peaks are cleaned very nicely from background events a gaussian fit function can be used in the peak region. The results for the fits are given in table 2.2 along with the results for other volume definitions with and without the neutron multiplicity cut. For the GC the quality of the fit is not perfect due to a slight asymmetry of the peak which affects the value of χ^2 per degrees of freedom (dof) significantly because of low statistical errors. It also has been checked, that the values for the number of events N_{events} from the fit of the gaussian part, the mean μ and the variance σ^2 are stable under rebinning.

We can see from the values that the application of the neutron multiplicity cut gives only slightly different results (deviations below 0.5 %) for the mean values of the peaks. The widths (sigmas) of the peaks are (almost) the same within 1 σ errors regardless of the application of the neutron multiplicity cut. This shows that the neutron multiplicity cut does not bias the charge distribution and therefore is adequate if a pure hydrogen capture event sample is needed. We also get the same mean hydrogen capture peak charge for the physical and restricted volumes within the errors. This result is interesting in itself, because it shows that the radial inhomogeneities in the photon collection efficiency appear to be small. If there was for example an increasing photon efficiency from the Target center to the GC wall we would see that the mean charge for the restricted Target is lower than for the physical Target where events close to the Target wall are included. More detailed results on the homogeneity of the photon collection efficiency are presented in chapter 6.

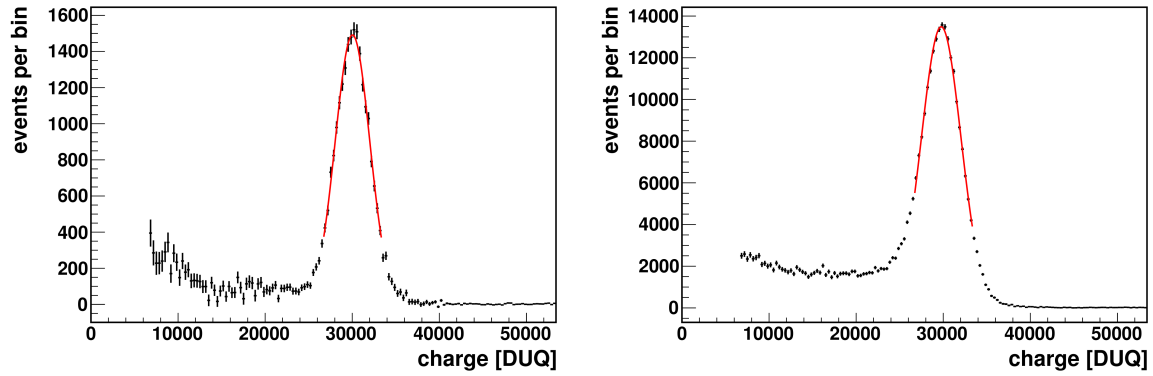

(a) (b)

Figure 2.18: (a) The hydrogen capture peak in the Target (a) and GC (b) volumes. Fits to the data have a range from 2 MeV_H to 2.5 MeV_H (1 MeV_H = 13350 DUQ). The statistical errors after the background subtraction procedure are shown.

Now finally the number for the PE yield of hydrogen capture events in the GC and Target is extracted. The number of PE should be a linear function of the total charge in DUQ which was used in this analysis. Currently, checks on different sources of a possible nonlinearity in the gain (DUQ/PE) are ongoing [84, 85, 86, 87]. The data which was used for this study is reprocessed before the first Double Chooz θ_{13} publication. The result given here is preliminary and will be rechecked since a gain nonlinearity could in principle also affect the ratio between the GC and Target total charge: If the gain for two or more PE is higher (or lower) than for one PE, events in the GC show a higher (lower) total charge. The reason is that, in the GC, the PE-per-channel distribution (for the hydrogen capture energy region) has less one-PE channels and more channels with two or more PEs than the Target due to geometrical reasons. In the GC the events are close to one wall and far away from the other wall. The total number of PE can be the same but still the charge can in principle be different.

In our analysis, the same ratio is obtained regardless of the neutron multiplicity cut and the choice of the restricted or physical volumes. The number for the ratio of the total number of PEs is quoted (assuming gain linearity and thus proportionality with the total charge) for the case with the highest number of events (without neutron multiplicity cut, physical volumes, see Figure 2.18):

$$\frac{\mathrm{PE_{GC}}}{\mathrm{PE_{Target}}} = (99.13 \pm 0.07)\ \%. \tag{2.4}$$

We conclude that the light yield and PE yield matching done with the help of the light yield model and laboratory measurements with a small cell appears to be successful within 1 % also for the multi-ton Double Chooz detector. From the last light yield measurements of the large scale samples after shipping to Chooz and from Monte Carlo

Volume	n mult. cut	N_{events}	μ [DUQ]	σ [DUQ]	χ^2/dof
Target (physical)	yes	10500 ± 130	30122 ± 27	2024 ± 31	15.2/17
GC(physical)	yes	101980 ± 450	29876 ± 11	2265 ± 14	30.1/17
Target (physical)	no	22220 ± 200	30031 ± 20	1983 ± 23	15.9/17
GC(physical)	no	229880 ± 820	29769 ± 9	2269 ± 11	41/17
Target (restricted)	yes	1580 ± 50	30099 ± 67	2013 ± 80	13.8/17
GC(restricted)	yes	64820 ± 400	29866 ± 15	2397 ± 20	31.8/17
Target (restricted)	no	3342 ± 78	29981 ± 49	1885 ± 55	16.2/17
GC(restricted)	no	149860 ± 740	29737 ± 12	2411 ± 16	44/17

Table 2.2: Fit results for the hydrogen capture peaks. The off-time window background subtraction is applied in each case. The mean values μ are remarkably similar which shows that light yield matching was successful.

simulations we expected a PE yield ratio of (98.1 ± 1.7) % (see section 2.6). The number which has been extracted from the detector is in good agreement with this expectation.

2.9 Light yield stability analysis of detector data

The same 1920 runs which were used for the PE yield matching study are used again for analyzing the stability of the light yield with detector data. The runs are divided into blocks of runs. We are most interested in the stability of the scintillators itself. Therefore, the Target and GC stability is considered separately. This can be achieved by looking at the restricted volumes where a layer of 30 cm around the Target vessel is excluded at each side. This minimizes the probability for a wrong assignment of the volume by the vertex reconstruction as explained in section 2.8.

For the GC the 1920 runs are divided into 10 parts to study the stability of the mean value of the hydrogen capture peak which is obtained by a gaussian fit. The result is shown in Figure 2.19 (a). Although the variations are small (2.3 %), with the high amount of events in the GC region we are able to observe that the mean charge for the hydrogen capture peak varies. The reason for this variation is a variation in the gain of the detector. In [83] it was shown that due to two power cuts the gain changed twice. The gain has been extracted from physics runs using the one and two PE peaks by the authors of this study. In order to confirm this hypothesis we split run-blocks 2 and 7 in two parts. The first part contains runs before the power cut and the second part includes the runs after the power cut. The new plot is shown in Figure 2.19 (b). The part of run-block 2 which was recorded before the power cut has been assigned the run-block number 1.5, the part after the power cut is now 2.5. For run-block 7 the same procedure was used. Two jumps have been seen and a clear correlation is observed between the mean charge of the hydrogen capture peak and the detector gain [83]. The gains are measured frequently with the IDLI system and can be corrected.

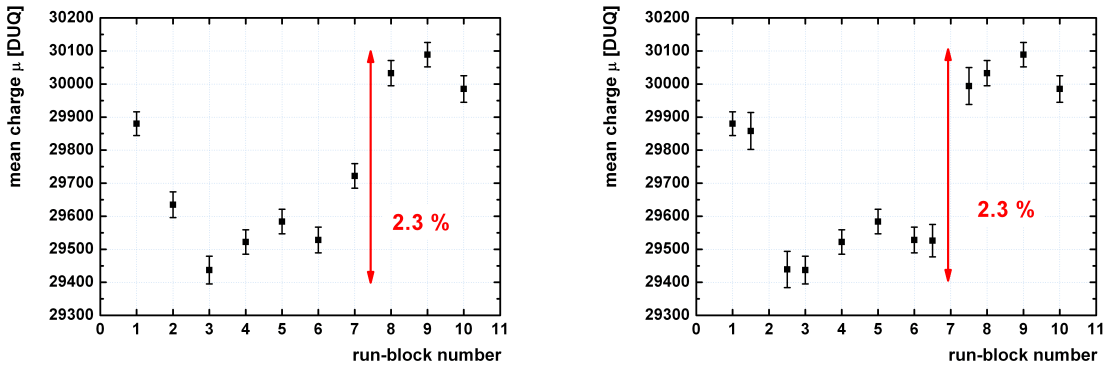

(a) (b)

Figure 2.19: The two plots show the stability of the mean charge of the hydrogen capture peak for the restricted GC volume. (a) The 1920 runs were divided in 10 parts with 192 runs each. (b) Two of the run-blocks (number 2 and 7) have been divided again (see text). The number of elapsed days between the first run in run-block number 1 and the last run in run-block 10 is 72.5 days.

For the restricted Target the number of events is quite low (see table 2.2). For this reason the 1920 runs were divided into four parts. For comparison with the gain behavior we also split the runs analogical to the GC case. Both cases are shown in Figure 2.20. The same behavior as for the GC is observed.

Stability of the sigma which is obtained from the gaussian fit to the hydrogen capture peaks is shown in Figure 2.21. From the GC data a correlation with the gain variation can be guessed but the data is also consistent with stable hydrogen capture peak widths.

From the results of the stability of the means of the gaussians we can conclude that there is no indication that the light yield of the two scintillators changed between April 13 and July 26, 2011. Consequently, the relative light yield between Target and GC is stable over this period as well. The small variations in the mean charge can be explained by variations in the gain which are clearly correlated. This result indicates as well that the attenuation lengths in the Target, GC and Buffer liquids are stable in this time range.

2.10 Summary

In a high precision neutrino experiment as Double Chooz a homogeneous detector response is mandatory to reduce systematic errors. In particular the number of photoelectrons (or PMT charge) for events in the Target and GC scintillators have to be matched.

An experimental setup was presented which is used to measure the light yield of

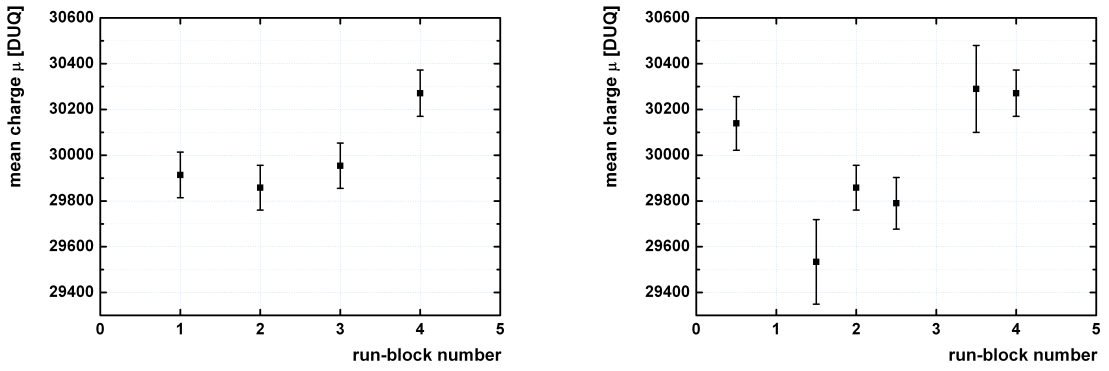

(a) (b)

Figure 2.20: The two plots show the stability of the mean charge of the hydrogen capture peak for the restricted Target volume. (a) The 1920 runs were divided in 4 parts with 480 runs each. (b) Two of the run-blocks (number 1 and 3) have been divided again because of two power cuts described in the text.

scintillators relative to each other. The different energy transfer paths which contribute to the light yield in multi-solvent liquid scintillator mixtures have been included in a light yield model. Measurement series have been done to determine the relative rates of the energy transfer paths. The model allows to gain quantitative understanding of the liquid scintillator light production. It is used to predict the light yield of the Double Chooz Target and GC scintillators with arbitrary concentrations of the components. An optimization of the Target light yield has been done using a combination of laboratory measurements and model predictions and including the general scintillator requirements. The Target scintillator light yield was found to be stable in laboratory measurements over a time span of approximately 2.5 years.

Simultaneous light yield and density matching of the Target and GC scintillators required to add a third solvent to the GC. The light yield model was extended to describe the three-solvent GC scintillator. GC candidate compositions have been identified by model predictions. Light yield measurement series with varying PXE and PPO concentrations around the predicted compositions have been done to finalize the matching at the percent level before the large scale production of the scintillators. Monte Carlo simulations have been done to get the mean light collection efficiencies of the Target and the GC in the Double Chooz detector geometry. The light collection efficiency in the GC is 3.3 % higher than in the Target. The GC composition was selected accordingly and after the large scale production its light yield was measured to be (96.9±1.0) % of the Target light yield.

A preliminary Double Chooz far detector data analysis of neutron captures on hydrogen has been presented. The cuts which have been used to get a clean sample of hydrogen capture events were discussed. In particular, background subtraction with an

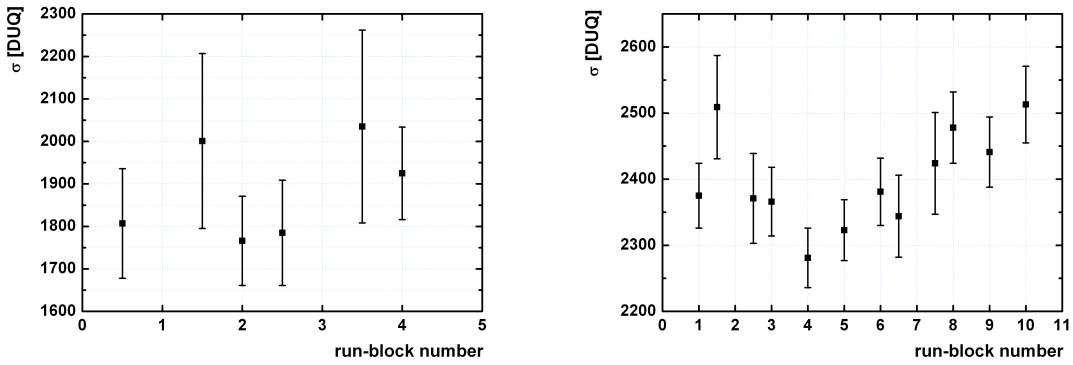

(a) (b)

Figure 2.21: Stability of the width (sigma of the fit) of the hydrogen peak for the restricted Target volume (a) and the restricted GC volume (b).

off-time window and a neutron multiplicity cut were used to isolate the neutron captures on hydrogen. With vertex reconstruction a localization of the events can be done and the sample was split into Target and GC events. The charge (or photoelectron) yield for neutron capture events in the GC is found to be (99.13±0.07) % of the charge yield in the Target. This preliminary result is in good agreement with the expectation coming from the laboratory measurements and the MC simulation. It shows that the matching which was done with a small cell was successful for the multi-ton Double Chooz detector within 1 %.

The Double Chooz far detector stability of the charge response of the peak from neutron capture on hydrogen was analyzed for a dataset which was recorded between April 13 and July 26, 2011. Small ($\approx$ 2.4%) variations can be explained by correlated gain variations which can be calibrated. The result shows no deterioation of the liquid scintillator optical properties during the first 3.5 months of data taking.

3 Nonlinearity in the scintillation light production of low energy electrons

3.1 Introduction and Motivation

At low electron energies (typically below $\mathcal{O}(100)$ keV in organic liquid scintillators) the scintillation efficiency is significantly reduced. The underlying physical effect is called *ionization quenching*, which is the loss of scintillation light "attributed to quenching of the primary excitation by the high density of ionized and excited molecules" [50] (see section 3.2). In Double Chooz this effect becomes important for a precise energy reconstruction, especially for gammas which typically deposit their energy via multiple Compton scatterings producing several low energy electrons. Gammas are involved in both the prompt and the delayed signal coming from the inverse beta decay neutrino detection reaction. The error on the gamma energy scale is thus important for the study of systematic uncertainties in the θ_{13} analysis due to energy cuts.

A laboratory experiment setup was constructed and commissioned in this work and measurements were done to characterize the nonlinearity in the light production quantitatively for the Double Chooz scintillators (section 3.3). The experiment principle is an improvement over another widespread method which selects the electron energies by measurement of the Compton scattering angle. With the method described here, the nonlinearity can be determined in less time with a high accuracy.

The results of the laboratory measurements, which are presented in section 3.4, have been analyzed with the commonly used description of the nonlinearity by Birks [50, 88]. Birks' equation is also used in the `Geant4`-based [47] Double Chooz Monte Carlo model which is tuned with the laboratory measurement results in section 3.5. During the tuning process, the relevant details of the simulation code have been studied and it turns out that carefulness is necessary to implement the measured nonlinearity behavior correctly.

3.2 The ionization quenching process

The energy loss of electrons per unit length passing through matter is described by the Berger-Seltzer equation [89]

$$\frac{dE}{dx} = 2\pi r_e^2 \, n_e \, \frac{m_e c^2}{1-\gamma^{-2}} \left[\ln\left(2(\gamma+1)\frac{m_e^2 c^4}{I^2} \right) + \frac{1}{\gamma^2} + \ln\left(\frac{\tau^2}{4}\right) + \frac{\tau^2}{8\gamma^2} - \frac{2\tau+1}{\gamma^2}\ln(2) \right], \tag{3.1}$$

with the classical electron radius r_e, the electron rest energy $m_e c^2$, the Lorentz factor γ and with $\tau = \gamma - 1$. Additionally, the material constants I (mean ionization energy) and n_e (electron density) are needed. Both quantities can be calculated for materials with known chemical composition. Values for the mean ionization energy of a given medium can be obtained by combining tabulated literature values for the single elements [90] with

$$\ln\left(I_{total}\right) = \frac{\sum_i w_i \frac{Z_i}{A_i} \, \ln(I_i)}{\sum_i w_i \frac{Z_i}{A_i}}. \tag{3.2}$$

The weight fraction for element i is denoted by w_i, the atomic number by Z_i and the mass number by A_i. The density effect [91] can be neglected at the electron energies in this experiment. It has therefore not been included in equation (3.1). It is derived from the Bethe equation and takes into account the indistinguishability of the electrons which pass through matter and the electrons which are part of the material.

For typical scintillator compositions, the energy loss dE/dx increases with decreasing energy until an energy of around 100 eV is reached. For energies lower than about 100 eV the specific energy loss decreases with decreasing energy. At even lower energies the equation gives negative values for dE/dx which is unphysical. In the analysis which is described in section 3.4 an approach from [92] is followed in order to remedy this situation: A linear extrapolation from dE/dx at 100 eV is done to no energy loss at zero energy. In section 3.5 the calculated energy loss is compared to the tabulated values for dE/dx which are used in `Geant4`. In Figure 3.1 the specific energy loss is shown as a function of the electron energy for the Target scintillator. All the investigated scintillators have similar values for the mean ionization energy I and the electron density n_e and thus similar specific energy loss functions.

Due to the higher specific energy loss at low energies the ionization and excitation density is higher which leads to an increase in scintillation inefficiencies due to ionization quenching processes. Thus, the total scintillation efficiency decreases with decreasing initial electron energy. A variety of different physical processes has been proposed to explain the ionization quenching mechanism (some of them were proposed originally for crystals rather than liquid scintillators), for example permanent molecular damage [93], collisions of two excited molecules [94], interaction between the Coulomb field of an ionized molecule with an excited molecule [95] and free radical formation [96].

The ionization quenching behavior can be described effectively by the Birks equation [50, 88] without considering the details of the underlying physical processes:

$$\frac{dL}{dx}(E) = \frac{L_0 \cdot \frac{dE}{dx}(E)}{1 + kB \cdot \frac{dE}{dx}(E)}. \tag{3.3}$$

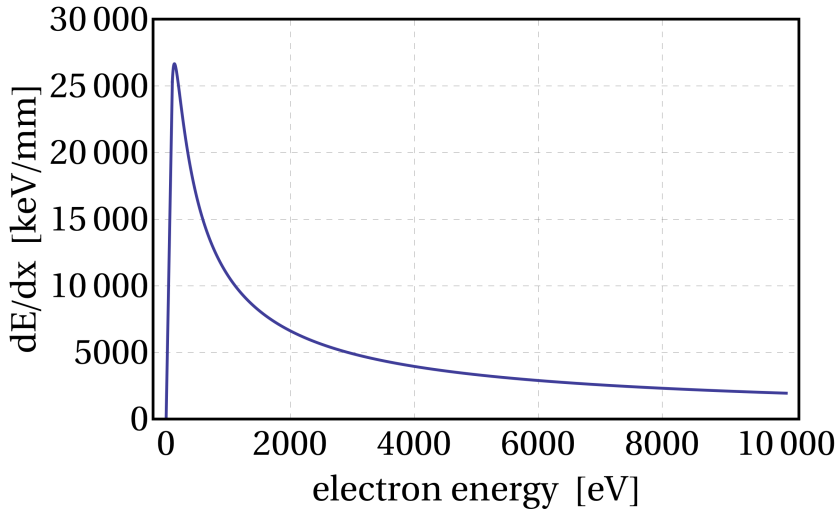

Figure 3.1: The specific energy loss dE/dx of electrons passing through scintillator described by the Berger-Seltzer equation. The mean ionization energy and the electron density of the Target scintillator have been used here. Note that only the peak region below 10 keV is shown here. With higher energies, dE/dx is decreasing: at 100 keV the specific energy loss is $dE/dx \approx 350$ keV/mm.

The amount of light which is produced per unit length is denoted by dL/dx. L_0 is a constant which characterizes the scintillation efficiency (light produced per deposited energy) in its linear regime, i.e. for small dE/dx. The Birks parameter kB is a material property which has to be determined experimentally. For $kB \cdot \frac{dE}{dx}(E) \ll 1$ ionization quenching is negligible and the specific light yield is proportional to the specific energy loss. At the end of the particle track the specific energy loss is high (Figure 3.1) and less light per unit length is produced. Approximately, the same kB can be used for different ionizing particles and dE/dx accounts for the difference in the relative strengths of the scintillation inefficiency. However, in general a better description of the light output for different particles can be achieved if the kB value is adjusted for each particle individually (section 4.6). Equation (3.3) was originally developed for scintillator crystals like anthracene but is also widely used for liquid scintillators. In [88] a motivation for the equation and the Birks parameter (in terms of the processes occurring in crystals) is given.

Next, the laboratory experiment is described and the results are presented in the following section. After that, we come back to Birks' model and determine the Birks parameter kB and tune the Monte Carlo software of Double Chooz.

3.3 Laboratory measurement setup

In order to measure the light output of the Double Chooz scintillators for various electron energies, a dedicated laboratory measurement was set up. The main difficulty is to

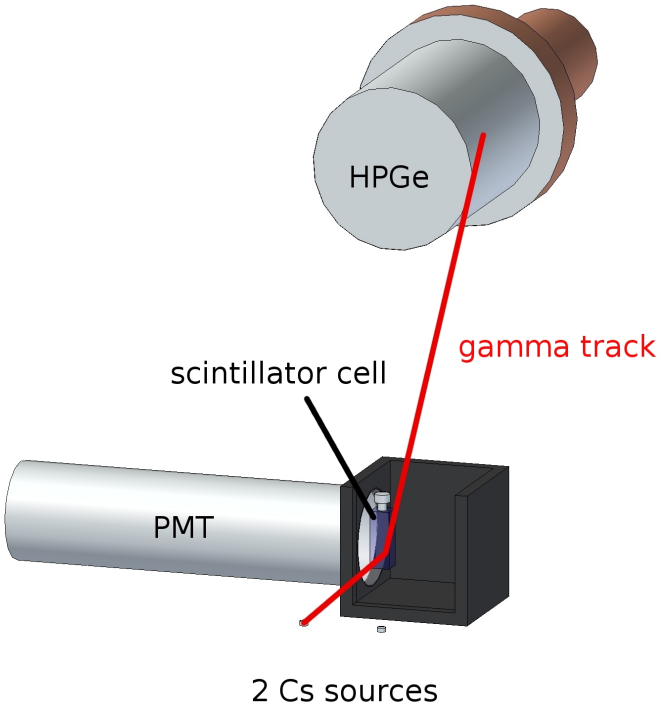

Figure 3.2: Setup for the measurement of the scintillation efficiency for low energy electrons. The black box is closed prior to the measurements and additional light protection and lead shielding surrounds the setup. The reflecting teflon cell carrier is not shown for clarity. The two ^{137}Cs sources below the setup have an activity of 200 kBq and 400 kBq respectively. The red line shows one possible gamma track which leads to a coincidence signal.

excite the scintillator with electrons of defined energy in the energy region of interest. In the approach described here, ^{137}Cs (662 keV gamma source) was used to excite the scintillator via Compton electrons. The energy of the scattered electrons varies with the scattering angle according to equation (2.1). In order to indirectly determine the energy of the scattered electron, a 0.83 kg high-purity germanium spectrometer (HPGe, Princeton Gamma-Tech) is used which measures the energy of the scattered photon (see Figure 3.2). The HPGe detecor has a high energy resolution of 3.92 keV (FWHM) at 662 keV. This energy resolution is the key for a precise determination of the electron energy

$$E_{e^-} = E_\gamma - E_{\gamma'} = 662 \text{ keV} - E_{\gamma'}. \tag{3.4}$$

In the chosen geometrical configuration two ^{137}Cs gamma sources are placed at different angles with respect to the quartz scintillator cell (1 cm $\times$ 1 cm $\times$ 3.5 cm) in order to cover a wider range of scattering angles simultaneously. A photon from one of the two sources can scatter inside the liquid scintillator vial and then be absorbed inside the sensitive volume of the HPGe detector. The signals from both the photomultiplier tube

(Photonis XP2262) which collects light from the scintillator cell, and the HPGe detector are used to build a coincidence signal. The maximal angle which leads to a coincidence (45°) corresponds to an electron energy of 180 keV. From the source which is placed directly below the scintillator cell a straight path through the scintillator to the HPGe detector is possible which means that in principle the range of 0 keV to 180 keV electron energy can be measured. Due to threshold limitations and low statistics for the largest scattering angles we measure between 19 keV and 140 keV which is the relevant region for the low energy quenching effect. There is no Cherenkov light contribution in this energy range since the electron energies are below the Cherenkov light production threshold. The threshold in our scintillator can be calculated using the measured refractive index of $n \approx 1.5$ for the liquid scintillators. The minimal velocity required for Cherenkov light production is $v_{min} = \frac{c}{n}$. For electrons this corresponds to a minimal energy of about 180 keV.

With the method described above the entire range can be probed in a reasonable time of a few days without changing the measurement settings. A similar setup has also been used in [92]. Another common approach is to determine the electron energy by fixing the scattering angle. This method has the drawback that analyzing a different electron energy requires a change in the geometry of the setup. Additionally, the distances between the source, the sample, and the device which is used to measure the scattered gamma, have to be chosen rather big to guarantee a precise determination of the angle. This leads to small counting rates or to high radioactive source activities.

The electronics to set up the coincidence measurement is shown in Figure 3.3. A

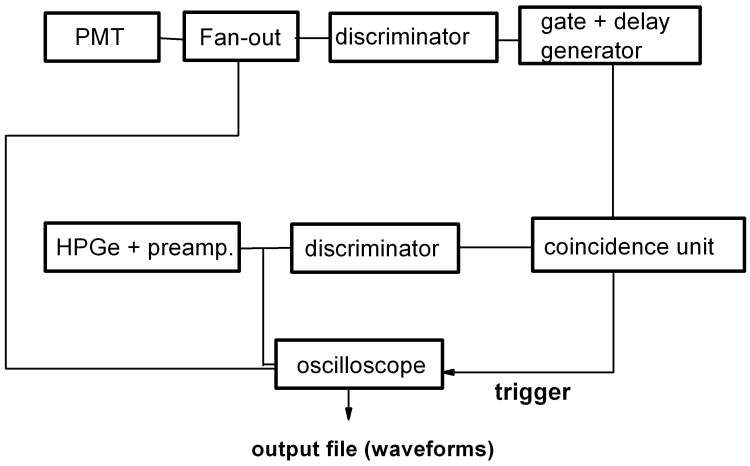

Figure 3.3: Electronics scheme for the measurement of the scintillation efficiency for low energy electrons.

LeCroy 428F fan-out module is used to duplicate the signals coming from the PMT which is attached close to the scintillator cell. One of the signals produces a logical

pulse if it is above the threshold of a Phillips scientific (PS) 730 discriminator module. The second identical signal is directly recorded with a TDS 7054 DPO oscilloscope if a coincidence signal triggers the readout. The logical pulse from the discriminator is used by an Ortec 416A gate and delay generator to open the coincidence gate of 500 ns by sending a logical pulse to the LeCroy 465 coincidence unit. The Ortec 416A module is able to delay the logical signal in order to adjust the timing with respect to the HPGe spectrometer pulse arrival.

The germanium detector has a built-in integrating preamplifier which provides two output signals. One signal is used to create a logical signal if it is above the threshold of another channel of the PS 730 discriminator. This logical pulse is fed to the coincidence unit. The second output signal from the HPGe spectrometer is routed to the oscilloscope.

If there is a coincidence the oscilloscope readout is triggered and two complete waveforms are recorded on an external hard disk drive connected to the oscilloscope. The time resolution of the waveforms is 0.4 ns and the resolution in voltage is 256 channels for the range of 1 V and 2 V for the HPGe-pulses and for the PMT-pulses, respectively. For each pulse, 10000 time samples are recorded which corresponds to waveforms of 4 μs length. The HPGe detector pulses have a much longer time scale of microseconds compared to the fast ($\approx$ 10 ns) photomultiplier pulses of the scintillation signal. The time scale of the HPGe detector pulses led to the coincidence window size of 500 ns and the length of the recorded wavelength of 4 μs. The technique of recording the pulses to disk has the advantage that the analysis can be tuned iteratively and controlled easily. The speed of the oscilloscope readout is sufficient to do one measurement with about 10^6 coincidence events in a few days which corresponds to a rate of the order of few events per second.

Analysis of the laboratory measurement data The two waveforms of each coincidence event are analyzed offline individually. The energy information of the PMT pulse is given by the charge. Thus, the pulse has to be integrated. The same method as for the light yield measurements (section 2.2) is used here as well: The baseline value of the signal is reconstructed, the onset time of the pulse is determined and then the integral over the pulse is calculated. For the HPGe detector signals the information about the deposited energy is in the pulse height since a built-in integrating (charge sensitive) preamplifier directly processes the signal. In the offline analysis the pulse height is determined with a moving average filter, which calculates the maximum value of the summed charge of 70 subsequent samples (equivalent to 28 ns). This increases the accuracy of the determination of the pulse height and thus the energy resolution for the scattered photons.

In order to calculate the energy of the scattered photon the HPGe detector was calibrated with the 662 keV line from ^{137}Cs and four gamma lines from ^{133}Ba with the energies 384 keV, 356 keV, 303 keV and 276 keV. The high voltage (HV) supply for the detector was carefully adjusted (3375 V), its stability was controlled and the linearity of the detector response was checked. The calibration was repeated before and after each measurement and the stability of the HPGe detector response was confirmed.

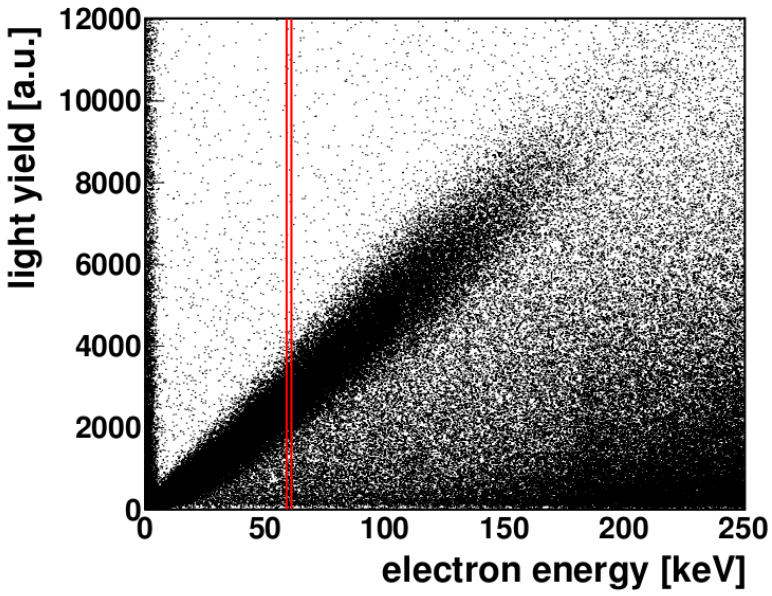

Figure 3.4: Scatter plot of electron energy versus scintillation light. The population along the diagonal consists of the relevant events where the complete gamma energy is divided between the liquid scintillator and the HPGe detector. Events on the right of the diagonal are background events where part of the gamma energy is neither deposited in the scintillator nor the HPGe detector. The population along the y axis can be explained by random coincidences between two gammas where one gamma deposits its full energy in the HPGe detector. The two red lines indicate the position of a sample energy 'slice' which are used for further analysis.

Figure 3.4 shows the result of a typical measurement in a scatter plot where one point represents one coincidence event. The reconstructed electron energy $E_{e^-} = E_\gamma - E_{\gamma'}$ is obtained from the HPGe detector signal and shown together with the light output of the liquid scintillator (coming from the integral of the PMT signal).

The response function (light output as a function of energy, $L(E)$) of the scintillator is smeared out due to the rather low photon statistics in this energy range. A rough estimate can be made of the number of photoelectrons in the PMT for a typical energy of around 60 keV. The absolute scintillator light yield for the Target was determined to be about 6000 photons/MeV (section 2.7). At 60 keV we arrive thus at roughly 360 photons. The collection efficiency of our setup is difficult to estimate but since we use a reflecting PTFE teflon cell carrier which surrounds the quartz vial, the losses up to the photocathode of the PMT are assumed to be less than 50 %. A typical combined quantum and collection efficiency for PMTs is 20 %. If we insert these numbers we get the rough estimate of 36 photoelectrons at 60 keV energy which explains the broadening

of the response function. This estimate shows the general difficulty in going to much lower electron energies than about 10 keV.

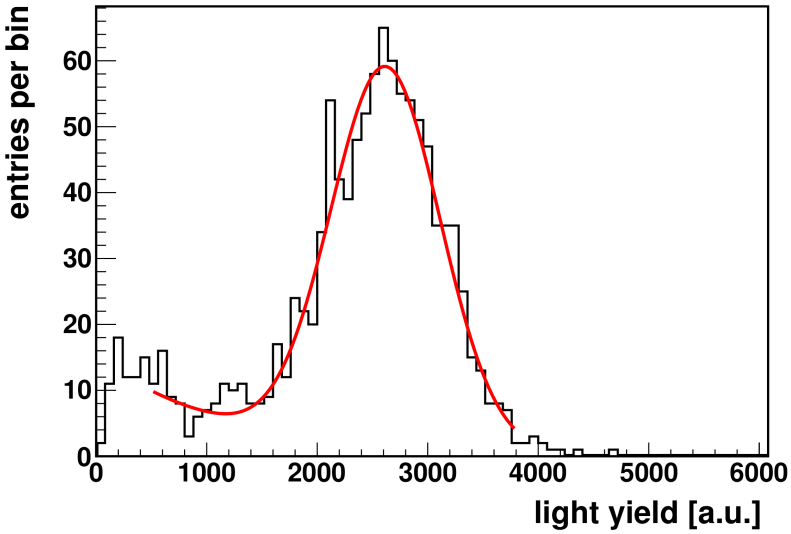

Figure 3.5: Typical measured light output distribution for electrons with reconstructed energies between 59 keV and 61 keV.

We divide the measured dataset into electron energy 'slices' of 2 keV energy. A finer binning does not lead to better results since 2 keV is about the energy resolution of the HPGe detector. The projection of the data in Figure 3.4 onto the y-axis is shown in Figure 3.5 for the electron energy slice from 59 keV to 61 keV. This distribution is fit. The background coming from events where not all of the 662 keV energy is deposited in either the scintillator or the HPGe detector is included in the fit function. An exponential background distribution is assumed and a gaussian function is used for the signal. Since we are in a regime with quite low photoelectron statistics especially for the low electron energy slices, the fit results were checked with a more elaborate fit assuming a poissonian distribution of the underlying number of photoelectrons. However, it turned out that the difference between the poissonian and gaussian fits is negligible for the mean of the distribution [97]. The mean of the gaussian and its error are plotted as a function of the mean energy of all the electrons in the respective energy slice in Figure 3.6. Another representation of the same data and the same fit which shows the non-proportionality is displayed in Figure 3.7.

Systematic errors study From Figure 3.6 it can be seen that the deviation from linearity in the light yield function $L(E)$ is small. Systematic effects which could in principle mimic the ionization quenching nonlinearity have to be excluded. Therefore a detailed study of possible sources for an instrumental nonlinearity has mainly been done by Stefan Wagner from MPIK Heidelberg and described in [98] and [97]. Here, only the main results are summarized. Five possible sources of nonlinearities have been studied:

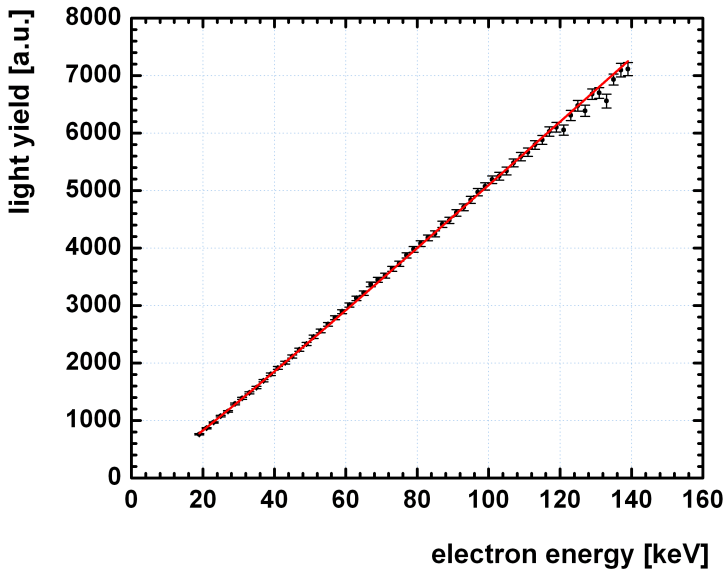

Figure 3.6: Response function (also: light yield function) $L(E)$ for low energy electrons in the Target scintillator. Only a slight deviation from linearity is observed in this energy range. The fit shows the Birks model (equation (3.5)) with $kB = 0.0158 \pm 0.0006$ cm/MeV. It is obtained by a fit procedure described in section 3.4.

- The germanium (HPGe) detector.
- The photomultiplier tube.
- The oscilloscope.
- The fan-out module which is needed for the duplication of the PMT signal.
- Discriminator effects for PMT signals close to the threshold.

The HPGe detector linearity was checked with the two calibration sources ^{137}Cs and ^{133}Ba. The PMT linearity measurement turned out to be more difficult since a defined quantity of light has to be used to check the linearity. A laser diode was used as light source and the stability of its intensity over time was checked [99]. In order to vary the light intensity, neutral density filters were used. The transmittance of the filters (Thorlabs NEK01 filter set) was measured with an UV/Vis spectrometer (Varian Cary400) at the diodes' wavelength of 438 nm as a part of this work. For the test of the oscilloscope and the fan-out module a pulse generator was used whose pulse height can be precisely adjusted. The signals were recorded with the oscilloscope and integrated

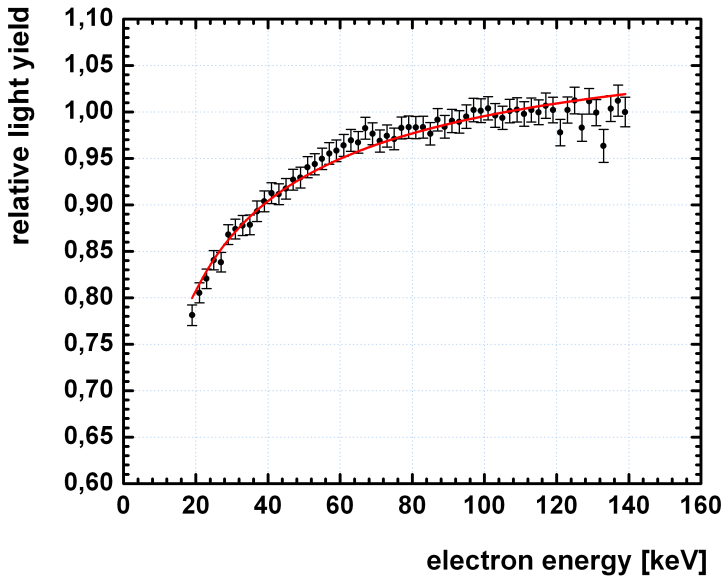

Figure 3.7: Relative light yield function for low energy electrons in the Target scintillator. The light yield for each electron energy is divided by a linear light yield function $L_1(E) = a \cdot E$ through the point at 139 keV to obtain the 'relative light yield'.

offline. These tests implicitly check the linearity of the offline analysis pulse integration. Discriminator threshold effects can bias the mean of the charge distribution of the PMT for small signals. In order to check the impact of these effects complete measurements of $L(E)$ were done for different threshold settings. In the end, a conservative approach was taken and only energy slices where the complete peak of the charge distribution is above threshold, were considered. For a discriminator threshold of 20 mV this leads to an electron energy threshold of 19 keV.

In all the systematic tests, no nonlinearity was observed. We can therefore give a small but conservative total systematic uncertainty of 1.2 % on the linearity of the instruments and analysis. The dominant uncertainty on the linearity comes from the PMT linearity measurement (1.1 %). The error bars in Figures 3.6 and 3.7 already include these systematic uncertainties and it can be seen that the non-proportionality coming from the ionization quenching is measured with high accuracy.

3.4 Laboratory measurement results

After the construction and commissioning of the setup the actual measurements of the Double Chooz scintillators have been performed by Stefan Wagner from MPIK Hei-

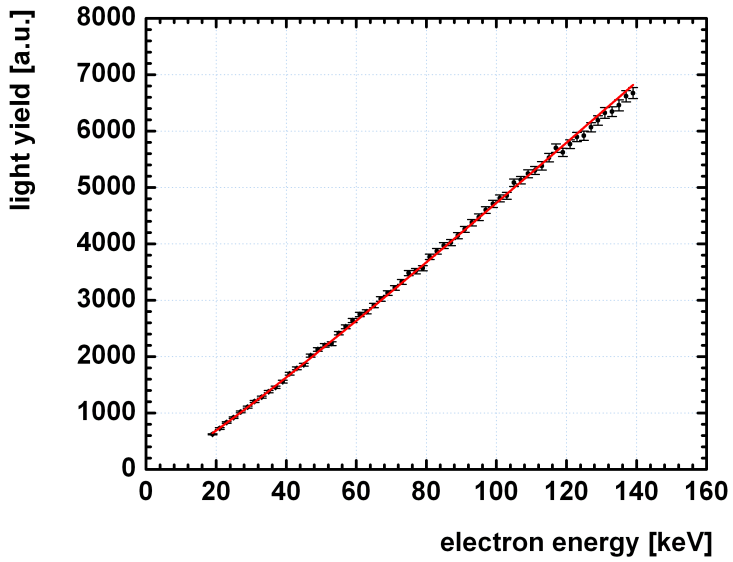

Figure 3.8: Response function $L(E)$ for low energy electrons in the GC scintillator.

delberg [98, 97]. Analysis software to fit the data with equation (3.3) was developed together. The results of the analysis are presented in this section. In section 3.5 the experimental results are used to tune the Double Chooz MC software which was done by the author of this thesis.

The experimental results for the Target have already been shown in Figures 3.6 and 3.7. In Birks' model, the light output in case of complete energy deposition inside the scintillator is given by the integral of the expression in equation (3.3):

$$L(E_0) = L_0 \cdot \int_0^{E_0} \frac{1}{1 + kB \cdot \frac{dE}{dx}(E)} \, dE \tag{3.5}$$

The initial energy is denoted by E_0. In order to fit the data with the Birks model a program was written which does a numerical integration of equation (3.3) since the expression for dE/dx (E) (Berger-Seltzer equation (3.1)) is a complicated function of the energy and the integral can not be solved analytically. Values for the mean ionization energy I and the electron density n_e have to be calculated for each scintillator separately. In the numerical integration we choose small integration step sizes such that the specific energy loss dE/dx is constant in good approximation before and after the integration step. Especially at energies in the region of the peak in dE/dx (see Figure 3.1) the step sizes have to be small (we choose $dx = 0.1$ nm) to fulfill this requirement.

The integral was calculated for each of the 61 electron energies for which a data point is available. This procedure was carried out for a range of values of the Birks parameter

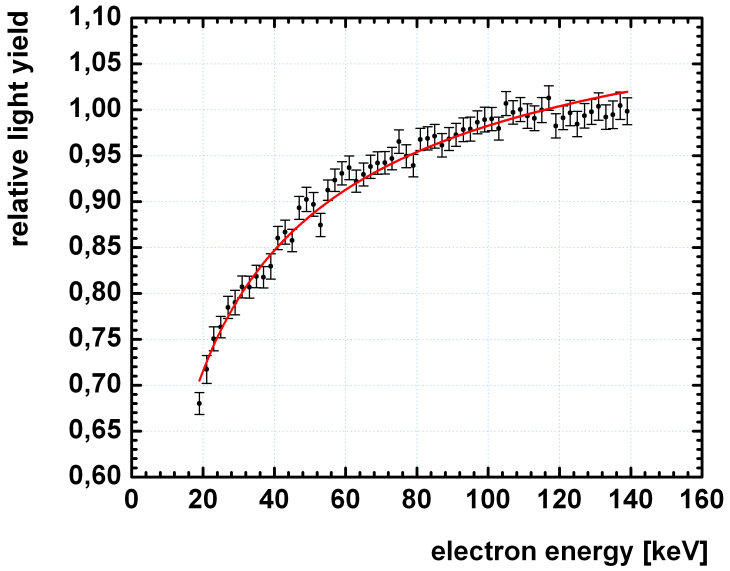

Figure 3.9: Relative light yield function for low energy electrons in the GC scintillator.

kB. Then, kB and a global normalization constant c_0 were used as free parameters to fit the data with a χ^2 minimization

$$\chi^2 = \sum_{i=1}^{n} \frac{\left(L_{data}(E_i) - c_0 \cdot L_{model,kB}(E_i)\right)^2}{\sigma^2_{data}(E_i)}. \tag{3.6}$$

The light yield for the ith data point is denoted by $L_{data}(E_i)$, the numerically integrated model light output is $L_{model,kB}(E_i)$ and $\sigma_{data}(E_i)$ is the error on the experimental light yield. The information on the Birks parameter is extracted from the shape of the response function $L(E)$ only, the global normalization is used to adjust the scale. The resulting fit for the Target scintillator is shown in Figures 3.6 and 3.7. Interpolating the fit values at the discrete electron energies leads to the continuous curves in the plots. The same analysis has been used for the Double Chooz Gamma Catcher, the results are shown in Figure 3.8 and Figure 3.9. Other scintillators have been analyzed as well. The results are given in table 3.1.

The scintillator Veto* was the Double Chooz Inner Veto candidate at the time these measurements were done. The aromatic fraction and the PPO concentration changed afterwards for the actual far detector liquid. Still, we can use the determined value for kB as an approximation. The GC with 5 g/l PPO has the same composition as the Double Chooz far detector GC (listed in table 1.2) except for the higher PPO concentration. It was the backup solution for the GC at the time the measurements were done. The

Scintillator	Birks parameter kB [cm/MeV]	χ^2/dof
Target	0.0158 ± 0.0006	46.0/59
GC (2 g/l PPO)	0.0279 ± 0.0009	57.8/59
GC (5 g/l PPO)	0.0245 ± 0.0008	57.8/59
Veto*	0.0152 ± 0.0006	51.9/59
PC + 1.5 g/l PPO	0.0172 ± 0.0006	45.4/59
plastic scintillator	0.0153 ± 0.0007	22.1/54

Table 3.1: Results for the Birks parameter for different scintillators. Veto*: 64 % tetradecane, 36 % LAB, 3 g/l PPO, 20 mg/l bis-MSB.

commercial plastic scintillator is based on polystyrene and includes p-terphenyl[1] and POPOP[2] as wavelength shifters. It is the scintillator used in the analogue hadronic calorimeter (AHCAL) prototype of the CALICE collaboration [100]. More detailed studies on the plastic scintillator can be found in [101].

Also other models apart from the common Birks model have been used. These analyses are described in more detail in [98]. No significant improvement over Birks' model was found with either the model by Wright [95] or Voltz [102]. Thus, the model by Birks is used also for the MC tuning since it is the the most common and well-known model of the three.

Discussion The values of the Birks parameters for the different scintillators can be well understood by considering the results from the light yield measurements (section 2.3) and the scintillation timing measurements (section 5.5). A similar discussion is presented for the values of the alpha quenching factors (QF) in section 4.5 where more different scintillator compositions have been measured. Here, the discussion is started with the scintillators which were analyzed in this chapter.

First, we observe a clear correlation between the alpha QFs and the Birks parameters kB for electrons. Both quantities describe the strength of the ionization quenching. In other words, high QFs and high kB reflect that the scintillator in question is affected strongly by the quenching effect: In this case, the scintillation efficiency due to quenching is reduced relatively strongly for alphas and the nonlinearity in the scintillation efficiency for electrons is higher. The correlation between the alpha QF values and the kB for electrons is expected since ionization quenching is the underlying physical effect which determines both. The degree of correlation is notable.

The GC scintillator with 2 g/l PPO has the highest alpha QF, the highest Birks parameter kB and the slowest time constants for the scintillator light emission. These observations can be explained consistently with a slow energy transfer from the solvents to PPO compared to the other scintillators. For more discussion along these lines on the

[1] CAS: 92-94-4

[2] 1,4-bis(5-phenyloxazol-2-yl) benzene, CAS: 1806-34-4

Target, the Veto and other scintillators please refer to the discussion in section 4.5. The PC[3] plus 1.5 g/l PPO scintillator is used in the solar neutrino experiment BOREXINO [103]. From the relatively low kB presented here we can conclude that, although the PPO concentration is as low as 1.5 g/l, the energy transfer from PC to PPO is rather effective. Our result of the Birks parameter of this scintillator deviates from that given in [104] (0.020 cm/MeV). This difference is most likely due to a different analysis technique used. The influence of different analysis methods on kB is discussed in the next section. Energy transfer from LAB to PPO seems to be rather effective as well. LAB is the aromatic solvent component in the Veto scintillator. Again, these results are confirmed by the timing measurements in section 5.5 and increase the level of understanding of the scintillator physics.

3.5 Monte Carlo tuning

The goal in this section is to tune the MC model such that the data presented in section 3.4 is well described. The Monte Carlo tuning of the ionization quenching effect was done for the Double Chooz offline group software `DOGS` (see section 1.2.5) for the Double Chooz scintillators. However, the general observations about the implementation details of the ionization quenching apply for the default `Geant4` implementation (in the class `G4EmSaturation`) as well since the same technique is used. `Geant4` is widely used in physics and thus the results and discussions presented here can be interesting for other groups who want to implement the ionization quenching effect for their detector simulation.

In both the Double Chooz Monte Carlo software `DOGS` (more specifically in `DCGLG4sim`) and in the default `Geant4` class `G4EmSaturation` Birks' quenching model is used.

`DCGLG4sim` is roughly speaking the interface between the particle tracking algorithms, which are implemented in `Geant4` on the one hand and the part of the simulation which is specific to Double Chooz (for example geometry and material properties implementation, choice of physics processes, etc.) on the other hand.

Simulated particles are propagated step by step with `Geant4`[4]. For each step the possible particle interactions are considered and one of them is chosen according to the probabilities for the processes. If a secondary particle is created which has a stopping range above a certain threshold the secondary particle is explicitly generated and tracked by `Geant4`. If the secondaries are below this threshold the energy loss of the primary particle is treated as a continuous energy loss. This continuous energy loss of the particle in a given medium is calculated with the help of the Berger-Seltzer equation in case of electrons. Fluctuations of this energy loss are drawn from a straggling function. The user can control the particle step size and specify the threshold for explicit secondary production. One can also enable or disable the fluctuations. More detailed information on these control commands and their impact is given below.
The continuous energy loss of a particle in a given step and the step length are calculated

[3] pseudocumene (1,2,4-trimethylbenzene), CAS: 95-63-6
[4] For this analysis `Geant4`.9.2p02 was used.

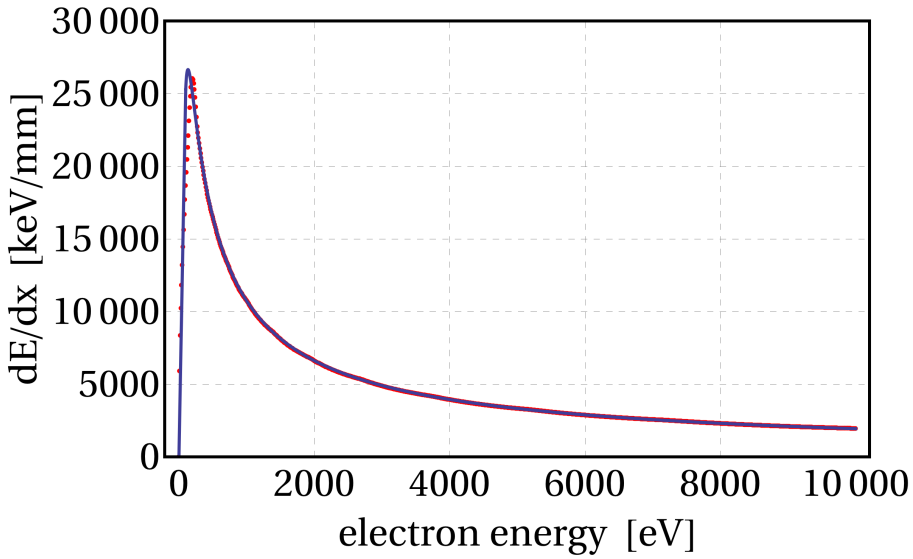

Figure 3.10: Comparison of the Berger-Seltzer equation (blue line) with tabulated values of dE/dx (red points) calculated by `Geant4` for the Target scintillator.

by `Geant4` and then passed to `DCGLG4sim`. The energy loss per step is denoted by ΔE_0. In the approach described here, which is also used in `Geant4` by default, the number of scintillation photons generated is proportional to the quantity ΔE_q which is called quenched energy (or visible energy) and is calculated using an equation which corresponds to equation (3.3):

$$\Delta E_q = \frac{\Delta E_0}{1 + kB\left(\frac{\Delta E_0}{\Delta x}\right)}. \tag{3.7}$$

Here Δx is the length of the considered step and kB is the Birks (quenching) parameter. As explained before, the energy loss of electrons calculated by `Geant4` is based on the Berger-Seltzer equation. The values for dE/dx are stored in tables for each scintillator before the particle tracking starts. It was checked if the equation given in 3.1 with the mean ionization energy I (see equation (3.2)) and the electron density n_e calculated manually, actually gives the same results as the calculation of dE/dx done by `Geant4`. The result of this check is shown for the Target scintillator in Figure 3.10. Good agreement is found between the calculation in `Geant4` and the calculation with equation (3.1) which was also used in the numerical integration analysis presented in section 3.4.

At first glance this would justify to directly use the kB values from the previous section in the Monte Carlo model. However, three main differences play a role when we compare the kB analysis using numerical integration of equation (3.3) with the MC calculation as in equation (3.7). First, the step length in `Geant4` will be higher than the 0.1 nm which was used for the numerical integration. Second, in the MC detector simulation a particle can generate secondary particles which are then affected by ionization quenching as well. Third, the simulation takes into account randomly drawn fluctuations for each

particle step. The effect of these three differences on the Birks parameter kB which describes the data best is analyzed below. Before that the relevant tracking commands are described in more detail.

`Geant4` particle tracking control commands There are several commands available to control the Monte Carlo tracking process. The user can control the step length using the command `/process/eLoss/StepFunction p1 p2`. The first parameter `p1` specifies which fraction of the stopping range a particle can travel at most within one step. This condition is alleviated by a minimal step length, which can be specified by the second parameter `p2`. The transition between the fractional condition on the step size and the minimal step length is smoothed by a function given in [105]. The default settings for the parameters are `p1`=0.2 and `p2`=1 mm.

I also studied the variation of the threshold for explicit secondary particle generation with the command `/run/particle/setCut p3`. If the energy loss in a single step for a chosen physics process is high enough that the particle generated in this process has a range above the threshold p3 then the particle is explicitly generated and tracked by `Geant4`. A lower threshold means that we get more secondary particles. For these secondary particles the energy loss for one step is calculated in the same way as for the primary particle and ΔE_q for this step is added to the total E_q which is proportional to the number of generated photons. The default parameter value is `p3`=0.01 mm.

The effect of switching off fluctuations in the energy loss calculation was studied with the command `/process/eLoss/fluct false`. By default the fluctuations are on. Physically, the variations in the energy loss come from the stochastic nature of multiple interactions with electrons in the medium. Details of the straggling functions from which the fluctuations are drawn are given in [105, 106].

Fit procedure In this paragraph, it is described how MC simulation of the ionization quenching and data are compared. For multiple kB values, and for each energy for which an experimental data point is available, 1000 electrons were simulated. This guarantees that the statistical error on the mean of the simulated distribution of E_q is small. With typically about 20 different values for kB and the 61 different electron energies which are available from the laboratory measurement this leads to over 10^6 electrons which have to be simulated for one scintillator. These extensive computing tasks can be efficiently done at the computing center in Lyon (CCIN2P3) where multiple simulation jobs can be processed in parallel. Then a χ^2 fit of the data with the simulated $\overline{E}_q$ values (mean of the distribution from 1000 particles) was done with two free parameters: one global normalization c_0 and kB:

$$\chi^2 = \sum_{n=1}^{61} \frac{\left(L_{data}(E_i) - c_0 \cdot \overline{E}_{q,MC,kB}(E_i)\right)^2}{\sigma^2_{data}(E_i) + c_0^2 \cdot \sigma^2_{MC,kB}(E_i)}. \tag{3.8}$$

The experimental data for the ith electron energy data point is denoted by $L_{data}(E_i)$ with its corresponding error $\sigma_{data}(E_i)$. For the simulation, $E_{q,MC,kB}(E_i)$ is the mean quenched energy for the ith energy and $\sigma_{MC,kB}(E_i)$ is the error on the mean. These small errors

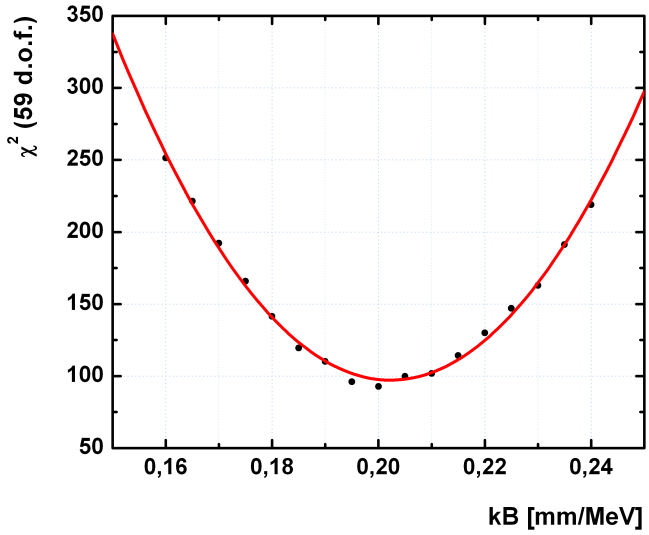

Figure 3.11: Results for the χ^2 fit of the MC output to the experimental data for the Target scintillator. Over the second free fit parameter (global normalization factor) has been marginalized (χ^2 was minimized with respect to the global normalization factor for each kB value). This $\chi^2(kB)$ function can be approximated by a quadratical function (red line).

from the simulation have been quadratically added to the experimental errors. However, the effect on the χ^2 is negligible since the experimental errors dominate.

In Figure 3.11 the χ^2 values from this analysis are shown for different kB for the default configuration of `Geant4`. The shape of the light yield function determines the best fit value of kB. Over the global normalization fit parameter was marginalized since a priori we do not have sufficient information on the true normalization factor between the experimental values and the simulation. From the quadratical approximation of the $\chi^2(kB)$ function the best fit value and the corresponding statistical error is extracted: kB=(0.202 $\pm$ 0.003) mm/MeV for the Target. This value can be used in the MC with the default settings.

Results Using the best fit value for kB the experimental data is well described. The fit of the data for the default settings in `Geant4` is shown in Figure 3.12. The value for the best fit kB differs significantly from the value obtained with the numerical integration of the Birks equation. The reason for this difference is due to the differences in the calculation of the visible energy which are presented in the 'Discussion' paragraphs below. These differences depend on the settings of the tracking control parameters.

In section 3.4 we presented the kB parameters obtained by the analysis which was done without using the MC software. There equation (3.3) was integrated numerically

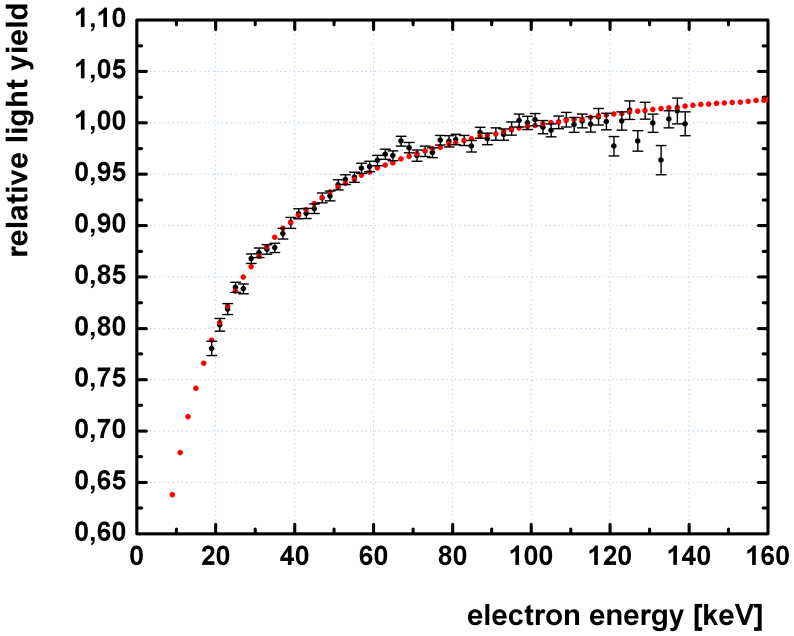

Figure 3.12: Best fit of Monte Carlo light production (red points, simulation of 10^4 electrons per point)) to data for the DC ν-Target scintillator. Here the default parameters for the stepping commands have been used. We only included statistical errors. The Birks parameter is tuned to kB=(0.202 $\pm$ 0.003) mm/MeV.

with small step sizes Δx. We did not explicitly calculate the energy loss for secondary particles and we did not include fluctuations. As a check of the consistency of this method with the MC tuning we can use the commands described above to check if the same result is obtained with MC if similar conditions are applied: A maximal relative energy loss per step of 5 % is chosen and a minimal step length of 10^{-5} mm to approach the small step size in the numerical analysis. No secondary particles were produced (a very high threshold for secondary particle production was chosen) and fluctuations were turned off. For the Target scintillator the result for kB is (0.0164 $\pm$ 0.0003) cm/MeV and thus perfectly agrees with the result of the numerical method (see second to last line in table 3.2 and first line in table 3.1). This was expected because it was explicitly confirmed that the dE/dx values for both analyses agree (see Figure 3.10). This check was done to confirm the understanding of the implementation of ionization quenching in the simulation.

The influence of the `Geant4` particle tracking parameters on the kB value which best describes the data has been further studied. It is found that the best fit values for kB vary significantly if the parameters of the stepping commands are changed (see table

3.2). Note that for the MC studies only statistical errors are considered. This explains why the error intervals are generally smaller than the ones in section 3.4.

/process/eLoss /StepFunction		/run/particle /setCut	/process/eLoss /fluct	kB [cm/MeV]
0.20	1 mm (d)	0.01 mm (d)	true (d)	0.0202 ± 0.0003
0.05	0.1 mm	0.01 mm	true	0.0232 ± 0.0004
0.05	0.001 mm	0.01 mm	true	0.0174 ± 0.0003
0.05	10^{-5} mm	0.01 mm	true	0.0107 ± 0.0003
0.05	10^{-5} mm	10^{5} mm	false	0.0164 ± 0.0003
0.20	1 mm	0.001 mm	true	0.0287 ± 0.0005

Table 3.2: Results for the best fit kB with different stepping commands for the ν-Target scintillator. The entries in the table are the parameter(s) of the corresponding command. The statistical errors of the fits are given. Default settings are marked with (d).

Figure 3.12 shows the resulting best fit for the default parameters. For these settings χ^2 of the fit to the experimental data is lowest of all the options which were tested and the ionization quenching effect is well described (see Figure 3.12). The χ^2 values per degree of freedom are generally higher than one. This can be due to small systematic nonlinearities in the measurement or due to the fact that the Birks equation implementation is not perfect for the description of the data. If the systematic errors are included, the values for χ^2/dof are close to one (see table 3.1).

One can see that the best fit values for kB change more than a factor of two when different settings in `Geant4` are compared. This leads to the conclusion that it is required to tune a given MC simulation software with the experimental data instead of using a value obtained by a different analysis method. But it also shows that for a wide range of `Geant4` parameter settings, description of the data is possible in the energy range of the available data by tuning of the Birks parameter.

Discussion: Effect of the MC step size The underlying reasons why the best fit kB parameters vary strongly with the applied `Geant4` settings are discussed in this paragraph. First, the dependency on the MC step size was investigated. The travel distance (also: stopping range) x_0 of an electron in the scintillator is calculated in `Geant4` from dE/dx:

$$x_0 = \int_0^{E_0} \frac{1}{\frac{dE}{dx}(E)} dE. \tag{3.9}$$

For an initial electron energy E_0 of 140 keV the travel distance is about 0.30 mm. As explained above the default parameter settings for `Geant4` include the condition that the minimal step length coming from the continuous energy loss process is 1 mm. This means

that an electron of 140 keV only takes one simulation step if it does not participate in another process than continuous energy loss. In the case of complete energy deposition within one step, equation (3.7) becomes

$$E_q = \frac{E_0}{1 + kB\left(\frac{E_0}{x_0}\right)}. \tag{3.10}$$

In the `Geant4` simulation the travel distance during one step Δx is always calculated via the integral over the inverse specific energy loss as in equation (3.9). For steps where not the complete energy is deposited, the integration range in equation (3.9) is adjusted. The value for the quenched (visible) energy E_q for a single step is different from the quenched energy for many steps. In the limit of an infinite number of steps we get

$$E_q = \int_0^{E_0} \frac{1}{1 + kB \cdot \frac{dE}{dx}(E)}\, dE. \tag{3.11}$$

As explained before, the normalization factor for the MC fit of the data is a free parameter. We can absorb any fractional loss in E_q which is common to all energies with this global factor in the fit. In the simulation one can increase the light yield constant L_0 (see equation (3.3)) by this common factor. The interesting quantity is the E_q ratio for two different energies. This corresponds to the shape of the light yield function and thus the impact of ionization quenching. To illustrate this the E_q numbers are calculated for 140 keV and 40 keV for both the single step equation (3.10) and the integral (infinite number of steps) equation (3.11). For kB in both cases 0.0158 cm/MeV is assumed which is the value from the numerical integration method for the Target scintillator. For the single step we get $E_{q,1}$(140 keV)=130.29 keV and $E_{q,1}$(40 keV)=33.76 keV. For infinite number of steps $E_{q,\mathrm{inf}}$(140 keV)=125.92 keV and $E_{q,\mathrm{inf}}$(40 keV)=31.87 keV is obtained. We are interested in the ratio between 40 keV and 140 keV since this reflects the shape of the light yield function. For one step a ratio of 3.859 is obtained and for the integral calculation 3.951 is calculated. The lower number for one step means that the simulated nonlinearity in the case of one step is weaker than for the limit of an infinite number of steps. This can be balanced by a higher kB parameter. If the kB factor is changed for the one-step case from 0.0158 cm/MeV to 0.0202 cm/MeV, which is the best fit value for the MC simulation default settings, the same ratio 3.951 as for the integral with kB = 0.0158 cm/MeV is obtained. This example illustrates how the number of steps leads to different effective Birks parameters kB. Thus, it can be understood why the value for the best fit kB for the default setting is smaller than for many steps (see table 3.2).

It turns out that for the default settings in `Geant4` only one step is performed for electrons with energies below about 315 keV. At 315 keV we get from equation (3.9) that the stopping range is 1 mm. This is the default lower limit for the step size. Above about 315 keV the particle is propagated in two steps in most of the cases. The transition from one step to two steps leads to a small difference in the mean quenched energy in the simulation. Figure 3.13 shows the difference between the quenched energy

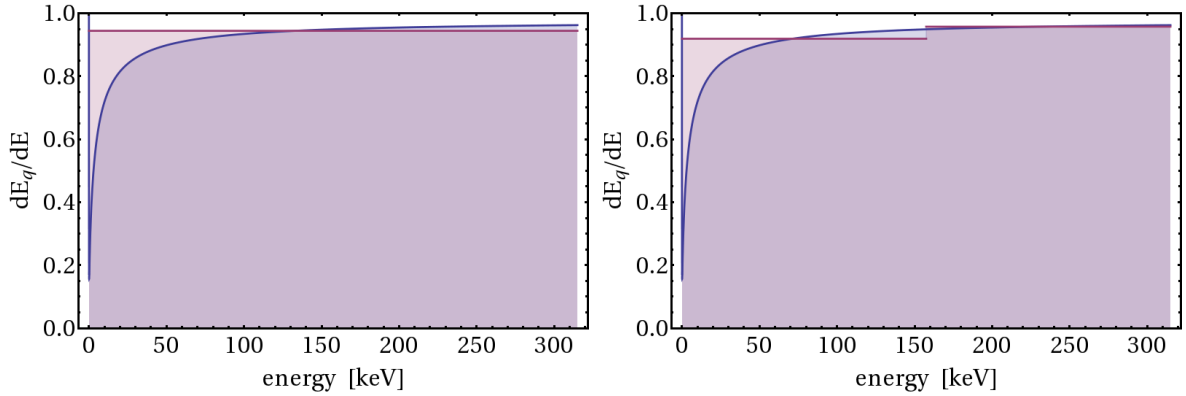

(a) 1 step

(b) 2 steps

Figure 3.13: Difference in visible energy calculation with one (a) and two (b) Monte Carlo simulation steps compared to the limit of infinite number of steps (blue line, equation (3.11)). The red lines correspond to the `Geant4` calculation with equation (3.7). The Birks parameter $kB = 0.0202$ cm/MeV has been used here. The area under each function represents the visible energy.

calculation for the case of one or two steps. It turns out that the value for E_q for two steps is slightly lower than for one step. This leads to a small bump in E_q/E_0 at the transition energy where the calculation switches from one step to two steps (see Figure 3.14 (a)). It has to be kept in mind that this effect, although small (0.4 %), occurs for the default stepping settings in `Geant4`. When choosing smaller step sizes with `/process/eLoss/StepFunction 0.05 0.1 mm` the energy at which the transition from one step to two steps takes place occurs at an energy of about 75 keV. This effect leads to a bump in the energy region where the experimental data has been taken. It is shown in Figure 3.14 (b). For a higher number of simulation steps the effect will shift toward lower energies. There are practical limitations to the number of steps since the CPU time needed for particle tracking becomes bigger with increasing number of steps. It has to be noted that the tracking of particles is canceled by `Geant4` if the size of the steps becomes too small. Also, the widths of the visible energy distributions depend on the number of steps (see below). These considerations have to be taken into account when the step size is chosen.

Another option which can be considered for the simulation is the calculation of the visible energy with the integral given in equation (3.11) using the energy before the step and the energy after the step for the limits of the integral. The `Geant4` tracking could still be done with the default settings and thus a low number of steps. This approach is described in [101]. It has the benefit that the best fit kB is insensitive to changes of the tracking parameters and that the small bumps in E_q/E_0, which occur for the default settings, disappear. On the other hand this 'integral approach' has the disadvantage that it is difficult to handle the fluctuations in the specific energy loss. For the default implementation with equation (3.7) the fluctuations are incorporated automatically.

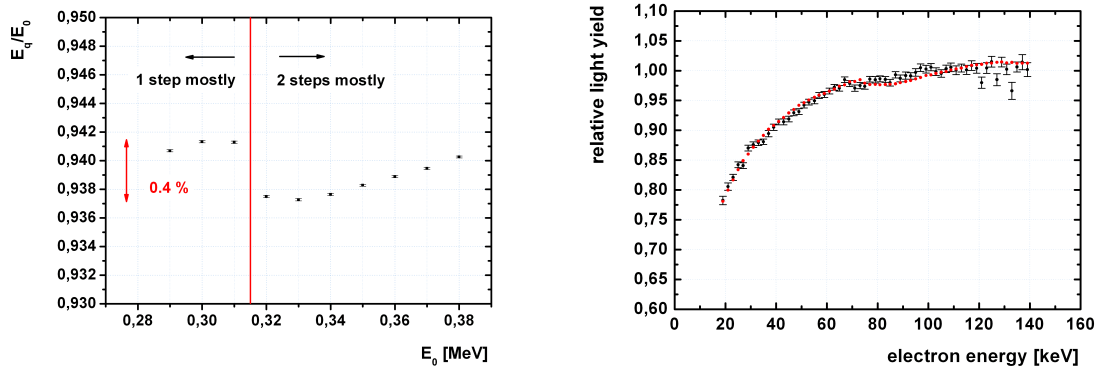

(a) (b)

Figure 3.14: (a) E_q/E_0 at the transition between one simulation step and two simulation steps. Note that the difference between E_q/E_0 for $E_0 = 0.30$ MeV and $E_0 = 0.33$ MeV is as low as 0.4 %. Here, the secondary particle production has been turned off to show the effect of the number of steps more clearly. (b) Fit of the data with `/process/eLoss/StepFunction 0.05 0.1 mm`. For this setting the transition between one and two steps can be seen at about 75 keV.

Discussion: Energy loss fluctuations and secondary particle production The threshold for production of secondary particles also has an impact on the best fit kB. In the case of electrons with energies between 20 keV and 140 keV, the secondary particles are mainly other electrons or gammas which in turn produce more electrons. Each charged secondary particle which is individually tracked by `Geant4` is subjected to quenching via equation (3.7). The energy lost by a secondary particle is quenched stronger since the dE/dx values at lower particle energies are higher. If the same energy loss is treated as a continuous energy loss of the primary particle, the energy is quenched less since the primary particle's energy is higher and thus the dE/dx is lower. Physically, this effect can be interpreted with the concept of an ionization column around the primary particle track. Secondary electrons with sufficiently high stopping range can escape the ionization column. Then they in turn produce a smaller ionization column with higher ionization density [102]. The effect of a different secondary production threshold on the quenched energy spectrum is shown in Figure 3.15. In total, the simulated quenched energy is lower if many secondary particles are crated due to a low secondary particle threshold. The best fit quenching parameter kB is sensitive to the shape of the light yield function. Since a higher effective kB is obtained for the lower secondary particle threshold (see last line in table 3.2) it seems that the relative decrease in E_q due to secondary particle production is dependent on the initial electron energy. The details depend on the energy-dependent cross sections for secondary particle production and have not been studied further here.

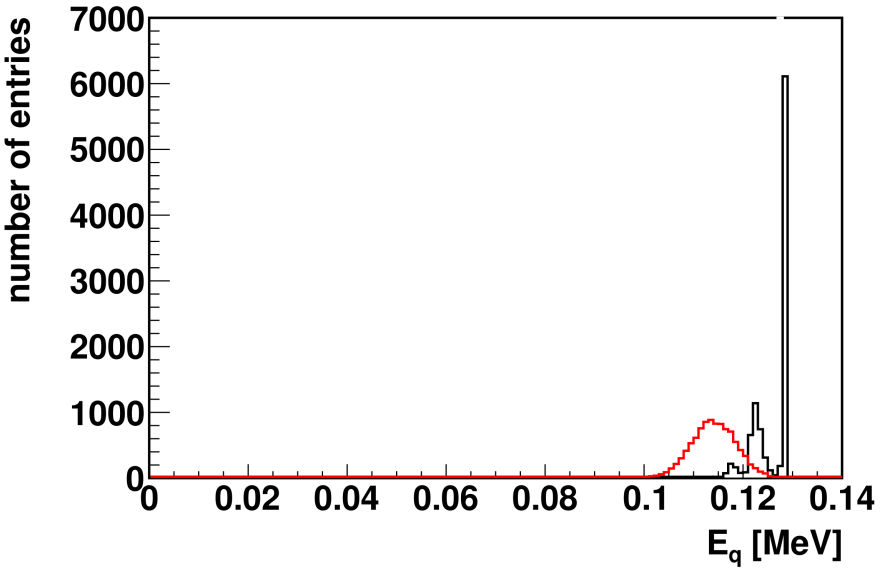

Figure 3.15: Simulation of 10000 electrons of 0.14 MeV energy. The visible energy spectrum calculated by `Geant4` for different secondary particle threshold settings is shown. Default settings (`/run/particle/setCut 0.01 mm`) give the black histogram. The peak at 0.128 MeV corresponds to particles where no secondary particle has been produced, the two smaller peaks correspond to one and two produced secondaries respectively. For the red histogram, the production threshold for secondary particles has been lowered (`/run/particle/setCut 0.001 mm`). Here, about 10 secondary particles per primary particle are produced.

The width of the simulated visible energy spectra also depends on the tracking parameter settings. Figure 3.15 shows that increased secondary particle production broadens the shape of the visible energy spectrum. Also the number of steps influences the widths and the mean value. For small step sizes (i.e. `/process/eLoss/StepFunction 0.05 1e-5 mm`) the width of the visible energy distribution is bigger and the mean is lower (see Figure 3.16). The right peak of the black histogram corresponds to electrons which do not produce a secondary particle and which lose all their energy within one step. In this case the fluctuations are small. It has been checked that the number of secondary particles is the same regardless of the step size. This means that the broadening of the red distribution comes from the dE/dx fluctuations, which are calculated for each step individually. For the red histogram the 140 keV electrons lose their energy in about 130 steps. For each step a fluctuation in the dE/dx is calculated and this leads to a broadening of the visible energy distribution through application of equation (3.7). The shift of the mean value has been explained in the paragraph 'Effect of the MC step size'.

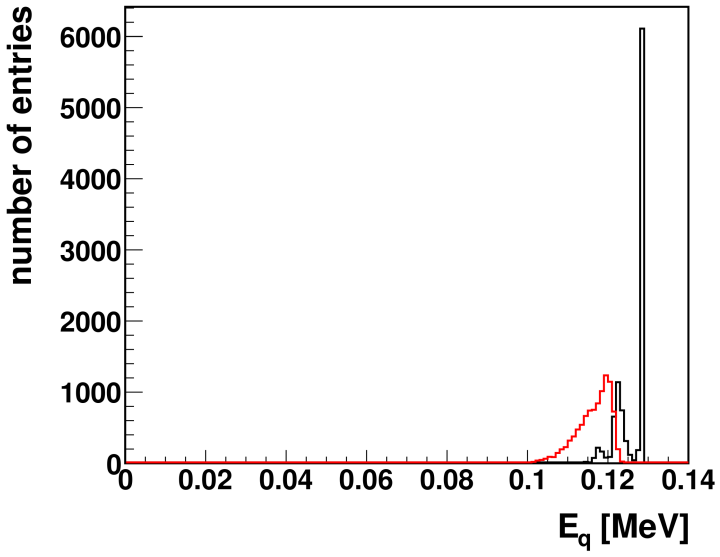

Figure 3.16: Monte Carlo visible energy spectra for the default settings (black histogram) and for a small step size setting (red histogram).

Summary of the Monte Carlo tuning It has been shown that the experimental data from the laboratory measurements can be well described with the Monte Carlo software (see Figure 3.12) using the default settings after tuning the Birks parameter in the simulation. Effective kB values for other simulation settings, which are able to describe the data as well, have been determined (see table 3.2). More detailed studies revealed several subtleties concerning the calculation of the visible energy and the implementation of Birks law. For different numbers of steps there are differences in the results for the visible energies. It has been shown that in the Monte Carlo simulation the widths depend on the tracking command settings as well. It would therefore be interesting to further study the actual widths of the distributions with measurements and adjust the MC settings accordingly. The energy range of the laboratory measurement was 20 keV to 140 keV. It is difficult to extrapolate to much higher energies. This can be seen by the fact that the MC fits for different tracking command settings can differ slightly at high energies (see Figure 3.17) although they both reproduce the data well in the 20 keV to 140 keV range. It is therefore proposed to review the best Monte Carlo parameter settings and the best method for calculating the visible energy with the help of calibration data from the Double Chooz far detector once other sources of nonlinearity not coming from scintillator physics are studied and controlled with precision. The Cherenkov effect will also contribute to the nonlinearity in the MeV energy range and has to be studied with detector data since the Monte Carlo simulation of the Cherenkov effect is difficult to tune a priori. The reason for the difficulties is that the refractive index of the scintillators can not be measured for all relevant wavelengths since photons are immediately absorbed by the scintillator at low wavelengths. Subsequent wavelength-shifting complicates the

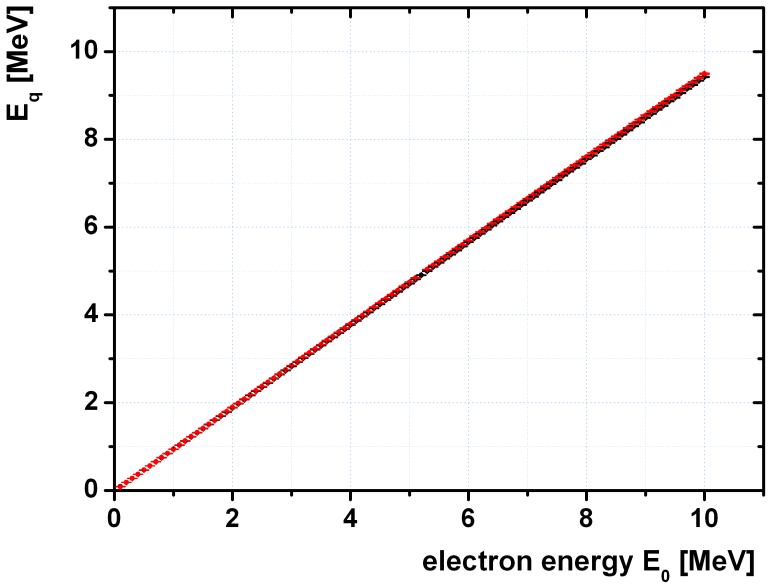

Figure 3.17: Monte Carlo electron energy scale prediction from 0.1 MeV to 10 MeV for default settings and small step settings. For both settings the effective kB values have been used which reproduce the laboratory measurement data at 20 keV to 140 keV.

prediction of the Cherenkov contribution to the measured charge in the photomultiplier tubes. Thus it is proposed to study the Cherenkov contribution with detector data and adjust the ionization quenching simulation together with the Cherenkov simulation. However, for the ionization quenching simulation a solid starting point has been obtained with the help of the laboratory measurements.

Currently, the default simulation settings are used and for each Double Chooz scintillator an effective Birks parameter has been found which is suitable to describe the data from the laboratory measurements. Finally, the results for the tuning of the effective kB are listed for these default settings for the Target (Figure 3.12), GC and the Veto scintillator. In Figure 3.18 the experimental data together with the best Monte Carlo fit is shown for GC and Veto. The same plot for the Target scintillator is shown in Figure 3.12. Table 3.3 summarizes the effective kB for the three scintillators.

3.6 Summary

The ionization quenching effect for electrons is important for the energy scale in Double Chooz. Positrons and gammas which are detected after neutrino interactions are af-

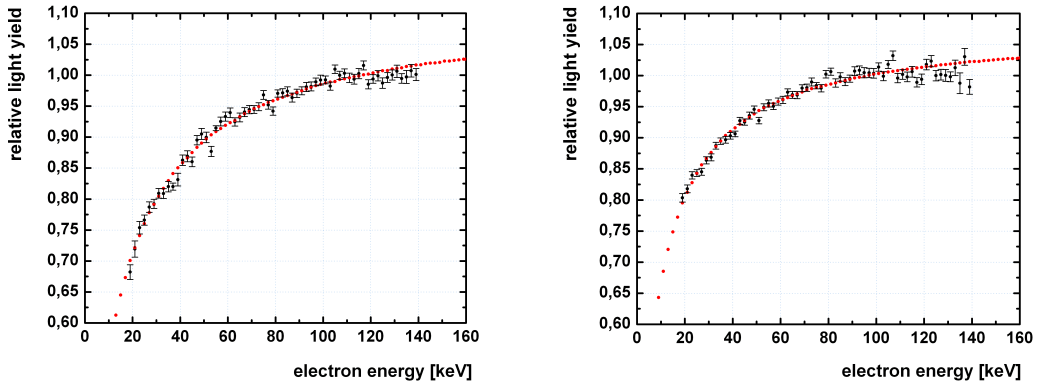

(a) GC (b) Veto

Figure 3.18: Monte Carlo fits (red points) of the experimental data for the Gamma Catcher scintillator (a) and the Veto* scintillator.

Scintillator	Birks parameter kB [cm/MeV]
Target	0.0202 ± 0.0003
GC (2 g/l PPO)	0.0335 ± 0.0006
Veto*	0.0205 ± 0.0004

Table 3.3: Results for the Monte Carlo effective Birks parameters for the three Double Chooz scintillators. The default `Geant4` tracking parameter settings have been used. Statistical errors are listed. Veto*: 64 % tetradecane, 36 % LAB, 3 g/l PPO, 20 mg/l bis-MSB.

fected differently by the nonlinearity in light production. The results presented here in combination with detector calibration data quantify the corrections for the energy scale.

A setup has been constructed which was used to measure the non-proportionality in light output of low energy electrons (20 keV to 140 keV). It includes a germanium detector to precisely measure the energy of Compton scattered gammas and thus determine the energy of the recoiled electrons which excite the scintillator. The analysis of the laboratory measurement data was presented and the energy dependent light output was obtained for multiple scintillators including the Double Chooz liquid scintillators.

A description of the experimental data was successfully done with Birks' equation using the Berger-Seltzer equation for the energy loss of electrons. Results for the Birks parameter kB for each scintillator are obtained with a numerical integration of the Birks equation. The differences in the kB values are discussed and understood with the help of the light yield model and the results from the scintillator emission time measurements.

The `Geant4`-based Monte Carlo simulation in Double Chooz was tuned with the results

from the laboratory measurements. The same implementation of ionization quenching is used as in the default `Geant4` algorithms. The results of the MC tuning are thus relevant for the implementation of ionization quenching in `Geant4` in general.

The Birks parameter kB for the Target scintillator, which has to be used in the Monte Carlo software to correctly describe the experimental data, varies significantly if the simulation tracking parameters (step size, secondary particle production and energy loss fluctuations) are changed (table 3.2). This means that values for kB have to be tuned for each setting individually to describe the laboratory measurements and kB values from an analysis with a given setting can not be used for other settings. These dependencies on the `Geant4` tracking parameters have been analyzed and they can be understood when looking into the details of the light production calculation of the simulation.

Currently the default `Geant4` parameter settings are used and kB is tuned accordingly with laboratory measurements (table 3.3). Additionally, tuned kB values are provided for a wide range of other parameter settings and the choice of these settings can be further optimized once calibration data from the detector is available which will provide additional information on the ionization quenching and Cherenkov effects.

4 Alpha quenching laboratory measurements and Monte Carlo simulation tuning

4.1 Introduction and Motivation

Alpha particles have a higher energy loss per unit length dE/dx than electrons of the same energy when passing through matter. This leads to higher ionization and excitation densities along the particle track. The ionization quenching process, which is described in more detail in section 3.2 and which is responsible for the nonlinearity in the light yield function for electrons (see chapter 3) is much more pronounced for alphas than for electrons. It leads to a considerable loss in scintillation efficiency and to nonlinearities at the scale of MeV ('alpha quenching'). For electrons the ionization quenching effect is most visible at energies below about 100 keV (section 3.4). This introductory section and section 4.2 describe the specific energy loss for alpha particles in more detail.
Laboratory measurements on the so-called 'alpha quenching effect' are presented for different liquid scintillator compositions including the Double Chooz scintillators. The alpha quenching factor (QF) at a given alpha energy is defined as the ratio of the alpha energy over the electron energy which produces the same amount of light $L = x_1$

$$QF = \frac{E_\alpha(L = x_1)}{E_{e^-}(L = x_1)}. \tag{4.1}$$

In order to determine the alpha QF we need to excite the scintillators with both electrons and alpha particles. In section 4.3 the two methods are presented which were used to dope the scintillators with alpha emitting isotopes. In order to excite the scintillator with electrons we use the same 'Compton Backscatter Peak' method which was described in section 2.2. Gamma sources of different energies are used to calibrate the light yield under electron excitation with high accuracy. A Monte Carlo simulation was performed to get the energy distribution of the backscattered electrons in the 'Compton Backscatter Peak' configuration (section 4.4).
The alpha quenching factors determine at which electron-like energies in the Double Chooz detector energy spectrum the alpha peaks occur. They are therefore important for the estimation of the background contribution coming from the alpha emitting isotopes from natural radioactivity in the detector.
In section 4.5 the results of the laboratory measurements are presented and discussed. They can be related to the light yield results and the scintillator emission time behavior

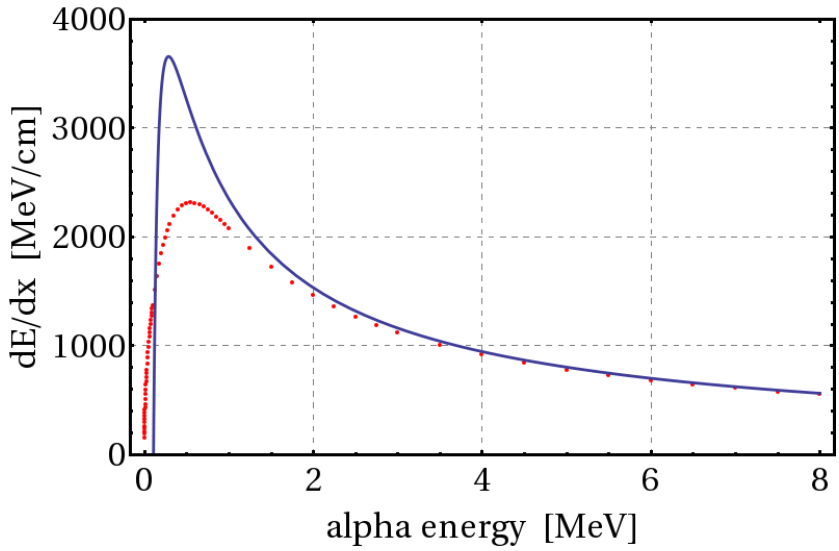

Figure 4.1: The specific energy loss for alpha particles. The blue line shows equation (4.2) without the density correction δ, the higher order corrections F and the shell corrections. It deviates significantly for energies below about 2 MeV from the red points, which have been obtained from tabulated values for dE/dx [106]. In both cases the material constants have been calculated for the Target scintillator composition.

which was studied in this work as well. The results can be understood with the help of the light yield model concepts and they contribute to our understanding of the physical processes in the Double Chooz scintillators.
Finally, the results of the measurements have been used to adjust the Double Chooz Monte Carlo light output for alpha particles in section 4.6. The results are discussed and compared to the quenching parameters obtained from electrons.

4.2 Energy loss of alpha particles passing through matter

The energy loss for ions is described by the Bethe equation [107]. This equation is used in many different forms and several generalizations and extensions have been put forward by various authors. An overview of the development of the equations and their derivation is given in [108]. In the simulation software `Geant4` several of these corrections are implemented. The equation which is used in [105] is

$$\frac{dE}{dx} = 2\pi r_e^2 m_e c^2 n_e \frac{z^2}{\beta^2}\left[\ln\left(\frac{2m_e c^2\beta^2\gamma^2 T_{max}}{I^2}\right) - 2\beta^2 - \delta - \frac{2C_e}{Z} + F\right]. \qquad (4.2)$$

The classical electron radius is denoted by r_e, the electron rest energy is given by $m_e c^2$, the electron density in the given medium is n_e, the charge of the incident hadron is z, β is the particle velocity divided by the speed of light, γ is the Lorentz factor, I is the mean ionization energy of the medium and the maximal energy which is transferable from an incident particle of mass M to an electron is

$$T_{max} = \frac{2m_e c^2(\gamma^2 - 1)}{1 + 2\gamma(\frac{m_e}{M}) + (\frac{m_e}{M})^2}. \tag{4.3}$$

The term δ accounts for the density correction effect [91] which can be neglected in our case for alpha particles with less than 10 MeV kinetic energy. Higher order corrections which are described in more detail in [108, 105] are summarized by the term F. The term $2C_e/Z$ describes the shell correction terms which become important for low energies. For alpha particles this term becomes significant below about 2 MeV and it is difficult to calculate. The effect of this term is illustrated in Figure 4.1, which shows the specific energy loss for alpha particles in the Target scintillator.
The red points in Figure 4.1 have been obtained by combination (summation weighted with the weight fraction) of tabulated dE/dx values [106] for hydrogen and carbon. These tabulated values (starting at 1 keV) combine information from measurements with model calculations and they are used by `Geant4` as well for low energies. Other elements are negligible in the scintillator compositions analyzed in this work. All the scintillators have similar H/C ratios, electron densities and mean ionization energies. Figure 4.1 is therefore representative for the other scintillators as well. The deviation of equation (4.2) without the shell correction from the tabulated values is significant. It was therefore decided to use the tabulated values for dE/dx rather than trying to do the difficult corrections. However, it is a good consistency check that the dE/dx obtained with the help of the tabulated values and equation (4.2) agree closely between 4 MeV and 8 MeV.
A peak in dE/dx at alpha energies below 1 MeV energy is obtained. The behavior is qualitatively similar to the behavior for electrons shown in Figure 3.1. However, for alphas the dE/dx values are about a factor of ten higher in the peak than for electrons (note the different scales in the two figures) and the peak is at much higher kinetic energies. Due to the higher dE/dx alpha particles have shorter travel distances than electrons. An alpha particle of 7.7 MeV energy has a stopping range of about 80 μm in our scintillators. The ionization and excitation density is higher and therefore their light production in liquid scintillators is more affected by ionization quenching. The underlying physics of ionization quenching is the same as for electrons (see section 3.2). This means that the Birks equation (3.3) for the description of the scintillation inefficiency can be used for alphas as well.
The natural radioactive alpha emitting isotopes come mainly from the uranium series (^{238}U) and the thorium series (^{232}Th). A smaller contribution comes from the ^{235}U series. They produce alpha particles with energies between 4 MeV and 9 MeV. For energies below 9 MeV, dE/dx is higher than 500 MeV/cm in the scintillators. For a typical Birks parameter of 0.02 cm/MeV the product $kB \cdot dE/dx$ is thus higher than 10.

This means that the Birks equation can be approximated roughly by

$$\frac{dL}{dx}(E) = \frac{L_0 \cdot \frac{dE}{dx}(E)}{1 + kB \cdot \frac{dE}{dx}(E)} \approx \frac{L_0}{kB}. \tag{4.4}$$

This approximation is not actually applied in the Monte Carlo analysis described in section 4.6 but it is useful for discussion purposes. It means that the total amount of light produced is approximately proportional to the total stopping range x_0 of the alpha particle which can be calculated from the specific energy loss with equation (3.9). It also means that, to first order, kB does not influence the shape of the light yield function, as it was the case for electrons, but only the normalization of the light production efficiency. This explains why both electron and alpha data is needed to extract the Birks parameter kB from alpha measurements. Additional information is required on the light yield scale for alphas. It is obtained by a combined analysis of the data from electrons and alphas. In section 4.6 the laboratory measurement data will be used together with Birks' equation to extract the Birks parameter kB. The tuning of the MC model is done with the same data.

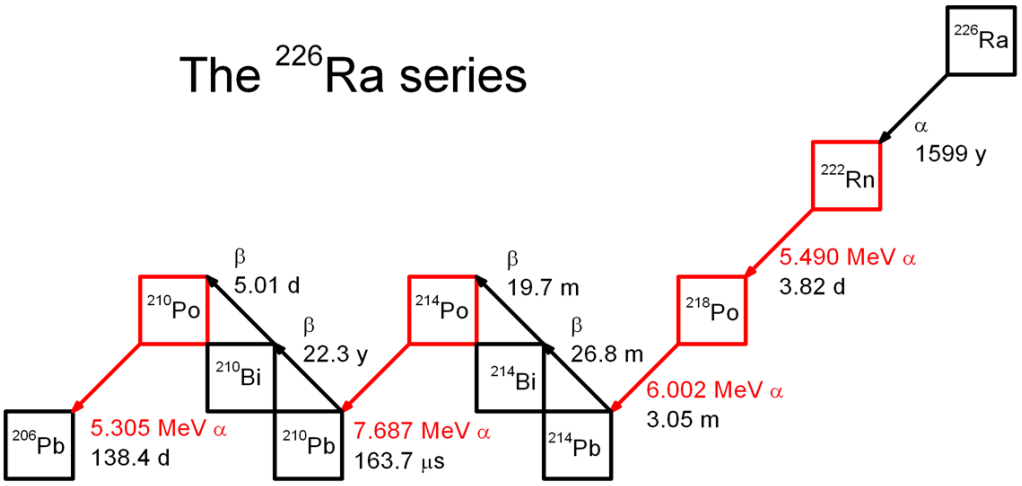

Figure 4.2: The main branch of the ^{226}Ra decay series. ^{226}Ra is produced in the ^{238}U decay series. Alpha particle emitting isotopes used in the measurements are shown in red. The half-lives are given in units of years (y), days (d), minutes (m) or microseconds (μs).

4.3 Alpha sources for the laboratory measurements

Two different alpha particle sources were used to conduct the alpha quenching measurements. In both cases different parts of the ^{226}Ra decay series shown in Figure 4.2

are used. The goal is to bring alpha emitting isotopes into the scintillator. In contrast to gamma rays alpha particles cannot be used to irradiate scintillator samples through the glass vial. Two methods are described which have been used to overcome this difficulty and bring the alpha emitting isotopes directly into the scintillator (sections 4.3.1 and 4.3.2). In total four different isotopes which emit alphas have been used in the measurements. They are listed together with the alpha energies in table 4.1.

Isotope	α energy
^{210}Po	5.305 MeV
^{222}Rn	5.490 MeV
^{218}Po	6.002 MeV
^{214}Po	7.687 MeV

Table 4.1: Alpha emitting isotopes and alpha energies used in the laboratory measurements.

4.3.1 The ^{210}Po source

Naturally occurring uranium salt with an activity of 1.3 MBq of ^{226}Ra decays was used as the primary source for ^{210}Po isotopes. The natural abundance fraction of the isotope ^{238}U is 99.3 %. The noble gas ^{222}Rn is produced in the main branch of the ^{238}U decay chain. A dedicated setup has been used to extract the radon from the Uranium salt and flush it through PPO powder. In Figure 4.3 this setup is shown. It consists of a bottle which contains the Uranium salt, a second glass bottle with PPO powder and a pump which circulates air through the two bottles. The ^{222}Rn atoms partially stick to the PPO crystals in the second bottle. Then ^{222}Rn and its daughters decay within the timescale of several days (see Figure 4.2) until ^{210}Pb is produced which has a half-life of 22.3 years. The pumping of air through the PPO powder has been done for 197 days in 2003 to grow in ^{210}Pb. After that the glass bottle with the PPO has been disconnected from the setup. When the study of alpha quenching was started in 2008 essentially all isotopes of the radium series prior to ^{210}Pb were gone and the ^{210}Bi and the desired ^{210}Po decays were in secular equilibrium with the ^{210}Pb decay. This follows from the much shorter half-lives of ^{210}Bi and ^{210}Po compared to the half-life of ^{210}Pb. This procedure allowed to have an alpha emitting isotope directly attached to PPO which is a component of the studied liquid scintillators. Thus the alpha-emitting ^{210}Po can be brought directly into the scintillator without introducing additional chemicals or changing the scintillator handling procedures.

4.3.2 The ^{222}Rn, ^{218}Po and ^{214}Po source

The second source for alphas is an acidic solution of HCl plus $BaCl_2$ in water. In this solution we have a ^{226}Ra activity of 25.6 Bq. The extraction of ^{222}Rn is shown

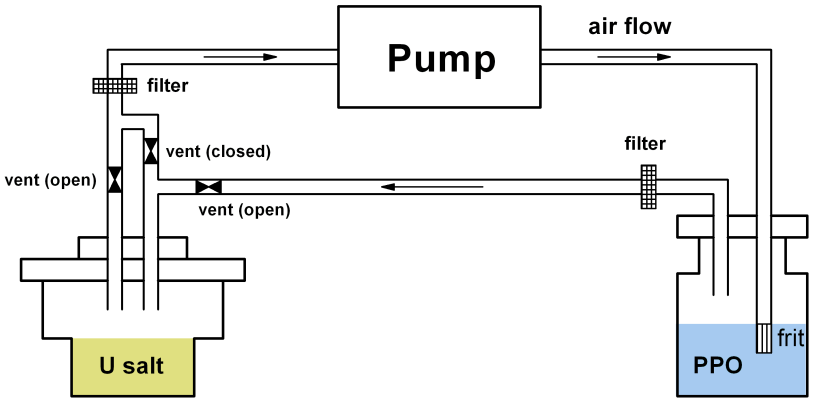

Figure 4.3: Setup to extract ^{222}Rn from Uranium salt and flush it through PPO powder. Two 0.2 μm (regenerated cellulose) filters were used to prevent particles from contaminating the setup.

schematically in Figure 4.4. After a time which is long compared to the half-life of ^{222}Rn (3.82 days) the activity of ^{222}Rn is approximately the same as for its parent ^{226}Ra. However, in order to perform a measurement of the light yield in a reasonable time scale (hours) an activity of several Bq is needed. This means that one does not need to wait until the ^{222}Rn activity in the source has fully recovered after the previous extraction. A few days after the measurement the ^{222}Rn activity in the source is already high enough again.
The solubility of ^{222}Rn atoms in gaseous nitrogen is higher than in the Ra solution and the solubility in the scintillator is even higher compared to nitrogen [109]. This helps to extract most of the ^{222}Rn atoms and transfer them efficiently to the scintillator sample with the help of a nitrogen gas bottle. The flux of the extraction has been controlled with a Tylan FC 280 mass flow controller at about 10 cm^3/min. Thus, the flux could be held stable and reproducible. Inside the scintillator we can now observe ^{222}Rn decays to ^{210}Pb via ^{218}Po and ^{214}Po emitting alpha particles with three distinct energies.
Both alpha sources have been carefully handled in a dedicated extractor hood in the MPIK radiochemical laboratory in order to guarantee safety and to avoid contamination of other equipment.

4.4 Experimental setup

The laboratory measurements have been performed at the MPIK Low Level Laboratory (LLL) to reduce the measurement background. It provides 15 m water equivalent of shielding which efficiently suppresses the hadronic component of the atmospheric radiation. Additionally, lead bricks have been used to shield the setup from gamma rays. A

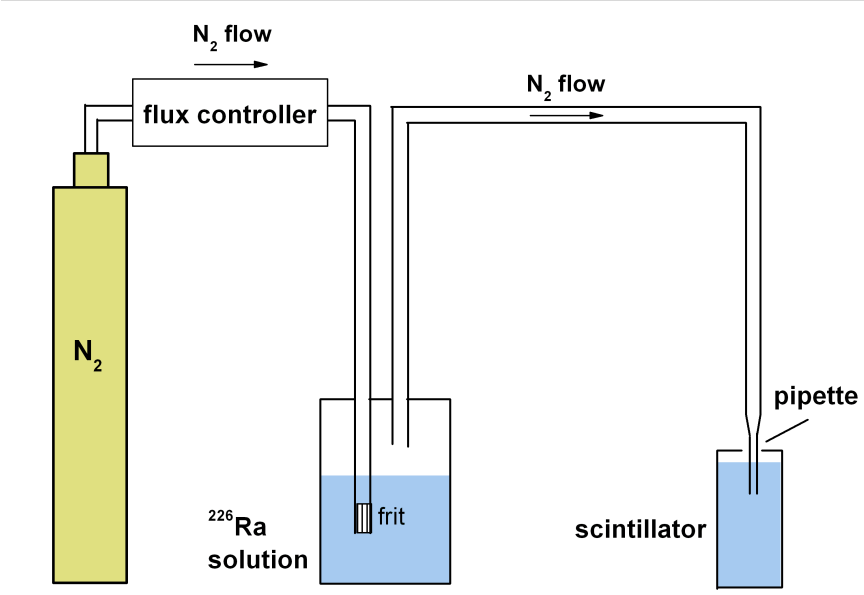

Figure 4.4: Setup to extract ^{222}Rn from a solution with ^{226}Ra and flush it directly through the scintillator sample.

comparison of light yield spectra with 40 g/l PPO and 7 g/l PPO in the Target scintillator show that the remaining background is dominated by the irreducible background from ^{210}Bi and ^{210}Pb.

The setup which was used for the measurement of the light output for electrons is the 'Compton Backscatter Peak' setup which was explained in section 2.2. For the case of excitation by alpha particles only the PMT 1 channel (see Figure 2.1) is analyzed without the coincidence configuration. An offline data analysis of the PMT pulses is done as it was explained before for the light yield measurements. The alpha emitting isotopes inside the scintillator can be assumed to be distributed homogeneously in the scintillator volume. Due to the very short travel distance (stopping range) of alpha particles in the liquid scintillators of the order of tens of micrometers it is likely that a given alpha particle deposits all its energy in the scintillator and does not hit the wall of the glass vial. We therefore see gaussian peaks in the scintillation light spectrum coming from the monoenergetic alpha lines as expected (see Figure 4.5). The spectra are fit with the sum of a constant term, an exponential term and one or three gaussian terms depending on the alpha source in use.

Compton backscatter peak electron energy distribution In order to calculate the quenching factors and tune the MC properly the scintillator samples have to be excited with alphas and electrons of known energies. For the alpha particles the energies are known from literature with precision. For electrons the Compton backscatter peak

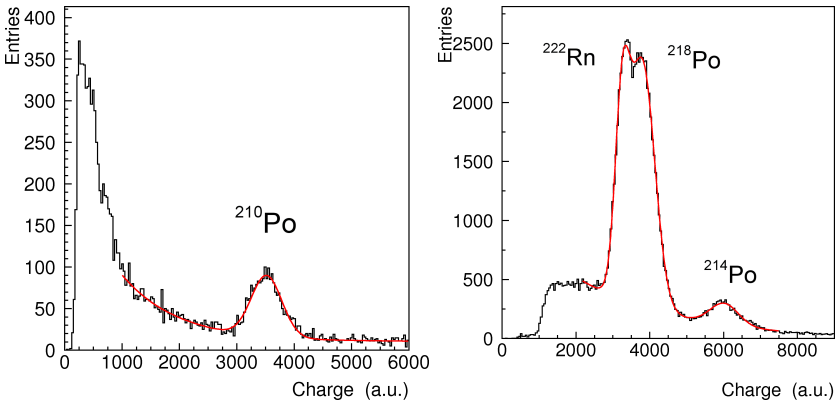

(a) (b)

Figure 4.5: The left plot shows a typical light yield spectrum for ^{210}Po (E_α=5.305 MeV) decay inside the scintillator. A typical spectrum for ^{222}Rn (E_α=5.490 MeV), ^{218}Po (E_α=6.002 MeV) and ^{214}Po (E_α=7.687 MeV) decay is shown in the right plot.

method is used. We know the initial gamma energy from literature but for the recoil electrons an energy distribution is obtained due to the variation in the Compton scattering angle. Choosing the backscatter configuration has the benefit that the electron recoil energies are less sensitive to the angle due to the flat cosine-dependency (see equation (2.1)). In this section, the small correction of the mean recoil energy is determined to first order. It comes from the deviation of the scattering angle from exactly 180 degrees. This correction depends on the geometry of the Compton backscatter peak setup and the materials involved.
A simple Monte Carlo (MC) model of the setup was written. The general idea of the MC model is to draw six random numbers which correspond to the coordinates of the two vertices of one coincidence event. These vertices are homogeneously distributed in the volume of the liquid scintillator vial and the sensitive NaI volume respectively. After this a part of the events are rejected in order to account for the fact that the vertices are not equally probable.
Three effects are taken into account in order to select the interaction points:

- The $1/r^2$ decrease in probability for both the initial photon and the scattered photon.
- The attenuation length of the backscattered photons in the NaI crystal.
- The angular dependence of the probability for Compton scattering (equation (4.5)).

The attenuation length for gammas in the relevant energy range in the liquid scintillator is more than one order of magnitude higher than the dimension of the vessel and thus can be neglected.

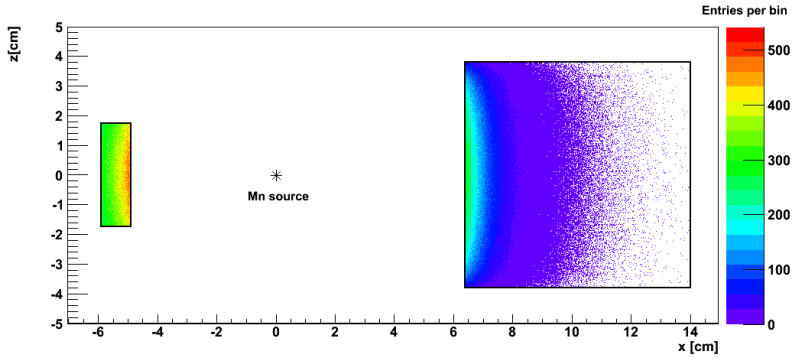

(a)

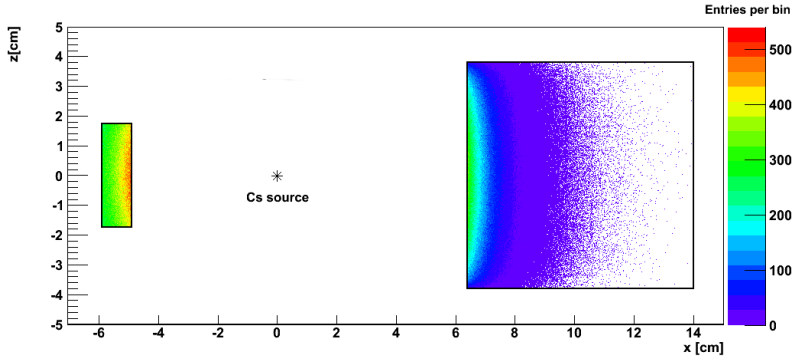

(b)

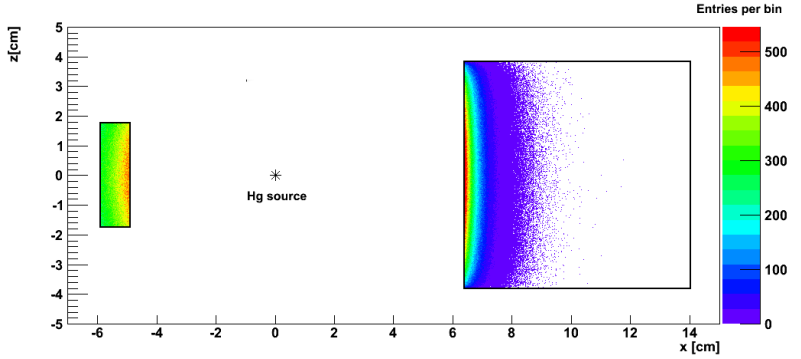

(c)

Figure 4.6: Side view of the vertex distributions for ^{54}Mn (a), ^{137}Cs (b) and ^{203}Hg (c).

The rejection of events is done with the acceptance-rejection method [110, 111]: given a probability density function (PDF) random numbers are generated which are distributed like this PDF by drawing an uniformly distributed random number x and rejecting it if $y > \mathrm{PDF}(x)$ where y is another uniformly distributed random number. The range from which the random number y is drawn has to be bigger than the maximum of PDF(x). Then the non-rejected x are distributed with PDF(x). This method is useful if the

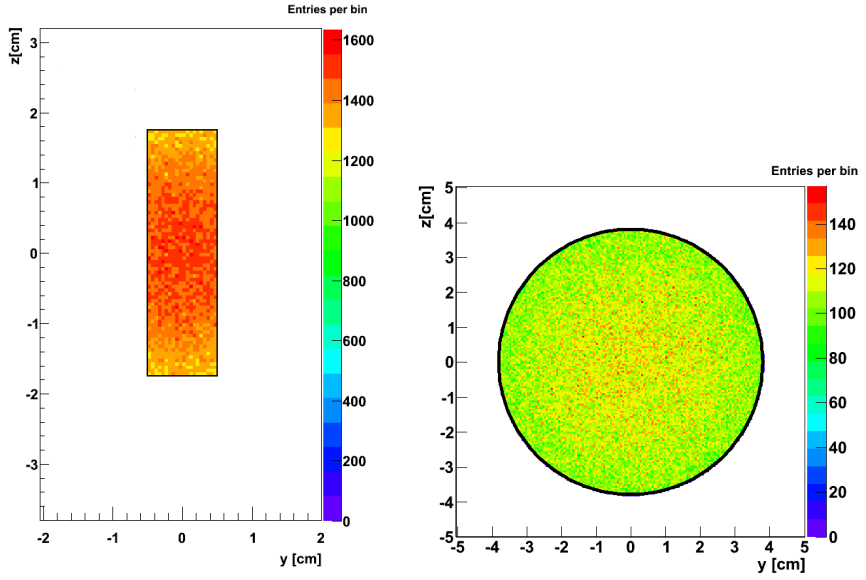

(a) (b)

Figure 4.7: Front view of the vertex distribution for the ^{137}Cs source. The liquid scintillator cell is shown in (a), the NaI crystal is shown in (b).

integration (or the subsequent inversion) of PDF(x) is not easy but the maximum of PDF in the relevant range can be estimated. The disadvantage is that it is more CPU intensive especially if PDF(x) spans over a big range, since two random numbers have to be drawn and the rejected x can not be used. In our case the drawbacks are not problematic.
For the partial rejection due to the solid angle effect we have a PDF which is proportional to $1/r^2$. To take into account the attenuation length in NaI a rejection is applied based on PDF which follows $e^{-r/\lambda}$. The attenuation lengths in NaI (density=3.67 g/cm^3) at the energies of the backscattered photons are listed in table 4.2 [112]. They have been cross-

γ source	Photon energy	Attenuation length λ
^{54}Mn	195.6 keV	0.80 cm
^{137}Cs	184.0 keV	0.70 cm
^{203}Hg	133.4 keV	0.34 cm

Table 4.2: Photon attenuation lengths in a NaI crystal.

checked with the XCOM photon cross sections database [113] and a good agreement has been found. Photoelectric absorption dominates for all three energies and scattering is neglected in the MC simulation. The angular distribution of the Compton scattering

follows the Klein-Nishina equation [114, 115]:

$$\frac{d\sigma}{d\Omega} = \frac{1}{2} r_e^2 \cdot \frac{1}{\left(1 + \frac{E_\gamma}{m_e c^2}(1 - \cos\phi)\right)^2} \cdot \left[\frac{\left(\frac{E_\gamma}{m_e c^2}\right)^2 (1 - \cos\phi)^2}{1 + \frac{E_\gamma}{m_e c^2}(1 - \cos\phi)} + 1 + \cos^2\phi \right]. \tag{4.5}$$

The classical electron radius is denoted by r_e, the rest energy of an electron is $m_e c^2$, ϕ is the scattering angle and E_γ is the gamma energy before scattering. Here the use of the acceptance-rejection method is beneficial since it is much easier to get an upper bound for this distribution than to integrate it and then invert the integral.
The coordinate system in our model is centered at the position of the gamma source. The distance from the source to the glass vial which contains the scintillator is 4.9 cm in the Compton backscatter peak geometry. The NaI crystal sensitive volume has a cylindrical shape and it is placed 6.4 cm away from the source. In Figure 4.6 and Figure 4.7 the distribution of the vertices after the rejection procedure is shown.
Finally, the energy of the scattered electron is calculated for each pair of vertices which passed the rejection steps. The distributions are shown in Figure 4.8. We observe that the deviation of the mean energy from the 180 degree backscattering value is below 1 %. As a result of the MC study in this paragraph the mean values of the electron energy distributions are given in table 4.3. These are the energies which have to be compared with the alpha energies in order to get the quenching factors.

γ source	electron energy
^{54}Mn	144.8 keV
^{137}Cs	475.7 keV
^{203}Hg	637.1 keV

Table 4.3: Mean simulated energies of backscattered electrons in the Compton backscatter peak geometry.

4.5 Quenching factor results from laboratory measurements

Two sets of measurements have been performed with the two different alpha sources for each scintillator. One set consists of five measurements: Three different gamma sources were used plus the measurement of the alpha source. The fifth measurement is a repetition of the ^{137}Cs or ^{54}Mn measurement. Usually, the first measurement was a measurement of the ^{137}Cs or ^{54}Mn source, then the alpha source was measured. After this, the same gamma source was measured again. Then the two other gamma sources were used. This procedure has the advantage that the stability of the mean LY can

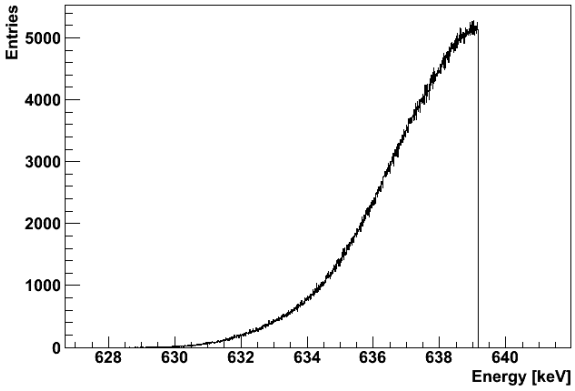

(a)

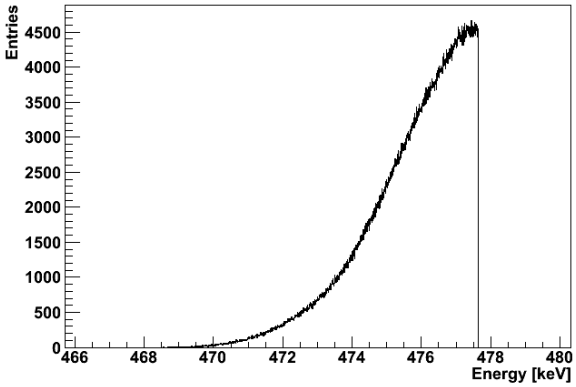

(b)

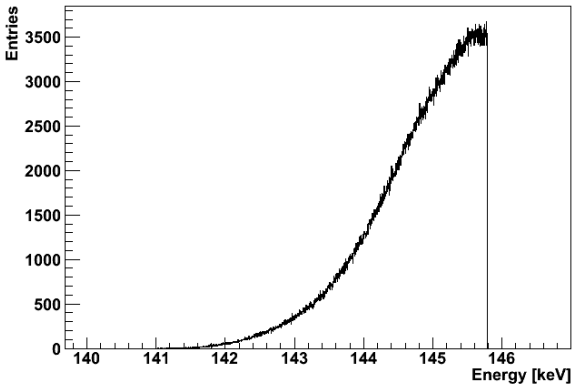

(c)

Figure 4.8: Energies of the scattered electrons in the Compton backscatter peak geometry for ^{54}Mn (a), ^{137}Cs (b) and ^{203}Hg (c).

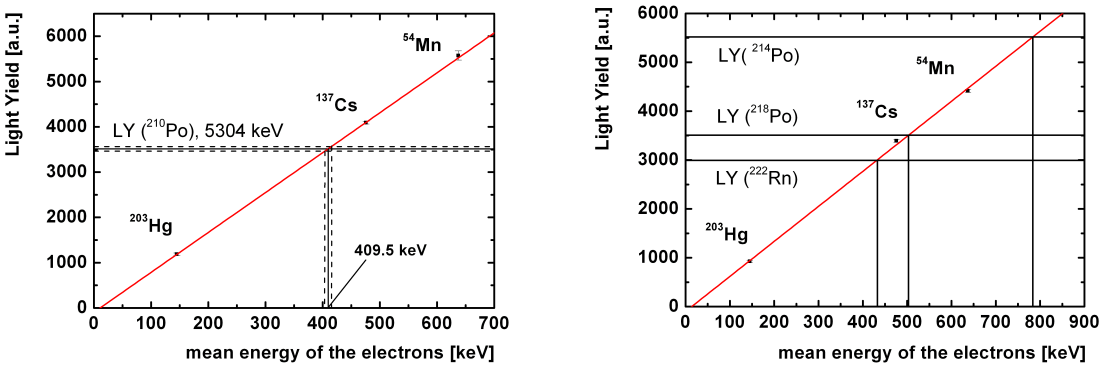

(a) (b)

Figure 4.9: Experimental results for the alpha quenching measurements in the Target. The left (right) plot shows the results for the measurement with ^{210}Po (^{222}Rn, ^{218}Po and ^{214}Po) as alpha emitter(s). The red line is a linear fit to the electron data, horizontal lines represent the light output after alpha excitation. The vertical lines indicate the corresponding electron energies. On the right plot the errors of the alpha light yields are omitted for clarity. They are of similar size than for the left plot. The errors of the determined quenching factors are given below.

be checked with the two measurements before and after the alpha measurement. Between each of the measurements the scintillator samples are flushed with nitrogen to remove oxygen which decreases the scintillation efficiency. More details on the sample preparation and liquid handling are given in section 2.2.

For the alpha measurements with source number two the nitrogen flushing happens directly through the bottle with the radium solution. It has been checked in a dedicated measurement that there is no significant light loss due to this procedure. In principle it is conceivable that during the flushing through the aqueous radium solution, water or even acid is transported into the scintillator sample. This could reduce the light yield. Therefore a check was done to exclude this with the GC with 2 g/l PPO since it has been seen with other impurity quenching tests that this scintillator is most affected by impurities (this is also expected from the light yield model studies because this scintillator has the least effective energy transfer from the solvents to PPO). First the scintillator was purged for about 10 minutes with nitrogen and then a measurement of the light yield with the ^{137}Cs source has been done. Then we flushed the scintillator with nitrogen but going through the radium solution and measured again the light yield with the ^{137}Cs source. After that step one was repeated. No significant light yield loss was seen when flushing through the radium solution. For the third measurement the light yield of the first measurement was recovered. Thus, no degradation was observed due to the flushing through the radium solution.

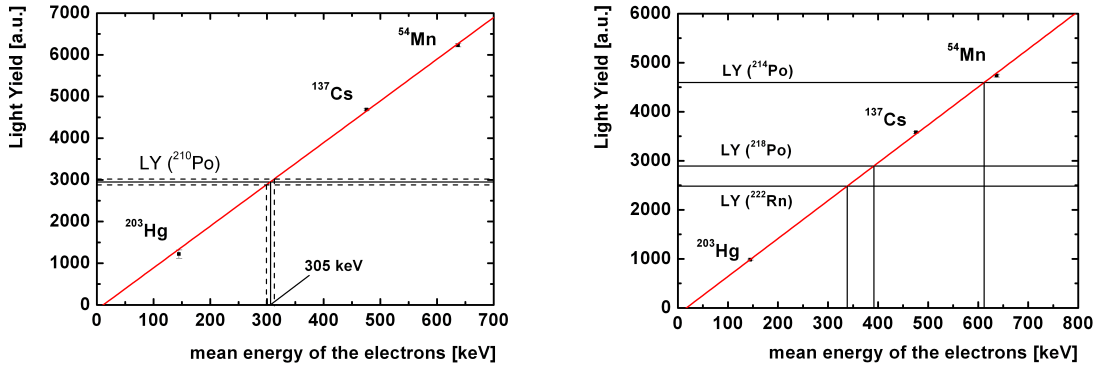

(a) (b)

Figure 4.10: Experimental results for the alpha quenching measurements in the GC.

We focus here on the Double Chooz scintillators. In Figure 4.9 the experimental results for the Target are presented. The light output for the gamma-induced electrons after Compton backscattering is given with the corresponding error bars. Then, a linear fit was done to calibrate the electron energy scale. The linear fit works well for the range of the three different electron energies (144.8 keV to 637.1 keV). The ionization quenching effect, which was discussed in the previous chapter, introduces a nonlinearity below about 100 keV. This can be seen in Figure 4.9 since the linear calibration line does not cross the point (0,0).

The light output values for alpha excitation are shown as horizontal lines in the plots. In the left plot of Figure 4.9 the error of the alpha excitation light output is shown as dashed horizontal lines. The quenching factor can now be calculated by using the electron energy scale calibration which is shown as a red line. For example, the quenching factor for ^{210}Po in the Target is $QF = \frac{5305\ keV}{409.5\ keV} = 13.0 \pm 0.3$. The error on the alpha excitation light yield is propagated using the electron energy scale function to get the error on the quenching factors. They turn out to be rather symmetric. The size of the errors can vary from measurement to measurement. Despite the careful removal of oxygen and the optimized sealing technique of the small cell, for some of the measurements slight drifts in the LY are observed (for time-scales of several hours up to few days). This is probably due to oxygen, which leaks into the cell. In these cases the drift of the light yield was corrected for which results in bigger error bars for these data points. The Target scintillator has been measured twice independently with ^{210}Po to check the stability of the result. The second measurement gave a consistent value of $QF = 13.2 \pm 0.3$.

Figures 4.10 and 4.11 show the measurements for the GC and Veto scintillators respectively. Other scintillator samples have been measured with the same procedure in order to get a better understanding of the ionization quenching behavior of the Double Chooz liquids. The results for the alpha quenching factors are listed in table 4.4. The GC* which was used for these measurements has a slightly different Ondina909 to do-

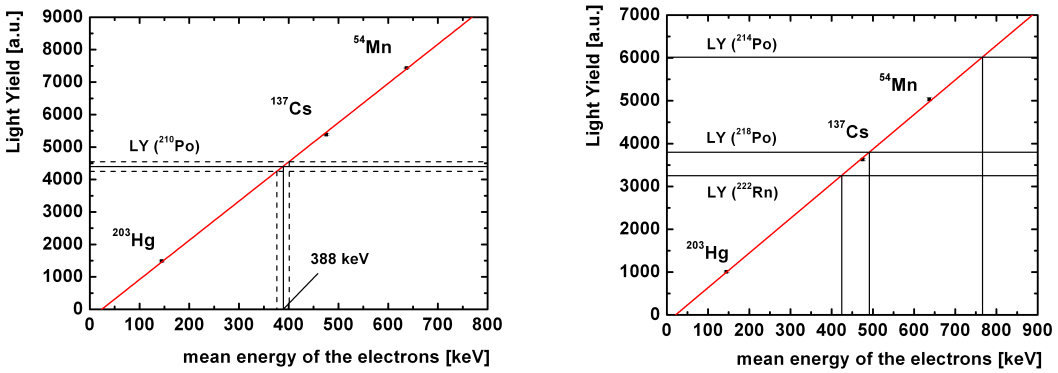

(a) (b)

Figure 4.11: Experimental results for the alpha quenching measurements in the Veto scintillator.

decane ratio than the final GC. This difference is expected to have a negligible effect on the results since Ondina909 has energy transfer properties which are similar to those of dodecane. The fine-tuning of the densities is the reason for the modification, as explained in section 2.6. The scintillator Veto* was the Veto candidate at the time these measurements were done. The aromatic fraction and the PPO concentration changed for the actual far detector liquid. Still, we can use it as a good reference and the measured QF should be close to the ones for the final Veto.

Discussion For all scintillators the quenching factor decreases with increasing energy. This is expected and understood since higher energy alpha particles have lower mean specific energy loss dE/dx and thus the ionization quenching effect is less pronounced. It also shows that the two different methods for alpha insertion into the scintillators give consistent results. Below, this can be seen in more detail when the MC software is tuned.

The differences between the different scintillators can be very well interpreted and understood with the help of the light yield model (section 2.3) and the scintillation timing measurements (chapter 5). Physically, the quenching process can be seen as an additional energy transfer path which is added to the diagram in Figure 2.5 for highly ionizing particles. For the scintillators which have a high combined transfer rate for all energy transfer processes except the ionization quenching process, the probability for ionization quenching to occur will be low. These are the scintillators which are emitting their light faster. The time constants for the various scintillators are presented in section 5.5.

The scintillator with the lowest quenching factor is the one with PXE plus PPO. It is also the scintillator with the lowest emission time constants of all the scintillators which were measured (see table 5.2). The physical reason is that the energy transfer between

Scintillator	QF (^{210}Po) 5.305 MeV	QF (^{222}Rn) 5.490 MeV	QF (^{218}Po) 6.002 MeV	QF (^{214}Po) 7.687 MeV
Target	13.1 ± 0.2	12.7 ± 0.3	11.9 ± 0.3	9.8 ± 0.4
GC* (2 g/l PPO)	17.4 ± 0.5	16.2 ± 0.4	15.3 ± 0.2	12.6 ± 0.6
GC* (5 g/l PPO)	15.4 ± 0.7	14.4 ± 0.4	13.7 ± 0.3	11.1 ± 0.3
Veto*	13.7 ± 0.5	13.0 ± 0.3	12.2 ± 0.3	10.0 ± 0.2
PXE + 7 g/l PPO	10.4 ± 0.3			
PXE + 7 g/l PPO + 20 mg/l bis-MSB	10.0 ± 0.4			
Dodecane + 7 g/l + 20 mg/l bis-MSB	16.9 ± 0.6			
Target without Gd and THF	14.4 ± 0.8			

Table 4.4: Alpha quenching factors for various scintillators at different alpha energies. GC*: 4 % PXE, 54 % Ondina909, 42 % dodecane, 20 mg/l bis-MSB. Veto*: 64 % tetradecane, 36 % LAB, 3 g/l PPO, 20 mg/l bis-MSB.

PXE and PPO is very effective and the corresponding time constant for the transfer is low. It was checked that the addition of bis-MSB does not change the quenching factor significantly for PXE plus PPO. At a concentration of 20 mg/l, the transfer to bis-MSB is mainly by emission and absorption of a photon [58] as opposed to the short-range non-radiative transfers between the other components. This means that the transfer to bis-MSB is an additional step which is not influenced by quenching since the photon leaves the region with high ionization density.

For dodecane plus 7 g/l PPO the quenching factor is higher and the emission times are longer due to the less efficient energy transfer from dodecane to PPO which was seen with the light yield measurements. The difference between Target with and without gadolinium can also be explained with the same type of argument. If gadolinium is present it opens an additional energy transfer path for the excited solvent molecules. This reduces the solvent deexcitation time and makes the scintillator faster (while the total light yield goes down). The scintillator with gadolinium is less affected by quenching because the additional ionization quenching energy transfer path has less weight compared to all other paths.

The same arguments apply for the comparison between Target and GC. The Target is faster because it has more of the efficient PXE to PPO transfer and it has gadolinium. The difference between the GC with 2 g/l PPO and 5 g/l PPO is also significant. In section 2.4 the critical concentrations for the transfer from dodecane to PPO, (1.38 ± 0.28) g/l, and for (molecules contained in) Ondina909 to PPO (1.54 ± 0.29) were determined. Dodecane and Ondina909 account for 96 % of the GC solvent and thus the

change from 5 g/l PPO to 2 g/l PPO makes the scintillator measurably slower (see also section 5.5).

The Veto scintillator components were not part of the light yield measurements and the light yield modeling. However, from the discussion above and the consistency we saw between the scintillator emission time data and the ionization quenching data we can conclude that the efficiency of energy transfer from the aromatic LAB to PPO is high because the Veto has low quenching constants and fast emission time constants.

4.6 Determination of the Birks parameter and Monte Carlo tuning

Monte Carlo simulation adjustment In order to simulate the light output of alpha particles with arbitrary energies correctly we use the experimental data for the Double Chooz liquid scintillators from the laboratory measurements to tune the Monte Carlo software. The quenching factors have already been extracted directly from the data (section 4.5). However, for simulating the ionization quenching for energies different from the experimentally probed energies a model of the ionization quenching is needed. In section 3.5 the details of the Double Chooz Monte Carlo Birks model have been described. Please refer to this section for the general discussion of the simulation details. Birks' model is used for all charged particles in the simulation including alpha particles. In this section the tuning of the Birks quenching parameter kB for alpha particles is described. In addition to the tuning of the MC a program was written which evaluates the Birks equation numerically as it was done before for the electrons. These results are compared with the Monte Carlo fit results in the next paragraph. The goal is to arrive at a consistent simulation and understanding for the ionization quenching process treatment for both alphas and electrons.

The data which is available for each of the Double Chooz scintillators consists of the light output (in units of the photomultiplier charge) for 3 different electron energies and 4 alpha energies. In section 4.2 it was explained that the Birks parameter for alphas can not be reliably extracted from the alpha measurements alone. The reason is that kB does hardly influence the shape of the light yield function $L_\alpha(E)$ for alphas as opposed to the light yield function for electrons $L_{e^-}(E)$. Instead a higher kB value reduces the overall light output efficiency rather independently of the alpha energy. We therefore need the data from the 3 different electron energies (where we already know the small effect of quenching from the previous chapter) to compare with the light yield scale of the alphas. If the electron and alpha data are fit together we thus arrive at a quenching parameter for alpha particles.

For about 50 different values of kB and for each of the three different electron energies, and for the four alpha energies used in the lab measurements, 1000 particles were simulated for each scintillator. These simulations were performed at the computing center in Lyon, where multiple computing jobs can be processed in parallel. As a reminder, at

each particle step the quenched (visible) energy is calculated with equation (3.7):

$$\Delta E_q = \frac{\Delta E_0}{1 + kB \cdot \frac{\Delta E_0}{\Delta x}}. \tag{4.6}$$

The total visible energy from the simulation is the sum from the individual steps. This quantity is proportional to the number of scintillation photons in the simulation. The mean values of the number of photons from the simulation were determined and then the best fit kB was obtained by comparing these mean values with the experimental data. In order to adjust the units of the experimental data to the units of the quenched energy in the simulation, a normalization factor c_0 has been used in the fit as a free parameter. A χ^2 minimization approach is used to fit the simulation light output to the experimental data:

$$\chi^2 = \sum_{n=1}^{3} \frac{\left(c_0 \cdot L_{data,e^-}(E_i) - \overline{L}_{MC,e^-,kB}(E_i)\right)^2}{c_0^2 \cdot \sigma^2_{data,e^-}(E_i) + \sigma^2_{MC,e^-,kB}(E_i)} + \sum_{n=1}^{1 \text{ or } 3} \frac{\left(c_0 \cdot L_{data,\alpha}(E_i) - \overline{L}_{MC,\alpha,kB}(E_i)\right)^2}{c_0^2 \cdot \sigma^2_{data,\alpha}(E_i) + \sigma^2_{MC,\alpha,kB}(E_i)}. \tag{4.7}$$

The first sum describes the electrons and the second sum is the contribution from either one or three alphas, depending on the alpha source which was used. The results for the two different alpha sources were analyzed independently since it is conceivable that different systematic errors are associated to the two methods. For the second method, which uses the radium solution, a dedicated test was done to check that the flushing through the solution has no effect on the light yield. It is found that the results of the two methods are consistent (see below).

The experimentally determined light output for electrons and alphas is denoted by $L_{data,e^-}(E_i)$ and $L_{data,\alpha}(E_i)$ respectively. The corresponding errors are $\sigma_{data,e^-}(E_i)$ and $\sigma_{data,\alpha}(E_i)$. The simulation (MC) is dependent on kB. The values for the light output (mean over 1000 simulated particles) is $\overline{L}_{MC,e^-,kB}(E_i)$ for electrons with the error on the mean $\sigma_{MC,e^-,kB}(E_i)$. The same notation with α instead of e^- has been used for the alpha simulation values.

In this analysis the same kB was used for electrons and for alphas. Cherenkov light was included in the simulation since it gives a small contribution to the light output for the electrons. The Cherenkov light threshold is calculated to be about 180 keV in the scintillators. Thus we have a small Cherenkov contribution ($\mathcal{O}(1\ \%)$) for the two gamma sources ^{137}Cs and ^{54}Mn which create electrons inside the scintillator with energies of 475.7 keV and 637.1 keV respectively.

The simulation studies discussed here have been done with small simulation step sizes. This means that the `Geant4` command `/process/eLoss/StepFunction 0.05 1e-5 mm` has been used. This command was described in section 3.5. For this setting the alpha particles lose their energy in about 100 steps. However, for alphas the total quenched energy does, in contrast to electrons, only depend very weakly on the number of steps which are taken. `Geant4` calculates the range of a given particle with the exact integral via equation (3.9). The range does therefore not depend on the step size. Since the condition $kB \cdot dE/dx \gg 1$ holds approximately for alphas with energies below 9 MeV

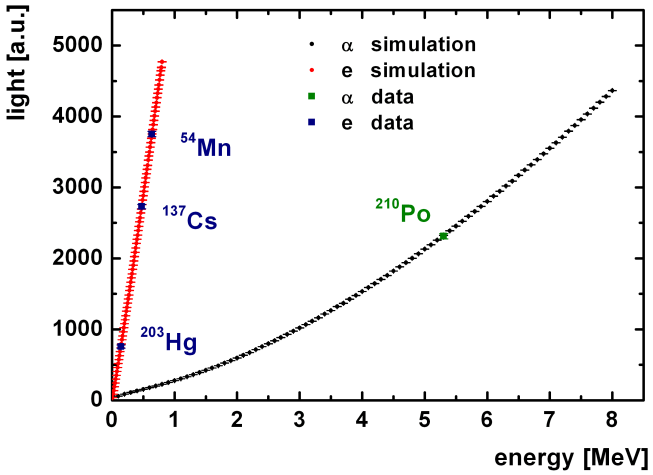

Figure 4.12: The combined electron and alpha Monte Carlo fit to the laboratory measurement data for the Target scintillator. Here a common energy axis has been used for both the alpha particles and the electrons. The best fit value for the Birks parameter is $kB = 0.0102 \pm 0.0002$ cm/MeV.

the visible energy is proportional to the range of the particle (see equation (4.4)) and thus is independent of the details of the step size: $\frac{dL}{dx} \approx \frac{L_0}{kB}$. This has been explicitly checked with `/process/eLoss/StepFunction 0.2 1 mm` which is the default setting. In this setting one step is performed for the alpha particles. Still, the visible energy does only differ marginally from the small step case. In the following the results are given for the small step case. For the other two stepping commands the default values have been used. The fluctuations on the energy loss which are calculated internally in `Geant4` influence the width of the visible energy spectrum. The mean value of the visible energy is however not changed. According to the approximation in equation (4.4) the mean visible energy depends only on the range. Thus, also the best fit kB is not influenced by fluctuations.

For the Target three independent measurements were done. Two times the first alpha source (^{210}Po) has been used. The experimental results for these two independent measurements were fully consistent within the errors. In the third measurement the second alpha source was used (^{222}Rn, ^{218}Po and ^{214}Po). The result from this measurement is consistent within the errors as well. The best fit to the experimental data is shown for the Target scintillator in Figure 4.12 for one of the two measurements with one alpha energy.

In Figure 4.13 the results for the Double Chooz Gamma Catcher are shown. As could be seen already in the evaluation of the quenching factors, the ionization quenching for alphas in the Gamma Catcher is stronger than in the Target. This is reflected in a

higher value for the Birks parameter kB. For the Veto* scintillator (composition can be

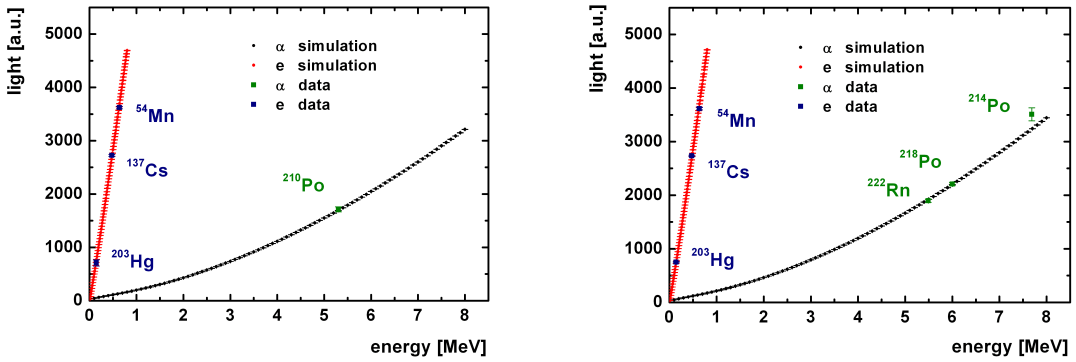

(a) (b)

Figure 4.13: The combined electron and alpha Monte Carlo fit to the laboratory measurement data for the GC* scintillator. The left Figure (a) shows the fit for the measurement with ^{210}Po, the right Figure (b) displays the results for the measurement with ^{222}Rn, ^{218}Po and ^{214}Po. The best fit value for the Birks parameter is $kB = 0.0139 \pm 0.0008$ cm/MeV for (a) and $kB = 0.0129 \pm 0.0007$ cm/MeV for (b).

found in table 4.4) the same analysis has been done. Again, similar values for the Birks parameter as for the Target are obtained. In table 4.5 the results for the three Double Chooz scintillators are summarized. Although the results between the two methods are

Scintillator	$kB_{1\alpha}$ [cm/MeV]	$kB_{3\alpha}$ [cm/MeV]	$kB_{comb.}$ [cm/MeV]
Target	0.0101 ± 0.0002	0.0096 ± 0.0005	0.0098 ± 0.0003
GC* (2 g/l PPO)	0.0139 ± 0.0009	0.0129 ± 0.0007	0.0134 ± 0.0005
Veto*	0.103 ± 0.006	0.093 ± 0.005	0.0098 ± 0.004

Table 4.5: Results for the best fit kB from Monte Carlo tuning for alpha particles. The results are given for the measurement with 1 α (^{210}Po), 3 α (^{222}Rn, ^{218}Po and ^{214}Po) and the combination of the two values.

consistent, there is a slight hint that the kB results from the measurements done with the first alpha source are systematically lower than the results for the second alpha source. The effect is for each of the three scintillators at the one sigma level. A possible explanation, apart from a mere fluctuation, would be a difference in the PPO which is used in the first method compared to the PPO in the second method. More interestingly, the effect could be due to a slight aberration of the true light yield function for alpha

particles from the shape predicted by Birks' equation. The results for the different scintillators are discussed in the next paragraph.

Consistency checks and discussion The results which were presented in the last paragraph have been checked again with a numerical integration of the Birks equation. The same procedure was also used to analyze the results for electrons in section 3.4. A program was written which implements the tabulated dE/dx values for alphas. They deviate from the Bethe equation for energies below 2 MeV (see section 4.2). Figure 4.1 shows the combination of the tabulated values for hydrogen and carbon in the correct abundance for the Target scintillator. At low energies, where the slope of dE/dx (E) is bigger, more values are tabulated. This allows to do a linear interpolation between the values. As for the electrons the Birks equation (3.3) is integrated numerically with small step sizes dx. It is an alternative way of getting the quenched energy, which was calculated with the full MC simulation in the previous paragraph. The same χ^2 fit analysis as for the MC simulation tuning can be done. In equation (4.7) we substitute the expressions for the MC quantities with the results for the quenched energy from the numerical integration. Again, kB is varied and the scale factor c_0 to get a fit of the experimental data.

It turns out that the results are fully consistent with the MC best fit kB values in table 4.5. There is a small difference due to the Cherenkov effect which was not included in the numerical calculation of the visible energy. With MC however we can turn the Cherenkov light contribution off and repeat the MC tuning procedure. It has thus been checked if the Cherenkov contribution is important for the extracted best fit value for kB_α. The inclusion of Cherenkov light slightly decreases the best value for kB since a small part of the difference in the efficiency of light production between electrons and alphas is then accounted for by the additional Cherenkov light for electrons. Another set of MC simulations was done and it was confirmed that the effect is small and kB is the same as without Cherenkov light within the errors. This was expected because the Cherenkov contribution is small at electron energies in the range of hundreds of keV. In the case with no Cherenkov light the conformance of the results with the numerical integration is even a little bit better, as expected.

For electrons, in general different results were obtained for the MC tuning and the numerical integration method. These differences were explained by the different step sizes, the secondary particle production and the fluctuations. For alphas we can explain why these differences do not affect the best fit kB values. Fluctuations are not important since the quenched energy approximately only depends on the total range for alphas below 10 MeV. It was explicitly checked that the fluctuations in dE/dx do not change the mean of the total stopping range. Thus it can be understood that they do not affect the best fit value for kB when the approximation in equation (4.4) is considered. The insensitivity of the best fit kB to the step size has already been discussed and explained.

Secondary particle production for alphas has been studied for alphas with 10 MeV. Only a negligible fraction of simulated alphas produced secondary particles in the simulation with the default threshold setting `/run/particle/setCut 0.01 mm`. If we change

the threshold to even higher values nothing will change. On the other hand if the threshold is lowered to 0.001 mm, secondary electrons are explicitly produced in `Geant4`. They will lead to different simulated total visible energies.

A detailed quenching model by Voltz et al. [102] uses the concept of an ionization column which is created by ionizing particles. There a distinction between excitation inside the ionization column and outside of it is made. The excitations outside the primary ionization column is created via secondary δ electrons which have a high enough energy to escape the ionization column. In the model by Birks, as it is implemented in the simulation, these effects are not included. Each secondary particle is treated as it was independent of the primary particle's ionization column. One has to be aware that the secondary production threshold can change the effective kB which is needed to describe the experimental alpha data and the threshold setting has to be handled carefully.

We can conclude that unlike for electrons, the Monte Carlo calculation of E_q for alpha particles is much less affected by changes in the tracking command settings for the step lengths and fluctuations. Thus the results obtained with the analysis above for the kB_α are valid rather independently of these MC settings. The secondary particle production is an exception since it can lead to more complicated effects but only for low thresholds. In our analyses we kept the threshold at the default value of 0.01 mm thus that for the relevant alpha energies no secondary electrons are explicitly produced and tracked in `Geant4`.

A check was made if the kB results for alpha particles differ if kB_{e^-} changes. The complete fit procedure was repeated for the Target with the default settings for `Geant4` and $kB_{e^-} = 0.0202$ cm/MeV was fixed for electrons. Only kB_α was used as a free parameter. The result for kB_α was still the same within the errors. This is expected from looking closer into the calculation of the visible energy. For single electrons, the ionization quenching effect at energies higher than 100 keV is relatively small. For the three electron energies used here the visible energies are only marginally sensitive (in the few percent range) to the value of kB_{e^-} and the stepping commands.

Finally we discuss why there are differences in the quenching parameters for electrons and alphas. The results of the numerical integration are compared. The kB_{e-} values were presented in table 3.1. The values for the numerical integration for alphas do not differ significantly from the MC fit values in table 4.5. For electrons the Birks parameters from the numerical calculation are significantly higher than for alphas. A possible explanation is that in the numerical analysis secondary particle production for electrons is not taken into account. In reality so-called δ (secondary) electrons occur. For electrons the energy which can maximally be transferred to another secondary electron is much higher than for alphas. This will result in another distribution of the energy deposition in space. The concept of an ionization column around the ionizing particle [102] has been shortly discussed above. In Birks' equation the details of the localization of ionized and excited molecules are not included. The only quantity which is used there is the specific energy loss of the primary particle. It can thus be understood that the Birks parameter for electrons and alpha particles are not the same. The difference can be interpreted as coming from differences in the actual ionization density profile around

the primary particle track.

However, Birks' equation is able to reproduce the data obtained from measurements for both electrons and alphas individually. It has to be seen as a semi-empirical equation which can be used with a tuned effective kB to reproduce the experimental results. It could be shown that it is better to not assume that for different particles or different analysis procedures the same kB value can be used.

4.7 Summary

The quenching factors for the Double Chooz scintillators allow to predict the electron-like energies at which alpha particles will appear in the Double Chooz energy spectrum. The contribution from alphas to the background depends on the quenching factors.

In order to measure the alpha quenching effect, multiple scintillator samples including the Double Chooz Target, GC and Veto have been excited with electrons and alpha particles. Two methods were presented to load the scintillator samples with the alpha emitting isotopes ^{210}Po (E_α = 5.305 MeV), ^{222}Rn (E_α = 5.490 MeV), ^{218}Po (E_α = 6.002 MeV) and ^{214}Po (E_α = 7.687 MeV). The light output after excitation with electrons has been measured with a Compton Backscatter Peak setup using a gamma source. Corrections on the energy distribution of the recoil electrons in the Compton Backscatter Peak geometry have been obtained by simulation.

The quenching factors were extracted from the laboratory measurements and presented in table 4.4. Several scintillator compositions have been analyzed and the differences in the quenching factors were discussed using the concepts of the light yield model. It was explained, why the data from light yield measurements, scintillator emission time measurements and ionization quenching measurements are strongly correlated.

Since the measured alpha quenching factors are ≥ 10 it can be concluded that alpha particles with energies smaller than about 7 MeV appear in the visible energy spectrum below the energy cut (0.7 MeV, to be fixed) for the prompt events. The remaining background for neutrino detection coming from alpha particles is thus expected to be small.

The Monte Carlo software has been tuned with the laboratory measurement results. The Birks equation which is used for electrons is applied for alphas as well to describe the ionization quenching effect. The results of the tuning of kB_α are, in contrast to electrons, rather insensitive to the details of the Monte Carlo settings. This can be explained by the high dE/dx values for alphas ($dE/dx \cdot kB \ll 1$). Results for the Birks parameters kB in the Double Chooz Monte Carlo simulation are listed in table 4.5.

The difference between the Birks parameters for alphas and electrons was explained: In Birks' model, only the specific energy loss of the primary particle is included. The differences in the localization of the excitation energy between alpha particles and electrons are neglected which occur in reality because of differences in the secondary particle production. The kB factors for alphas and electrons can in fact be similar if settings different from the defaults are chosen in the Monte Carlo simulation. For the correct description of the experimental data however, the Birks model is equally well suited

as more complicated models (e.g. [102]) which try to include these effects, as long as different kB are used for different particle types and simulation settings.

5 Scintillator emission time studies

5.1 Introduction and Motivation

In this chapter, measurements of the probability density function (PDF) for the scintillator photon emission time are presented. A well understood timing of the detector response depends on the scintillator PDFs. For example, the PDF is relevant for the adjustment of the readout time window of the experiment and the vertex reconstruction tuning. Additionally, the information about the photon emission times can be applied in Double Chooz using pulse shape discrimination (PSD) techniques. PSD uses differences in the emission time PDFs of different scintillators or different ionizing particles. This technique is widely used for particle identification. A difference between the scintillator emission time PDFs (also called time profiles) induced by electrons and alpha particles due to differences in the excitation processes is found experimentally.

Additionally, the time profiles for the ν-Target and Gamma Catcher scintillators differ significantly. In order to enhance the differences, the composition of the GC was tuned while the light yield matching requirement was met simultaneously (section 2.6). The difference can be used to distinguish the origin of events without using vertex reconstruction techniques or as additional information complementary to the vertex reconstruction. Especially for events which are close to the physical Target-GC boundary the resolution of the vertex reconstruction is not sufficient to distinguish between the two volumes. Here, the application of PSD can give additional information.

Different energy transfer paths in scintillators were identified and studied in chapter 2. The contribution of the individual paths was quantified with light yield measurements and their integration in the light yield model. Each path has its own effective time constant which can be a combination from multiple physical processes. For example a solvent molecule can be excited into a triplet or singlet state and the subsequent energy transfer to the solute follows different physical mechanisms and therefore has different time constants. In section 2.3 it was described how the transfer rates depend on the choice of solvents and solutes (fluors) and their concentrations. Furthermore, the scintillator light emission after alpha excitation is usually slower than for electrons because the triplet state formation probability is higher. In the last two chapters the specific energy loss of electrons and alphas were compared in detail. The higher dE/dx of alpha particles leads to higher probabilities for ionization compared to direct excitation of the molecules. After ionization and subsequent recombination the probability for a molecule to be in its triplet state is enhanced compared to direct excitation. In this chapter these arguments are explored experimentally.

For each of the individual physics processes it is assumed that the individual photon

emission time PDF is an exponential function. This leads us to the usual effective mathematical ansatz for the probability density function for photon emission

$$P(t) = \sum_{i=1}^{n} \frac{q_i}{\tau_i} e^{-t/\tau_i}. \tag{5.1}$$

The exponential time constant for the ith individual process is denoted by τ_i and its weight is given by q_i. The normalization of the probability density function (here: integration from 0 to ∞) leads to

$$\sum_{i=1}^{n} q_i = 1. \tag{5.2}$$

The time difference between excitation of the scintillator and emission of a single photon is denoted by t (the time of the excitation is chosen to be $t = 0$) and the probability that a photon is emitted between t and $t + dt$ is $P(t) \cdot dt$.

Measurements of the emission time PDFs for the Double Chooz scintillators have been performed in this work for both electrons and alpha particles. The experimental technique and the analysis of the laboratory data is described in section 5.2. The analysis of the raw data in order to obtain the emission time PDFs and the fit of the PDFs are discussed in sections 5.3 and 5.4 respectively. The results are presented and discussed in section 5.5.

5.2 Experimental setup

Measurement principle The principle idea behind the laboratory measurement setup is the start-stop technique which has been used successfully before [116, 117, 55]. The start time is a measurement of the excitation time ($t = 0$) and the stop time is a measurement of the emission time of a single photon. Time differences within the time interval $[t,t + dt]$ occur with the probability $P(t) \cdot dt$. Thus, after many repetitions of the start-stop measurement, the measured time differences $t_{stop} - t_{start}$ are distributed approximately like the probability density function $P(t)$.

The experimental setup for this measurement is shown in Figure 5.1. A scintillator cell with the dimensions 1 cm × 1 cm × 3.5 cm is used for the liquid scintillator samples. Two different techniques have been used to excite the scintillators with electrons and alpha particles respectively. They are described below. The scintillator cell is optically coupled to a window inserted in the black box. On the other side of the window a photomultiplier tube (Photonis XP2262) is attached and optically coupled with silicon grease. The start-photomultiplier tube (start-PMT) is supposed to collect many of the scintillation photons coming from the scintillator cell. Since the smallest time constant τ_1 is typically in the few nanosecond range and since it usually has the biggest weight q_1, many photons are produced shortly after the excitation. If many photons are collected by the PMT the arrival time of the first photon is close to the time of the scintillator excitation. Thus, the start time of the PMT pulse can be used as the start time. The second photomultiplier (Hamamatsu R1527P) is supposed to measure only one photon in

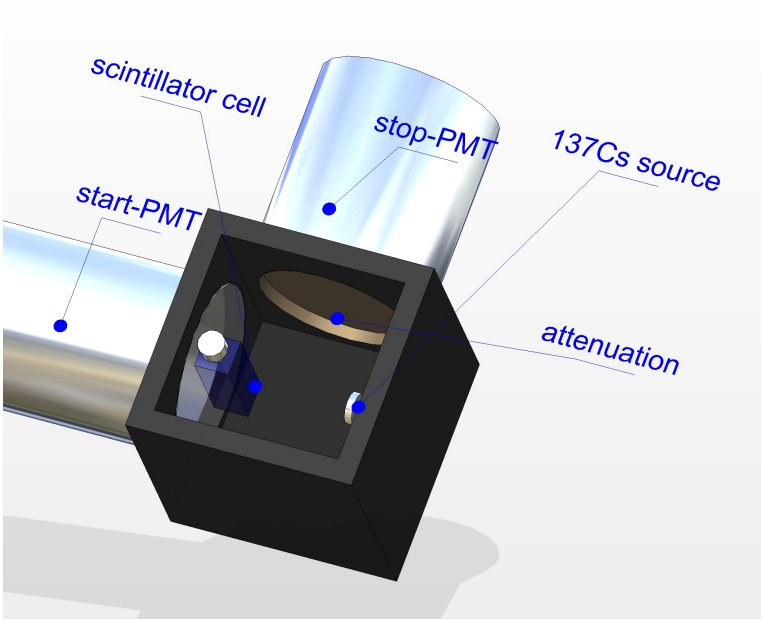

Figure 5.1: Setup for the measurement of scintillator emission time probability density functions. Gamma rays from the ^{137}Cs source Compton scatter inside the liquid scintillator. The scattered electrons excite the scintillator. Many photons per event are collected by the start-PMT. Ideally, only one photon is measured by the stop-PMT. The ^{137}Cs source is omitted for the measurements with alpha particles where the isotopes are directly loaded into the scintillator.

order to get a clean measurement of the stop time. In order to achieve this an attenuator is placed between the second photomultiplier and the scintillator cell. More details on the realization of the principle idea is given in the paragraph 'Statistics of the start and stop times' below.

Electronics In Figure 5.2 the electronics for the setup is shown. First, the signals from the PMTs are duplicated (branching of the signal lines after the PMTs) and one signal is directly routed to the oscilloscope. The start-PMT signal is discriminated with a LeCroy LRS623 octal discriminator module. If the signal is above the discrimination threshold, the generated logical pulse is used to define the relative timing between the two PMTs and the size of the coincidence window with a Phillips Scientific PS794 quad gate and delay generator. The logical output signal of the gate and delay generator is fed into a PS755 coincidence unit.

The duplicated stop-PMT signal is first amplified with a Tennelec TC205 linear amplifier in order to get signals with high enough amplitudes for the discriminator LRS623. The threshold of the discriminator has to be carefully tuned in order to avoid a contam-

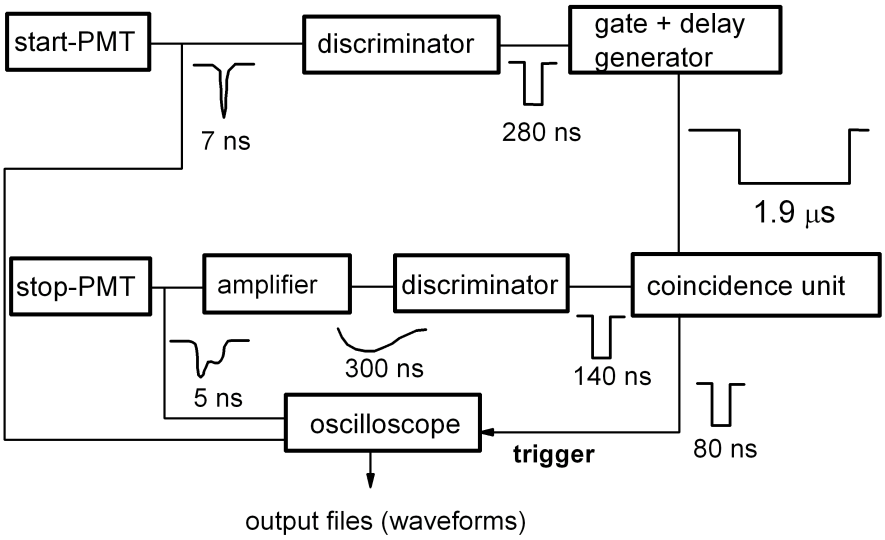

Figure 5.2: Scheme for the electronics of the time profile measurement setup. Typical times of the signals are shown together with a sketch of the pulses.

ination from baseline fluctuations but still get the single PE signals. The logical signal from the discriminator is routed to the coincidence unit which then triggers the oscilloscope if two coincident signals from both PMTs occur within the coincidence time window (1.9 μs). The oscilloscope records the complete waveforms on an external hard disk drive. One waveform comprises 10000 samples with a time resolution of 200 ps/sample corresponding to a length of 2 μs. Then an offline analysis of the single pulses is done (see below).

Radioactive sources For electron excitation ^{137}Cs sources are used with an activity of either about 200 kBq or 400 kBq. In order to excite the scintillators with alpha particles they are loaded with the alpha emitting isotopes ^{222}Rn, ^{218}Po and ^{214}Po. A similar technique was already described in section 4.3. Another radium solution is used here with higher activity than for the alpha quenching measurements. The high activity is needed for two reasons: First, the illumination of the stop-PMT has to be low to not bias the photon emission time PDFs (see details in the next section). This means that not every event in the liquid scintillator cell results in a coincidence. Second, the multiexponential time profiles decline rapidly. In order to measure the PDF at times of about 100 ns after excitation, up to 10^6 events have to be recorded.

A radium solution similar to the one described in section 4.3.2 but with a higher ^{226}Ra activity of 28.5 kBq is used. The ^{222}Rn extraction from this source has been done with a slightly improved setup shown in Figure 5.3. First, the setup is purged through a bypass (vent 3 open, vents 1 and 2 closed) to remove oxygen from the glass line. Then the flux is

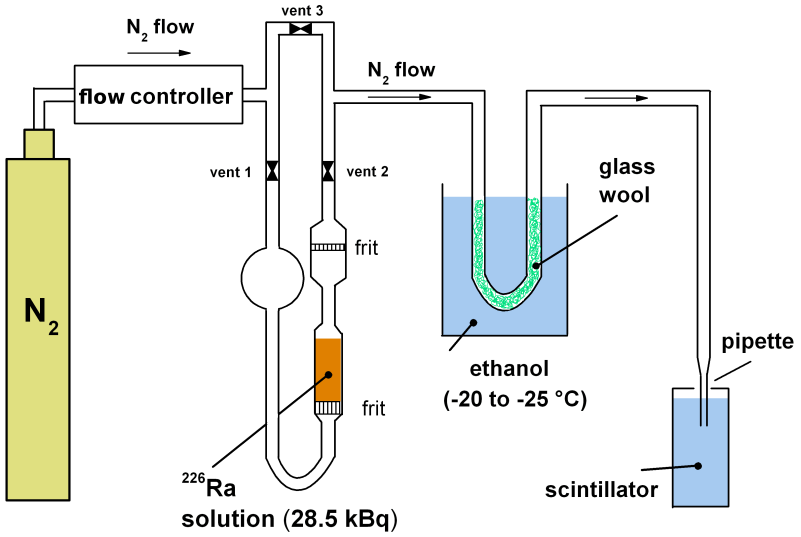

Figure 5.3: Setup for the extraction of ^{222}Rn isotopes from a ^{226}Ra-doped solution for the measurement of the photon emission time PDFs.

set with the flow controller to 6 cm^3/min, vent 3 is closed and vents 1 and 2 are opened to flush through the source. The transfer from the alpha source to the scintillator is quite efficient since the solubility of ^{222}Rn is higher in the scintillator than in nitrogen and it is higher in nitrogen than in the radium solution (H_2O+HCl+$BaCl_2$+$RaCl_2$) [109]. Behind the radium solution a cryo trap was installed. Glass wool in a tube was cooled with ethanol to a temperature of around -20 °C (adjusted with liquid nitrogen) to get rid of a possible residual contamination by water. If there is water, it adsorbs at the large surface of the wool while ^{222}Rn can pass the trap at these temperatures [118]. It turned out that the resulting activity in the liquid scintillator cell is reproducible with this procedure. The requested activity in the scintillator cell (of the order of kBq) is reached. It can be controlled by adjusting the flushing time through the radium solution.

Statistics of the start and stop times The most important requirement for an unbiased measurement is the detection of a single photon in the stop-PMT. If the illumination of the PMT is too high and two photoelectrons (PE) are created in the same event the time of the first one will be measured while the information on the second one is lost leading to a bias in the measured PDFs. The level of illumination is characterized by the mean number of detected photoelectrons per event m in the stop-PMT. From Poissonian statistics the probability of measuring at least one photoelectron is

$$p_1 = 1 - e^{-m}. \tag{5.3}$$

In [119] the joint probability for the detection of at least n photoelectrons and the detection of the ith PE in the interval $[t,t+dt]$ is calculated for the case of a poissonian distribution of the number of photoelectrons in one event. Here, we are only interested in

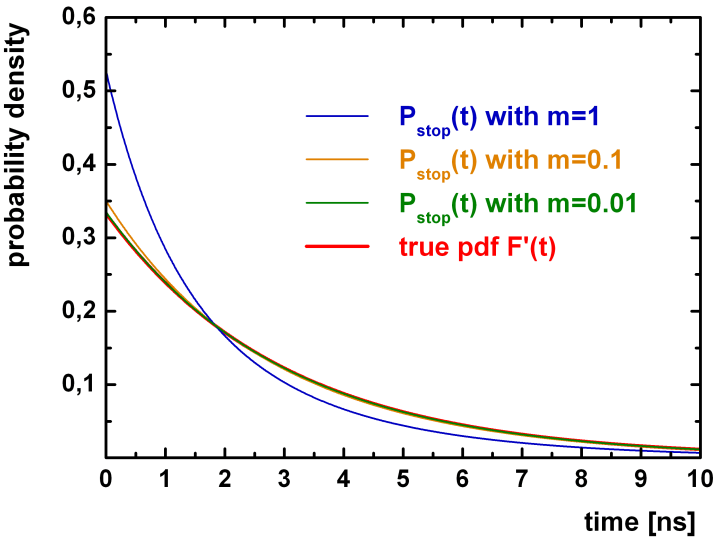

Figure 5.4: The red line shows an example for a probability density function for photoelectron detection: $F'(t) = 1/\tau \cdot e^{-t/\tau}$ with $\tau = 3$ ns. The blue, black and green lines show the distributions for the first photoelectron ($P_{stop}(t)$) for different numbers of photoelectrons per event m.

the first detected PE since with our setup only the time of the first PE will be evaluated. The joint probability for the detection of at least one PE ($n \geq 1$) and the detection of the first PE in the time interval $[t,t+dt]$ is

$$p_{joint,first}(t, n \geq 1)\ dt = me^{-mF(t)}F'(t)\ dt. \tag{5.4}$$

Here, $F'(t)$ is the probability density function for photoelectron detection. In an ideal case without detector resolution effects and backgrounds $F'(t)$ is equal to $P(t)$. The cumulative distribution function is denoted by $F(t)$ (integral of the probability density function F' from 0 to t). Since we only measure something if at least one photoelectron is detected we are interested in the conditional probability density function for the first PE with the precondition that at least one photoelectron is seen:

$$P_{stop}(t) = p_{cond,first}(t|n \geq 1) = \frac{p_{joint,first}(t, n \geq 1)}{p_1} = \frac{me^{-mF(t)}F'(t)}{1 - e^{-m}}. \tag{5.5}$$

In summary, this probability density function $P_{stop}(t)$ is obtained if the mean number of photoelectrons per event is m. For $m \to 0$ one gets (with the first order expansion of the exponential term in the denominator) $P_{stop}(t) = F'(t)$. In Figure 5.4 the deviation between $P_{stop}(t)$ and $F'(t)$ is shown for different m. For m=1 a clear deviation is obtained. If only in one out of one hundred events a photoelectron is detected (m=0.01)

the probability for a detection of two or more photoelectrons is reasonably low and thus the bias is small. Consequently, the probability density function for the first photon approaches $F'(t)$.

The relative error on the determination of the probability function at t is

$$\Delta p = \frac{P_{stop}(t) - F'(t)}{F'(t)} = \frac{me^{-mF(t)}}{1 - e^{-m}} - 1. \tag{5.6}$$

For $t \to 0$ and $t \to \infty$ the absolute value of the relative error is extremal and we get:

$$\frac{me^{-m}}{1 - e^{-m}} - 1 \leq \Delta P_{stop} \leq \frac{m}{1 - e^{-m}} - 1. \tag{5.7}$$

The relative error is thus below 0.5 % for $m = 0.01$. The optical attenuation between the scintillator cell and the stop-PMT was adjusted such that $m \approx 0.01$. In this sub-poissonian regime no correction has to be applied to the measured $P_{stop}(t)$. In order to check the value for m experimentally the rates for the events above threshold for the two PMTs have been measured individually (without coincidence condition). The rate for the start-PMT is of the order of 1000 s^{-1} and the rate for the stop-PMT is of the order of 10 s^{-1}.

For the start signal the opposite case of high illumination is needed in order to minimize the bias. Neglecting threshold effects and the details of the evaluation of the pulse onset determination, we measure again the time of the first photoelectron. This means that equation (5.5) can be used as the probability density function for the arrival of the first PE. The scintillators have a light yield of about 6000 photons/MeV (see section 2.7). For typical energies of a scattered electron of few hundreds of keV we get typically 1000 photons per event of which (in a conservative estimate) about one third reach the photocathode. Of these typically more than 20 % are measured as photoelectrons. We thus conservatively estimate the number of PE per event in the start-PMT to be 50. For a typical case of a time constant of $\tau = 3$ ns the photon which leads to the first detected photoelectron originates within the first 0.2 ns after excitation. More interesting than this number is the spread of the measured start times since the absolute time difference of the signal processing chain between the start and stop-PMT is not known and can be treated as a fit parameter. The spread will be even lower than 0.2 ns and thus negligible compared to the instrumental transit time spread of the PMTs.

Background, instrumental effects and resolution An important background for this measurement in the single photon regime comes from random coincidences of a dark rate event in the stop-PMT with a scintillation pulse in the start-PMT. The dark rate pulses are not distinguishable from events which are induced by scintillation photons. In the previous section it was explained that illumination regime is required in order to not bias the probability density function. Thus the effect of the dark pulses on the measurement can not be reduced by increasing the light level. Therefore, a specialized Hamamatsu R1527P PMT is used with a very low dark rate of about 4 s^{-1} at a high voltage of

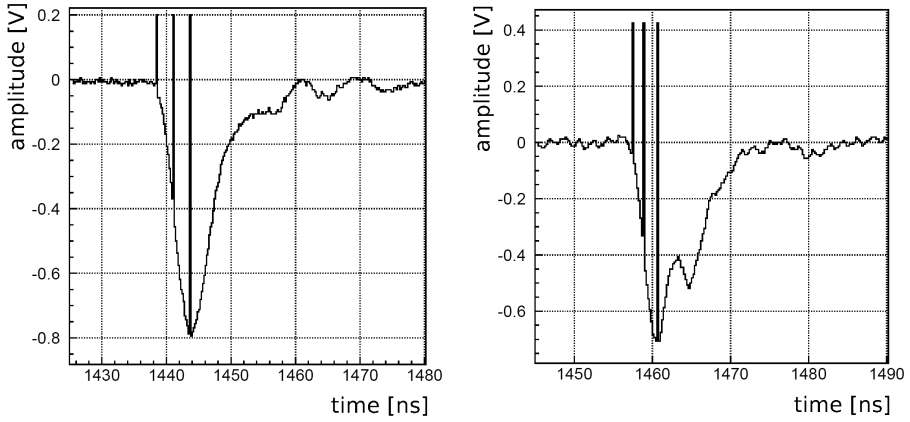

(a) (b)

Figure 5.5: (a): Typical start-PMT pulse. The three lines indicate the time of the pulse onset, the time when half of the maximum pulse height is reached and the time channel with the maximal amplitude (from left to right). (b): Typical stop-PMT pulse. The same lines from the offline analysis (see text) are shown here. The second, smaller peak is a characteristic feature of the stop-PMT.

-1000 V in order to simultaneously have a high signal-to-noise ratio and subpoissonian statistics:

$$R_{dark} \cdot t_{coinc.} \ll m \ll 1. \tag{5.8}$$

The dark rate of the stop-PMT R_{dark} multiplied with the coincidence window time $t_{coinc.} = 1.9$ μs gives the probability for dark rate induced background of approximately $7.6 \cdot 10^{-6}$ per event. This background can in principle influence the tail of the distribution. In general the background distribution is not uniformly distributed in the coincidence window [116]. However, the variation of the background rate is small for $m \approx 0.01$ and the small rate of random coincidences. The background is later included in the fit function for the emission time PDF as a constant.

For the start-PMT a dark rate of about 700 s^{-1} was measured at +1600 V. These dark counts do not contribute to the background of the experiment since a sufficiently high threshold can be used to remove them without cutting on the scintillation induced events.

Additional instrumental background can come from PMT late pulses where a PE is first reflected at the first dynode before it is attracted again by the dynode and then releases secondary electrons. The additional time which is needed for the reflection and re-accelerating process delays the signal and thus leads to a biased $t_{stop} - t_{start}$. The stop PMT has a special 'side-window' geometry to minimize the late pulse probability.

Afterpulses occur in the PMT if the residual gas in the vacuum tube is ionized and the ion is accelerated to the first dynode where it releases electrons which are then amplified. Thus, a second pulse is created with a time delay which depends on the PMT

geometry and high voltage settings. In the stop-PMT the time delays can be as low as few hundreds of ns and therefore the afterpulses can be seen in the coincidence time window as a second signal. Usually this does not contribute to background since the time of the first signal is determined and used as t_{stop}. In some cases however, the first signal can be below threshold and the second one above threshold which then would contribute to the background. For the start-PMT the late pulses and afterpulses are not dangerous since they come after the usually high prompt signal from several tens of photoelectrons which have the correct timing.

The time resolution of a $t_{stop} - t_{start}$ measurement is determined by several factors:

- Due to slightly different photoelectron paths in the PMT dependent on where the photocathode is hit and dependent on the electrical field configuration between the dynodes, PMT pulses show a so-called transit time spread.
- The offline analysis of the pulse onset times can depend on the amplitude of the pulses and the corresponding rise time. In order to minimize these effects the constant fraction timing technique is applied (see section 5.3).
- The resolution of the waveforms is chosen low enough to ensure that the rise time of the pulses can be resolved accurately (200 ps/sample).
- Differences in $t_{stop} - t_{start}$ due to different photon travel distances for different locations of the excitation inside the scintillator cell are negligible due to the small cell dimensions (cm scale).

It turns out that the time resolution can be described approximately with a gaussian function. An even better fit to the experimental data can be obtained with an asymmetric gaussian function (different values for σ on the left and right side of the maximum, see section 5.4). This time resolution function is convoluted with the expression for the scintillator emission time PDF $P(t)$ from equation (5.1). Typical values for σ are 1 ns.

5.3 Extraction of the time profiles

A program which is similar to the program used for the light yield analysis was written to analyze the waveforms offline individually. Thus, we adjust the parameters of the analysis iteratively and optimize the data evaluation with the same set of data and check the results of cuts. Here, the steps are described briefly which are needed to extract the pulse times t_{start} and t_{stop}.

Typical pulses from both the start-PMT and the stop-PMT are shown in Figure 5.5. The first step is a computation of the baseline at the beginning of each waveform. Then, the onset of the pulses are searched for by looking for several (typically around 8) consecutive channels below an adjustable threshold. The number of subsequent channels below the threshold and the value of the threshold are tuned together in order to find the pulse onset reliably and accurately. The best values depend on the level of the baseline fluctuations. After the pulse onset determination the baseline is evaluated directly in

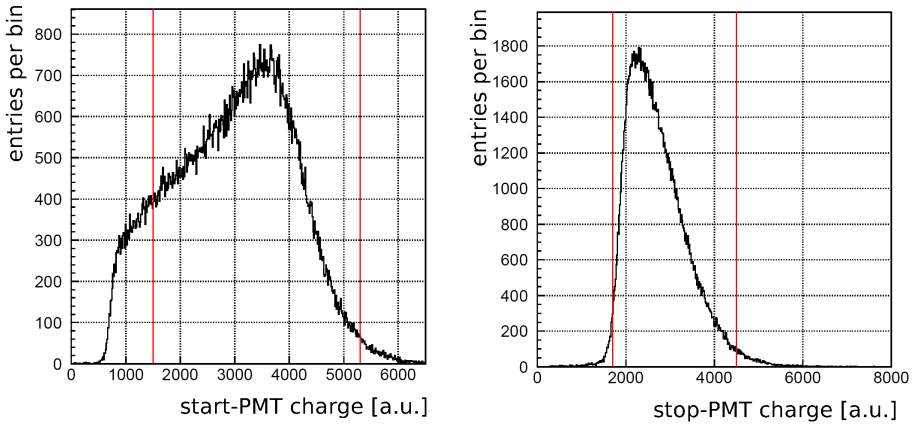

(a) (b)

Figure 5.6: Quality cuts on the charge for start- (a) and stop-PMT (b) are shown as red lines. Only pulses with a charge within these two values are accepted for the final time PDF. In (a) a typical spectrum for electron excitation (Compton scattering of γ) is shown.

front of the pulse in order to minimize the effect of possible slow baseline movements. Then, the pulses are integrated with a fixed time window to get the charge.

The integrated charge is used to define quality cuts which are shown in Figure 5.6. The shapes of the charge spectra for both PMTs can be explained qualitatively: We expect a Compton spectrum for the energies which are deposited in the scintillator cell. However, the spectrum is deformed since only events where a coincidence between both PMTs occurred are selected. For events with a high energy deposition the probability for a single photon measurement in the stop-PMT is higher and thus these events lead to coincidences more often. The Compton spectrum is therefore deformed. The spectrum for alpha particle excitation is shown in section 5.5.

In the stop-PMT charge spectrum we see the single PE peak which is cut by the threshold of the discriminator on the left side. The quality cuts on the charge remove events where the charge in either PMT has an unexpected high or low value. Especially the removal of low charge events has a positive effect on the time resolution of the measurement since for higher charges the determination of the pulse times are more accurate. Additionally to the charge quality cuts defective events are rejected in the offline analysis, for example pulses which exceed the range of the oscilloscope readout.

A precise determination of the time when the pulses occurred is done using the constant fraction timing method. The determined time of the pulse onset can depend slightly on the amplitude of the pulse (leading edge discrimination). A big pulse reaches the threshold level (which is set to determine the onset) faster than a small pulse. In the constant fraction timing method the information on the pulse height is used additionally: The pulse maximum is determined and then the time when the pulse reaches half

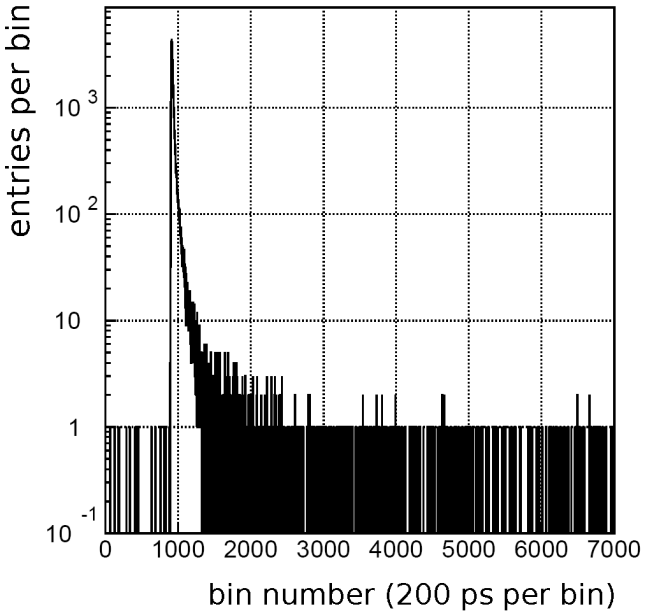

Figure 5.7: Typical measured spectrum of the scintillator photon emission time PDF. Here, the result is shown for a range of 1.4 μs. The background of the measurement can be estimated to the left of the distribution. It is at the level of about 10^{-6} of the value in the peak. For the late part of the time profile (bin number $>$ 5000) the background level is comparable with the level to the left of the distribution again.

of the maximum is taken. The rise of the pulse is usually steepest around the half of the maximum and thus the accuracy is high. For pulses of different amplitudes which occur at the same time, the bias on this time is smaller than on the pulse onset time. This could be verified when the combined time resolution of the measurement was extracted from the fit with and without constant fraction timing.

The determined times for the start-PMT and stop-PMT pulses are used as t_{start} and t_{stop}. The differences $t_{stop} - t_{start}$ represent the measurement of the photon emission time PDF which is shown in Figure 5.7.

5.4 Evaluation of the experimental emission time probability density functions

The fit function for the experimental photon emission time PDFs is a convolution of the probability density function for photon emission $P(t)$ (plus background) with a time resolution function $R(t)$. In the fit the constant instrumental time offset t_0 between the two PMTs is used as a free parameter. The fact that there is no light emission before

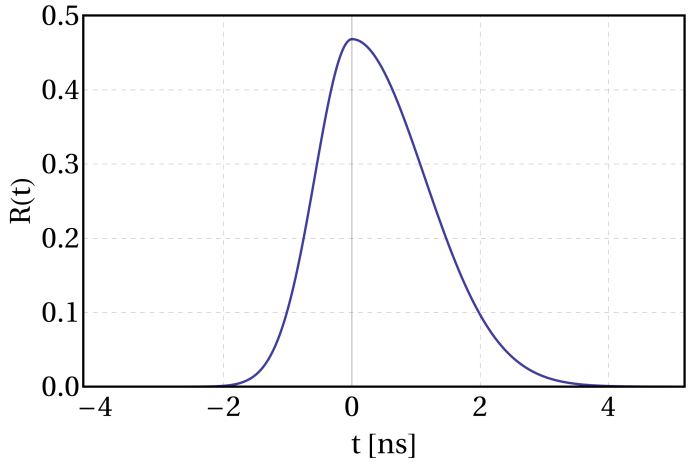

Figure 5.8: Normalized asymmetric gaussian resolution function $R(t)$ with $\sigma_1 = 0.58$ ns and $\sigma_2 = 1.1$ ns (fit values for Target with α excitation).

excitation is expressed mathematically by the Heaviside step function $\Theta(x)$ ($\Theta(x) = 0$ for $x < 0$ and $\Theta(x) = 1$ for $x \geq 0$). We thus have for the ideal case of no detector resolution effects

$$P(t) = \sum_{i=1}^{n} \frac{q_i}{\tau_i} e^{-(t-t_0)/\tau_i} \cdot \Theta(t - t_0). \tag{5.9}$$

The number of exponential terms n is not fixed a priori. If a good fit is obtained with a certain n there is no reason to go to a higher n with this effective description of the emission time PDF. It was therefore checked for which minimal n a good fit is obtained. The resolution function $R(t)$ is described as a normalized asymmetric gaussian function shown in Figure 5.8:

$$R(t) = \frac{2}{\sqrt{2\pi}(\sigma_1 + \sigma_2)} \cdot \left[e^{-\frac{1}{2}(\frac{t}{\sigma_1})^2} \cdot \Theta(-t) + e^{-\frac{1}{2}(\frac{t}{\sigma_2})^2} \cdot \Theta(t) \right] \tag{5.10}$$

It turns out that the convolution can be expressed in a closed form and the fit function is

$$\begin{aligned} f(t) &= [c_0 \cdot P(t) + b] \otimes R(t) \\ &= \sum_{i=1}^{n} \frac{c_0}{\sigma_1 + \sigma_2} \left[\frac{q_i}{\tau_i} \cdot \sigma_1 \cdot e^{\frac{\sigma_1^2}{2\tau_i^2} + \frac{t_0}{\tau_i} - \frac{t}{\tau_i}} \cdot \left(\mathrm{Erf}\left[\frac{\sigma_1}{\sqrt{2} \cdot \tau_i} \right] - \mathrm{Erf}\left[\frac{\sigma_1^2 + \tau_i(t_0 - t)}{\sqrt{2} \cdot \sigma_1 \cdot \tau_i} \right] \right) \cdot \Theta(t - t_0) \right. \\ &\quad \left. + \frac{q_i}{\tau_i} \cdot \sigma_2 \cdot e^{\frac{\sigma_2^2}{2\tau_i^2} + \frac{t_0}{\tau_i} - \frac{t}{\tau_i}} \cdot \left(\mathrm{Erfc}\left[\frac{\sigma_2^2 + \tau_i(t_0 - t)}{\sqrt{2} \cdot \sigma_2 \cdot \tau_i} \right] \cdot \Theta(t_0 - t) + \mathrm{Erfc}\left[\frac{\sigma_2}{\sqrt{2} \cdot \tau_i} \right] \cdot \Theta(t - t_0) \right) \right] \\ &\quad + b. \end{aligned} \tag{5.11}$$

The background b is assumed to be constant. It is estimated from the number of events which occur left of the peak of the time profiles (for example below channel 800 in Figure

parameter	explanation
c_0	normalization of the signal
b	constant background, fixed before the fit
t_0	constant instrumental time offset between the two PMTs
τ_i	time constant of the ith exponential term
q_i	weight of the ith exponential term
σ_1	time resolution 1 (left)
σ_2	time resolution 2 (right)

Table 5.1: Fit parameters for the photon emission time fit function $f(t)$.

5.7) and is then fixed in the fit. The parameter c_0 is the normalization depending on the number of measured events,

$$\text{Erf}\,[x] = \frac{2}{\sqrt{\pi}} \int_0^x e^{-v^2} dv \tag{5.12}$$

is the error function and $\text{Erfc}\,[x] = 1 - \text{Erf}\,[x]$ is the inverted error function. The parameters of the fit function are summarized in table 5.1.

A χ^2 minimization is performed by `MINUIT` [120]. `MINUIT` is called within a `Fortran` program (original version written by Dr. Florian Kaether), which implements the fit function. The χ^2 function is defined as

$$\chi^2(\{p_j\}) = \sum_{i=i_1}^{i_2} \frac{\left[N(t_i) - f(t_i, \{p_j\})\right]^2}{N(t_i)} \tag{5.13}$$

with the parameters $\{p_j\}$ from table 5.1 and the number of entries in time bin i $N(t_i)$. The error of each bin is assumed to be the square root of the entries in this bin.

5.5 Results and discussion

Excitation with electrons The experimental photon emission time PDF for the Target scintillator and the GC scintillator (measured with e^-) are shown in Figure 5.9 together with the fit function $f(t)$ which was described in the previous section. One can see the different exponential contributions to the time profile in the data. The quality of the fit (for example the χ^2/dof is 367/341 for the Target scintillator with electron excitation) does not improve if more than three exponential terms are used. The complete spectrum can be described since the asymmetric resolution function is well suited to describe the data also in the peak region. A symmetric resolution ($\sigma_1 = \sigma_2$) has been used as well. The peak region can not be fit as well as with the asymmetric function in this case, but it was found that the weights and the time constants of the exponential terms are

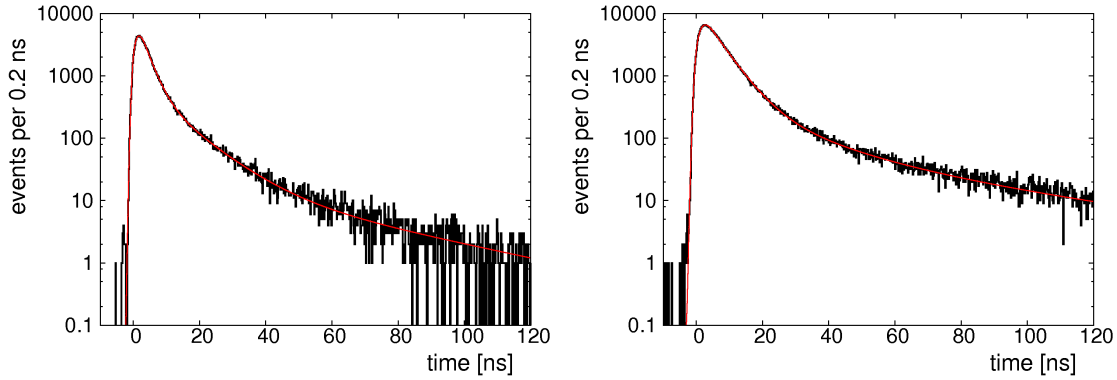

(a) (b)

Figure 5.9: Experimental photon emission time PDFs for electrons in the Target (a) and GC (b) scintillators.

close to the ones with the asymmetric resolution function. In fact, results for q_i and τ_i which have been obtained with a symmetric gaussian resolution function can be directly compared with results using the new method.

Several scintillators apart from the Target and GC have been measured in order to increase the understanding of the scintillator physics and thus optimize the composition of the Double Chooz scintillators. The fit results for various compositions are summarized in table 5.2.

Generally, one has to be careful when comparing the fit parameters of different scintillators directly. The weights and the time constants are correlated. For example a slightly lower weight and shorter time constant in the first component can be balanced by a higher weight in the second component. Additionally, the number of exponential terms in the chosen effective mathematical description is not specified. Here it was chosen to use three components since the data can be described well. If the data is fit with four exponentials different numbers for the first three components will be obtained. The results also depend on the range which is fit. The range can vary for the different scintillators due to differences in the PDFs and differences in the number of recorded events. The comparison of single fit parameters should therefore not be overstressed. The main results are discussed graphically in order to see the complete fit functions. With these limitations in mind we can nevertheless look at the main tendencies with the help of the fit parameters.

Different solvents have been tested with a PPO concentration of 6 g/l to check the efficiency of transfer between the solvent and PPO. In these three samples no bis-MSB is contained. A comparison of the emission time PDFs is shown in Figure 5.10. It can be seen that for PXE the weight of the fastest component (q_1) is higher than for dodecane and LAB. This reflects that the efficiency for the main energy transfer path is high (excitation of PXE into a singlet state, transfer to PPO and emission of a photon). The weight of the second component is highest for dodecane. In general the less efficient

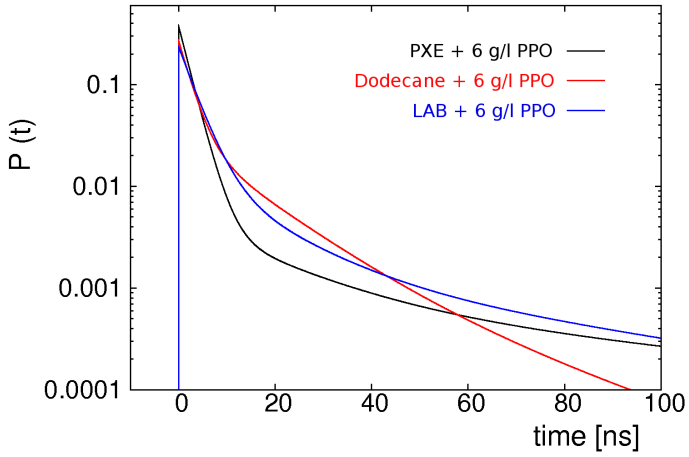

Figure 5.10: Comparison of the photon emission time PDF of three different solvents containing 6 g/l PPO each.

transfer from dodecane to PPO is thus reflected in a higher mean photon emission time. The LAB plus PPO scintillator is in between dodecane and PXE. This shows that the combination of PXE and PPO is a good choice for a fast and efficient scintillator. This observation corresponds to the fact that PXE plus PPO has also the highest light yield of these three scintillators.

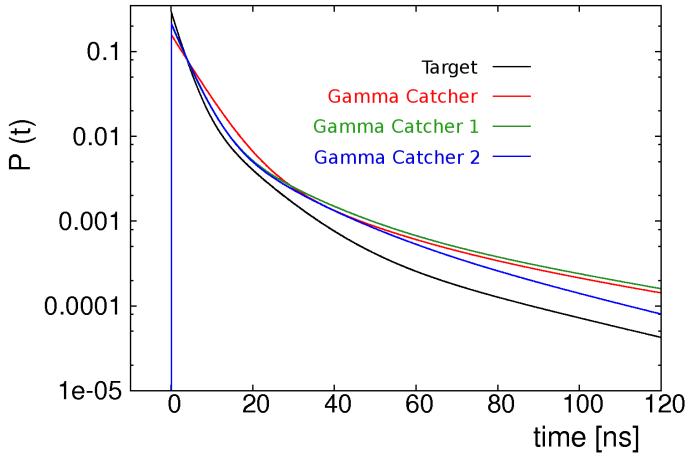

Figure 5.11: Comparison of the photon emission time PDF of three Gamma Catcher candidates before large scale production and the Target.

In section 2.6 the light yield and density matching of the Gamma Catcher and Target scintillators were described. Before the large scale production of the Double Chooz far detector liquids several options for the Gamma Catcher scintillator were discussed. The

results for three Gamma Catcher candidates have been presented in [55] in more detail. Here the main results are discussed. The photon emission time PDFs are shown in Figure 5.11 together with the Target for discussion purposes. It has been checked with an additional measurement that the dodecane/Ondina909 ratio in the Gamma Catcher, which changed during the light yield and density matching process has negligible effect on the time profile. This is expected since dodecane and the molecules in Ondina909 are chemically similar. We thus can focus on the differences in the aromatic fraction (PXE) and the PPO concentration. Gamma Catcher 1 has a higher PPO concentration of 5 g/l. The first component is significantly faster than for the Double Chooz far detector Gamma Catcher and its weight is higher. This can be explained with the light yield results and the model as well. With 2 g/l PPO we are close to the critical concentration in dodecane and Ondina909. This reduces the light yield since it decreases the efficiency of energy transfer which also leads to higher photon emission times. Gamma Catcher 2 has 5 g/l PPO and 3 % PXE. Its PDF is very similar to the PDF of Gamma Catcher 1, only the third exponential component has slightly less weight at 3 % PXE. A possible explanation is that the transfer from dodecane to PXE ('cross term') in Figure 2.5 accounts for this part of the PDF. At 3 % PXE this term is less important than at 4 % PXE. As a result of the PDF measurements, we decided to use the slower GC with 2 g/l PPO (with 4 % PXE) instead of the 5 g/l PPO versions in order to maximize the difference between Target and Gamma Catcher. This difference can be used to distinguish between pulses from the two volumina with pulse shape discrimination techniques.

Multiple checks for systematic effects and reproducibility have been carried out in order to probe the robustness of the results:

- The light yield stability during the measurements has been checked.
- Additionally, the time profile fit has been carried out for a split sample. The first half of the data has been selected to have lower energy depositions in the start-PMT, the second half contains the higher energy events. In other words, the sample which passes the quality cut in Figure 5.6 (a) is split in two subsamples: one with higher charge and one with lower charge. No systematic difference between the two subsamples has been found in the time profile. This confirms the considerations about the statistics of the start-PMT first photon arrival time in section 5.2. There it has been estimated that the bias on the start time is low if enough PE are observed.
- The measurements have been carried out with and without a half-open teflon cell carrier which reflects more of the light to the start-PMT. This improves the energy resolution. As expected from the second systematic test, also here no difference was observed.
- Measurements of the same scintillator have been carried out twice to check the reproducibility of the results. The deviations have been found to be negligible.

Scintillator	q_1	q_2	q_3	$\tau_1[ns]$	$\tau_2[ns]$	$\tau_3[ns]$
Target	0.710	0.253	0.037	2.63	9.69	38.4
GC (4 % PXE, 2 g/l PPO)	0.813	0.123	0.064	5.36	17.0	56.7
GC 1 (4 % PXE, 5 g/l PPO)	0.73	0.19	0.08	3.7	14.0	53
GC 2 (3 % PXE, 5 g/l PPO)	0.75	0.18	0.07	3.7	13.4	38
Nucifer EJ-335	0.887	0.086	0.027	4.9	20.6	95.0
PXE + 6 g/l PPO	0.86	0.07	0.07	2.3	17	90
Dodecane + 6 g/l PPO	0.59	0.34	0.07	2.4	12	28
LAB + 6 g/l PPO	0.71	0.18	0.10	3.2	13	60
Target (α excitation)	0.654	0.210	0.136	2.87	13.9	70.8
GC (α excitation)	0.706	0.218	0.076	5.00	16.9	74.6

Table 5.2: Fit parameters from the measured time profiles for various scintillators. The commercially available scintillator EJ-335 (Eljen Technology, with 0.5 % gadolinium) is used for the Nucifer experiment [121].

Excitation with alpha particles For the evaluation of the time profiles measured with alpha excitation one additional analysis step is required. Since we have ^{222}Rn inside the scintillator we get decays from the isotopes ^{222}Rn, ^{218}Po, ^{214}Pb, ^{214}Bi and ^{214}Po until ^{210}Pb is generated which has a half-life of 22.3 years (see Figure 4.2). This means that, apart from the three alpha emitting isotopes, decays from two β^- emitters occur inside the scintillator which create a background for the time profile measurement with alpha particles. Unfortunately, due to quenching, the visible energies of the alphas with 5 to 8 MeV and the betas (plus accompanying gammas) which have typically several hundreds of keV up to few MeV overlap. Thus, the beta like events (electrons and gammas which in turn can produce electrons) are a background for the time profile measurements with alpha excitation. In order to correct for this background, the contribution from electron events in the measurement sample is estimated. As explained in section 5.3, the PMT charge of the pulses is determined.

The charge of the start-PMT corresponds to the deposited energy in the scintillator. In Figure 5.12 (a) a typical charge spectrum is shown. The energy resolution is worse than for the light yield measurements done in section 4.4 for the alpha quenching because there it was possible to use a fully closed reflecting teflon cell holder which increases the amount of light collected in the PMT. For the time profile measurements it is not possible to use the same reflector since it would block the optical path to the stop-PMT. The fully closed teflon block shows the clearest peak structure in the spectrum (see Figure 5.12 (b)). The red lines in the left plot (a) of Figure 5.12 represent typical quality cuts which are applied for the time profile measurements. The relative positions of the cut values to the double peak (^{222}Rn and ^{218}Po) are used to translate the quality cuts to the high energy resolution plot (b). The combined signal and background fit of the spectrum in (b) yields the fraction of background (β-like) events which pass the quality cuts.

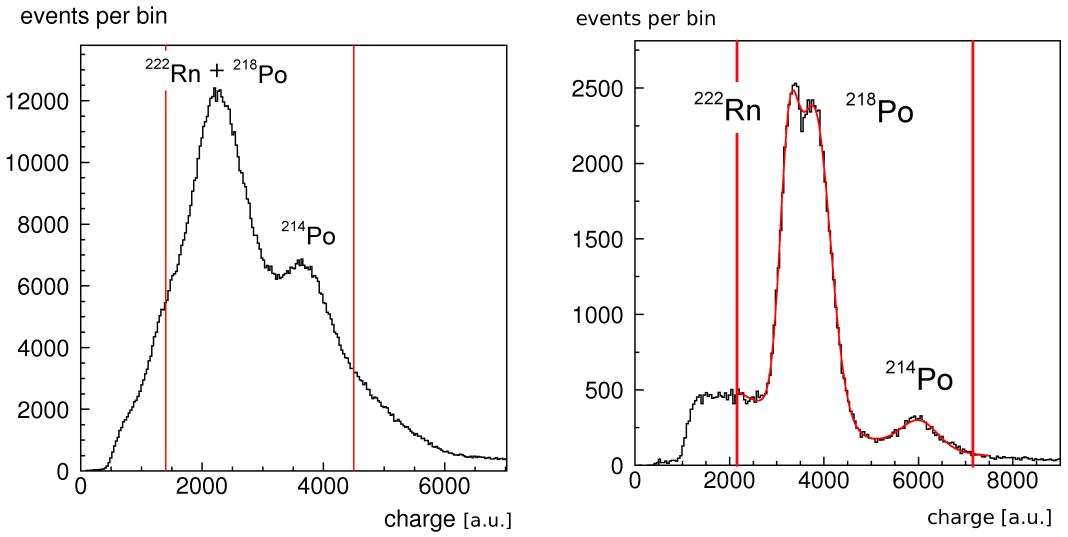

(a) (b)

Figure 5.12: (a): Typical charge spectrum for the time profile measurement with alpha particle excitation. The two lines indicate a typical choice of the quality cuts. (b): Charge spectrum for the light yield measurements with the teflon cell holder block (higher energy resolution).

For the alpha measurements a beta contribution of 25 % to 35 % is obtained with this procedure. The error on this number comes from different effects:

- The spectrum evolves with time. The ^{222}Rn daughters have to be produced first before they contribute to the spectrum. The effect is visible for the first few hours of the measurement according to the half-lifes of the isotopes in the decay chain. A time profile measurement lasts few days. For the light yield measurement only hours are needed. This leads to a smaller peak at 7.687 MeV in Figure 5.12 (b) compared to (a).
- In the left histogram of Figure 5.12 only events with a coincidence between start- and stop-PMT are included. Thus, events with higher charge are selected more often than events with lower charge since the probability that a single photon is measured at the stop-PMT increases with the number of photons produced in the scintillator.

The effects listed above contribute to the error on the fraction of beta like events in the selected sample. We hence use the best estimate of 30 %. An additional test has been done to see the influence of the beta contamination: The quality cuts on the start-PMT charge distribution (Figure 5.6 (a)) have been relaxed. Thus, a larger fraction of beta events is in the sample. Indeed, it was found that the time constants are slightly lowered.

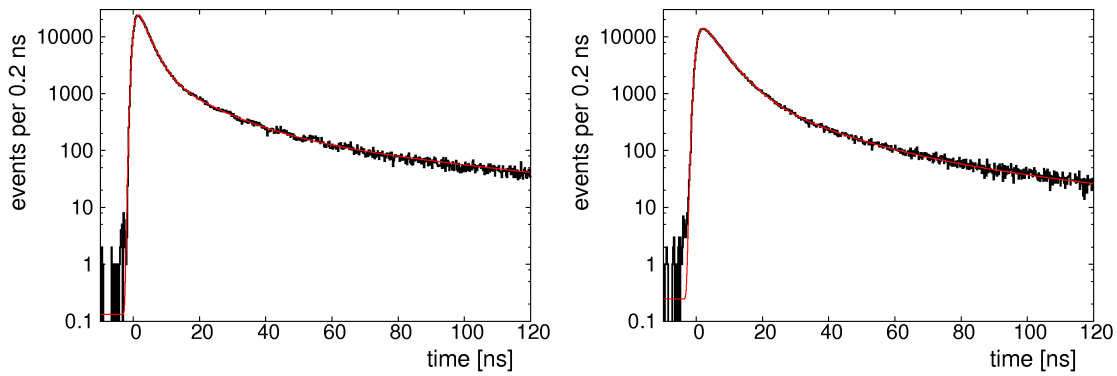

(a) (b)

Figure 5.13: Experimental photon emission time PDFs for alphas in the Target (a) and GC (b) scintillators. The red line shows the fit with three exponential terms from alpha excitation plus the fixed contribution from beta excitation.

In order to include the beta contamination in the fits of the alpha particle measurements first the total number of events is determined. 30 % of this number are estimated to be beta events. The time profile for beta events has been measured and fit (see Figure 5.9) and can be used to correct for the contamination. Instead of subtracting events from data, a different approach is chosen: The beta contribution is added to the fit function as three additional exponential terms with fixed parameters which have been obtained by the fit to the electron data. The weight of this contribution is fixed to be 30 %.

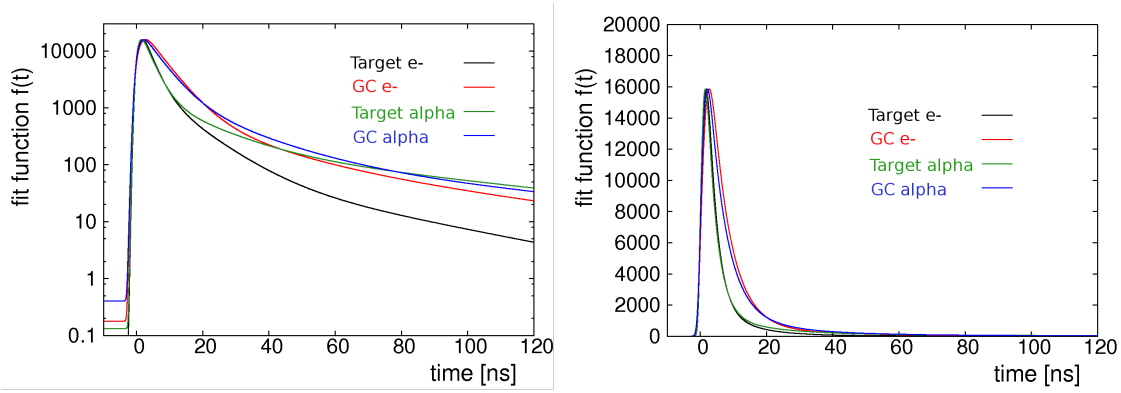

(a) (b)

Figure 5.14: Comparison of the fit functions for alpha and beta excitation in Target and GC with logarithmic scale (a) and linear scale (b). The fit functions have been normalized at the peak for better comparability.

Results for the measurement of the time profile with alpha excitation are shown in Figure 5.13 for the Target and GC. Together with the results obtained with the ^{137}Cs

source we can now compare the photon emission time PDFs for electrons and alphas in Target and GC (Figure 5.14). Figure 5.15 shows the extracted PDFs normalized to one. From these figures we can see that the difference between Target and GC is

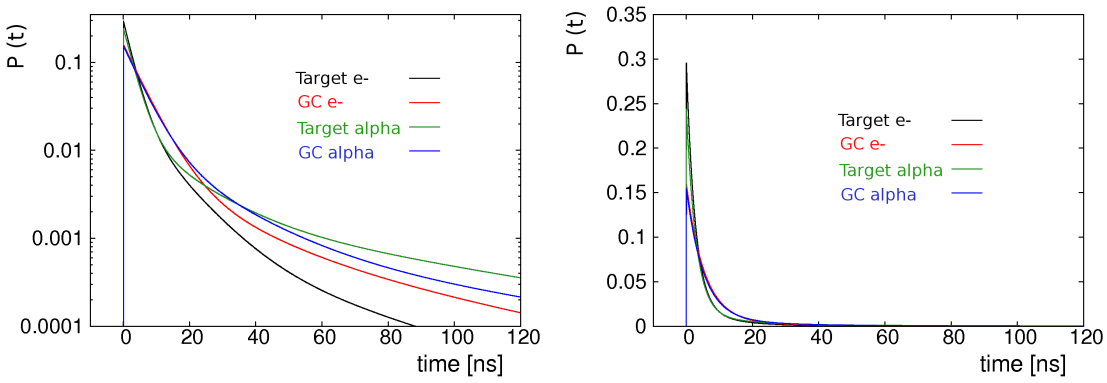

(a) (b)

Figure 5.15: Comparison of the extracted photon emission time PDFs $P(t)$ for alpha and beta excitation in Target and GC with logarithmic scale (a) and linear scale (b).

more significant than the difference between electrons and alpha particle excitation in one of the volumes. This is evident especially when looking at the linear plots. The difference between electrons and alphas is more pronounced in the Target than in the GC. This can be explained by differences in the excitation of the solvent molecules: In the Target the PXE to PPO energy transfer path contributes most to the light output. In the GC there is only a fraction of 4 % PXE and thus the energy transfer paths from dodecane (and the chemically similar molecules in Ondina909) to PPO becomes more important. For aliphatics (for example dodecane) the complicated radiochemical processes before excitation include bond breaking and free radical formation [122] also for electron excitation. It is therefore intelligible that for example triplet states are formed by both electrons and alphas with similar probabilities. Thus, excitation with alphas and electrons lead to similar photon emission time PDFs.

For the Target we clearly see that there is an additional component with a rather long time constant for the excitation with alphas which can in principle be exploited for particle discrimination. It has to be studied with actual detector data or Monte Carlo simulations whether the difference in the pulse shapes between electrons and alphas is sufficient. The difference between Target and GC is promising for pulse shape discrimination. In fact, the Gamma Catcher composition has been deliberately tuned such that the time profile can be more easily distinguished from the Target. This difference can be for example used to check the size of the spill-in/spill-out effect for neutrino candidates [45].

The Monte Carlo simulation has been tuned for alpha particles and electrons separately with the results shown in Figure 5.15. In the Double Chooz detector other time

resolution effects occur than with the small cell laboratory measurement tests. For example the light travel times in the detector are of the order of nanoseconds. Also time offsets between the PMTs contribute to the time resolution. With the work presented here the Monte Carlo simulation was used to study pulse shape discrimination quantitatively [45]. Also the standard vertex reconstruction algorithm `RecoBAMA` [80] relies on time information and can be improved with the accurate photon emission time PDF information provided here.

5.6 Summary

Pulse shape discrimination techniques and event localization are important to understand and reduce background events in Double Chooz. The determination of the scintillator emission time probability density functions (PDFs) is essential for these methods. In general, a better understanding of the scintillator signal characteristics is provided which leads to a better modeling of the detector response for neutrino signals and backgrounds.

A dedicated setup for measuring scintillator emission time PDFs has been presented. The requirements for an unbiased measurements were quantified. A description of the laboratory measurement data analysis was given including a fit function to describe the data. The scintillator photon emission time PDF could be described by the sum of three exponential terms. For the resolution function of the setup an asymmetric gaussian function is used. The results of the scintillator photon emission time measurements are presented in table 5.2. Additionally, the main results are presented graphically for better comparability of different scintillators.

In general, scintillators with efficient energy transfer paths have low time constants. If the sum of all rates related to the possible energy transfer paths is high, the time constant for the processes including light emission is low. The understanding of the correlation between the time profiles and the scintillator energy transfer paths led to a tuning of the emission times in the GC. Simultaneously with light yield and density matching an adjustment of the emission time profile was made by choosing 2 g/l as the PPO concentration in the GC. The resulting photon emission times are higher than for the other GC candidates with 5 g/l PPO. By choosing 2 g/l the difference between Target (faster) and GC (slower) photon emission times is increased. This difference can be used to distinguish Target events from GC events by pulse shape discrimination.

Alpha emitting isotopes were brought into Target and GC scintillator samples to measure the emission time profiles after alpha excitation in the laboratory experiment. The decay chain of the introduced ^{222}Rn includes beta and gammas as well. A procedure to statistically subtract the background from beta and gamma events was discussed.

The results for the time profiles under electron and alpha excitation were compared for Target and GC. In the Target scintillator the relative weight of photons being emitted at times higher than about 15 ns is increased for alpha particle excitation compared to electrons. This can be explained by the increased excitation of triplet states in the excitation process due to the higher specific energy loss of alpha particles. The

difference can potentially be used to apply particle discrimination. For the GC the difference between alpha and electron excitation is less pronounced. An explanation is the high probability for triplet state formation for electrons as well as alphas at the high concentration of non-aromatic solvents in the GC.

The results presented in this chapter have been used to tune the Double Chooz Monte Carlo software. Pulse shape discrimination techniques can be studied quantitatively with the tuned MC.

6 Detector homogeneity studies with simulation

6.1 Introduction and Motivation

Sufficiently high light attenuation lengths in the liquid scintillators on a timescale of years is critical for the success of the Double Chooz experiment. It is planned to take data with Double Chooz for about five years (see sensitivity in Figure 1.5). In particular for the Target scintillator, which contains the gadolinium complex, this task is non-trivial. In the past, other experiments like Chooz [30] and Palo Verde [53] observed a significant degradation of attenuation lengths in their gadolinium-loaded scintillators on a timescale of hundreds of days. It is therefore of interest to quantify the requirements on the attenuation lengths for Double Chooz. For the first months of data taking, no indication for a scintillator degradation was observed.

In addition to a decrease in the absolute number of photoelectrons, a degradation of the attenuation length would lead to a less homogeneous detector response. A degradation in the homogeneity leads to a degradation in energy resolution. This motivates the study of a correction method for detector light collection efficiency inhomogeneities.

This chapter starts with Monte Carlo (MC) simulation studies on the effects of a hypothetical degradation of the Double Chooz Target scintillator attenuation length: Electrons with 1 MeV kinetic energy are simulated in order to analyze the loss of photoelectrons (PEs) and the increasing inhomogeneity with degrading Target attenuation length (section 6.2). In section 6.3 it is simulated at which Target attenuation lengths the efficiency of neutrino detection would be degraded. This attenuation length is compared with the design goal of an attenuation length of 5 meters in the Target scintillator. Section 6.4 deals with a correction method for detector efficiency inhomogeneities in general.

6.2 Attenuation length effects with 1 MeV electrons

6.2.1 Implementation of a hypothetical attenuation length degradation in the Monte Carlo simulation

Before the actual study, the attenuation lengths of the single components for the Target and Gamma Catcher liquids have been adjusted in the MC simulation as a part of this work. Spectrometer measurements of the attenuation lengths of the final components for the large scale production have been used. These measurements were done with a Varian

Cary 400 UV/Vis spectrometer by our group at MPIK. If batch-to-batch variations for a single component are observed, the measurement with the highest attenuation length was chosen because this measurement corresponds to the cleanest sample with fewest impurities. Since the wavelength region of interest is outside the main absorption band of the pure chemicals, it is dominated by impurities. Although chemicals of high purity have been chosen small remaining impurities can have a sizeable impact on the attenuation length. The attenuation lengths in the MC simulation have been kept updated during this work. Thus, the results in this chapter have been obtained with attenuation lengths which were tuned to the best of our knowledge at the time the simulations were done. Before the discussion is continued, some terms and definitions are clarified. With the spectrometer, the attenuation A is measured:

$$A(x) = \log_{10}\left(\frac{I(0)}{I(x)}\right). \tag{6.1}$$

The light intensity decreases from $I(0)$ to $I(x)$ when passing through a sample of the length x in the spectrometer:

$$I(x) = I(0) \cdot e^{-x/\Lambda}. \tag{6.2}$$

Here, Λ is the attenuation length. It includes absorption and scattering. Scattering is neglected in the simulation. The attenuation of multiple components in a mixture is additive. Consequently, via the relation

$$\Lambda = \log_{10}(e) \cdot \frac{x}{A}, \tag{6.3}$$

which is obtained from equation (6.1) and (6.2), the inverse of the total attenuation length is the sum of the inverse attenuation lengths of the components. In the simulation study reported here, the Target attenuation length has been varied while the Gamma Catcher and the Buffer attenuation lengths are kept constant. Since the liquids surrounding the Target are not metal-loaded they are not as sensitive to degradation. The attenuation lengths before filling the Double Chooz far detector are listed in section 1.2.6. For a possible variation in the Target a measured spectrum has been used: Two light attenuation measurements of a scintillator sample with PXE, dodecane and the gadolinium complex $Gd(thd)_3$ were done at a time span of about 3 years (August 2006 to June 2009). This measurement might not reflect the evolution of the large scale Target scintillator in the detector. Scintillator production was optimized since 2006 and there are effects influencing the scintillator stability when working on the laboratory scale which are not critical for the large scale production. However, the spectrum of the attenuation difference in this small scale sample is more realistic than a simple scaling factor in order to simulate a degradation. PPO and bis-MSB are omitted here in order to be able to measure the spectra at lower wavelengths since they would otherwise dominate the attenuation.

The wavelength-dependent difference after 3 years in the attenuation of the small scale sample shown in Figure 6.1 can be used: In order to simulate different degrees of the hypothetical degradation in the Target scintillator, this spectrum was scaled with various

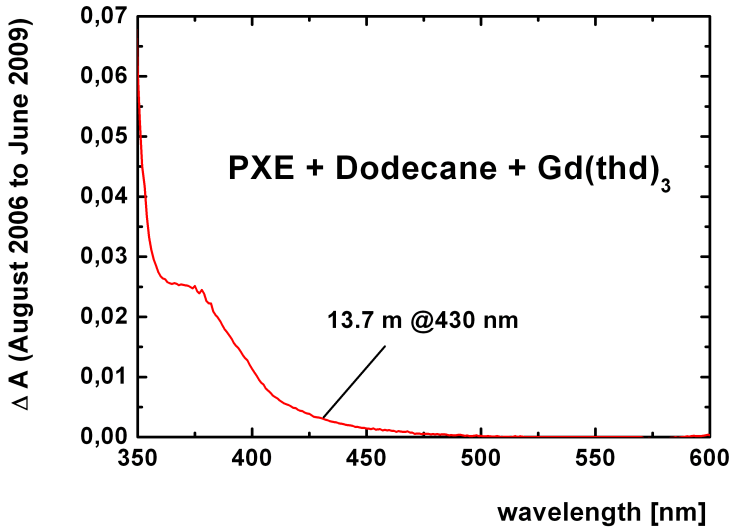

Figure 6.1: Difference in the attenuation (Δ A) of a PXE, dodecane and Gd(thd)$_3$ mixture after about 3 years measured with a 10 cm cell. The small difference corresponds to an additional attenuation length of 13.7 m at 430 nm (see equation (6.3)).

factors and then added to the attenuation spectrum as a mere absorption component without reemission. A given factor f leads to a total attenuation length at 430 nm of

$$\Lambda = \left(\frac{1}{12.5 \text{ m}} + \frac{1}{f \cdot 13.7 \text{ m}} \right)^{-1} . \tag{6.4}$$

The hypothetical degradation contributes with an attenuation length of $f \cdot 13.7$ m while the sum of the Target components (from the purest samples) is 12.5 m. In the following, different Target attenuation lengths Λ_{Target} are obtained using this procedure.

6.2.2 Results for 1 MeV electrons

The MC study of attenuation length effects was started with 1 MeV electrons which have been homogeneously distributed in the Target[1]. A simulation of 30000 electrons has been done for 94 different Target attenuation lengths. Thus, $2.82 \cdot 10^6$ electrons and their light production were simulated at the computing cluster CCIN2P3 in Lyon with parallelized jobs.

The first result is the sum of the photoelectrons in all inner detector PMTs simulated by `DCGLG4sim` (PE_{true}, as opposed to PE_{reco} after the electronics simulation and pulse

[1]For this study `Geant4.9.1.p01` and `DOGS` Prod-05-01 have been used (with manually updated attenuation lengths for Target and Gamma Catcher components).

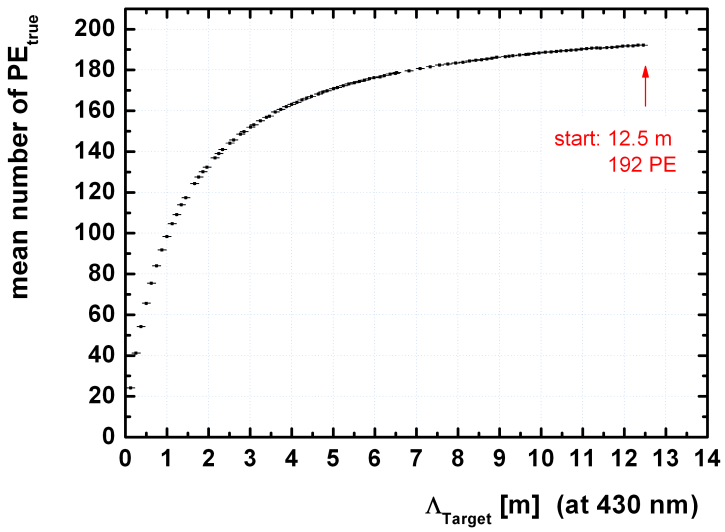

Figure 6.2: The number of PE_{true} (mean over 30000 electron simulations) dependent on the attenuation length in the Target at 430 nm.

reconstruction which is used later) for different Target attenuation lengths (Figure 6.2). The starting point is the ideal attenuation length of 12.5 m. If not specified otherwise, 430 nm is used as a reference wavelength since this is a typical wavelength of the bis-MSB emission spectrum (see Figure 1.8). As explained above, the measurements with the highest attenuation lengths for the single components have been used in the simulation. In reality, there are batch-to-batch variations of the chemicals and thus a lower attenuation length is expected. Attenuation lengths for the Target above 5 m (design goal) are satisfactory as a starting point for Double Chooz. After the liquids have been shipped to Chooz the complete Target mixture was measured to be 7.8 m at 430 nm and the attenuation length was adjusted in the simulation [49, 123]. The focus of this study is the dependency of the detector performance on the attenuation length. It can be discussed with the presented results for different starting points of the Target attenuation length.

The number of PE is slowly decreasing with decreasing attenuation lengths for high Λ_{Target}. At an attenuation length of 5 m, the number of photoelectrons is still 90 % of the value at 12.5 m (and 93 % of the value at 7.8 m). The variation in photoelectron statistics is thus rather flat above the design goal of $\Lambda_{\text{Target}} = 5$ m. The diameter of the Target vessel is 2.3 m. If the attenuation length becomes comparable to the size of the vessel, it is clear that significant attenuation of the light generated in the Target occurs. This can be seen as a more rapid decrease of the number of photoelectrons with decreasing attenuation lengths at attenuation lengths below 2.3 m.

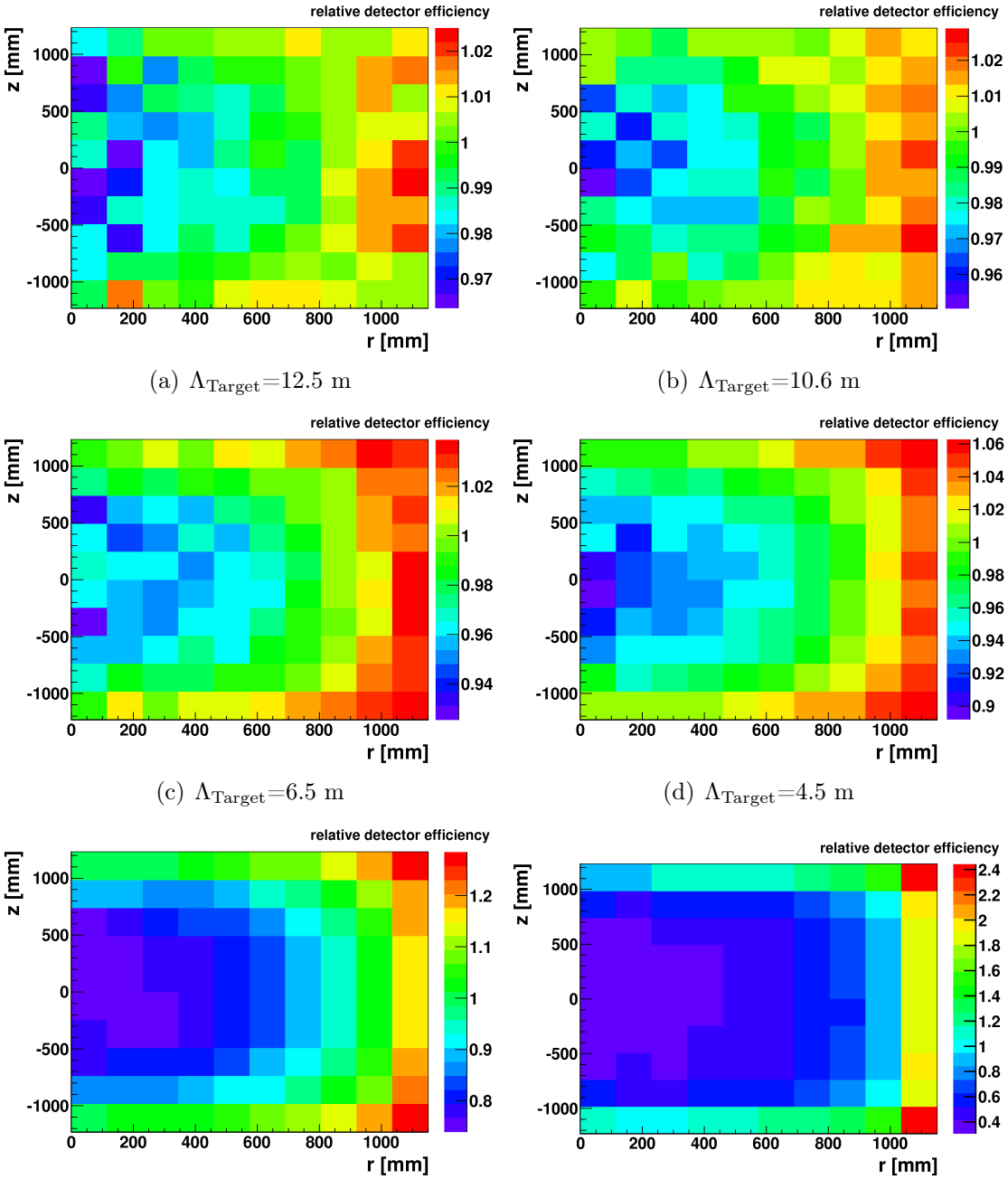

(a) Λ_{Target}=12.5 m

(b) Λ_{Target}=10.6 m

(c) Λ_{Target}=6.5 m

(d) Λ_{Target}=4.5 m

(e) Λ_{Target}=1.23 m

(f) Λ_{Target}=0.13 m

Figure 6.3: The relative detector efficiency (see text for the definition) for different attenuation lengths in the Target. It is taken advantage of the cylindrical symmetry of the Double Chooz detector: The horizontal axis is the two-dimensional radius $r = \sqrt{x^2 + y^2}$. The vertical axis is the z coordinate. A two-dimensional bin thus represents a ring in the detector. Note that the color scales have been adjusted for each attenuation length for better visibility of the inhomogeneities.

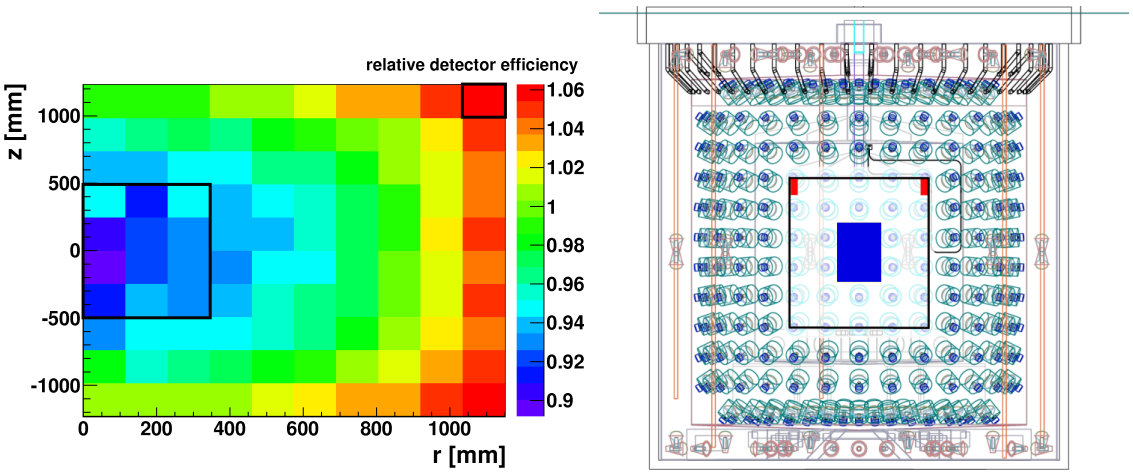

(a) (b)

Figure 6.4: The black rectangles in the left figure show the definition of a cylinder in the Target center and a ring in the Target corner. The right figure shows a view of the detector geometry implementation in the simulation (true to scale) with a cross section through the cylinder (blue) and the ring (red).

The energy resolution of the detector becomes worse if less photoelectrons are detected per MeV. In addition to the degradation due to lower photoelectron statistics the resolution is affected by the homogeneity of the detector response: For different locations in the Target (and GC), particles of the same type and the same energy can yield a different number of PE. As already mentioned in section 2.6, there has been an effort to position the PMTs such that the homogeneity is high at the nominal attenuation length. However, if the attenuation length of the Target decreased significantly, the homogeneity is affected. This degradation of the homogeneity was further investigated. In section 6.4, a method is presented which can be used to correct for detector response inhomogeneities irrespective of the underlying physical cause.

In Figure 6.3, the light collection efficiency at different positions in the Target is shown relative to the mean efficiency in the Target (relative detector efficiency) for different Target attenuation lengths. The homogeneity at the starting point with an attenuation length Λ_{Target}=12.5 m is at the level of few percent across the Target volume. At Λ_{Target}=6.5 m the inhomogeneity is slightly increased but still in the same range. For lower attenuation lengths the inhomogeneity increases more rapidly with decreasing attenuation lengths.

In order to quantify the inhomogeneity across the Target volume further, a simple quantity is constructed: At the corner of the Target the detector efficiency is in general high (see Figure 6.3) while it is low in the Target center. These two regions are used to calculate the spread of the detector efficiency. In Figure 6.4 the definition of the two volumes is shown graphically. The relative difference between the two volumes (spread) is shown in Figure 6.5 for varying attenuation lengths in the Target. The focus in this

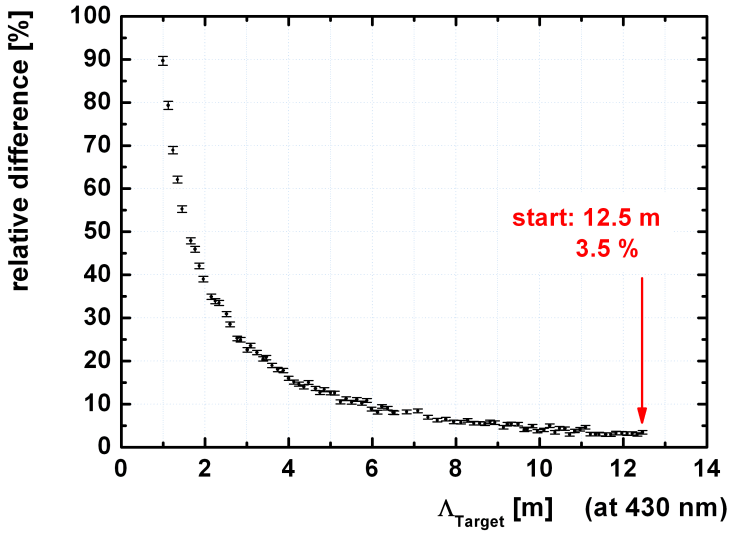

Figure 6.5: The relative difference in percent between the center of the Target and the corner with statistical error bars. Note that this is close to the maximum spread in the Target. The numbers are not to be confused with a mean deviation from the overall Target efficiency.

study is on the variation with the attenuation length rather than the absolute numbers of the spread. As for the total number of PE, the level of homogeneity is rather stable for high attenuation lengths and decreases with decreasing attenuation length more rapidly at lower attenuation lengths. A method to correct for the inhomogeneity can help to improve the energy resolution. In section 6.4 such a method is presented. Prior to that the effect of a decreasing attenuation length on the neutrino selection is studied in the next section.

6.3 Attenuation length effect on neutrino candidate selection

In order to investigate the effects of a degrading attenuation length on the Double Chooz experiment, an analysis of the neutrino selection efficiency has been done with MC. Standard cuts for the neutrino candidate selection have been used and a simple energy calibration has been done.

In this analysis the complete simulation chain has been used[2] (see section 1.2.5): First, 25000 neutrino events have been generated with `DCNuGen2` and distributed ho-

[2]The used `DOGS` versions were Prod-05-01 and Prod-06-00. `Geant4.9.2p02` was used.

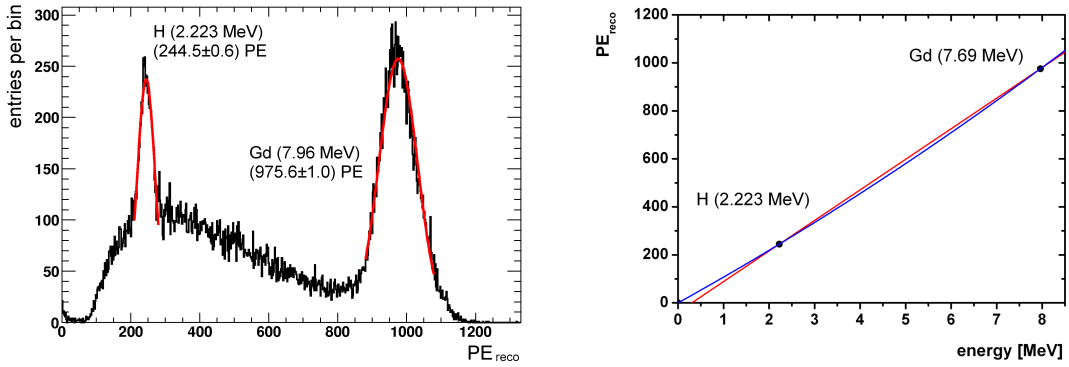

(a) (b)

Figure 6.6: (a): Simulated PE_{reco} spectra of prompt and delayed events in the neutrino sample for $\Lambda_{Target} = 12.5$ m. A gaussian fit is done in order to get the mean number of PE_{reco} for the hydrogen and gadolinium peaks. (b): Linear calibration with offset (red) and quadratic calibration function (blue).

mogeneously in the Target volume. At a rate of about 50 neutrino interactions per day this corresponds to 500 days. Second, the light production and number of PEs for the neutrino prompt event (positron) and delayed event (neutron) is simulated with `DCGLG4sim`. The simulated number of PE after `DCGLG4sim` is called PE_{true}. From this stage on the simulation is repeated for 11 different attenuation lengths in the Target. In order to get different attenuation lengths, the spectrum in Figure 6.1 has been scaled with 11 different factors as explained in the previous section and was added as pure absorption component. Third, `DCRoSS` is applied in order to simulate the PMT behavior and electronics effects.

After the three simulation steps, the reconstruction software tool `DCRecoPulse` is applied in order to retrieve a reconstructed number of photoelectrons (PE_{reco}) from the simulated waveforms. In general, PE_{reco} is lower than PE_{true} due to several effects like inefficiencies and the size of the charge integration window. However, in this analysis the reconstructed energy E_{reco} is obtained by calibrating PE_{reco} with the known energies of the hydrogen and gadolinium neutron capture signals from the delayed events. The combined simulated PE_{reco} spectrum for prompt and delayed events is shown in Figure 6.6 (a). The mean number of PE_{reco} has been extracted for the hydrogen (2.223 MeV) and gadolinium (7.96 MeV) peaks at a Target attenuation length Λ_{Target} of 12.5 meters. A slight nonlinearity in the calibration factor is found. The pulse reconstruction `DCRecoPulse`, at the time this study was done, introduces the nonlinearity which is not seen for PE_{true}. However, the focus of this study is the effect of the attenuation length in the Target which can be done regardless of this nonlinearity. Two different simple energy calibration functions (see Figure 6.6 (b)) have been used to transform PE_{reco} to E_{reco}. Both the linear and the quadratic function give compatible results. The quadratic function is used in this study since it is more realistic for energies $\lesssim 0.5$ MeV.

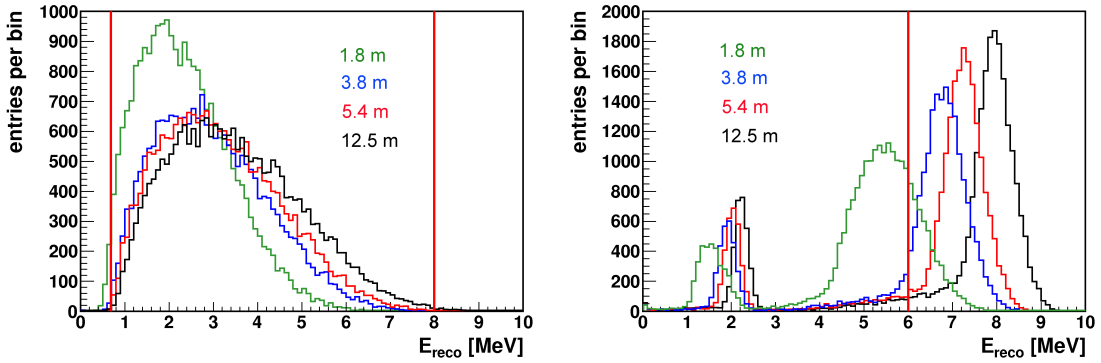

(a) (b)

Figure 6.7: Monte Carlo reconstructed energy spectra for the prompt (a) and delayed (b) events. The colors correspond to different Target attenuation lengths after the hypothetical degradation has been applied (see legend). Neutrino candidate selection cuts are displayed as red vertical lines. The calibration of the reconstructed energy has been done at $\Lambda_{\text{Target}} = 12.5$ m with the quadratic function (see Figure 6.6). Calibration with the linear function yields compatible results.

The neutrino selection cuts used in this selection are:

1. Energy cut on the prompt event: 0.7 MeV $\leq \text{E}_{\text{prompt}} \leq$ 8 MeV.
2. Energy cut on the delayed event: 6 MeV $\leq \text{E}_{\text{delayed}} \leq$ 12 MeV.
3. Cut on the time difference Δt between the prompt and delayed events: 0.5 μs $\leq \Delta t \leq$ 200 μs.

For the final detector data analysis additional cuts are under discussion which are not needed for the purpose of this simulation study. Also the values of the cuts listed above can be different for the final Double Chooz analysis. The efficiency of the time cut is unaffected by the attenuation length of the Target scintillator. Time differences due to absorption and reemission are in the range of nanoseconds while the time difference between prompt and delayed event is of the order of tens or hundreds of microseconds. It was explicitly checked that the efficiency of cut 3 is independent of the attenuation length in the Target. As from now, the first two cuts are studied in more detail.

Figure 6.7 shows the effect of the attenuation length in the Target on the prompt and delayed reconstructed energies. First, we use a conservative approach and use one calibration (obtained at $\Lambda_{\text{Target}} = 12.5$ m) for all attenuation lengths. Thus, the effect of an unnoticed degradation in the Target on the neutrino selection efficiency can be investigated. In the reconstructed energy spectrum of the delayed events, the two peaks from hydrogen and gadolinium are in the correct position for $\Lambda_{\text{Target}} = 12.5$ m, since the calibration has been done at this attenuation length. If the same calibration is applied

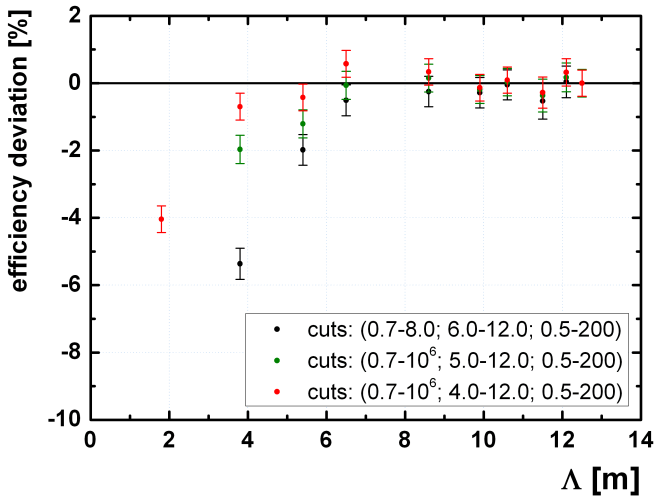

Figure 6.8: The combined cut efficiency deviation from the nominal efficiency at $\Lambda_{\text{Target}} = 12.5$ m is represented by the black points for the standard cuts 1-3. Statistical error bars are shown. The quadratic energy reconstruction is used (only marginally different results are obtained for the linear energy calibration). The green and red data show a relaxed lower cut on the delayed energy deposition of 5 MeV and 4 MeV respectively. The cuts are given in the format (prompt;delayed;time). The different higher energy cut for prompt events has only marginal influence.

for the spectra which have been obtained with lower Target attenuation lengths, lower energies are reconstructed as expected.

The tails in the delayed spectrum come from gammas which escape the Gamma Catcher vessel into the non-scintillating Buffer volume. In this case only part of the energy is converted to scintillation light. From Figure 6.7 it can be already seen that the low energy cut for the delayed energy deposition is the most critical cut discussed here. The efficiencies of the cuts will be presented quantitatively in the next paragraph.

For the prompt events we observe a shift of the reconstructed energies as well. However, the cut efficiencies do not change as dramatically as for the delayed events. If a neutrino rate-only analysis is done, the prompt event efficiency is not affected strongly by a decreasing attenuation length even in the conservative scenario with no re-calibration. Interestingly, the shape of the spectrum changes with decreasing attenuation length. If there was a small, unnoticed and uncalibrated degradation of the Target attenuation length this has an influence on a shape analysis. A positive θ_{13} leads to a smaller signal especially for the lower prompt energies. An uncalibrated degradation of the attenuation length counteracts this change in shape and thus θ_{13} would be underestimated. This shows the importance of detector stability checks (for example with hydrogen captures

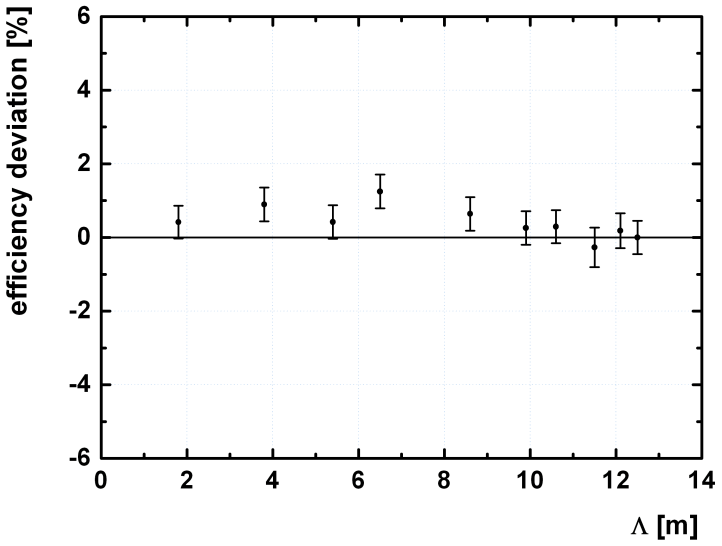

Figure 6.9: Deviation from the neutrino selection efficiency at $\Lambda_{\text{Target}} = 12.5$ m. The neutron capture peaks have been used to recalibrate for each Target attenuation length.

presented in section 2.9) and subsequent recalibration, if needed.

Cut efficiencies For a neutrino rate-only analysis the cut efficiencies of the neutrino candidate selection have been studied. The absolute efficiencies from this simulation at $\Lambda_{\text{Target}} = 12.5$ m are about 0.997 for the prompt cut, 0.989 for the time cut and 0.809 for the delayed cut. The combined simulated efficiency is about 80.7 %. The main inefficiency comes from captures at hydrogen instead of gadolinium. In the experiment the efficiency can be quantified by using neutron source calibration in the Target. In this study, the focus is on the effect of the attenuation length and thus on the deviation from the nominal efficiency at $\Lambda_{\text{Target}} = 12.5$ m. In Figure 6.8, the decrease in cut efficiency for decreasing Target attenuation lengths is shown with the black points. At an attenuation length above about 6 to 7 meters, the efficiency is stable on the level of the statistical errors of the simulation. Below, the efficiency decreases significantly if the starting point of the initial calibration is at $\Lambda_{\text{Target}} = 12.5$ m. For a starting point and initial calibration at 7.8 m the change in neutrino detection efficiency starts at attenuation lengths which are lower. This is for the very conservative case that no recalibration is done over this range. Still, it shows in which range the Target attenuation length begins to affect the rate-only analysis. It can be concluded that in the range of $\Lambda_{\text{Target}} \approx 5$ m (5 m is the design goal), careful calibration of the detector is necessary.

Of the studied cuts, the low energy cut on the delayed events is the dominant source

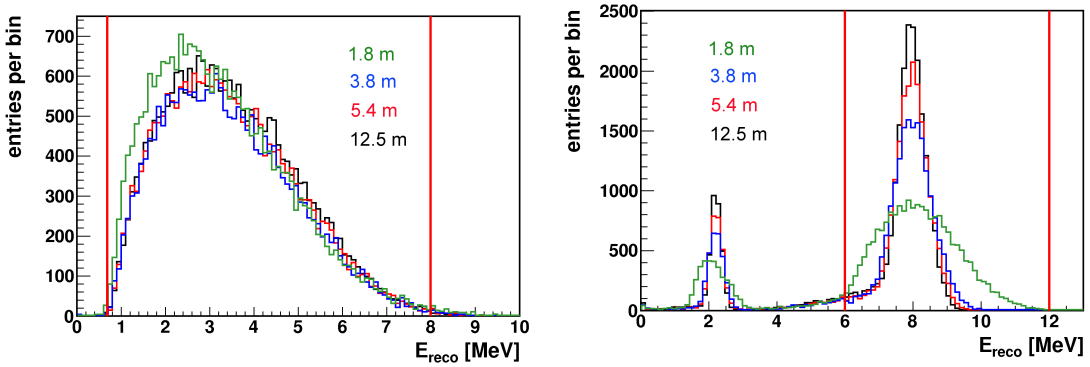

(a) (b)

Figure 6.10: Prompt and delayed spectra for different Target attenuation lengths (see plot legend) after recalibration. Note that the number of events is not the same for the different Λ_{Target} due to technical reasons in the MC production.

of inefficiency for the neutrino candidate selection. Physically, captures on hydrogen and escaping gammas account for this inefficiency. This cut also accounts for the main part of the efficiency decrease with decreasing Target attenuation length. Therefore, the analysis of the simulation results has been repeated with a relaxation of this cut (see red and green points in Figure 6.8). This study shows, that a relaxation of the lower energy cut on the delayed event energy stabilizes the efficiency down to lower attenuation lengths. However, the final cut for the detector data in Double Chooz depends on the background in this region. Finally, a compromise has to be made between a lower background contamination on the one hand and a higher efficiency and lower efficiency uncertainty on the other hand.

To conclude this section the efficiency is studied with a recalibration of the energy scale with the hydrogen and gadolinium peak for each attenuation length. The deviation from the efficiency at $\Lambda_{\text{Target}} = 12.5$ m is shown in Figure 6.9. It is found that,within the statistical errors, a recalibration can recuperate the efficiency of the MC neutrino signal in a rate-only analysis for Target attenuation lengths as low as about 2 m.

The corresponding recalibrated prompt and delayed energy spectra are shown in Figure 6.10. While the peaks in the delayed energy spectrum are reconstructed at the correct positions, the recalibration with the simple quadratic function is not enough to recover the shape of the prompt spectrum. In order to do so, one also has to correct for the increasing detector inhomogeneity which results in worse energy resolution (see Figure 6.10 (b)). Although the efficiency for neutrino candidates is stable after recalibration, for a rate-only analysis with detector data the background has to be included as well. The systematic error for the θ_{13} analysis which corresponds to the background estimate increases with decreasing energy resolution. The energy resolution degradation in case of a degrading attenuation length comes from a decrease in the photoelectron

statistics and an increase in the detector inhomogeneity. In the next section a method will be presented which can be used to correct for the inhomogeneity of the detector response and thus improve the energy resolution again.

6.4 Detector efficiency inhomogeneity correction

6.4.1 Detector efficiency map concept

The general idea for the detector efficiency inhomogeneity correction is based on the application of a vertex-dependent correction. Correction factors have to be determined for each vertex in the detector. The ensemble of the vertex-dependent efficiency correction factors is also called 'efficiency map'. In order to get the efficiency map, Monte Carlo simulations of millions of particles have been done (up to the PE_{true} level from DCGLG4sim) at various positions in the detector. The resulting total number of photoelectrons and the corresponding initial vertex are stored in a file. These data from Monte Carlo can be compared with calibration data from the Articulated Arm system (section 1.2.4) which plans to deploy sources at positions in the Target volume which are distributed in three dimensions.

The MC file can be used to get a correction factor for a given event in Double Chooz. After the pulse reconstruction and vertex reconstruction has been applied (either for data or MC), the reconstructed number of photoelectrons (PE_{reco}) and the reconstructed vertex $\vec{x}_{reco}$ are available. The correction factor can now be obtained from the Monte Carlo events in the file which are closest to the reconstructed vertex (details are given below). The mean efficiency of these events relative to the overall detector (Target plus GC) mean efficiency is used as a correction factor for PE_{reco}. Thus, the energy resolution degradation due to detector efficiency inhomogeneities can be compensated for.

6.4.2 Production of the Monte Carlo detector efficiency map

Three different MC files have been produced[3]: The first file contains about 1.25 million electrons (1 MeV) which are distributed homogeneously in the Target and GC volumes. The default configuration for `DCGLG4sim` has been used (with a Target attenuation length of $\Lambda_{Target} = 11.9$ m). Another file with the default configuration but with 4.80 million events has been produced to investigate the accuracy of the method with an increased number of events. The third file was produced with a reduced attenuation length in the Target scintillator of $\Lambda_{Target} = 5$ m (1.02 million events). At the lower attenuation length the performance of the correction can be checked if the inhomogeneity in the detector is increased. In the files, the vertices for particle insertion by `DCGLG4sim` ($\vec{x}_{true}$) and the simulated number of photoelectrons after `DCGLG4sim` (PE_{true}) are stored.

A graphical representation of the obtained detector efficiency map is shown in Figure 6.11. Similar plots have been shown for the Target only and with less statistics in section 6.2.2. The Target vessel can be seen at a radius of 1150 mm and at z=± 1250 mm. At

[3]The HEAD version of `DOGS` (as of July 9, 2010) has been used.

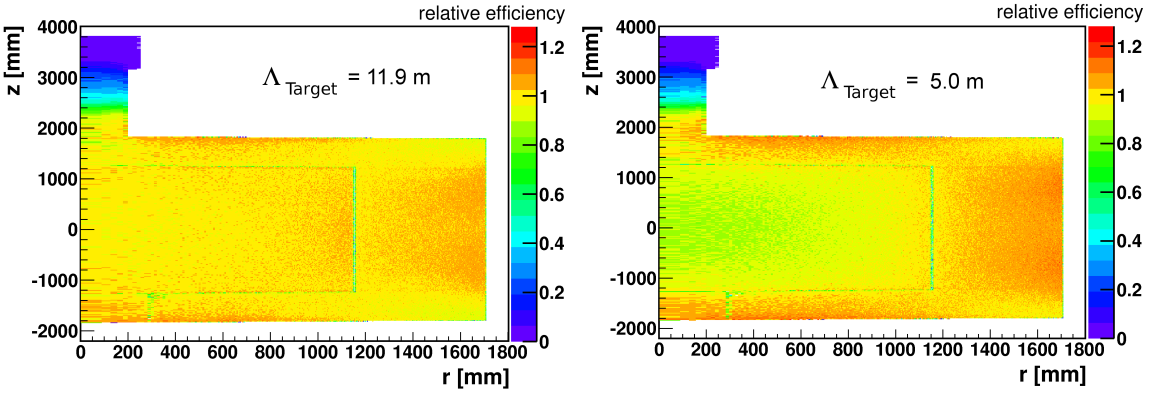

(a) $\Lambda_{\text{Target}} = 11.9$ m (b) $\Lambda_{\text{Target}} = 5.0$ m

Figure 6.11: Graphical representation of the simulated relative detector efficiency for different locations in the Double Chooz detector. The relative efficiency is defined as the mean number of PE_{true} for the events originating from a given bin divided by the mean number of PE_{true} for Target and GC. On the horizontal axis the two-dimensional radius $r = \sqrt{x^2 + y^2}$ is shown. The bin size has been chosen such that the 3-dimensional volume which is represented by the bins is constant.

a radius of about 290 mm the Target support structure is visible. Close to the vessel the efficiency is lower due to light reflection and partial energy deposition in the vessel instead of the scintillator. In the chimney region of the detector, the detector efficiency is found to be low as well. Light produced in this region has a lower probability to be collected by the photomultipliers. However, the chimney volume is small compared to the Target and GC volumes.

The difference between the two Target attenuation lengths can be seen clearly. For $\Lambda_{\text{Target}} = 5$ m the center of the Target has a significantly reduced efficiency. The inhomogeneity of the detector response is increased as expected. The most efficient spots in the detector simulation are at the edge and at the top and bottom of the Gamma Catcher close to the PMTs.

6.4.3 PE_{reco} correction with the detector efficiency map

The MC data presented in the previous section can be used to correct the number of PE_{reco}. Three different methods to calculate the efficiency correction factors have been implemented. The difference is in the way events from the files are selected which are close to the reconstructed vertex $\vec{x}_{\text{reco}}$ of the event whose PE_{reco} is to be corrected.

1. For the first method the detector is divided in 3-dimensional bins of the size 10 cm $\times$ 10 cm $\times$ 10 cm. The efficiency correction factor for each bin is calculated from the events in the MC file for which $\vec{x}_{\text{true}}$ is in this bin.

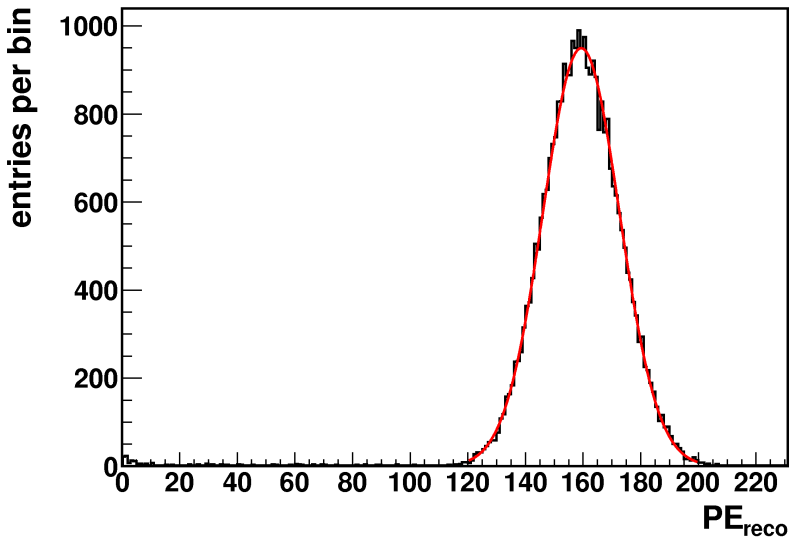

Figure 6.12: Simulated reconstructed photoelectron spectrum from `DCRecoPulse` for a Target attenuation length of Λ_{Target}=11.9 m. The peak of the distribution can be fit with a gaussian function with the mean $\mu = 159.34 \pm 0.08$ and $\sigma = 13.29 \pm 0.06$.

2. The second method executes a search for the N_{nearest} events in the file whose vertices are closest to $\vec{x}_{\text{reco}}$. After optimization, it was found that $N_{nearest} = 200$ gives good results.

3. In the third method, a sphere of the size r_{sphere} around the reconstructed vertex $\vec{x}_{\text{reco}}$ is defined. Events from the MC file whose vertices are inside the sphere are used to calculate the efficiency correction factor. Different sizes of the sphere were tested and finally a radius r_{sphere}=10 cm was used.

The first method is simple and fast since the list of MC events in the file has to be filled to a histogram only once. Disadvantages of this method are that some bins contain less events than others and sometimes vertices are reconstructed outside the GC by the vertex reconstruction `RecoBAMA`, where no correction factor can be obtained since the bins are not filled. A bin size of 10 cm per dimension was chosen because the vertex reconstruction accuracy is in this range. Thus, a smaller bin size does not increase the accuracy of the reconstruction significantly. The second method is the most accurate but it is slower since for each event which has to be corrected a list of millions of events has to be sorted. A compromise in accuracy and execution speed is implemented with the third method.

Test of the correction performance In order to test the correction methods, two additional samples (Λ_{Target}=11.9 m and 5.0 m) of 32000 electrons with 1 MeV energy

have been simulated with homogeneously distributed vertices in Target and GC. For these events the electronics simulation has been done (`DCRoSS`) and after that the pulse reconstruction `DCRecoPulse` and vertex reconstruction `RecoBAMA` have been applied. The uncorrected PE_{reco} spectrum is shown in Figure 6.12 for Λ_{Target}=11.9 m. The relative energy resolution can be extracted from the gaussian fit: $\Delta E/E = \sigma/\mu = 8.34$ %. If the correction with the efficiency map is applied the energy resolution improves. The results are listed in table 6.1.

Target attenuation length	Method	$\Delta E/E$ [%]
Λ_{Target}=11.9 m	uncorrected	8.34 ± 0.04
	method 1	8.28 ± 0.04
	method 2	8.12 ± 0.03
	method 3	8.17 ± 0.04
Λ_{Target}=5.0 m	uncorrected	9.79 ± 0.05
	method 1	8.65 ± 0.04
	method 2	8.42 ± 0.04
	method 3	8.49 ± 0.04

Table 6.1: Relative energy resolution for simulated 1 MeV electrons with different detector inhomogeneity corrections.

As expected, method 2 gives slightly better results than method 3 and significantly better results than method 1. The results in the table have been obtained with the map with 1.25 million events for Λ_{Target}=11.9 m. The map with 4.80 million events has been used as well. It was found that the energy resolution increases only marginally for method 1 while it stays the same for method 2 and 3. At Λ_{Target}=11.9 m, the improvement after the correction is generally small since the detector inhomogeneity is small. The relative energy resolution for 1 MeV electrons in the simulation is dominated by the statistical fluctuations in the number of photoelectrons. For a lower Target attenuation length Λ_{Target}=5.0 m the inhomogeneity in the detector efficiency is higher and the relative energy resolution is worse. With the correction applied, an energy resolution close to the one for Λ_{Target}=11.9 m can be re-established.

The corrected PE_{reco} spectrum is shown for Λ_{Target}=5.0 m in Figure 6.13. It turns out that for the small fraction of events in the chimney region, the vertex reconstruction algorithm reconstructs the vertex of the events systematically too low. This means that the chimney events have a $\vec{x}_{reco}$ which is below the chimney where the simulated detector efficiency is close to one. The applied correction factors are thus not high enough to correct for the true efficiency in the chimney and the events remain in the tail of the distribution. Apart from the chimney events the correction method works well and an improvement of the energy resolution is obtained. In particular for low Target attenuation lengths the correction is powerful since in this case the detector inhomogeneities are more significant. In Appendix A, a software tool called `ERecoHD` is

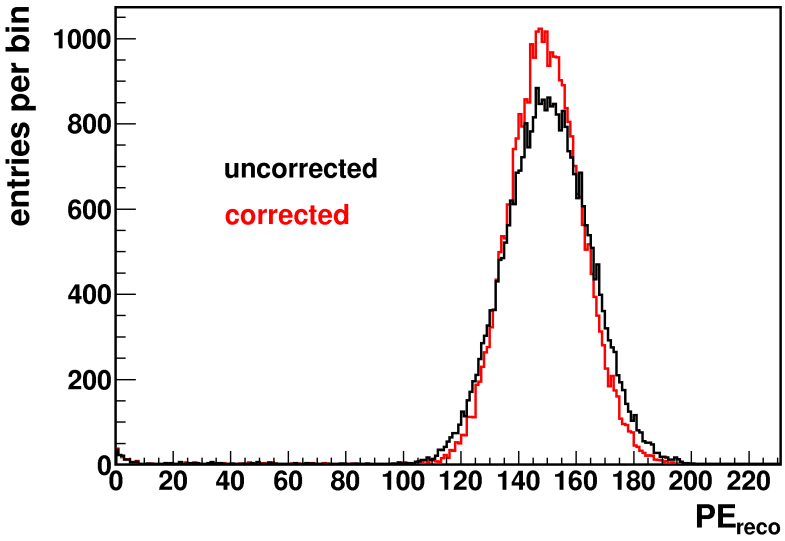

Figure 6.13: Comparison of the uncorrected (black) and corrected (red, method 2) photoelectron spectra for Λ_{Target}=5.0 m.

presented which implements the detector inhomogeneity correction.

6.5 Summary

A homogeneous light collection efficiency is important for the energy resolution of the Double Chooz experiment and thus a method to correct for possible inhomogeneities can improve the systematic error associated with energy cuts.

The number of photoelectrons and the detector efficiency homogeneity have been simulated for varying attenuation lengths. Below about 4-5 m the inhomogeneity increases to a level of about 10 %. If an inhomogeneity of this size was observed with calibration data at different detector positions, these data could be used to estimate the attenuation length in the Target. With a simple neutrino rate-only simulation analysis it could be found that the efficiency is degraded below about $\Lambda_{\text{Target}} = 6$ m if no recalibration is done and the starting point is 12.5 m. For a starting point calibration at 7.8 m the neutrino detection efficiency stays stable longer. If a recalibration is done the neutrino selection efficiency can be kept constant for Target attenuation lengths above 2 meters. The shape of the prompt spectrum is affected by a degrading Target attenuation length as well. If a shape analysis is done a more careful energy reconstruction is needed.

The studies show, that 5 m is a reasonable design goal for the Target attenuation length for the Double Chooz experiment. With the measured 7.8 m attenuation length in the Target before filling, the design goal specification is exceeded [49]. First detector stability analyses as for example presented in section 2.9 show that over a time-span of several months, no degradation in the photomultiplier charge is seen for both events

located in the Target and GC which indicates that the attenuation lengths are stable.

In the second part of this chapter, a correction method for detector efficiency inhomogeneities was presented. The correction improves the energy resolution in particular if the detector inhomogeneity is high. For a decreasing Target attenuation length below 5 m, the inhomogeneity increases more rapidly and correction is more important. Also other sources of detector inhomogeneity (for example switched-off PMTs) can be corrected if an efficiency map can be produced with detector data.

7 Summary

Neutrino oscillations provide a window to physics beyond the Standard Model. The search for the last unknown neutrino mixing angle θ_{13} is ongoing with the complementary accelerator-based and reactor neutrino approaches. The combined analysis of neutrino oscillation experiments gives a hint for a non-zero θ_{13} in a region which can be explored by the current reactor neutrino experiment generation.

The Double Chooz experiment uses a two-detector concept to determine the reactor electron antineutrino flux at a baseline of one kilometer relative to the unoscillated flux closer to the source. The projected sensitivity at 90 % confidence level is $\sin^2(2\theta_{13}) = 0.03$.

Electron antineutrinos are detected with inverse beta decay reactions in a newly developed gadolinium-loaded organic liquid scintillator. Both the Neutrino Target and a gadolinium-free Gamma Catcher scintillator have to meet multiple requirements simultaneously. In this work, optical properties of the scintillators have been studied by performing laboratory measurements, Monte Carlo simulations and first analyses of real Double Chooz far detector data.

Measurements and a model of the light yield have been used to identify Target and Gamma Catcher candidates which fulfill, among other requirements, light yield and density matching for an unbiased energy reconstruction and mechanical stability of the detector, respectively. The mean light collection efficiencies in Target and GC (3.3 % less in the Target) have been obtained by Monte Carlo simulations. Before the large scale production the light yield of the GC was therefore tuned to be (96.9±1.0) % of the Target light yield. In this tuning process the final design for the chemical compositions of the Double Chooz scintillators was determined. Analyzing Double Chooz far detector data, the photoelectron yield matching within one percent has been preliminary verified at the multi-ton scale with hydrogen capture events. In addition, no degradation in the optical properties was found for the first 3.5 months of data taking.

The light production inefficiency and the associated non-proportionality of the light output due to ionization quenching has been determined experimentally for electrons and for alpha particles. At the precision which is aimed for in Double Chooz these effects are important for the energy reconstruction and thus the energy cut efficiencies. Birks model is applied to interpret the experimental results. For different Monte Carlo simulation settings an effective Birks parameter kB was found which leads to a correct description of the experimental data. The changes in kB have been thoroughly analyzed and were understood. For alpha particles the quenching factors were given which allow to calculate the visible energy. It was found that for most of the alphas in natural radioactivity the visible energy is below the energy cut for prompt events and thus the contribution to accidental background is lowered due to ionization quenching.

In order to model the timing of the detector response for scintillator-induced signals, the scintillation photon emission time probability density functions were measured with a dedicated laboratory measurement. Differences between Target and GC have been enhanced by deliberately increasing the photon emission times of the GC via choosing a rather low PPO concentration of 2 g/l. Light yield and density matching have been simultaneously done. The higher difference in Target and GC photon emission times enhances the possibility of pulse shape discrimination of Target and Gamma Catcher events which can be used complementary to vertex reconstruction information. Photon emission times have been measured for alpha excitation of the Target and GC and the Monte Carlo simulation has been tuned to provide the possibility to study particle identification with pulse shape discrimination.

The neutrino selection efficiency was studied with Monte Carlo simulations for different Target attenuation lengths with and without re-calibration of the energy scale. For low Target attenuation lengths frequent re-calibration becomes more important to control the error on the cut efficiencies. The detector light collection efficiency homogeneity is related to the energy resolution of the experiment. It has been studied how the homogeneity degrades for a hypothetical degradation in the Target attenuation length. Above a Target attenuation length of 5 m at 430 nm the inhomogeneities lead to a contribution to the energy resolution at 1 MeV which is rather small compared to the minimal energy resolution coming from photoelectron statistics. Below 5 m the inhomogeneity would become more important. A method has been developed with Monte Carlo simulations to correct for detector inhomogeneities. The studies show, that 5 m is a reasonable design goal for the Target attenuation length. With the measured 7.8 m attenuation length in the Target before filling, the design goal specification is exceeded and no degradation is observed so far.

A The energy reconstruction tool ERecoHD

The energy reconstruction tool `ERecoHD` (Energy Reconstruction Heidelberg) has been developed together with Dr. Bernd Reinhold from MPIK. It has been tested and tuned with the help of Monte Carlo simulations. The code is however suited to handle the data from the detector as well. The input for the tool is the Common Trunk (CT) output (MC or detector data) and more specifically the reconstructed vertex $\vec{x}_{\text{reco}}$ and the reconstructed number of photoelectrons PE_{reco}. It performs a two-step reconstruction: As a first step, the inhomogeneity of the detector efficiency is corrected for. This method has been described in more detail in section 6.4. Here, the second step is described:

The corrected number of reconstructed photoelectrons is used to derive the reconstructed energy. For each event, several reconstructed energies are calculated, one for each of the relevant particle types in Double Chooz. Concretely, the energies for electrons, positrons and gammas are provided up to now. These particles have different effective light production (and thus PE production) efficiencies due to ionization quenching and Cherenkov light production. This is why the energy estimates differ for the different particle types. The decision which particle caused the signal can be postponed and left to a particle identification tool since the energies for different particle types are stored in parallel. The code for `ERecoHD` has been derived from the common Double Chooz `DCReco` base classes (`C++`) and it is foreseen to run it as a part of the automatized data processing chain.

Pulse reconstruction nonlinearity correction The results presented in this appendix have been obtained with the Double Chooz MC simulation `DOGS`[1]. As explained in section 1.2.5, the pulse reconstruction tool `DCRecoPulse` provides the number of reconstructed photoelectrons PE_{reco}. The ratio between PE_{reco} and PE_{true} from the detector simulation `DCGLG4sim` was observed to be slightly dependent on the absolute number of PE. This nonlinearity was corrected prior to the following reconstruction steps, since it mimics the nonlinearity induced by ionization quenching and Cherenkov light production. The nonlinearity has to be revisited for newer versions of `DCRecoPulse` and `DCRoSS`. Currently, efforts are made to understand this nonlinearity to higher precision.

After this step, an estimator of PE_{true} is obtained. Next, the correction for the detector efficiency inhomogeneity is applied (see section 6.4). The corrected number of photoelectrons ($\text{PE}_{\text{corr.}}$) is proportional to the actual light output of the particle (visible energy). It is stressed that the output of this inhomogeneity-corrected visible energy is

[1] The HEAD version of `DOGS` (as of July 9, 2010) has been used.

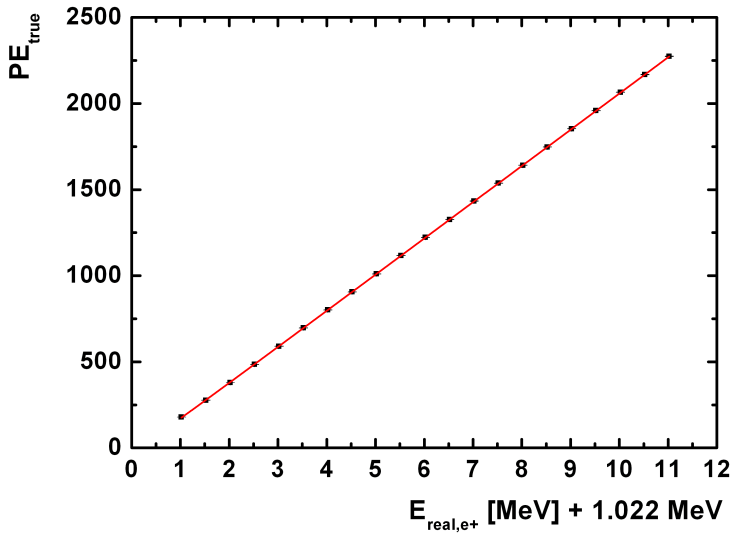

Figure A.1: Number of simulated photoelectrons after `DCGLG4sim` (PE_{true}) dependent on the positron energy. The fit function from equation (A.1) is used.

the main output of `ERecoHD`. The following step additionally provides a reconstructed real particle energy which can be convenient. The final analysis of the spectra in Double Chooz is foreseen to be done in visible energy rather than reconstructed real energy. Nevertheless, the reconstruction of the real particle energies with `ERecoHD` can be used for cross-checks and quick analyses.

Reconstruction of the real particle energy In order to reconstruct the real particle energy from the visible energy ($PE_{corr.}$), ionization quenching (see section 3.2) and Cherenkov light production have to be included. The contribution from both effects leads to a nonlinearity in the light production. In order to quantify this effect, the Monte Carlo simulation has been used. It has been tuned with laboratory measurement results of the ionization quenching (see section 3.5) for electrons. Positrons are described with the same effective Birks parameter as for electrons in the simulation.

For each of the three particle types, simulations have been done for energies between 0.5 MeV and 10 MeV. Two fixed positions have been used: The Target center and a central position in the GC volume. For the fixed positions, the inhomogeneity does not affect the results. Thus, the number of photoelectrons after the detector simulation (PE_{true}) corresponds directly to the visible energy. As an example, the results of such a simulation series is shown for positrons in Figure A.1 in the Target center. In order to describe the ionization quenching and Cherenkov light effect, an effective function is

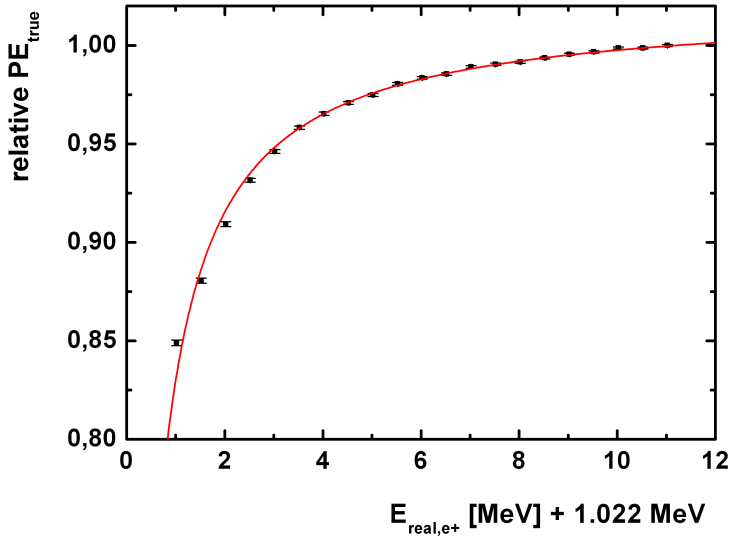

Figure A.2: Different representation of the simulation results in Figure A.1. The number of photoelectrons $\mathrm{PE}_{\mathrm{true}}$ has been divided by a linear function $\mathrm{PE}_{\mathrm{true}} = c \cdot E_{\mathrm{real}}$ with $c = \mathrm{PE}_{\mathrm{true}}(11.022\ \mathrm{MeV})/11.022\ \mathrm{MeV}$ which goes through the point at 11.022 MeV. This ratio is called relative $\mathrm{PE}_{\mathrm{true}}$.

used:

$$\mathrm{PE}_{true}(E_{real}) = \frac{a \cdot E_{real}^2}{1 + b \cdot E_{real}}. \tag{A.1}$$

The two free parameters a and b characterize the nonlinearity. Figure A.2 shows the same data and fit in another representation which shows the effect of quenching and Cherenkov light production more clearly.

The values a and b from the fit function can then be used in `ERecoHD` to transform the corrected number of photoelectrons to a real energy. For Target and GC the parameter pair $\{a,b\}$ is different in general since the ionization quenching effect is more pronounced in the GC (see section 3.4). From the reconstructed vertex it can be decided in which volume the event took place (with some uncertainty due to the vertex reconstruction resolution). Also for gammas and electrons such constants have been obtained by simulation analog to positrons. The shape of the function is particle dependent because the effect of ionization quenching and Cherenkov light differs. Gammas produce multiple electrons by Compton scattering which are each affected by the ionization quenching effect individually as described in section 3.2. Therefore the overall scintillation efficiency is decreased for gammas compared to electrons.

Positrons lose their kinetic energy in the scintillator and directly produce scintillation light. After that, the positron annihilates with an electron in the scintillator and pro-

duces two gammas which on their part create Compton electrons. This explains why also for positrons the total scintillation efficiency is different than for electrons in general. In ERecoHD, no assumptions are made on the particle type. Rather, multiple energies are given as output, one for each relevant particle type.

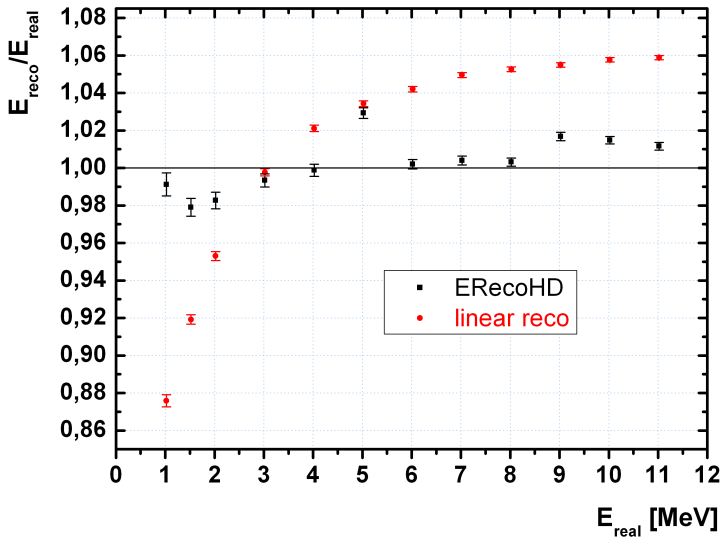

Figure A.3: Result of the energy reconstruction with ERecoHD for simulated positrons distributed in the Target. The real energy consists of the kinetic energy of the positron plus the 1.022 MeV from the two annihilation gammas. The reconstructed energy for positrons from ERecoHD is used to show the performance of the energy reconstruction. It is compared with a simple linear energy reconstruction. The value at E_{real}=5 MeV has been rechecked. The cause for the deviation has to be investigated.

Energy reconstruction performance test As a test for the energy reconstruction tool, MC samples have been produced containing positrons with multiple energies distributed homogeneously in the Target volume. With MC the real energy of the particle which was inserted can be compared with the reconstructed energy for positrons which is obtained after ERecoHD has been applied. Therefor the complete MC chain is run: DCGLG4sim, DCRoSS, DCRecoPulse, DCRecoBAMA and ERecoHD. In Figure A.3 the result is presented for positrons compared with a simple reconstruction which does not take into account the nonlinearity effects (a simple conversion factor between $\text{PE}_{\text{corr.}}$ and E_{real} obtained from 1 MeV electrons in the Target center is applied). For a range of 0.5 MeV to 10 MeV, which is the relevant range for the prompt events in the neutrino detection reaction in Double Chooz, and for a sample which is distributed homogeneously in the

Target volume, the energy reconstruction bias is typically as low as one or two percent. For gammas and electrons, the performance is even slightly better. The inhomogeneity correction is applied using a detector efficiency map which has been produced with electrons. It turns out that this is sufficient to correct the inhomogeneity to first order for positrons and gammas as well. Since only one map has to be produced the tool can be easily updated without consuming too much time.

Once detector calibration data is analyzed, the function in equation (A.1) can be checked and retuned to get a calibration of `ERecoHD` which can be applied for detector data. Other particles like for example alpha particles can be included in the future as well.

Conclusions and summary In this appendix the main features of the energy reconstruction tool `ERecoHD` were presented. It combines the correction for detector inhomogeneities with a correction for the ionization and Cherenkov light production nonlinearities. It has been tuned and tested with Monte Carlo simulations. However, it can be applied to detector data as well. Before that, it has to be re-tuned directly with detector data (spallation neutrons with subsequent capture on hydrogen can be studied with sufficient statistics). Alternatively, the MC software itself has to be tuned with detector data and then the parameters needed in `ERecoHD` can be derived from the tuned MC. Results on the detector efficiency inhomogeneity correction have been shown in section 6.4. For the reconstruction of the real particle energy it could be shown with MC that an energy reconstruction bias of the order of one to two percent over an energy range of 0.5 MeV to 10 MeV is achievable with a well-tuned `ERecoHD`.

B List of analysed runs

11000, 11001, 11007, 11008, 11009, 11010, 11011, 11013, 11014, 11016, 11017, 11018, 11019, 11152, 11153, 11154, 11155, 11164, 11165, 11167, 11168, 11169, 11170, 11171, 11181, 11182, 11183, 11192, 11193, 11210, 11219, 11220, 11221, 11222, 11231, 11232, 11233, 11234, 11243, 11244, 11245, 11246, 11255, 11256, 11477, 11478, 11479, 11480, 11489, 11490, 11491, 11492, 11504, 11505, 11506, 11507, 11516, 11517, 11518, 11519, 11520, 11521, 11545, 11546, 11547, 11548, 11549, 11558, 11559, 11560, 11561, 11570, 11571, 11572, 11573, 11574, 11583, 11584, 11585, 11586, 11587, 11596, 11597, 11598, 11599, 11608, 11609, 11610, 11611, 11634, 11635, 11636, 11637, 11638, 11639, 11648, 11650, 11651, 11652, 11661, 11662, 11663, 11664, 11673, 11674, 11675, 11676, 11700, 11701, 11702, 11703, 11704, 11713, 11714, 11715, 11716, 11725, 11727, 11728, 11729, 11739, 11740, 11741, 11742, 11751, 11752, 11753, 11754, 11775, 11776, 11777, 11778, 11787, 11788, 11789, 11790, 11799, 11800, 11801, 11802, 11814, 11815, 11816, 11817, 11826, 11827, 11828, 11829, 11830, 12046, 12047, 12048, 12057, 12058, 12059, 12060, 12069, 12070, 12071, 12072, 12073, 12074, 12083, 12084, 12085, 12086, 12107, 12108, 12109, 12110, 12119, 12121, 12122, 12131, 12132, 12133, 12134, 12143, 12144, 12145, 12146, 12155, 12156, 12157, 12158, 12179, 12180, 12181, 12182, 12191, 12192, 12193, 12194, 12203, 12204, 12205, 12206, 12215, 12216, 12217, 12218, 12227, 12228, 12229, 12230, 12239, 12240, 12241, 12242, 12263, 12264, 12265, 12266, 12275, 12276, 12277, 12278, 12287, 12288, 12289, 12290, 12299, 12300, 12302, 12303, 12304, 12313, 12314, 12315, 12316, 12325, 12326, 12327, 12328, 12349, 12350, 12351, 12352, 12361, 12362, 12363, 12364, 12373, 12374, 12375, 12376, 12377, 12387, 12388, 12389, 12398, 12399, 12400, 12402, 12423, 12424, 12425, 12426, 12435, 12436, 12437, 12438, 12447, 12448, 12449, 12450, 12459, 12460, 12461, 12462, 12471, 12472, 12473, 12690, 12691, 12692, 12693, 12703, 12704, 12705, 12714, 12715, 12716, 12717, 12726, 12727, 12728, 12729, 13120, 13122, 13143, 13144, 13145, 13146, 13155, 13157, 13158, 13167, 13168, 13169, 13170, 13179, 13180, 13181, 13182, 13191, 13192, 13193, 13194, 13203, 13204, 13205, 13206, 13207, 13228, 13229, 13230, 13240, 13241, 13242, 13243, 13244, 13253, 13254, 13255, 13256, 13265, 13266, 13267, 13268, 13289, 13290, 13291, 13292, 13301, 13302, 13303, 13304, 13313, 13314, 13315, 13316, 13326, 13327, 13328, 13329, 13338, 13339, 13340, 13341, 13362, 13363, 13364, 13365, 13374, 13375, 13376, 13378, 13379, 13388, 13389, 13390, 13391, 13392, 13401, 13402, 13403, 13404, 13413, 13414, 13415, 13416, 13425, 13426, 13427, 13428, 13449, 13450, 13451, 13452, 13461, 13462, 13463, 13464, 13473, 13474, 13475, 13476, 13485, 13486, 13487, 13488, 13497, 13498, 13499, 13500, 13501, 13527, 13528, 13529, 13531, 13534, 13535, 13536, 13537, 13538, 13547, 13548, 13549, 13550, 13559, 13560, 13561, 13562, 13571, 13572, 13573, 13574, 13598, 13599, 13600, 13601, 13610, 13611, 13612, 13613, 13622, 13624, 13625, 13635, 13636, 13638, 13647, 13648, 13650, 13659, 13660, 13661, 13662, 13686, 13689, 13690, 13691, 13700,

13701, 13702, 13703, 13712, 13714, 13724, 13725, 13727, 13926, 13927, 13928, 13929, 13930, 13939, 13941, 13953, 13954, 13955, 13956, 13966, 13967, 13968, 13969, 13979, 13980, 13981, 13982, 13983, 14004, 14005, 14006, 14007, 14015, 14016, 14017, 14018, 14027, 14028, 14029, 14039, 14040, 14042, 14043, 14044, 14053, 14054, 14055, 14056, 14057, 14066, 14067, 14068, 14069, 14082, 14083, 14084, 14085, 14094, 14095, 14096, 14106, 14108, 14118, 14119, 14120, 14121, 14142, 14143, 14144, 14145, 14154, 14156, 14157, 14158, 14159, 14160, 14161, 14170, 14171, 14172, 14173, 14174, 14175, 14184, 14185, 14186, 14187, 14188, 14197, 14198, 14199, 14200, 14201, 14202, 14223, 14224, 14225, 14226, 14235, 14236, 14237, 14238, 14251, 14252, 14253, 14254, 14255, 14264, 14265, 14266, 14267, 14268, 14277, 14278, 14279, 14280, 14281, 14282, 14303, 14304, 14305, 14306, 14307, 14316, 14317, 14318, 14319, 14320, 14321, 14331, 14332, 14333, 14342, 14343, 14344, 14345, 14354, 14355, 14356, 14357, 14366, 14367, 14368, 14369, 14370, 14391, 14392, 14393, 14394, 14395, 14404, 14405, 14406, 14407, 14415, 14417, 14418, 14427, 14428, 14429, 14430, 14439, 14440, 14453, 14454, 14455, 14465, 14466, 14467, 14468, 14477, 14478, 14479, 14480, 14489, 14490, 14492, 14502, 14503, 14504, 14505, 14694, 14695, 14696, 14697, 14706, 14707, 14708, 14709, 14718, 14719, 14720, 14721, 14730, 14731, 14732, 14733, 14742, 14743, 14744, 14745, 14746, 14767, 14768, 14769, 14770, 14779, 14780, 14781, 14782, 14804, 14805, 14806, 14815, 14816, 14817, 14818, 14819, 14820, 14821, 14842, 14843, 14844, 14845, 14854, 14855, 14856, 14857, 14858, 14859, 14869, 14870, 14871, 14872, 14873, 14882, 14883, 14884, 14885, 14895, 14896, 14897, 14898, 14899, 14900, 14901, 14922, 14923, 14924, 14925, 14934, 14935, 14936, 14937, 14938, 14939, 14948, 14949, 14950, 14951, 14960, 14961, 14962, 14963, 14972, 14973, 14974, 14975, 14984, 14985, 14999, 15000, 15001, 15002, 15011, 15012, 15013, 15014, 15023, 15024, 15025, 15026, 15035, 15036, 15037, 15038, 15047, 15048, 15049, 15051, 15052, 15066, 15067, 15068, 15069, 15070, 15079, 15080, 15081, 15082, 15091, 15092, 15093, 15094, 15103, 15104, 15105, 15106, 15115, 15116, 15117, 15317, 15318, 15319, 15320, 15329, 15330, 15331, 15332, 15341, 15342, 15343, 15344, 15353, 15354, 15355, 15356, 15357, 15379, 15380, 15381, 15382, 15391, 15392, 15393, 15394, 15395, 15404, 15405, 15406, 15407, 15408, 15409, 15418, 15419, 15420, 15421, 15430, 15431, 15432, 15433, 15434, 15443, 15444, 15445, 15446, 15455, 15456, 15457, 15471, 15472, 15473, 15482, 15483, 15484, 15485, 15494, 15495, 15496, 15497, 15506, 15507, 15508, 15509, 15519, 15520, 15522, 15523, 15532, 15533, 15546, 15547, 15548, 15557, 15558, 15559, 15560, 15569, 15570, 15571, 15572, 15581, 15582, 15583, 15584, 15605, 15606, 15607, 15608, 15617, 15618, 15619, 15620, 15629, 15630, 15631, 15632, 15641, 15642, 15643, 15644, 15653, 15654, 15655, 15656, 15665, 15666, 15667, 15668, 15669, 15670, 15691, 15692, 15693, 15694, 15703, 15704, 15705, 15706, 15715, 15716, 15717, 15718, 15719, 15720, 15729, 15730, 15731, 15732, 15733, 15742, 15743, 15744, 15745, 15746, 15767, 15768, 15770, 15779, 15780, 15781, 15782, 15791, 15792, 15793, 15794, 15803, 15804, 15805, 15806, 15815, 15816, 15818, 15820, 15924, 15925, 15926, 15927, 15936, 15937, 15938, 15939, 15948, 15949, 15950, 15951, 15960, 15961, 15962, 15963, 16072, 16073, 16074, 16075, 16084, 16085, 16086, 16087, 16096, 16097, 16098, 16099, 16108, 16109, 16110, 16111, 16112, 16121, 16122, 16123, 16124, 16133, 16134, 16135, 16136, 16137, 16138, 16159, 16160, 16161, 16162, 16163, 16164, 16173, 16174, 16175, 16176, 16185, 16194, 16195, 16196, 16197, 16206, 16207, 16208, 16209, 16224, 16225,

16226, 16235, 16236, 16237, 16238, 16239, 16248, 16249, 16250, 16260, 16262, 16263, 16264, 16275, 16276, 16277, 16279, 16300, 16301, 16303, 16304, 16313, 16314, 16316, 16325, 16326, 16328, 16338, 16339, 16340, 16349, 16350, 16351, 16352, 16374, 16375, 16376, 16377, 16387, 16388, 16389, 16390, 16391, 16400, 16402, 16403, 16412, 16413, 16414, 16415, 16416, 16425, 16426, 16427, 16428, 16450, 16451, 16452, 16453, 16454, 16463, 16464, 16465, 16466, 16467, 16468, 16477, 16478, 16479, 16480, 16489, 16490, 16491, 16492, 16595, 16597, 16598, 16607, 16608, 16609, 16610, 16611, 16620, 16621, 16622, 16623, 16632, 16633, 16634, 16635, 16752, 16753, 16754, 16755, 16764, 16765, 16766, 16767, 16776, 16777, 16778, 16779, 16788, 16789, 16790, 16791, 16800, 16801, 16802, 16803, 16804, 16814, 16815, 16816, 16817, 16818, 16840, 16841, 16842, 16843, 16852, 16853, 16854, 16855, 16864, 16865, 16866, 16867, 16876, 16877, 16878, 16879, 16880, 16881, 16882, 16883, 16884, 16893, 16894, 16895, 16896, 16905, 16918, 16919, 16920, 16921, 16930, 16931, 16932, 16933, 16956, 16957, 17005, 17054, 17067, 17068, 17069, 17078, 17079, 17080, 17081, 17090, 17091, 17092, 17093, 17102, 17103, 17104, 17105, 17114, 17115, 17116, 17117, 17159, 17161, 17162, 17171, 17172, 17173, 17174, 17183, 17184, 17185, 17186, 17195, 17196, 17197, 17198, 17207, 17208, 17209, 17210, 17219, 17221, 17222, 17231, 17232, 17234, 17243, 17244, 17245, 17246, 17255, 17256, 17257, 17258, 17267, 17268, 17269, 17270, 17280, 17281, 17283, 17284, 17294, 17328, 17378, 17390, 17427, 17439, 17440, 17464, 17500, 17501, 17502, 17503, 17512, 17513, 17524, 17536, 17537, 17538, 17550, 17552, 17574, 17576, 17587, 17589, 17602, 17611, 17612, 17613, 17614, 17624, 17625, 17626, 17627, 17637, 17650, 17651, 17652, 17653, 17662, 17663, 17664, 17665, 17674, 17675, 17676, 17677, 17687, 17688, 17689, 17690, 17718, 17719, 17720, 17721, 17812, 17813, 17814, 17815, 17825, 17826, 17827, 17829, 17838, 17839, 17840, 17841, 17850, 17851, 17852, 17853, 17971, 17985, 17995, 17997, 18006, 18007, 18008, 18009, 18018, 18019, 18020, 18021, 18051, 18053, 18054, 18056, 18065, 18066, 18067, 18068, 18077, 18078, 18195, 18196, 18197, 18198, 18207, 18208, 18209, 18210, 18219, 18220, 18221, 18222, 18231, 18232, 18233, 18234, 18235, 18338, 18339, 18340, 18341, 18342, 18351, 18352, 18353, 18354, 18355, 18364, 18365, 18366, 18367, 18376, 18377, 18378, 18379, 18388, 18389, 18390, 18391, 18412, 18413, 18414, 18415, 18424, 18425, 18426, 18427, 18428, 18437, 18438, 18439, 18440, 18441, 18450, 18451, 18452, 18453, 18462, 18463, 18464, 18465, 18486, 18487, 18488, 18599, 18600, 18610, 18611, 18612, 18728, 18729, 18730, 18739, 18740, 18741, 18742, 18751, 18752, 18753, 18754, 18763, 18764, 18765, 18766, 18787, 18788, 18789, 18790, 18799, 18800, 18801, 18802, 18811, 18812, 18813, 18814, 18815, 18824, 18825, 18826, 18827, 18836, 18837, 18838, 18839, 18840, 18841, 18842, 18863, 18864, 18865, 18866, 18875, 18876, 18877, 18878, 18879, 18888, 18889, 18890, 18891, 18900, 18901, 18902, 18904, 18913, 18914, 18915, 18916, 18925, 18927, 18928, 18949, 18950, 18951, 18952, 18961, 18962, 18963, 18964, 18973, 18974, 18975, 18976, 18985, 18986, 18987, 18988, 18997, 18998, 18999, 19000, 19244, 19245, 19246, 19247, 19256, 19257, 19258, 19259, 19268, 19269, 19270, 19271, 19280, 19281, 19282, 19283, 19293, 19295, 19296, 19413, 19414, 19415, 19416, 19425, 19426, 19427, 19428, 19437, 19438, 19439, 19440, 19441, 19450, 19451, 19452, 19453, 19474, 19475, 19476, 19477, 19486, 19487, 19488, 19489, 19498, 19499, 19500, 19501, 19510, 19511, 19512, 19513, 19522, 19523, 19524, 19525, 19534, 19535, 19536, 19537, 19558, 19559, 19560, 19561, 19570, 19571, 19572, 19573, 19582, 19583,

19584, 19585, 19594, 19595, 19596, 19597, 19606, 19607, 19608, 19609, 19704, 19705, 19706, 19707, 19716, 19717, 19718, 19719, 19728, 19729, 19730, 19731, 19740, 19741, 19742, 19743, 19752, 19753, 19755, 19756, 19777, 19778, 19779, 19780, 19789, 19790, 19791, 19792, 19801, 19802, 19803, 19804, 19813, 19814, 19815, 19816, 19817, 19826, 19827, 19828, 19829, 19851, 19852, 19855, 19864, 19865, 19867, 19868, 19869, 19878, 19879, 19880, 19881, 19890, 19891, 19892, 19893, 19894, 19903, 19904, 19905, 19906, 20010, 20011, 20012, 20013, 20023, 20024, 20025, 20026, 20027, 20028, 20037, 20038, 20039, 20040, 20041, 20050, 20051, 20052, 20053, 20170, 20171, 20172, 20173, 20182, 20183, 20184, 20185, 20194, 20195, 20196, 20197, 20206, 20207, 20208, 20209, 20218, 20219, 20220, 20221, 20242, 20243, 20244, 20254, 20255, 20256, 20257, 20267, 20268, 20269, 20278, 20279, 20280, 20281, 20282, 20283, 20292, 20293, 20294, 20295, 20316, 20317, 20318, 20327, 20328, 20329, 20330, 20339, 20340, 20341, 20342, 20343, 20352, 20353, 20354, 20355, 20364, 20365, 20366, 20367, 20389, 20390, 20391, 20392, 20402, 20403, 20404, 20405, 20414, 20415, 20416, 20417, 20427, 20428, 20429, 20438, 20439, 20441, 20442, 20463, 20464, 20465, 20466, 20475, 20476, 20477, 20478, 20487, 20488, 20489, 20490, 20499, 20500, 20501, 20502, 20511, 20512, 20513, 20514, 20523, 20524, 20525, 20526, 20527, 20548, 20549, 20550, 20551, 20560, 20561, 20562, 20563, 20572, 20573, 20574, 20575, 20584, 20585, 20586, 20587, 20588, 20597, 20598, 20599, 20600, 20621, 20622, 20623, 20624, 20633, 20634, 20635, 20636, 20645, 20646, 20647, 20648, 20649, 20658, 20659, 20660, 20661, 20670, 20671, 20672, 20673, 20694, 20695, 20696, 20697, 20706, 20708, 20709, 20710, 20719, 20720, 20721, 20722, 20723, 20732, 20733, 20734, 20735, 20744, 20745, 20746, 20747, 20768, 20769, 20770, 20771, 20780, 20781, 20782, 20783, 20792, 20793, 20794, 20795, 20804, 20805, 20806, 20807, 20816, 20817, 20818, 20819, 20828, 20829, 20832, 20891, 20892, 20893, 20894, 20903, 20904, 20906, 20909, 20910, 20911, 20912, 20933, 20934, 20935, 20936, 20945, 20946, 20947, 20948, 20957, 20958, 20959, 20960, 20969, 20970, 20971, 20972, 20973, 20982, 20983, 20984, 20985, 20994, 20995, 20996, 20997, 20998, 20999, 21000, 21001, 21014, 21015, 21016, 21017, 21026, 21027, 21028, 21029, 21030, 21039, 21040, 21041, 21042, 21043, 21052, 21053, 21055, 21057, 21058, 21079, 21080, 21133, 21134, 21135, 21136, 21137, 21138, 21147, 21149, 21150, 21151, 21160, 21161, 21162, 21163, 21164, 21255, 21256, 21257, 21258, 21267, 21268, 21269, 21270, 21279, 21280, 21281, 21282, 21291, 21293, 21294, 21303, 21304, 21305, 21306, 21307, 21316, 21317, 21318, 21319, 21328, 21329, 21330, 21331, 21335, 21336, 21337, 21338, 21347, 21348, 21349, 21350, 21359, 21360, 21361, 21362, 21363, 21364, 21483, 21484, 21485, 21486, 21487, 21496, 21497, 21498, 21499, 21508, 21509, 21510, 21511, 21520, 21521, 21522, 21534, 21535, 21537, 21568, 21569

List of Figures

1.1 Survival probability for electron antineutrinos. 5
1.2 Global θ_{13} analysis results from [14]. 7
1.3 The Double Chooz experiment site. 8
1.4 Shape of the observed neutrino spectrum from [27]. 9
1.5 Double Chooz sensitivity on $\sin^2(2\theta_{13})$. 10
1.6 Cross section through the Double Chooz detector. 11
1.7 Preliminary energy spectrum of events after a muon. 14
1.8 Simulated wavelength shifting in the Double Chooz scintillators. 20
1.9 Extinction and emission spectra of Double Chooz scintillator components. 21
1.10 Attenuation length spectrum of the Double Chooz far detector Target scintillator. 24

2.1 Compton Backscatter Peak setup for the LY measurements. 27
2.2 Logic of the electronics for the Compton Backscatter Peak setup. 28
2.3 Liquid scintillator and NaI crystal pulses. 30
2.4 Compton backscatter peak charge spectrum. 31
2.5 Scheme of considered energy transfer paths in the light yield model. . . . 32
2.6 Variation of PPO and $Gd(thd)_3$ in simple liquid scintillators. 34
2.7 Variation of the PXE/dodecane ratio and Gamma Catcher matching. . . 35
2.8 Light yield fine tuning with the PXE concentration in the Gamma Catcher. 39
2.9 Light yield with varying PXE/dodecane ratio and Gamma Catcher matching. 40
2.10 Q_{max}/Q_{tot} distribution before and after additional cuts. 44
2.11 T_{rise} distribution for a hydrogen capture peak detector data analysis. . . 46
2.12 Combined T_{rise} vs. Q_{max}/Q_{tot} distribution for a hydrogen capture peak detector data analysis. 47
2.13 Combined RMS_{Tstart} vs. Q_{max}/Q_{tot} distribution for a hydrogen capture peak detector data analysis. 48
2.14 Background subtraction for a hydrogen capture peak detector data analysis. 49
2.15 Neutron multiplicity cut effect in a hydrogen capture peak detector data analysis. 50
2.16 Vertex distributions for hydrogen capture events after muons. 51
2.17 Two-dimensional vertex distributions for hydrogen capture events after muons. 52
2.18 Hydrogen capture peaks in Target and GC with detector data. 53

2.19 Stability of the mean charge of the hydrogen capture peak for the GC (detector data). 55
2.20 Stability of the mean charge of the hydrogen capture peak for the Target (detector data). 56
2.21 Stability of the width of the hydrogen capture peak for Target and GC (detector data). 57

3.1 Specific energy loss for electrons passing through the Target scintillator. . 60
3.2 Setup for the measurement of the scintillation efficiency for low energy electrons. 61
3.3 Electronics scheme for the measurement of the scintillation efficiency for low energy electrons. 62
3.4 Scatter plot of electron energy versus scintillation light. 64
3.5 Typical measured light output distribution at a fixed electron energy. . . 65
3.6 Light output $L(E)$ for low energy electrons in the Target scintillator. . . 66
3.7 Non-proportionality of the light output $L(E)$ for low energy electrons in the Target scintillator. 67
3.8 Light output $L(E)$ for low energy electrons in the GC scintillator. 68
3.9 Non-proportionality of the light output $L(E)$ for low energy electrons in the GC scintillator. 69
3.10 Comparison of Berger-Seltzer equation with tabulated values of dE/dx calculated by `Geant4`. 72
3.11 $\chi^2(kB)$ of the Monte Carlo fit to low energy electron data for the Target. 74
3.12 Best fit of Monte Carlo light production to low energy electron data for the Target. 75
3.13 Difference in calculation of visible energy with one or two Monte Carlo simulation steps. 78
3.14 Effect on the relative light yield at the transition between one simulation step and two simulation steps. 79
3.15 Comparison of the visible energy for different secondary particle production threshold settings. 80
3.16 Difference between the MC visible energy for the default settings and a small step size setting. 81
3.17 Monte Carlo electron energy scale prediction from 0.1 MeV to 10 MeV for default settings and small step settings. 82
3.18 MC fits of the light yield function for GC and Veto. 83

4.1 Specific energy loss for alpha particles passing through the Target scintillator. 86
4.2 The main branch of the ^{226}Ra decay series. 88
4.3 Setup to extract ^{222}Rn from Uranium salt and flush it through PPO powder. 90
4.4 Setup to extract ^{222}Rn and flush it through scintillator samples. 91
4.5 Typical light yield spectra for alpha excitation. 92

4.6 Side view of the simulated vertex distributions of coincidence events in the Compton Backscatter Peak geometry. 93
4.7 Front view of the simulated vertex distributions of coincidence events in the Compton Backscatter Peak geometry. 94
4.8 Simulated energy distribution of the scattered electrons in the Compton backscatter peak geometry. 96
4.9 Experimental results for the alpha quenching measurements in the Target. 97
4.10 Experimental results for the alpha quenching measurements in the GC with 2 g/l PPO. 98
4.11 Experimental results for the alpha quenching measurements in the Veto. 99
4.12 Combined Monte Carlo fit for electron and alphas to the laboratory measurement data for the Target scintillator. 103
4.13 Combined Monte Carlo fit for electron and alphas to the laboratory measurement data for the GC scintillator. 104

5.1 Setup for the measurement of scintillator emission time probability density functions. 111
5.2 Scheme for the electronics of the time profile measurement setup. 112
5.3 Improved setup for the extraction of ^{222}Rn isotopes and flushing through scintillator samples. 113
5.4 Illustration of a possible bias in the measurement of the scintillator photon emission time PDFs. 114
5.5 Signals from start- and stop-PMT for the measurement of the photon emission time PDFs. 116
5.6 Quality cuts on the charge of the pulses for the photon emission time PDF measurement. 118
5.7 Typical measured spectrum of the scintillator photon emission time PDF. 119
5.8 Shape of an asymmetric time resolution function. 120
5.9 Experimental photon emission time PDFs for electrons in Target and GC. 122
5.10 Comparison of the photon emission time PDF with three different solvents. 123
5.11 Comparison of the photon emission time PDF of three Gamma Catcher candidates. 123
5.12 Charge spectrum for the time profile measurement with alpha particle excitation. 126
5.13 Experimental photon emission time PDFs for alphas in Target and GC. . 127
5.14 Photon emission time PDF fit functions for alpha and beta excitation in Target and GC. 127
5.15 Photon emission time PDFs for alpha and beta excitation in Target and GC. 128

6.1 Difference in the attenuation of a PXE, dodecane and Gd(thd)$_3$ mixture after about 3 years in a small sample. 133
6.2 Simulated number of PEs for different Target attenuation lengths. 134
6.3 Simulated detector homogeneity for different Target attenuation lengths. 135

6.4 Visualization of two reference volumes for the calculation of the spread in the detector light collection efficiency. 136
6.5 Difference in photon collection efficiency between two reference volumes. 137
6.6 Simulated PE_{reco} spectra of prompt and delayed events in a neutrino sample. 138
6.7 Simulated reconstructed prompt and delayed energy spectra. 139
6.8 Simulated neutrino selection efficiency variation at different Target attenuation lengths. 140
6.9 Simulated neutrino selection efficiency variation at different Target attenuation lengths with recalibration. 141
6.10 Simulated reconstructed prompt and delayed energy spectra after recalibration. 142
6.11 Simulated relative detector efficiency at different locations in the Double Chooz detector. 144
6.12 Simulated reconstructed photoelectron spectrum. 145
6.13 Photoelectron spectra uncorrected and corrected for the detector inhomogeneities (simulation). 147

A.1 Simulated number of photoelectrons (PE_{true}) dependent on positron energy. 152
A.2 Simulated relative number of photoelectrons (PE_{true}) dependent on positron energy. 153
A.3 Result of the energy reconstruction with `ERecoHD` for simulated positrons distributed in the Target. 154

List of Tables

1.1 Neutrino oscillation parameters. 4
1.2 Components and concentrations of the Double Chooz far detector liquid scintillators. 23
1.3 Selected properties of the Target and GC scintillators. 25

2.1 Energy transfer rate parameter values obtained by LY measurements. . . 36
2.2 Mean charge for hydrogen capture peaks in different volumes (detector data). 54

3.1 Results for the Birks parameter for different scintillators using numerical integration of Birks' equation. 70
3.2 Results for the Birks parameter for different `Geant4` parameter settings. . 76
3.3 Results for the Monte Carlo effective Birks parameters kB for the Double Chooz scintillators. 83

4.1 Alpha emitting isotopes and alpha energies used in the laboratory measurements. 89
4.2 Photon attenuation lengths in a NaI crystal. 94
4.3 Mean simulated energies of backscattered electrons in the Compton backscatter peak geometry. 95
4.4 Alpha quenching factors for various scintillators. 100
4.5 Results for the best fit Birks parameter kB from Monte Carlo tuning for alpha particles. 104

5.1 Fit parameters for the photon emission time PDF fit function. 121
5.2 Results for the exponential time constants and weights in scintillator photon emission. 125

6.1 Relative energy resolution for simulated 1 MeV electrons with different detector inhomogeneity corrections. 146

Bibliography

[1] B. Pontecorvo: Soviet Physics JETP 6 (1957) 429.

[2] V.A. Kuzmin, V.A. Rubakov, M.E. Shaposhnikov: Phys. Lett. B 155 (1985) 36.

[3] M. Fukugita, T. Yanagida: Phys. Lett. B 174 (1986) 45.

[4] F. Reines, C.L. Cowan: Nature 178 (1956) 446.

[5] F. Reines, C.L. Cowan: Science 124 (1956) 103.

[6] G. Danby, J.-M. Gaillard, K. Goulianos, L.M. Lederman, N. Mistry, M. Schwartz, J. Steinberger: Phys. Rev. Lett. 9 (1962) 36.

[7] DONUT collaboration: Phys. Lett. B 504 (2001) 218.

[8] Z. Maki, M. Nakagawa, S. Sakata, Prog. Theor. Phys. 28 (1962) 870.

[9] S. Bilenky, B. Pontecorvo: Lettere Al Nuovo Cimento 17 (1976) 569.

[10] V. Gribov, B. Pontecorvo: Phys. Lett. B 28 (1969) 493.

[11] K. Nakamura et al. (Particle Data Group), J. Phys. G 37 (2010) 075021.

[12] L. Wolfenstein: Phys. Rev. D 17 (1978) 2369.

[13] S.P. Mikheyev, A.Y. Smirnov: Prog. Part. Nucl. Phys. 23 (1989) 41.

[14] T. Schwetz, M. Tórtola, J.W.F. Valle: arXiv:1108.1376 [hep-ph] (2011).

[15] T. Schwetz, M. Tórtola, J.W.F. Valle: arXiv:1103.0734v2 [hep-ph] (2011).

[16] S. Abe et al. (KamLAND collaboration): Phys. Rev. Lett. 100 (2008) 221803.

[17] Double Chooz collaboration: arXiv:0606025 [hep-ex] (2006).

[18] RENO collaboration: arXiv:1003.1391 [hep-ex] (2010).

[19] Daya Bay collaboration: arXiv:0701029 [hep-ex] (2007).

[20] P. Huber, M. Lindner, T. Schwetz, W. Winter: Nuclear Physics B 665 (2003) 487.

[21] International Scoping Study of a Future Neutrino Factory and Superbeam Facility (ISS): *Physics at a future Neutrino Factory and super-beam facility* arXiv:0710.4947v2 [hep-ph] (2007).

[22] ISS Accelerator Working Group: *Accelerator design concept for future neutrino facilities*, arXiv:0802.4023v2 [physics.acc-ph] (2008).

[23] ISS: *Detectors and flux instrumentation for future neutrino facilities*, arXiv:0712.4129v1 [physics.ins-det] (2007).

[24] K. Abe et al. (T2K collaboration): Phys. Rev. Lett. 107 (2011) 041801.

[25] P. Adamson et al. (MINOS collaboration): arXiv:1108.0015v1 [hep-ex] (2011).

[26] S. Yamamoto et al. (K2K collaboration), Phys. Rev. Lett. 96 (2006) 181801.

[27] T.A. Mueller, D. Lhuillier, M. Fallot, A. Letourneau, S. Cormon, M. Fechner, L. Giot, T. Lasserre, J. Martino, G. Mention, A. Porta, and F. Yermia: Phys. Rev. C 83 (2011) 054615.

[28] G. Mention, M. Fechner, T. Lasserre, T.A. Mueller, D. Lhuillier, M. Cribier, A. Letourneau: arXiv:1101.2755 [hep-ex] (2011).

[29] A.A. Hahn, K. Schreckenbach, W. Gelletly, F. von Feilitzsch, G. Colvin, B. Kruschea: Phys. Lett. B 218 (1989) 365.

[30] M. Apollonio et al. (CHOOZ collaboration): Phys. Lett. B 466 (1999) 415.

[31] M. Apollonio et al. (CHOOZ collaboration): Eur. Phys. J. C 27 (2003) 331.

[32] Palo Verde collaboration: Phys. Rev. D 64 (2001) 112001.

[33] Double Chooz collaboration: arXiv:0405032 [hep-ex] (2004).

[34] C. Buck, F.X. Hartmann, D. Motta, S. Schönert, U. Schwan: *Metal beta-diketone scintillators*, Workshop on Future Low Energy Neutrino Experiments, Technische Universität München (2003).

[35] F.X. Hartmann: *Double Chooz and the Search for Short Range Electron-Antineutrino Oscillations*, Proceedings of the Carolina International Symposium on Neutrino Physics, J. Phys. Conf. Ser. 173 (2009) 012023.

[36] C. Buck, F.X. Hartmann, S. Schönert, U. Schwan: *Development of an optically pure Gd-beta-diketonate for the liquid scintillator of anti-neutrino detectors*, article in preparation for Journal of Radioanalytical and Nuclear Chemistry.

[37] N. Schmitz: Neutrinophysik, Teubner, Wiesbaden (1997).

[38] G. Mention: Ph.D. Thesis, APC-Collège de France, Paris, 2005.

[39] P. Pfahler for the Double Chooz collaboration: *Search for the mixing angle θ_{13} with the reactor disappearance experiment Double Chooz*, TAUP conference, München (2011).

[40] C. Bauer, E. Borger, R. Hofacker, K. Jänner, F. Kaether, C. Langbrandtner, M. Lindner, S. Lucht, M. Reissfelder, S. Schönert, A. Stüken, C. Wiebusch: JINST 6 (2011) P06008.

[41] T. Matsubara et al.: arXiv:1104.0786v1 [physics.ins-det] (2011).

[42] K. Zbiri: Nucl. Instrum. Meth. A 597 (2008) 219.

[43] E. Browne, J.M. Daikiri, R.E. Doebler: Table of Isotopes, Wiley, New York (1978).

[44] S. Abe et al. (KamLAND collaboration): arXiv:0907.0066 [hep-ex] (2010).

[45] C. Langbrandtner, Ph.D. Thesis, Ruprecht-Karls-Universität Heidelberg, 2011.

[46] F. Suekane: Double Chooz internal document 2835-v3 (2011).

[47] S. Agostinelli et al. (Geant4 collaboration): Nucl. Instrum. Meth. A 506 (2003) 250.

[48] I.B. Berlman, Handbook of Fluorescence Spectra of Aromatic Molecules, Academic Press, New York, 1971.

[49] C. Aberle, C. Buck, B. Gramlich, F.X. Hartmann, M. Lindner, S. Schönert, U. Schwan, S. Wagner, H. Watanabe, *Large scale liquid scintillator production for antineutrino detection*, to be published in JINST.

[50] J.B. Birks: The Theory and Practice of Scintillation Counting, Pergamon Press, Oxford (1964).

[51] T. Förster, Annalen der Physik 2 (1948) 55.

[52] T. Förster, Discuss. Faraday Soc. 27 (1959) 7.

[53] A.G. Piepke, S.W. Moser, V.M. Novikov: Nucl. Instrum. Meth. A 432 (1999) 392.

[54] F.X. Hartmann, R.A. Naumann: Nucl. Instrum. Meth. A 313 (1992) 237.

[55] C. Aberle: Diploma Thesis, Ruprecht-Karls-Universität Heidelberg, 2008.

[56] C. Aberle, C. Buck, F.X. Hartmann, S. Schönert: *Light yield and energy transfer in a new Gd-loaded liquid scintillator*, submitted to Chem. Phys. Lett. (2011).

[57] C. Buck, Ph.D. Thesis, Ruprecht-Karls-Universität Heidelberg, 2004.

[58] C. Buck, F.X. Hartmann, D. Motta, S. Schönert: Chem. Phys. Lett. 435 (2007) 252.

[59] H. Kallmann, M. Furst, Phys. Rev. 79 (1950) 857.

[60] D.L. Dexter, Journal of Chem. Lett. 21 (1952) 836.

[61] O. Stern, M. Volmer, Physikalische Zeitschrift 20 (1919) 183.

[62] BC-505 Liquid Scintillator Product Data Sheet, `http://www.detectors.saint-gobain.com/uploadedFiles/SGdetectors/Documents/Product_Data_Sheets/BC505-Data-Sheet.pdf`, Saint-Gobain Ceramics and Plastics, Inc., accessed August 2011.

[63] G.F. Knoll: Radiation Detection and Measurement, second edition, John Wiley and sons, New York (1989).

[64] I. Holl, E. Lorenz, G. Mageras: IEEE Trans. Nucl. Sci. 35 (1988) 105.

[65] I.H. Campbell, B.K. Crone, Applied Physics Letters 90 (2007) 012117.

[66] R. Tayloe, H.O. Meyer, D.C. Cox, J. Doskow, A. Ferguson, T. Katori, M. Novak, D. Passmore: Nucl. Instrum. Meth. A 562 (2006) 198.

[67] M. Gierlik, M. Moszynski, A. Nassalski, A. Syntfeld-Kazuch, T. Szczesniak, L. Swiderski: IEEE Trans. Nucl. Sci. 35 (2007) 1367.

[68] M. Moszynski, M. Kapusta, M. Mayhugh, D. Wolski, S.O. Flyckt: IEEE Trans. Nucl. Sci. 44 (1997) 1052.

[69] Y.-F. Wang, V. Balic, G. Gratta, A. Fassò, S. Roesler, A. Ferrari: Phys. Rev. D 64 (2001) 013012.

[70] M. Fechner: Double Chooz internal document 2845-v1 (2011).

[71] A. Stüken: Double Chooz EU++ internal document (2011).

[72] C. Palomares: Double Chooz internal document 2815-v1 (2011).

[73] A. Cabrera, A. Remoto: Double Chooz internal document 2244-v1 (2011).

[74] P. Novella, C. Palomares, A. Cabrera: Double Chooz internal document 649-v2 (2009).

[75] A. Collin, A. Cucoanes, M. Fechner, D. Lhuillier: Double Chooz internal document 2398-v1 (2011).

[76] S. Wagner: private communication (2011).

[77] N. Rupp: Bachelor Thesis, Ruprecht-Karls-Universität Heidelberg, 2011.

[78] A. Cabrera, M. Ishitsuka, T. Konno, P. Novella, K. Terao: Double Chooz internal document 2507-v1 (2011).

[79] C. Aberle, B. Reinhold: Double Chooz internal document 2566-v1 (2011).

[80] I. Stancu, Y. Sun: Double Chooz internal document 2573-v1 (2011).

[81] I. Stancu: Double Chooz internal document 2245-v1 (2011).

[82] I. Stancu: Double Chooz internal document 2898-v1 (2011).

[83] Y. Abe, M. Ishitsuka: Double Chooz internal document 2726-v2 (2011).

[84] M. Ishitsuka: Double Chooz internal document 2547-v1 (2011).

[85] J. Dawson, D. Kryn: Double Chooz internal document 2545-v1 (2011).

[86] D. Franco: Double Chooz internal document 2550-v2 (2011).

[87] P. Novella: Double Chooz internal document 2867-v2 (2011).

[88] J.B. Birks: Proc. Phys. Soc. A 64 (1951) 874.

[89] S.M. Seltzer and M.J. Berger, Int. J. Appl. Radiat. Isot. 33 (1982) 1189.

[90] International Commission on Radiation Units and Measurements: *Stopping powers for electrons and positrons*, ICRU Report 37, Bethesda, 1984.

[91] R.M. Sternheimer, R.F. Peierls: Phys. Rev. B 3 (1971) 3681.

[92] M.-N. Peron and P. Cassette: Bulletin du Bureau National de Metrologie 105 (1996) 34.

[93] J.B. Birks, F.A. Black: Proc. Phys. Soc. A 64 (1951) 511.

[94] M. Furst, H. Kallman: Physical Review 85 (1952) 816.

[95] G.T. Wright: Phys. Rev. 91 (1953) 1282.

[96] H. Kallmann, G.J. Brucker: Physical Review 108 (1957) 1122.

[97] S. Wagner: Diploma Thesis, Ruprecht-Karls-Universität Heidelberg, 2010.

[98] C. Aberle, C. Buck, F.X. Hartmann, S. Schönert, S. Wagner: *Light output for Double Chooz scintillators for low energy electrons*, submitted to JINST (August 2011).

[99] J. Haser: Diploma Thesis, Ruprecht-Karls-Universität Heidelberg, 2010.

[100] C. Adlof et al. (CALICE collaboration): JINST 5 (2010) 05004.

[101] A. Tadday, C. Aberle, E. Garutti, V. Morgunov, A. Kaplan, R. Stamen, S. Wagner and H.-C. Schultz-Coulon: *A measurement of Birks' coefficient for the polystyrene based AHCAL scintillator and its impact on the energy scale of particle shower simulations*, submitted to Nucl. Instrum. Meth. A.

[102] R. Voltz and G. Laustriat: Journal de Physique 29 (1968) 159.

[103] G. Alimonti et al. (BOREXINO collaboration): Nucl. Instrum. Meth. A 600 (2009) 568.

[104] W. Maneschg: Ph.D. Thesis, Ruprecht-Karls-Universität Heidelberg, 2011.

[105] Geant4 Physics Reference Manual, version 9.4 (2010), `http://geant4.web.cern.ch/geant4/UserDocumentation/UsersGuides/PhysicsReferenceManual/fo/PhysicsReferenceManual.pdf`, accessed August 2011.

[106] International Commission on Radiation Units and Measurements: *Stopping Powers and Ranges for Protons and Alpha Particles*, ICRU Report 49, Bethesda, 1984.

[107] H. Bethe: Annalen der Physik 397 (1930) 325.

[108] S.P. Ahlen, Rev. Mod. Phys. 52 (1980) 121.

[109] H. Simgen: private communication (2010).

[110] J. von Neumann: Various techniques used in connection with random digits, Nat. Bureau Standards Appl. Math. Series 12 (1951) 36.

[111] S. Brandt: Datenanalyse, Spektrum Akademischer Verlag GmbH Heidelberg, Berlin, 1999.

[112] E. Storm, H.I. Israel: Nuclear Data Tables A7 (1970) 565.

[113] M.J. Berger, J.H. Hubbell, S.M. Seltzer, J. Chang, J.S. Coursey, R. Sukumar, D.S. Zucker, K. Olsen: XCOM Photon Cross Section Database (version 1.5), http://physics.nist.gov/xcom [Monday, 27-Jun-2011 08:42:05 EDT]. National Institute of Standards and Technology, Gaithersburg, MD.

[114] O. Klein, Y. Nishina: Zeitschrift für Physik A 52 (1929) 853.

[115] O. Nachtmann: Elementarteilchenphysik Phänomene und Konzepte, rev. ed., Vieweg, Braunschweig (1991).

[116] G. Ranucci, P. Ullucci, S. Bonetti, I. Manno, E. Meroni, A. Preda: Nucl. Instrum. Meth. A 350 (1994) 338.

[117] D. Motta: Ph.D. Thesis, Ruprecht-Karls-Universität Heidelberg, 2004.

[118] S. Lindemann: private communication (2010).

[119] G. Ranucci: Nucl. Instrum. Meth. A 335 (1993) 121.

[120] F. James, M. Roos: Computer Physics Communications 10 (1975) 343.

[121] A. Porta for the Nucifer collaboration: Journal of Phys. Conf. Ser. 203 (2010) 012092.

[122] I.A. Shkrob, M.C. Sauer, A.D. Trifunac, in: C.D. Jonah, B.S.M. Rao (Eds.), Radiation Chemistry: Present Status and Future Trends, Elsevier, Amsterdam, 2001.

[123] C. Aberle: Double Chooz internal document 1928-v2 (2010).

Danksagung

Hiermit möchte ich mich bei allen Leuten bedanken, die mich während der Doktorarbeit unterstützt haben, insbesondere bei:

Prof. Manfred Lindner, der mir die Arbeit als Betreuer ermöglicht hat.

Prof. Klaus Blaum für die Bereitschaft, das Amt des Zweitkorrektors zu übernehmen.

Dr. Christian Buck für die ausgezeichnete, umfangreiche Betreuung der Arbeit.

Dr. Francis X. Hartmann for many hints, ideas and discussions concerning this work and for insights to general physics topics.

Dr. Bernd Reinhold für eine produktive Zusammenarbeit im Bereich der Monte Carlo Simulationen und Detektoranalysen und für interessante Diskussionen.

Dr. Florian Kaether, Dr. Hideki Watanabe und Dr. Conradin Langbrandtner, die immer bereit waren, bei verschiedenen Aufgabenstellungen dieser Arbeit weiterzuhelfen.

Julia Haser und Stefan Wagner für eine gute Zusammenarbeit und für die sehr schöne Arbeitsatmosphäre in unserem Büro.

Ute Schwan und Benjamin Gramlich für freundliche Hilfe im Chemie-Labor.

Dr. Stefan Schönert für Tipps und Vorschläge zur Verbesserung der experimentellen Methoden.

Allen anderen MPIK-Mitarbeiterinnen und Mitarbeitern, die zu einem Gelingen dieser Arbeit beigetragen haben.

Meiner Frau Judith, die mich vor allem in der letzten Phase der Arbeit unter nicht leichten Umständen stark unterstützt hat.

Meinen Eltern Dieter und Waltraud Aberle danke ich für ihre Unterstützung während meiner gesamten Ausbildung.